Numerical study of filament-stretching and step-strain in viscoelastic fluid flows.

Ban, Mohammad Javad

Numerical Study of Filament-Stretching and Step-Strain in Viscoelastic Fluid Flows

by

MOHAMMAD JAVAD BANAAI

B.Sc., M.Sc.

THESIS SUBMITTED TO SWANSEA UNIVERSITY IN CANDIDATURE FOR THE DEGREE OF PHILOSOPHIAE DOCTOR
INSTITUTE OF NON-NEWTONIAN FLUID MECHANICS

Department of Computer Science
Swansea University
JULY 2007

DECLARATION

This work has not previously been accepted in substance for any degree and is not being concurrently submitted in candidature for any degree.

Signed ..... (candidate)

Date ... 2/10/07 .....

STATEMENT 1

This thesis is the result of my own investigations, except where otherwise stated. Where correction services have been used, the extent and nature of the correction is clearly marked in a footnote(s).

Other sources are acknowledged by footnotes giving explicit references. A bibliography is appended.

Signed ..... (candidate)

Date ... 2/10/07 .....

STATEMENT 2

I hereby give consent for my thesis, if accepted, to be available for photocopying and for inter-library loan, and for the title and summary to be made available to outside organisations.

Signed ..... (candidate)

Date ... 2/10/07 .....

Acknowledgements

I wish to express my sincerest thanks to my supervisor Prof. M. F. Webster for his guidance and assistance during this study.

I gratefully acknowledge friendly cooperation, patience, guidance and contributions of all the colleagues in the *Computational Fluid Rheology and Dynamics* (CFRD) lab of the INNFM.

Contents

Abstract

This thesis is concerned with the numerical prediction of two-dimensional viscoelastic filaments under stretching and step-strain within cylindrical-like domains. A hybrid finite element/finite volume (*fe/fv*) scheme has been implemented in this study to solve the governing equations (mass and momentum conservation and constitutive model). A time-stepping procedure is utilised in the *fe/fv* algorithm.

A number of rheological models have been employed to stimulate the desired rheological response. Amongst these is the Oldroyd-B model. This is considered as a strong strain-hardening model being widely used due to its sound physical background and its ability to reproduce qualitative response of polymer melts in rheometrical flows. The linear version of Phan-Thien/Tanner (LPTT) and Giesekus models are also studied to compare simulation results for both dilute and concentrated polymeric systems against the Oldroyd-B model. For fluids with higher degree of strain-hardening, larger stress values cause a reduction in stretching period. In addition, Boger-like response has been represented under increasing levels of solvent within the system. Filament-stretching has been studied under two modes of stretching, exponential and linear for multi-mode and single-mode representations, that has included a numerical study on mesh refinement and algorithms developed for free-surface movement. Bead-like structure formation has been studied for a variety of surface tension coefficients in the absence/presence of body forces. ALE methods and free-surface techniques have been analysed for Volume-of-Fluid (VOF) mesh and Compressed-Mesh (CM) procedures. VOF mesh procedures are outperformed by their CM counterparts. For free-surface curvature to be determined precisely, a particle-tracking approach has been found to be preferable to a kinematic condition for surface-level. Variation of anisotropy levels and ξ-parameter settings has been studied for the Gieskus and LPTT models, respectively.

A further chapter is included where the recently addressed subject of step-strain is considered, to simulate sudden cessation of stretching across the three viscoelastic models. Sudden decline and sharp rise in axial stress have been observed and interpreted alongside filament radial evolution in the context of step-strain. The effect of inertia has been neglected but the effect of capillary and body forces has been brought into consideration. Larger stress values are observed for fluids with a higher degree of strain-hardening, and consequently, cause an increase in the step-strain period. Similar dynamic trends are followed for LPTT fluids with parameter settings of $\xi=\{0.0,0.13\}$ under the context of step-strain. Here, rheological differences would emerge in shear. A paper which has been recently submitted for publication is included in the appendix. There, different aspects of gradual plate halt are discussed.

Chapter 1

Introduction

Computational rheology encompasses design and implementation of numerical methods to perform computer simulation in complex geometries. A major focus is commonly upon the numerical prediction for viscoelastic effects with polymeric liquids.

Over the last quarter century, this complex field of research has attained relative maturity (see [114-119] for reviews).

Complementary theoretical approaches

Structured Polymer solutions and melts, like other rheologically complex fluids, display various non-Newtonian flow properties. Specifically speaking, polymeric solutions are identified as viscoelastic materials implying that the stress endured by a fluid element is a function of the deformation history experienced by that element. Numerous flow phenomena of scientific and industrial relevance [59] arise from

viscoelastic properties, which need to be predicted, understood, and possibly controlled via a combination of numerical methods and appropriate physical models.

Flow-induced evolution of non-Newtonian fluids stems from their internal microstructure which constitutes their rheological properties [120]. Orientation and degree of stretch of the macromolecules conform the relevant microstructure of the flowing polymers. A large number of polymers with a *statistical distribution* of conformations are contained in each macroscopic fluid element. While the polymer conformations along the fluid trajectories are altered by the flow, the macroscopic stress carried by each material element is itself influenced by the polymer conformation distribution within that element. Moreover, the frozen-in microstructure, which develops in processing flows, plays a crucial role in the physical properties of the final product. Thus, rheologists encounter a complicated *non-linear coupling* between rheological behaviour, flow parameters (e.g. geometry and boundary conditions), flow-induced evolution of the microstructure and final product properties. Computational rheology has certainly a key role to play to elucidate this coupling.

Kinetic theory

For polymer solutions, kinetic theory models or melts are most naturally exploited numerically by means of *stochastic simulation* or *Brownian dynamic* methods [121]. Kinetic theory offers several levels of description of a given fluid [122]. For instance, a dilute solution of linear polymers in a Newtonian solvent can be described in some detail by a freely jointed, bead-rod *Kramers chain*, which is made of a number of beads (of order 100) connected linearly by rigid segments. A coarser model of the same polymer is the freely jointed bead-spring chain, consisting of a smaller number of beads (of order 10) connected linearly by entropic springs. Finally, another even coarser model is the single dumbbell, namely two beads connected by a spring. Conspicuously, these models of kinetic theory are not intended to offer description for the chemical structure of the polymer. However, they do exhibit in a more or less detailed fashion the important

features required to describe the evolution of polymer conformations in a macroscopic flow. Recent Brownian dynamics studies of rheometrical flows of Boger fluids using Kramers chains [123-125], bead-spring chains [126-128], and dumbbells [129-130], have cast fresh light on the applicability of available kinetic theory models for dilute polymer solutions. These numerical studies alongside the direct experimental observation of flow-induced conformation for single polymers [131-133], have significantly broadened the scope of polymer dynamics.

The most successful kinetic theory, based on the reptation model, was first proposed by de Gennes and further developed by Doi and Edwards [134] for concentrated solutions or melts of linear polymers. Since the Doi-Edwards theory predicts a non-monotonic dependence of the shear stress as a function of shear rate it cannot be used as such for simulating complex flows. Recently, significant modifications have been proposed to rectify this and other deficiencies of the basic theory [135-139]. More detailed reptation models, suitable for stochastic simulations, have become available [140], with significant progress in extending the theory to branched polymers [141]. Now, reptation-based models can be effectively utilised in the numerical prediction of complex flows. Applying a kinetic theory model to the numerical simulation of complex flows, combined with the macroscopic conservation laws, constitutes the micro-macro approach to computational rheology.

Continuum mechanics

In the macroscopic approach of *continuum mechanics* [18], details of fluid microstructure are not explicitly taken into account. Rather, a suitable *constitutive equation* relates the stress experienced by the macroscopic fluid elements to the deformation history. When the constitutive model is combined with the conservation laws, a set of partial differential (or integro-differential) equations is gathered that can be solved via an appropriate numerical method, such as the mesh-based finite element

technique [142]. The macroscopic approach has been the basis of a large number of publications in computational rheology.

Notably, most constitutive equations employed today in numerical work [64] have been derived from a molecular model of kinetic theory ("pom-pom" constitutive equation is a recent addition to the list for branched polymers [143-144]). Quantitative information on the distribution of polymer conformations within a macroscopic fluid element (in the form of averaged quantities, such as the second moment of distribution of conformations) can be presented through such molecular-based constitutive equations. Unfortunately, in the derivation of a constitutive model from kinetic theory, closure approximations of a purely mathematical nature are often required with potentially significant secondary impact [145]. Thus, with regard to closure, the link with the parent molecular model becomes somewhat corrupted, and explanation of macroscopic findings in molecular terms becomes distorted.

Rheology and computation

The viscoelastic character of any given flow is often measured through a dimensionless Deborah number, *De*, defined as the product of a characteristic deformation rate of the flow and a characteristic relaxation time of the fluid.

While *De* vanishes for Newtonian fluids, it is typically of O(1) or O(10) for the polymer flows of interest here. Developing numerical schemes to obtain accurate numerical solutions for the governing equations at values of *De* of practical interest, whilst implementing a physically-realistic mathematical model, is the major challenge for computational rheologists. Assuming an (ideal) situation, in which reliable computational rheology software is readily available on standard computer hardware, one may consider some of the numerous benefits and opportunities that arise. For example, theoretical rheologists would have a tool for the critical evaluation in complex flows of new theories, whether a constitutive equation, a molecular model, or an improved description of boundary conditions. Complex flows are indeed characterized

by transient kinematics in the Lagrangian sense (i.e. following the fluid elements). By combining shear and elongational deformation, they constitute a harsh testing ground for any theoretical model. Theoretical rheologists would be able to use computational rheology tools to bridge the gap between several levels of description utilised to predict polymer dynamics. An example is the evaluation in complex flows of suitable closure approximations, invariably needed to derive a macroscopic constitutive equation from a molecular model. Non-Newtonian fluid mechanics studies would be most helpful in better understanding of mechanisms responsible for observed macroscopic flow phenomena (such as vortex growth [146-147] and purely-elastic instabilities [148-150]).

Benefits would abound experimentally also. For instance, experimentalists could perform useful computational rheometry trials alongside the experiment to interpret the data more accurately. That is, to translate more clearly measurement (such as torques, forces and deformation) into well-interpreted rheological information. Experimental complications (such as flow inhomogeneity and secondary motion) could be identified and possibly avoided, through improved design of rheometrical equipment, or explicitly taken into consideration at the data reduction phase. In addition, the combination of numerical simulation and flow experiments could be useful to characterize rheological behaviour in complex flows, yielding the optimal rheological model and material parameters for the fluid under study. Finally, and most importantly in industrial practice, the polymer engineer could perform detailed Computer Aided Design (CAD) studies, through which links may be established between molecular architecture of the raw material and final product properties. Improved design can provide the required tools to predict and partially overcome production-related complications (such as extrusion instabilities [151]). An on-line computational rheology model, in concert with appropriate control algorithms, can be a revolutionising idea to provide intelligent physics-based process control techniques. Unrealisable, at present, yet, significant collective advance has been made recently towards this goal.

In summary, computational rheology has largely adopted the macroscopic approach since the pioneering days (circa 1975) of numerical techniques. Recently, the complementary micro-macro approach has become feasible, which involves the coupled solution of the conservation laws and a microscopic model of kinetic theory. This has become a possibility since computer processing capacity has advanced and pushed the boundaries of numerical achievements far beyond expectation.

Numerical methods and applications

In classical CFD technology, a broad spectrum of numerical algorithms is offered based on finite difference, finite element, finite volume, boundary integral, spectral methods, and combinations thereof. Modern computational rheology benefits from similar diversity. Yet, the range of application of a particular numerical technique may be problem and context dependent.

Most published works deal with finite element methods for solving two-dimensional steady-state flows (in the Eulerian sense), employing a differential constitutive equation [118,152-153]. Recently, these methods have been extended to transient stability analysis for complex flows [7,154-155], and the computation of transient problems [156-161]. During the past few years, finite volume methods have also been actively developed, often in combination with finite elements, to solve two- and three-dimensional transient problems [162-165].

Over the last decade, there has been considerable advance with methods for integral models, most notably through the introduction of Lagrangian finite element schemes [166] (wherein the mesh deforms with the fluid) and the Deformation field method [167-168] (which uses a fixed Eulerian grid). These techniques have paved the way for two- and three-dimensional time-dependent simulations using integral models. Further specific methods for high-Reynolds number viscoelastic flows have also been developed, recently [169-171] to study drag-reduction, based on spectral and finite difference schemes and designed for simple geometries. The development of specific

iterative solvers [172] and parallel algorithms [173-176] are examples of algorithmic advance here.

Through the progress made in numerical technology, macroscopic simulation has been exploited over the last few years in two important directions. Firstly, in the evaluation of constitutive equations for solutions and melts within benchmark complex flows, often involving detailed comparison with experimental observation [2,177-188]. Secondly, through rheological prediction, as a useful aid to experimental data reduction [4,14,41,189]. In this manner, computational rheology, though not mature, has already proven a powerful scientific branch of study.

Specifically, this study is concerned with the simulation of viscoelastic fluid flows in filament-stretching and step-strain for axisymmetric configurations. Emphasis is given to interpret the flow response of constitutive models employed and relate differences to their rheometrical behaviour. Shear and extensional viscosity material functions assist to provide insight into the nature of the deformation occurring in complex flows. This information guides to the selection of particular material properties required to stimulate certain desired flow response. Filament-stretching and step-strain processes are present in many industrial processes, such as film blowing. They have also acted as a standard benchmark for testing numerical procedures. In this area, tensile stress dynamics, mid-plane radial evolution and axial velocity are common problem-specific features reported in the literature (theory/experiment) and quoted in the present work.

In numerical simulation, finite element and finite volume algorithms have proven their capability as powerful tools in a number of complex geometries and many areas, such as aircraft design, noise minimization in acoustics and computational rheology. Here, a scheme consisting of a hybrid formulation with finite element and finite volume components is employed to solve the range of flow-settings and configurations investigated.

The basic equations of fluid mechanics and rheology are introduced in chapter two. Explanation for rheometrical flows is given, establishing the basis for a large part of the analysis presented. The focus is on Oldroyd-B, Phan-Thien/Tanner (PTT) and Giesekus models and their material functions, describing some of the numerous modifications proposed for these models. Note that, additional rheological plots are included in other chapters when further relevant.

Chapter three deals with the numerical procedures and techniques employed, the hybrid finite element/finite volume (*fe/fv*) method, explaining the background fundamental equations. This method has been configured to satisfactorily represent viscoelastic flows. The *fe/fv* algorithm has been generated through the consideration of the different mathematical-type of the momentum equation (balance of forces) and the constitutive law for stress. The capability of such an algorithm has been proven in solving problems with Oldroyd-B and Phan-Thien/Tanner models, amongst others.

Modelling of multi-mode viscoelastic flows is considered in chapter four for the three models of Oldroyd-B, LPTT and Giesekus. There, an Arbitrary Lagrangian/Eulerian temporal formulation is coupled with a particle-tracking procedure for free-surface movement. Again, the hybrid finite volume/element method is employed to analyze the transient viscoelastic response of these strain-hardening fluids. The results for single-mode solution response have been compared between a shear-thinning Giesekus and a constant shear viscosity Oldroyd-B model. Hence, the rheology induced through shear-thinning contributions may be gathered. Surface tension and body force effects have been studied parametrically, showing the emergence of bead-like structures and asymmetries.

In chapter five, ALE methods and free-surface techniques are analysed for volume-of-fluid mesh and compressed-mesh procedures. Volume-of-fluid mesh procedures are shown to be outperformed by their compressed-mesh counterparts. When the latter are

coupled to an *ALE*-formulation governing mesh movement, a powerful technique is adopted to access impressively large levels of Hencky-strain. A particle-tracking approach is displayed to be preferable to a kinematic condition for surface-level when free-surface curvature is to be determined precisely. Comparison is made between the results obtained in this chapter and those reported in the literature, in terms of trends and Trouton ratio measures, minimum radial evolution and extensional viscosity predictions.

The subject of chapter six is computational investigation of filament stretching at high Hencky-strain levels. Predictions are extended on the multi-mode representation through elevated Hencky-strains, and single-mode predictions via rheological variation. Additionally, linear versus exponential-stretching configurations are studied under Oldroyd modelling. Computational predictions are compared to theoretical solutions and through discrete mesh refinement for consistency. For such strain-hardening fluids, dominance of tension-thickening over shear-thinning properties is established. Shear effects are studied together with foot pinching aspects and filament mid-plane radial evolution, as a consequence of reduction in hardening and less extension at the filament centre. The importance of each mode has been addressed by comparing and contrasting single- versus multi-mode modelling (multi-timescale). In addition, the appearance of bead-like structures has been explored at elevated Hencky-strain levels.

The numerical modeling of capillary breakup procedures (*CaBER*) with amended Arbitrary Lagrangian/Eulerian (*ALE*) methods is discussed in chapter seven. Various strain-hardening fluids, fluid viscosity ratios and aspect-ratios are studied, again employing a hybrid finite element/finite volume spatial approach. The results are validated against equivalent experimental results recorded in the literature. Bead-like structure formations for filaments with different initial aspect-ratios and viscosity ratios are studied. The influence of surface tension and elastic forces upon these particular filament stretching flows is also explored in this chapter.

Finally, some overall concluding comments are offered in a separate chapter to close.

Chapter 2

Rheology and Governing Equations

In this chapter, rheological models are presented which relate surrounding forces with the internal response from the fluid along with the basic equations of fluid mechanics. This allows for the description of motion and conservation of mass. Models such as Maxwell, Oldroyd-B, Phan-Thien/Tanner, and Giesekus are briefly explained.

2.1 Introduction

The term 'Rheology' founded by Professors M. Reiner and E. Bingham is part of physical science and is primarily concerned with the description of the flow of matter and its deformation. Rheology can be applied to all materials encompassing Hookean elastic solids to Newtonian viscous liquids [109]. Normally, of great interest to rheologists is the flow of *complex* fluids. Any fluid whose viscosity may vary, even at constant temperature and pressure, is termed a non-simple fluid. Paint is a typical example of a non-simple fluid with variable viscosity.

Fluids can be classified as Newtonian and non-Newtonian. Since the 17^{th} century, Newtonian fluids have been considered as a standard to describe general

fluid behaviour. Viscoelastic materials are a special class of non-Newtonian fluids. To explain the term viscoelastic, it is appropriate to define terms of what is called *solid* and *liquid.* If a material does not change its shape continuously when subjected to a given stress, it is referred to as a solid. Alternatively, if it deforms continuously under the action of applied shear/extensional forces and stresses, without consideration of how small the stress or force might be, it is termed a fluid [109]. Solid-like elasticity can often be modelled by means of Hooke's law and liquid-like viscous behaviour through Newton's law. Two different Newtonian fluids may deform at different rates under the action of the same applied shear stress. For instance, water exhibits far less resistance to deformation than Glycerine. The Newtonian viscosity is only a function of temperature and pressure, and is independent of time and shear rate. Water, milk, mineral oil and sugar solutions are examples of Newtonian fluids. By contrast, viscoelastic materials are those which exhibit both solid-like and liquid-like response. A material represents viscoelastic properties if, following a cessation of applied stress, the time of the fluid to adopt a rest state (relaxation time) can be observed or measured. The viscosity of such fluids at a given temperature and pressure may be a function of other factors such as shear rate. Non-Newtonian fluids can be categorized as having time-dependent or time-independent behaviour. The viscosity of a non-Newtonian time-independent fluid is a function of temperature and pressure. Shear-thinning or pseudo-plastic fluids are those for which viscosity is inversely proportional to shear rate. Most non-Newtonian fluids are shear-thinning; examples include fruit juices, ketchup, paint, shampoo, colloidal suspensions and slurries. In contrast, the term shear-thickening (or dilatant) applies to fluids if their viscosity increases with rising shear-rate. Wet sand and suspensions of starch are two examples of such fluids. Shear-thinning fluids have a broader range of industrial application compared to their shear-thickening counterparts. Also, there is a special class of non-Newtonian viscous fluids which are termed Bingham plastics, which resist a small shear stress (yield stress) prior to the onset of flow. These fluids behave like Newtonian fluids above a certain yield stress

value. Toothpastes, tomato paste, grease, drilling mud and clay suspensions are all examples of this type of fluid.

In contrast, for time-dependent non-Newtonian fluids viscosity is a function of temperature, shear-rate and time for which shear stress is applied. The term thixotropic is applied to fluids such as yoghurt and paint, which display decreasing viscosity in time; as opposed to rheopectic fluids, which exhibit a viscosity proportional to time under a constant applied force, e.g. gypsum paste.

Continuum theory, in which fluid microstructure detail is not explicitly taken into account, constitutes the research of the present study. Ideally, intermolecular distances and the alteration of properties induced by these lengths are ignored. Rather, properties are averaged for an arbitrary large number of molecules that represent a fluid *element* adequately. The response of the element under deformation is obtained via energy, mass and force balances (*conservation laws*). These are applied through differential and integral operators over small volumes, yet sufficiently large to satisfy the continuum assumption. Real material response approximation in flow is performed under the context of both, rheology and continuum mechanics. Employment of *Constitutive relations* bridges the gap between these two fields. Since constitutive equations are typically derived from a molecular model of kinetic theory, they contain specific information (internal stress, pressure, molecular extension) which is responsible for the idealized fluids behaviour.

2.2 Rheometrical flows

The study of fluid behaviour in *simple flows* is regarded as essential in correlating the response of a fluid in more complex flow-settings. *Simple shear* and *extensional deformation* are examples of such simple *rheometrical* flows.

2.2.1 Simple shear flow

Considering any fluid confined between two parallel planes, separated by a gap (height) of 'h', with the upper-plate moving at constant velocity U, the force per unit area (stress σ) necessary to maintain the constant velocity of the plate is proportional to the velocity gradient (shear-rate $\dot{\gamma}$), i.e.

$$\sigma = \eta_s(\dot{\gamma})\dot{\gamma}. \tag{2.1}$$

Where η_s (viscosity or *resistance to flow*) is a constant coefficient of proportionality for a Newtonian fluid. Under this type of flow, a volume of fluid is deformed, losing its original shape. For example, if a cubic fluid element is observed at any other time, the fluid volume has internal angles that may differ from 90° (see Fig. 2.1).

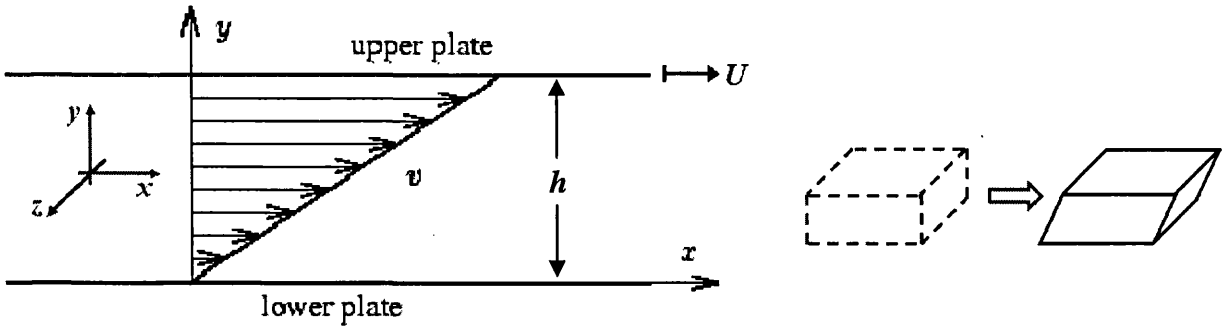

Fig. 2.1. Schematic representation of simple shear flow.

Under simple shear deformation, the velocity field $\mathbf{u} = (u,v,w)$ and deformation-rate tensor $\mathbf{d}$ are represented as:

$$\begin{aligned} u(y) &= \dot{\gamma} y \\ v &= 0 \\ w &= 0 \end{aligned} \qquad \text{and} \qquad \mathbf{d} = \frac{1}{2}\begin{bmatrix} 0 & \dot{\gamma} & 0 \\ \dot{\gamma} & 0 & 0 \\ 0 & 0 & 0 \end{bmatrix}. \tag{2.2}$$

Other properties varying between Newtonian and non-Newtonian fluids are the first and second normal stress differences, N_1 and N_2, which are zero for Newtonian fluids and for non-Newtonian fluids, are defined as follows:

$$N_1(\dot{\gamma}) = \sigma_{xx} - \sigma_{yy} = \psi_1(\dot{\gamma})\dot{\gamma}^2, \tag{2.3}$$

$$N_2(\dot{\gamma}) = \sigma_{yy} - \sigma_{zz} = \psi_2(\dot{\gamma})\dot{\gamma}^2, \tag{2.4}$$

normally leading to relations,

$$N_1 > 0 \qquad \text{and} \qquad N_1 >> |N_2|. \tag{2.5}$$

2.2.2 Extensional flows

In uniaxial deformation, the fluid volume is *stretched* in one particular direction, and due to incompressibility, compression occurs in the remaining axes. The fluid sample as depicted in

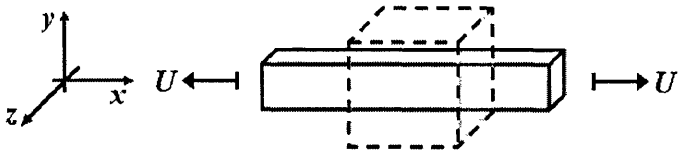

Fig. 2.2. Schematic representation of pure extensional deformation

Fig. 2.2 is assumed to be a cubic shape control volume at a chosen initial time (dotted border lines). Subsequent to stretching deformation, the fluid volume is extended uniaxially (x), whilst undergoing compression along the remaining two (y, z) axes, to preserve the original volume.

The constant deformation-rate in this elongational flow is termed the strain-rate or stretch-rate $\dot{\varepsilon}$. In this particular case, lengths are modified and as there is no shear

deformation, the fluid volume maintains essentially the same internal angles. The velocity field and deformation-rate tensor can be expressed as:

$$\begin{aligned} u(x) &= \dot{\varepsilon}\, x \\ v(y) &= -\tfrac{1}{2}\dot{\varepsilon}\, y \\ w(z) &= -\tfrac{1}{2}\dot{\varepsilon}\, z \end{aligned} \qquad \text{and} \qquad \mathbf{d} = \begin{bmatrix} \dot{\varepsilon} & 0 & 0 \\ 0 & -\tfrac{1}{2}\dot{\varepsilon} & 0 \\ 0 & 0 & -\tfrac{1}{2}\dot{\varepsilon} \end{bmatrix}. \tag{2.6}$$

The resistance or extensional viscosity can then be related to the normal stress differences and deformation rate through the relationship,

$$\sigma_{xx} - \sigma_{yy} = \sigma_{xx} - \sigma_{zz} = \eta_e(\dot{\varepsilon})\,\dot{\varepsilon}. \tag{2.7}$$

As expressed above, for Newtonian fluids, η_e is constant under all strain-rates (stretch-rates), and the following relationship is always satisfied:

$$\eta_e = 3\eta_s. \tag{2.8}$$

In addition, at low deformation-rates, all fluids including those representing viscoelastic properties, satisfy(2.8), that is,

$$\eta_e(\dot{\varepsilon} \to 0) = 3\eta_s(\dot{\gamma} \to 0). \tag{2.9}$$

Pure extensional deformation takes place in contraction and contraction/expansion flows along the centreline, whilst close to the contraction a combination of shear and extension is present.

Trouton ratio (Tr) is defined as the ratio of extensional viscosity to shear viscosities. Jones et al. [29] proposed the following definition for the Trouton ratio to relate $\dot{\gamma}$ and $\dot{\varepsilon}$ and evaluate shear and extensional viscosities:

$$Tr = \frac{\eta_e(\dot{\varepsilon})}{\eta_s(\dot{\gamma} = \sqrt{3}\,\dot{\varepsilon})}. \tag{2.10}$$

For Newtonian fluids, Tr is three for all values of $\dot{\varepsilon}$ and for viscoelastic fluids this ratio is anticipated to satisfy the following relation at very small deformation rates,

$$Tr\left(\dot{\varepsilon} \to 0\right) = 3. \tag{2.11}$$

2.3 Constitutive models and basic equations

At every instant in the type of flow problems considered, the basic principle of mass conservation must be satisfied. This principle is expressed mathematically by the continuity equation (see [110]),

$$\frac{\partial \rho}{\partial t} + \nabla \cdot \left(\rho \mathbf{u}\right) = 0. \tag{2.12}$$

In equation(2.12), ρ is the fluid density, $\mathbf{u}$ the velocity vector and t, time. For incompressible flows, this reduces to

$$\nabla \cdot \mathbf{u} = 0. \tag{2.13}$$

Newton's second law of motion can be applied to a fluid element, this law states that the change of linear momentum in a system is equal to the sum of the forces acting upon it (also known as the principle of conservation of linear momentum). The forces acting on the system may be classified into two types: *body* forces acting on the volume of fluid, such as gravitational and electromagnetic forces, and *internal* forces, representing the friction between fluid molecules, affecting the fluid volume through its bounding surfaces. In differential form this is stated as [112]:

$$\rho\left(\frac{\partial \mathbf{u}}{\partial t} + \mathbf{u} \cdot \nabla \mathbf{u}\right) = -\nabla p + \nabla \cdot \mathbf{T} + \rho \mathbf{F}, \tag{2.14}$$

where p is the pressure, $\mathbf{T}$ is the stress without the hydrostatic contribution* and accounts for viscous/viscoelastic phenomena. Body forces, $\mathbf{F}$, are neglected since contributions from gravity are less significant than those from other forces such as pressure or stress.

As discussed above, Newtonian fluids represent a constant viscosity in shear and elongational flows. Another characteristic is the instantaneous response to deformation. The general expression for the Newtonian (incompressible) model is,

$$\mathbf{T} = 2\mu\mathbf{d}. \tag{2.15}$$

Navier-Stokes equations are constructed upon substitution of equation (2.15) into (2.14) . All flow settings in this study are assuming as under isothermal conditions and laminar flow. In equation (2.15), the deformation-rate tensor for general flows is defined as,

$$\mathbf{d} = \tfrac{1}{2}\left(\nabla\mathbf{u} + [\nabla\mathbf{u}]^{\mathrm{T}}\right). \tag{2.16}$$

Constitutive or rheological models must satisfy the following basic criteria to adequately represent fluid response from a mathematical point of view [111].

- *Determination of stress*: stress for a viscoelastic fluid is determined through the history of the motion of that body.
- *Local action*: stress at any point in the fluid is determined from the history of the deformation of an arbitrarily small vicinity of fluid around that point.
- *Frame invariance*: the form of constitutive equations must be independent of the coordinate system.

* Tensor $\boldsymbol{\sigma}$ is called the Cauchy stress tensor and is related to the tensor $\mathbf{T}$ by $\boldsymbol{\sigma} = -p\mathbf{I} + \mathbf{T}$, where $\mathbf{I}$ is the identity tensor.

- *Invariance under superposed rigid body motion*: the constitutive equations must reflect independence of absolute motion in space; that is, if the equations are correct, any rigid body motion imposed on the whole fluid must not affect the response of the material.

2.3.1 Maxwell and Oldroyd-B models

The Maxwell model [113] is considered as the first to model viscoelastic fluids via a differential system of equations. The one-dimensional form of this model is obtained by a combination of a Hookean spring and a Newtonian dashpot in series (see Barnes et al. [109]).

$$\mathbf{T}+\frac{\mu_0}{G_0}\frac{\partial}{\partial t}\mathbf{T}=2\mu_0\mathbf{d}, \tag{2.17}$$

where G_0 and μ_0 are the elastic modulus and the viscosity, respectively. The relaxation time for a Maxwell fluid is defined by $\lambda=\mu_0/G_0$.

Applying the principles stated above, this equation (2.17) can be re-written as the upper-convected Maxwell (UCM) model,

$$\mathbf{T}+\lambda\overset{\nabla}{\mathbf{T}}=2\mu_0\mathbf{d}, \tag{2.18}$$

or the lower-convected (LCM) form

$$\mathbf{T}+\lambda\overset{\Delta}{\mathbf{T}}=2\mu_0\mathbf{d}, \tag{2.19}$$

where for an arbitrary tensor $\mathbf{A}$, the upper- ($\overset{\nabla}{\mathbf{A}}$) and lower- ($\overset{\Delta}{\mathbf{A}}$) convected derivatives are defined, respectively, as

$$\overset{\nabla}{\mathbf{A}} = \frac{\partial}{\partial t}\mathbf{A} + \mathbf{u}\cdot\nabla\mathbf{A} - (\nabla\mathbf{u})^{\mathrm{T}}\cdot\mathbf{A} - \mathbf{A}\cdot\nabla\mathbf{u}, \tag{2.20}$$

$$\overset{\Delta}{\mathbf{A}} = \frac{\partial}{\partial t}\mathbf{A} + \mathbf{u}\cdot\nabla\mathbf{A} + (\nabla\mathbf{u})^{\mathrm{T}}\cdot\mathbf{A} + \mathbf{A}\cdot\nabla\mathbf{u}. \tag{2.21}$$

The Maxwell model does not contain a term to account for solvent presence (purely viscous component). To overcome this, a retardation time, λ_J, is introduced in equation (2.18):

$$\mathbf{T} + \lambda\overset{\nabla}{\mathbf{T}} = 2\mu_0\left(\mathbf{d} + \lambda_J\overset{\nabla}{\mathbf{d}}\right). \tag{2.22}$$

Equation (2.22) is known as the Oldroyd-B model. However, numerical (discretisation) difficulties arise when dealing directly with the term $\overset{\nabla}{\mathbf{d}}$, due to the presence of second-order derivatives of velocity. Hence, the model is split into two different equations, one for the polymeric component and other for the solvent, where

$$\boldsymbol{\tau} + \lambda\overset{\nabla}{\boldsymbol{\tau}} = 2\mu_1\mathbf{d}, \tag{2.23}$$

$$\boldsymbol{\tau}_s = 2\mu_2\mathbf{d}, \tag{2.24}$$

$$\mathbf{T} = \boldsymbol{\tau}_s + \boldsymbol{\tau}, \qquad \mu_0 = \mu_1 + \mu_2, \qquad \text{and} \qquad \lambda_J = \frac{\mu_2}{\mu_1 + \mu_2}\lambda. \tag{2.25}$$

In equations (2.23)-(2.25), $\boldsymbol{\tau}$ and μ_1 denote the stress and zero shear-rate viscosity contributions from the polymeric component, respectively; in a similar fashion, $\boldsymbol{\tau}_s$ and μ_2 are the contributions to the solvent part. The extensional viscosity predicted by Maxwell and Oldroyd-B models tends to infinity as the strain-rate approaches $1/(2\lambda)$. Additionally, the shear viscosity is constant for all shear-rates

and the second normal stress difference is zero (except for the lower-convected Maxwell model, which excessively predicts N_2).

A more reasonable prediction of N_2 is achieved by using a combination of lower-convected operator and the upper-convected derivative. The Johnson-Segalman model introduces an operator consisting of both convected derivatives. Nevertheless, at low strain-rates, the extensional viscosity remains unbounded. The model is:

$$\mathbf{T}+\lambda\overset{\square}{\mathbf{T}}=2\mu_0\mathbf{d}, \tag{2.26}$$

where, on an arbitrary tensor **A**, the new operator is defined as:

$$\overset{\square}{\mathbf{A}}=\left(1-\tfrac{1}{2}\zeta\right)\overset{\nabla}{\mathbf{A}}+\tfrac{1}{2}\zeta\overset{\Delta}{\mathbf{A}}=\overset{\nabla}{\mathbf{A}}+\zeta\left(\nabla\mathbf{u}^{\dagger}\cdot\boldsymbol{\tau}+\boldsymbol{\tau}\cdot\nabla\mathbf{u}\right). \tag{2.27}$$

ζ is the parameter controlling the proportion of the two derivatives, and generally lies within the interval $0\le\zeta\le 2$, where $N_2/N_1=-\frac{1}{2}\zeta$ and $\zeta=0.2$ yields reasonable N_2 (see reference [111]).

2.3.2 Phan-Thien/Tanner models

Phan-Thien/Tanner (PTT) constitutive equations correct the prediction of unphysical values of extensional viscosity with the Johnson-Segalman model. The creation and destruction of network junctions are considered in this model. Extension-hardening/softening and shear-thinning are predicted by this class of models, which is expressed as:

$$f(\boldsymbol{\tau})\mathbf{T}+\lambda\overset{\square}{\mathbf{T}}=2\mu_1\mathbf{d}, \tag{2.28}$$

where, the extra function $f(\boldsymbol{\tau})$ is,

$$f(\boldsymbol{\tau}) = \begin{cases} e^{\left(\varepsilon_{PTT}\frac{\lambda}{\mu_1}tr(\boldsymbol{\tau})\right)} & \textit{exponential,} \\ 1+\varepsilon_{PTT}\dfrac{\lambda}{\mu_1}tr(\boldsymbol{\tau}) & \textit{linear.} \end{cases} \tag{2.29}$$

The linear form is extracted from a Taylor series expansion of the exponential form. Both forms predict shear-thinning behaviour and extension-hardening; strain-softening is anticipated for the exponential form. Alternatively, the linear form displays sustained hardening.

2.3.3 Giesekus model

In 1966, a class of constitutive equations was proposed by Giesekus based on anisotropic drag. The motivation behind adoption of the model comes from considering how the relaxation of an elastic dumbbell is modified when being surrounded by other oriented dumbbells. As such, Giesekus attempted to derive a theory for concentrated melts or solutions by starting from the simple dumbbell theory for dilute solutions. The upper-convected Maxwell (UCM) equation 2.18 is the appropriate constitutive equation for a dumbbell in dilute solution and can be expressed in the following form,

$$\overset{\nabla}{\boldsymbol{\sigma}} + \frac{8kT\beta^2}{\zeta}(\boldsymbol{\sigma} - G\boldsymbol{\sigma}) = \mathbf{0} \tag{2.30}$$

Here ζ is the bead friction coefficient and the term $8kT\beta^2/\zeta$ is the reciprocal relaxation time, $1/\lambda$. The speculation of Giesekus was that anisotropic drag was created by the surrounding sea of oriented molecules; thus, ζ becomes direction dependent. To represent this, Giesekus replaced $8kT\beta^2/\zeta$ by anisotropic mobility tensor, $\mathbf{B}/\lambda$:

$$\lambda\overset{\nabla}{\boldsymbol{\sigma}} + \mathbf{B}\cdot(\boldsymbol{\sigma} - G\boldsymbol{\sigma}) = \mathbf{0} \tag{2.31}$$

B is a function of the anisotropy of the orientation of surrounding molecules and hence is dependent on the state of stress in the material. At equilibrium, the stress is isotropic, so **B** must be isotropic also; i.e. **B** = **σ** when $\boldsymbol{\sigma} = G\boldsymbol{\sigma}$. When the stress becomes anisotropic, so does **B**. Giesekus assumed that the anisotropies in **B** and **σ** are proportional :

$$\mathbf{B} - \boldsymbol{\sigma} = \alpha\left(\frac{\boldsymbol{\sigma}}{G} - \boldsymbol{\sigma}\right) = \mathbf{0}. \tag{2.32}$$

Here α is an empirical constant of proportionality. The resulting constitutive equation can be written, viz.,

$$\lambda \overset{\nabla}{\boldsymbol{\tau}} + \boldsymbol{\tau} + \frac{\alpha}{G}\boldsymbol{\tau}^2 = 2G\lambda\mathbf{D}, \tag{2.33}$$

where $\boldsymbol{\tau} = \boldsymbol{\sigma} - G\boldsymbol{\delta}$ is a stress tensor that differs from **σ** by the isotropic constant, $G\boldsymbol{\delta}$. For compressible fluids, the stress tensor is only defined to within an isotropic constant, hence either **δ** or **τ** can be used. The simple Giesekus equation, eq. (2.33); differs from the UCM equation by a term quadratic in stress.

The minimum and maximum anisotropies correspond to α=0 and α=1, respectively. α may not lie outside this range; if it does stress magnitudes may rise rather than relax when deformation ceases. When α=0 (isotropic drag), the upper-convected Maxwell (UCM) is recovered. As α changes from zero to unity, strain softening increases from that of the UCM equation, which is defined to have no strain-softening.

2.4 Non-dimensional form

Under isothermal conditions, the governing equations for this incompressible, viscoelastic flow may be written as

$$\mathrm{Re}\frac{\partial \boldsymbol{u}}{\partial t} = -\mathrm{Re}\,\boldsymbol{u}_c.\nabla\boldsymbol{u} - \nabla p + \nabla.(2\mu_2\boldsymbol{d} + \boldsymbol{\tau}) + \boldsymbol{F}_g, \tag{2.34}$$

$$De\frac{\partial \boldsymbol{\tau}}{\partial t} = -De\boldsymbol{u}_c.\nabla\boldsymbol{\tau} - f\boldsymbol{\tau} + 2\mu_1\boldsymbol{d} + De(\boldsymbol{L}\cdot\boldsymbol{\tau} + \boldsymbol{\tau}\cdot\boldsymbol{L}^{\dagger}) - De\cdot\xi(\boldsymbol{d}\cdot\boldsymbol{\tau} + \boldsymbol{\tau}\cdot\boldsymbol{d}) - \alpha\frac{De}{\mu_1}\boldsymbol{\tau}\cdot\boldsymbol{\tau}. \tag{2.35}$$

Eq. (2.13) can be rewritten in the non-dimensionalized form. 'α' is related to the Giesekus model alone and is termed as the mobility factor which is associated with anisotropic material response. The remaining parameter and function definitions, over the models in question vary, viz.,

Oldroyd-B: $f=1,\ \xi=0,\ \alpha=0;$

LPTT: $f=\{1+(\varepsilon_{ptt}De/\mu_1)*tr(\tau)\};\ 0\le\xi\le2;\ \alpha=0;$

Giesekus: $f=1,\ \xi=0,\ 0\le\alpha\le1.$

In chapter seven and following that in (Matallah, Banaai et al. 2006), for the default LPTT model, we use $\varepsilon_{ptt}=0.035$, $\xi=0$ and for Giesekus, $\alpha=0.3162$. When LPTT ($\xi=0.13$) is taken instead, slightly earlier shear-thinning properties are revealed, however, with little impact particularly for the step-strain problem. With, $\boldsymbol{u}$, p and $\boldsymbol{\tau}$ denoting the fluid velocity, the hydrodynamic pressure and the polymeric extra-stress, respectively, the convective velocity is defined as $\boldsymbol{u}_c = \boldsymbol{u} - \boldsymbol{u}_m$, where $\boldsymbol{u}$ is the fluid velocity, and $\boldsymbol{u}_m$ is the mesh velocity. The choice of mesh velocity defines the Arbitrary Lagrangian/Eulerian formulation employed. The total viscosity μ_0 comprises polymeric (μ_1) and Newtonian solvent (μ_2) contributions, so that $\mu_0=\mu_1+\mu_2$; $\boldsymbol{d} = (\boldsymbol{L}+\boldsymbol{L}^{\dagger})/2$ corresponds to the rate-of-deformation tensor and $\boldsymbol{L}^{\dagger} = \nabla\boldsymbol{u}$, the velocity gradient. The ratio of gravitational to viscous forces is represented as $\boldsymbol{F}_g$ and given by $\boldsymbol{F}_g$ = $(0,\ F_g)$= $(0,\frac{\rho L^2}{U\mu_0}g)$, with axial coefficient $F_g=Bo/Ca$. This extracts the Bond number, Bo, and the surface tension Capillary number, Ca. The non-dimensional group numbers such as Reynolds number (*Re*), Deborah number (*De*), Bond number (*Bo*), and capillary number (*Ca*) are defined as

follows:

$$Re = \frac{\rho \dot{\varepsilon}_0 L_0^2}{\mu_0},\ De = \lambda \dot{\varepsilon}_0,\ Bo = \frac{\rho L_0^{\ 2}}{\chi} g,\ Ca = \frac{\mu_0 \dot{\varepsilon}_0 L_0}{\chi}. \tag{2.36}$$

The scales and non-dimensional variables for length, time, velocity, pressure, stress and viscosity are defined as follows,

$$\boldsymbol{x} = \boldsymbol{x}^* L,\ t = (\dot{\varepsilon}_0)^{-1} t^*,\ \boldsymbol{v} = \boldsymbol{v}^* U,\ p = \mu_0 \frac{U}{L} p^*,\ \boldsymbol{\tau} = \mu_0 \frac{U}{L} \boldsymbol{\tau}^*,\ \mu = \mu_0 \mu^*. \tag{2.37}$$

Here, the initial filament length (L=L_0) is adopted as the length-scale and the time-scale is derived from the initial stretch-rate ($\dot{\varepsilon}_0$). Thus, the velocity scale is yielded as equivalent to the initial plate-velocity (U_0= $\dot{\varepsilon}_0 L_0$).

Chapter 3

Numerical Techniques[†]

3.1 Introduction

In the past decades numerical methods have constantly been in the focus of attention owing to their broad applications in providing solutions in scientific and engineering realms. Mathematical models which are able to describe the physical phenomena are essentially the first step in adopting numerical methods. Based on mathematical models appropriate equations can be constructed in terms of velocity, pressure, stress, temperature, viscosity and other physical parameters. These equations can be either in integral or differential forms, for which analytical solutions are desired. However, due to the non-linear nature of the governing equations describing the physical phenomena analytical solutions are generally unavailable.

[†] The basic numerical techniques employed in this thesis are those developed already in the Institute of Non-Newtonian Fluid Mechanics (INNFM), Swansea group. These have been extended by incorporating the associated constitutive equations and algorithms discussed in this thesis.

Hence, numerical solution is required for which schemes have been developed to obtain approximate solutions for systems of partial differential equations which describe fluid flow. Such techniques can be applied to incompressible and compressible flows alike, for both Newtonian and non-Newtonian fluids. Due to the appropriate nature of these numerical solutions, accuracy, stability and convergence are crucially important to ensure that numerical methodologies are as applicable and reliable as possible. One may classify spatial numerical techniques into three main methodologies; namely, Finite Difference (FD) [85], Finite Element (FE) [86] and Finite Volume (FV) methods [87, 88]. Each of those methods has both advantages and disadvantages. For example, the finite difference method is coherent and straightforward to implement but becomes more convoluted and less accurate for complex domains and stress boundary conditions, particularly in dealing with deforming free-surface domains. With this method the strong equation is maintained and point-wise difference operators approximate differential operators. Consequently, attention has been switched to integral-variational methods (finite element). A comparison between the three numerical methods has been made in [89, 90]. Published articles of Keunings [91] and Walters and Webster [92] draw such comparison for non-Newtonian flows.

Ritz [93] was the first to propose an approximate method of a potential function in terms of trail functions with unknown coefficients for use in structural engineering analysis. Then, Courant [94] made a remarkable improvement over the method of Ritz through the idea of triangular-area discretization, defining piece-wise linear polynomials for each triangle. Thereafter, Turner et al. [95] and Argyris [96] applied the triangular element approximation to solve planar structurally stress problems. Having incorporated these ideas, Clough [97] introduced a fully-fledged development of the Finite Element method (FEM). Though the fundamental concepts behind the FEM were originated in mid-1950s from structural engineering analyses, due to its flexibility and robust mathematical basis, it has been employed in non-structural problems as well. Among the first to apply FEM to field problems, were

Zeinkiewicz and Cheung [98]. They applied this method to such field problems as irrotational flow, involving the solution of Laplace and Poisson equations. Early work on viscous flows using finite element methods was published by Martin [99]. Afterwards, Oden [100] reported solving Navier-Stokes equations via FEM, by virtue of a velocity-pressure primitive variable formulation. Later, Chang et al. [101] used a stream-function/vorticity formulation for the same purpose. An alternative formulation, with split stages, is the pressure-correction scheme. This approach has been used widely in FEM, FV and FD discretised forms- see SIMPLE scheme under FV developed by Patankar & Spalding [87]. There are many reviews and applications of FEM which indicate the method employment in a variety of areas.

The FEM is based upon integral formulations which may be derived either from variational or weighted-residual methods. Rayleigh-Ritz [103] and Galerkin are two most popular methods used; others include sub-domain and least-squares methods. The Galerkin method is straightforward to implement and obtain a consistent approximation to the differential equation system. This method is optional for elliptic self-adjoint problems. In addition, it has the flexibility to accurately discretise complicate-shaped boundary conditions. These features have made the Galerkin method the most utilized and popular method, in which both weighting (test) and interpolation (trial) functions are chosen over the same spaces.

Unfortunately, when conventional Galerkin methods are applied to non-self adjoint (elliptic) equations, that may include significant convection terms, a number of deficiencies may emerge. Among them, one can observe spatial wiggles in solution or lack of monotonicity, which may appear when downstream boundary conditions cause rapid solution changes [105]. Negative artificial diffusion [104] is another disadvantage of the Galerkin method which can lead to under-diffusive solutions. It has been found that addition of a suitable amount of artificial diffusion can lead to stabilized solutions. To overcome such deficiencies a variety of stabilization techniques have been introduced, including upwinding, Petrov-Galerkin

and streamline diffusion approximations. Such techniques can be applied consistently, or not, and variants may appear in strong (FD-upwinding) or weak-form (FEM/FV). The most common forms developed have been based upon:

(i) artificial diffusion, a correction to physical diffusion,

(ii) Petrov-Galerkin techniques,

(iii) Modifications of convection terms through quadrature rules.

Upwinding techniques were first introduced by Christie et al. [102] and Heinrich et al. [190] for 1-D and 2-D problems, respectively. Subsequently, Hughes [103] applied quadrature rules to convection terms and presented a method to generate upwinding elements. Although these techniques were effective for 1-D problems, they were shown lacking when applied to multidimensional instances as a result of crosswind-diffusion [104]. Brooks and Hughes [105] later adopted a formulation termed, 'streamline-upwinding/Petrov-Galerkin', in order to remove crosswind-diffusion. Despite significant advances to date, convection-diffusion problems are yet amongst the most challenging to numerical solution.

In recent years, FV methods have emerged as alternative spatial discretisation techniques in providing solutions to viscoelastic problems. The incentive behind this stems from the nature of the constitutive equation for stress that, in differential form, assumes a 1^{st}-order, space-time, hyperbolic representation. The conservation features of such equations may well suit FV discretisation. For the momentum-continuity sub-problem which is essentially of parabolic-hyperbolic type, FE formulation provides an optimal fit. Thus, a combination of both FE and FV methods has been sought, leading to the production of hybrid FE/FV methods [106,107]. Such methods are now well-established and play a significant role in the simulation of complex viscoelastic flows. A variant of hybrid FE/FV methods is used in the present work.

3.1.1 Brief description of Galerkin finite element method

The finite element method deals with dividing the spatial problem domain (geometry) into a number of finite elements (mesh) over which solution is sought. As an example, consider the following time independent Poisson equation,

$$\frac{\partial^2 u}{\partial x^2} = f(x). \tag{3.1}$$

Suitable functions (typically polynomial type of first or second order) can be used to interpolate the unknown solution variables. The problem residuals are then weighted and applied to each of the finite elements belonging to the original domain. Interpolation per finite element takes the form,

$$u(x) = \sum_{i}^{nt} \phi_i(x) u_i , \tag{3.2}$$

where $\phi_i(x)$ are the trial functions, u_i are unknown solution nodal values and nt is the number of nodes in the generic finite element. Substituting (3.2) in (3.1) and inserting $w_j(x)$ as weighting functions yields,

$$\int_{\Omega_e} \frac{\partial^2}{\partial x^2}\left[\phi_i(x) u_i\right] w_j(x)\, d\Omega_e = \int_{\Omega_e} f(x) w_j(x)\, d\Omega_e . \tag{3.3}$$

With the Galerkin method, weighting functions and trial functions are selected from the same space, that is $w_j(x) = \phi_j(x)$. Then, integration by parts yields,

$$\left.\frac{\partial \phi_i(x)}{\partial x}\phi_j(x)\right|_{\Gamma_e} - u_i \int_{\Omega_e} \frac{\partial \phi_i(x)}{\partial x}\frac{\partial \phi_j(x)}{\partial x} d\Omega_e = \int_{\Omega_e} f(x)\phi_j(x) d\Omega_e . \tag{3.4}$$

Summation of all elemental contributions leads to system assembly over the geometry ($\Omega = \sum_e \Omega_e$). When solution values are known at the outer domain boundary

(Dirichlet conditions), the term evaluated on the boundary (Γ_e) of the element is set to zero; otherwise, it cancels out on interior elements. Neumann conditions (natural, weak-form) would be incorporated with the full equations. In the present study when velocity is imposed on boundaries, Dirichlet conditions apply; on other boundaries, such as free-surface, Neumann conditions apply.

In matrix notation, the full system of equations resulting from (3.4) can be expressed as

$$\mathbf{K}\mathbf{u} = \mathbf{b}, \tag{3.5}$$

with nodal values contained in the column-matrix $\mathbf{u}$. $\mathbf{K}$ and $\mathbf{b}$ may be evaluated either analytically or numerically and defined as follows,

$$K_{ij} = \int_{\Omega} \frac{\partial \phi_i(x)}{\partial x} \frac{\partial \phi_j(x)}{\partial x} \mathrm{d}\Omega, \qquad b_j = \int_{\Omega} f(x)\phi_j(x)\mathrm{d}\Omega. \tag{3.6}$$

Configuration of all elements with their contribution into a total system must encompass the specified boundary conditions. For instance, since certain values are known and imposed in this example, accordingly nodal values are specified on the domain boundary (Γ) and may be substituted directly into the corresponding positions for $\mathbf{K}$, $\mathbf{b}$ and deleted from the solution vector, $\mathbf{u}$. Direct or iterative algebraic solution procedures are required to solve equation (3.5), depending on the size of the problem, which is governed by the number of elements/nodes and the shape functions involved.

3.1.2 Brief description of the finite volume method

With the finite volume technique, an integral expression for a conservation law is considered, rather than solving the differential form directly. The technique can be applied to the differential constitutive equation, which is integrated over an *fv*-subdomain. This can be classified as a subclass of the finite element procedure with

weighting functions set to unity, $w(x)=1$. A conservation law can be written in a general integral form as,

$$\frac{\partial}{\partial t}\int_{\Omega}\varsigma\,\mathrm{d}\Omega+\int_{\Gamma}\mathbf{f}\cdot\mathbf{n}\,\mathrm{d}\Gamma=\int_{\Omega}\mathbf{q}\,\mathrm{d}\Omega, \tag{3.7}$$

where ς can be any quantity to be 'conserved' such as mass, momentum or energy; $\mathbf{f}$ is its flux (divisable into diffusive and convective parts), of outward unit normal vector $\mathbf{n}$ across the surface Γ surrounding the volume Ω; and $\mathbf{q}$, body forces or source terms. On each *fv*-cell and in cell-centred discrete form, mean values can be expressed as,

$$\varsigma_i=\frac{1}{|\Omega_i|}\int_{\Omega_i}\varsigma\,\mathrm{d}\Omega_i. \tag{3.8}$$

Applying (3.7) on a single finite volume, with mean values ς_i and q_i yields,

$$\frac{\partial}{\partial t}\varsigma_i+\frac{1}{|\Omega_i|}\sum_k\int_{\Gamma_k}\mathbf{f}\cdot\mathbf{n}_k\mathrm{d}\Gamma_k=q_i, \tag{3.9}$$

where k and Γ_k are the number of 'faces' of the *fv*-subcell and the area of those faces, respectively. An advantage of the FVM is the natural conservation of variables in integral form on each individual *fv*-cell, and hence, over the entire domain.

Mean value approximation can be carried out following numerical integration procedures,

$$\int_{\Omega_i}\varsigma(x)\,\mathrm{d}\Omega_i\approx\sum_{i=0}^{nc}\varphi_i\varsigma_i(x), \tag{3.10}$$

where nc is the number of nodes and $\varphi_i\geq 0$ are weights of the integration procedure. Surface integrals can be approximated as,

$$\int_{\Gamma_k} \mathbf{f} \cdot \mathbf{n}_k \mathrm{d}\Gamma_k \approx \sum_k F_k \,. \tag{3.11}$$

F_k is an approximation of $\mathbf{f} \cdot \mathbf{n}_k$ and k is the number of faces of the *fv*-cell.

Employment of such approximations over each finite volume, including their contributions to represent the total domain, introduces the discretised form of equation (3.7). This generates a system of algebraic equations to be solved similar to that for the finite element approach represented by equation (3.5).

3.2 Discretisation of field equations

A time-dependent hybrid finite volume/element discretisation forms the basis to provide solutions to the relevant governing field equations. This scheme is a high-order, semi-implicit, incremental pressure-correction algorithm (TGPC), applying a two-step Lax-Wendroff approach, and a temporal Taylor series expansion up to second-order. The scheme can be explained assuming a one-dimensional problem of the following form,

$$\frac{\partial u}{\partial t} + \frac{\partial}{\partial x} f(u) = 0 \,. \tag{3.12}$$

Where, $u(x,t)$ is a scalar field dependent solution variable, with x and t independent spatial/temporal variables, respectively.

Through operator-splitting, a three-stage system emerges, which is discretised in space and time, constructing a reduced fractional-staged set of equations. At stage one and via a predictor-corrector scheme, a non-solenoidal velocity field is computed (Stage 1a, 1b). Temporal pressure-difference on the time-step is computed via a Poisson equation [Eq. (3.1)] at stage two. Eventually, at stage three and to complete the time-step loop a solenoidal velocity field is recovered. To improve temporal quality through an area-weighting procedure, the numerical algorithm is further modified .

The two-step Lax-Wendroff procedure, over time-step $t \in \left[t^n, t^{n+\frac{1}{2}}\right]$ and $t \in \left[t^n, t^{n+1}\right]$, can be expressed as,

$$u^{n+\frac{1}{2}} = u^n + \tfrac{1}{2}\Delta t\left[-\frac{\partial}{\partial x} f(u)\right]^n, \tag{3.13}$$

$$u^{n+1} = u^n + \tfrac{1}{2}\Delta t\left[-\frac{\partial}{\partial x} f(u)\right]^{n+\frac{1}{2}}. \tag{3.14}$$

Here, as elsewhere, terms with subscript n display evaluation at a specific time step (t^n).

The resulting generalised space-time discrete matrix-vector system may be expressed as follows,

Stage 1a: $$A_u(\boldsymbol{U}^{n+\frac{1}{2}} - \boldsymbol{U}^n) = b_u^a(\boldsymbol{P}^n, \boldsymbol{P}^{n-1}, \boldsymbol{U}^n, \boldsymbol{T}^n, \boldsymbol{D}^n),$$

$$\frac{2}{\Delta t} A_t^\tau(\boldsymbol{T}_k{}^{n+\frac{1}{2}} - \boldsymbol{T}_k{}^n) = b_\tau(\boldsymbol{U}^n, \boldsymbol{T}_k{}^n, \boldsymbol{D}^n),$$

Stage 1b: $$A_u(\boldsymbol{U}^* - \boldsymbol{U}^n) = b_u^b(\boldsymbol{P}^n, \boldsymbol{P}^{n-1}, \boldsymbol{U}^n, \boldsymbol{U}^{n+\frac{1}{2}}, \boldsymbol{T}^{n+\frac{1}{2}}, \boldsymbol{D}^{n+\frac{1}{2}}),$$

$$\frac{1}{\Delta t} A_t^\tau(\boldsymbol{T}_k{}^{n+1} - \boldsymbol{T}_k{}^n) = b_\tau(\boldsymbol{U}^{n+\frac{1}{2}}, \boldsymbol{T}_k{}^{n+\frac{1}{2}}, \boldsymbol{D}^{n+\frac{1}{2}}),$$

Stage 2: $$A_2(P^{n+1} - P^n) = b_2(\boldsymbol{U}^*),$$

Stage 3: $$A_3(\boldsymbol{U}^{n+1} - \boldsymbol{U}^*) = b_3(P^n, P^{n+1}), \tag{3.15}$$

Where total stress nodal vector is comprised of its modes $(\boldsymbol{T})_j^n = \sum_{k=1}^{M} (\boldsymbol{T}_k)_j^n$ and

$$A_u = \frac{2Re}{\Delta t} M + \frac{\mu_2}{2} S,$$

$$b_u{}^a = \{StX + F_g M_1 - [\mu_2 S + ReN(U)]U - B_1 T\}^n + L^T\{P^n + \theta_1(P^n - P^{n-1})\},$$

$$b_u{}^b = \{StX + F_g M_1 - [\mu_2 S + ReN(U)]U - B_1 T\}^{n+1/2} + L^T\{P^n + \theta_1(P^n - P^{n-1})\},$$

$$0 \le \theta_1 \le 1,$$

$$\mathrm{A}_2 = \mathrm{K},\ b_2 = \frac{2Re}{\Delta t} LU^*,\ A_3 = \frac{2Re}{\Delta t} M, \text{ and } b_3 = -L^T(P^{n+1} - P^n).$$

M, S, and *N(U)* represent the consistent mass-matrix, diffusion matrix and advection matrices, respectively. Boundary integral terms for surface tension are indicated via the $(St)\cdot(X)$ matrix-vector product whilst gravitational force is included through M_1-term. Note, that convection terms disappear under the *ALE*-implementation. Utilising implied summation with repeated indicial notation over the problem domain Ω, corresponding matrices are,

$$M_{ij} = \int_\Omega \phi_i\phi_j d\Omega,\ S_{ij} = \int_\Omega \nabla\phi_i \nabla\phi_j d\Omega,\ N(U)_{ij} = \int_\Omega \phi_i(\phi_l U_l)\nabla\phi_j d\Omega,$$

$$(St)_{ij} = \int_\Gamma \phi_i\phi_j d\Gamma,\ (X)_j = (\sigma\cdot n)_j = (-p_a n + Ca^{-1}(\frac{1}{R_1} + \frac{1}{R_2})n)_j,\ (M_1)_i = \int_\Omega \phi_i d\Omega. \quad (3.16)$$

The pressure stiffness matrix, K, and remaining matrices adopt forms:

$$K_{ij} = \int_\Omega \nabla\psi_i \nabla\psi_j d\Omega,\ (L_k)_{ij} = \int_\Omega \psi_i \frac{\partial\phi_j}{\partial x_k} d\Omega,\ (B_1)_{ij} = \int_\Omega \nabla\phi_i\phi_j d\Omega. \quad (3.17)$$

The additional stress-related matrices and vectors (A_i^τ and b_τ) are described below, as they emerge, under the fv-context. The scheme becomes further implicit and stable as approximation of diffusion terms is carried out in the momentum equation, via a Crank-Nicolson discretisation over each time-step. On the parent triangular *fe*-cell, pressure is represented through linear ($\psi_j(x)$) interpolation, whilst that on velocity ($\phi_j(x)$) is quadratic. In nodal (j) notation, such trial space interpolation can be represented, viz.

$$u(x,t^n)=\sum_j \phi_j(x)U_j^n,\ p(x,t^n)=\sum_j \psi_j(x)P_j^n. \tag{3.18}$$

No explicit assembly of system matrices (minimum storage overhead) is required at stages one and three as an accelerated Jacobi iteration is applied to solve the resulting algebraic equations. A few iterations (three to five iterations) are demanded. This space optimal computationally efficient element-by-element procedure demonstrates linear time-complexity in time-step and overall linear space-complexity in nodal degrees of freedom. Since the Jacobi scheme is well-suited for parallelisation (see Grant et al. [30]), it is an appropriate choice for these mass-matrix equations, according to their suitable conditioning properties. In contrast to stages one and three, a direct Choleski reduction scheme is employed to compute the current pressure-difference over the time-step at stage two. The previous time-step pressure-difference at stage one, serves as a back-reference for the incremental version of this scheme. As such, over the alternative non-incremental pressure-correction schema, superior uniform temporal error bounds are yielded. At the second-stage, the order of efficiency of the overall scheme is upheld and iterative solution is avoided via the choice of direct solver for the scalar pressure-difference equation. Here, severe practical difficulties may often arise from conditioning and is best dealt with independently of the remainder of the system. The symmetrical, sparse, banded nature of the resultant matrix leads to computational efficiency, a state that also holds for three-dimensional implementations, see Grant et al. [30].

3.2.1 Free-surface treatment and algorithm

3.2.1.1 Lagrangian/ALE approach (CM)

To compute free-surface movement, a particle-tracking technique is employed. We assume that the fluid surface located at nodes from the start of a time-step consists of a series of distributed particles. Typically, a fluid particle is shifted using an Eulerian procedure:

$$X_i^{n+1}=X_i^n+\Delta t u(X_i^n,t^n),$$

where, a particle at location i on the free-surface, is positioned at (X_i^n, X_i^{n+1}) for times (t^n, t^{n+1}), with velocity $\boldsymbol{u}(X_i^n, t^n)$ at position X_i^n and time t^n. In a similar fashion, particles and mesh-nodes are all relocated to their updated end-of-time-step position,

$$r^{n+1}=r^n + u_r\Delta t \quad \text{and} \quad z^{n+1}=z^n + u_z\Delta t.$$

Mesh-nodes are shifted both radially and axially through application of this particular strategy. This lies in distinct contrast to other earlier approaches, which relied upon a surface height function description, h(x,t) [10] where the free-surface movement is assumed to be purely radial.

To solve the present problem, the dynamics for the space-time domain may be described through either an Eulerian or a Lagrangian frame-work. The generalised Arbitrary Lagrangian/Eulerian technique (*ALE*) has proved a powerful tool to unite features of both such descriptions, through the concept of a mesh velocity. A material time derivative of a physical quantity,Φ, within the reference configuration can typically be expressed as,

$$\frac{D\Phi}{Dt} = \frac{\partial \Phi}{\partial t} + \boldsymbol{u}_c.\nabla\Phi ,$$

$$\boldsymbol{u}_c = \boldsymbol{u} - \boldsymbol{u}_m ,$$

where $\boldsymbol{u}_c$, $\boldsymbol{u}$ and $\boldsymbol{u}_m$ represent the convective velocity, fluid velocity and mesh velocity, respectively. The particular form of the Arbitrary Lagrangian/Eulerian formulation employed is based on mesh velocity allocation which is purely Eulerian if $\boldsymbol{u}_m$=0; purely Lagrangian if $\boldsymbol{u}_m$=$\boldsymbol{u}$; with hybrid configurations adopting alternative choices in between. An *ALE* interpretation is invoked in the present work, for which on all boundaries, $\boldsymbol{u}_m$=$\boldsymbol{u}$ and $\boldsymbol{u}_c$=$\boldsymbol{0}$. Via pure lubrication, interior node movement is dominated by axial centreline fluid velocity (u_z) and radial movement by mid-plane fluid velocity (v_r). As such, mesh quality is maintained by re-projection of mesh-nodes and solution onto horizontal pure lubrication mesh-lines, coinciding with forward-time axial centreline nodes. Consequently, the complexity of mesh-folding

is avoided, which may occur otherwise in the close neighbourhood of the plates (filament-foot extremity zone). Inclusion of additional convective correction stages (Stage 1c) to the scheme has revealed practically that, adjustment arising from such approximation in $\boldsymbol{u}_m$, incurs insignificant contribution for extensionally-dominated flow, and hence, can be discarded.

An alternative procedure is to apply an *ALE*-approach on the domain with two different strategies to track the free-surface. Since, using this technique there is radial mesh adjustment with free-surface movement, the procedure is termed a compressed-mesh (*CM*)-approach. In this instance, the fluid domain is stretched in the axial direction upon retracting the plates, and compressed radially inwards from the free-surface.

One procedure to govern the evolution of the deforming flow domain is to interpret this movement through a local kinematic condition using a height function [33], h(**x**, t):

$$\frac{\partial h}{\partial t} = u_r - u_z \frac{\partial h}{\partial z}. \tag{3.19}$$

Here, u_r is the inward radial velocity component, which diminishes at the top-plate and increases to a maximum at the filament mid-plane. In contrast, the axial velocity component, u_z, reaches a maximum in absolute value on the two moving end-plates and vanishes at the filament mid-plane. Consequently, the free-surface is dynamically compressive, moving inwards radially, and the velocity and underpinning boundary condition at the plate-fluid interface engender shifts in fluid-surface position. To compensate for this, there must be a relative reset for internal nodal positions, in proportion to the shift in the free-surface. The height function restricts free-surface movement to only radial adjustment. Previous work [10] utilised a (CM, $\partial h/dt$)-approach with mesh redistribution but with no explicit mesh velocity. This method suffered from deficiencies, particularly at higher levels of Hencky-strain ($\varepsilon \geq 1$), degrading solution quality close to the fluid-plate contact positions.

Under *CM*-methodology, the various phases involved within a single Hencky-strain step (Δt_{Hencky}) are as follows:

Step 1. Update Hencky-strain, $t_{n+1} = t_n + \Delta t_{Hencky}$

Step 2. Fix plate-boundary conditions at t_{n+1}

Step 3. Shift plate locations through single step (Δt_{Hencky})

Step 4. Shift free-surface nodes to updated t_{n+1} position

Step 5. Reproject position and solution at internal /free-surface mesh nodes for particle-tracking method[1]. With height function method, use elliptic-mapping mesh redistribution for interior nodes in axial direction

Step 6. Temporally update kinematic fields (velocity and pressure) on shifted domain(t_{n+1}), solving fractional-stages with dynamic boundary conditions

Step 7. Synchronise velocity, pressure, and stress fields; solving field fractional-staged equations, through prescribed inner/local steps, $M=(\Delta t_{Hencky}/\Delta t_{inner})$ time-steps

Step 8. Verify local time of stretch (Hencky strain); if not termination time, go to step 1

3.2.1.2 Volume-of-Fluid (VOF) approach

The flow domain is split into two parts: one wet and another dry under the *VOF*-method. Conventionally, the fluid is viewed as flowing over a fixed mesh, and hence, the frame of reference is essentially Eulerian. This is amended in the present context to consider the predominant axial motion through which the mesh is moved. The domain is assumed to be fully wet at the outset. The interface between wet and dry zones is defined by the position of the free-surface. Finite element calculations are performed in the wet-fluid zone to obtain field variables, such as velocity, pressure and stress, as only there, material assignment is non-zero. When employing the *VOF*-method to model free-surface deformation, the initial rectangular mesh is

[1] May adopt horizontal z-mesh lines governed independently, either by axial filament movement or free-surface position. Empirical evidence would favour the former, pure lubrication choice.

stretched purely axially and the axial redistribution is performed through an elliptic-mapping mesh redistribution strategy (log-tanh, [34]). Based on particle trajectories, free-surface positions are re-established upon each Hencky-strain time-step. This is performed under the assumption that the free-surface boundary can be identified through a series of particles (not to be confused with nodal mesh points). Then, through a time-stepping procedure, one can track the movement of such surface-particles.

Once the plates have been moved at a particular Hencky-strain, via the prescribed velocity, surface particles are repositioned and updated according to the above steps. Subsequently, the newly shaped wet and dry regions are identified and the status of all nodes (either wet or dry) is reassigned. For part-wet elements, material properties are adjusted within a single element. Boundary conditions are naturally incorporated within the finite element calculations via assigning suitable material properties to each sample quadrature (Gauss) point within an element. As such, local re-meshing close to the free-surface would not be required since explicit boundary conditions are not imposed on the free-surface. Sampling precision can be enhanced through the number and location of quadrature points; thereby proportions of wet versus dry segments are depicted more accurately. After reassigning nodal status and material properties, velocity, pressure and stress fields are computed on the updated domain in an iterative fashion. A prescribed increment tolerance is met in solving the fractional-staged equations via a set number of local/inner steps, synchronized to match the (true-time) Hencky-strain step. Then, calculation advances to the next Hencky-strain time step, and until achieving the respective target time (Hencky-strain) the cycle repeats itself, or premature numerical failure (divergence) is encountered.

Under VOF and for a single Hencky-strain step (Δt_{Hencky}), the following *alternative* sequence of algorithmic steps is used at *steps 4* and *5* above:

Step 4. Via elliptic-mapping mesh redistribution, interior mesh-point axial locations are updated and take new positions relative to plate-

movement,

Step 5. Via surface tracking, updated free-surface positions are determined

There is a choice in the VOF-instance, of the time to invoke the free-surface update, either immediately after plate shifting (as above), or after making correction to the solution at *step 7.* According to current experience this has made no practical difference. Both options have performed equally well, in free-surface profile and nodal solution predictions, with only a slight difference relative to the Hencky-strain solution-state utilised.

3.2.1.2.1 Surface particle velocity estimation

Based on empirical findings, for the accurate prediction of free-surface movement, precise estimation of surface particle velocity is crucial. To quantify this position, three different estimation techniques have been studied. With the first method, free-surface particle velocities are computed purely from element-nodal values, based upon the element to which the particle belongs, viz.

$$U(X_p,t^n)=\sum_j \phi_j(X_p^n)U_j^n. \tag{3.20}$$

It is implied from the notation that particle p, at location X_p^n and time t^n, has velocity $U(X_p,t^n)$. U_j^n denotes the nodal (j) velocity values for the particular element containing particle (p). Unfortunately, this strategy fails to predict particle velocities with adequate accuracy when particles migrate too close to dry (stationary) nodes. Thus, this method was discarded due to undesirable weighting of static nodes. With a second strategy, the initial particle velocity is transported along with the particle, and adjusted at each time-step as the front advances through the mesh. With such an approach, particle velocities are represented as,

$$U(X_p,t^{n+1})=U(X_p,t^n)+\sum_j \phi_j(X_p^n)(U_j^n-U_j^{n-1}). \tag{3.21}$$

This procedure performed well whilst tracking free-surfaces within a dough-kneading scenario, where wetting/peeling occurred at fluid-solid interfaces (see

[34]). Nonetheless, in the context of filament-stretching, this option again caused degradation in surface representation. Under either of these two strategies, the surface particle velocity is strongly influenced by dry nodal velocities. Hence, a third procedure has been proposed where particle velocity estimation is entirely dependent on wet-nodal velocities (see Fig. 3.1). Surface particles are represented in Fig. 3.1 as dark filled circles (•) and mesh-nodes by filled triangles. There is radial interconnection between horizontal mesh-lines and nodes, across the filament span-wise. Figure 3.1a displays a scenario where there is alignment between surface particles and internal nodes, whereas the converse, under misalignment is demonstrated in Fig. 3.1b. Moreover, in Fig. 3.1a, the two closest radial wet-nodes must be located at the same height level (z_p) as that of the surface-particle; see for example, surface-particle (p), locating nodes (a) and (b). One may derive the velocity for surface-particle (p) through extrapolation from these (a,b) internal nodal velocities, assuming suitable radial variation (either linear or quadratic).

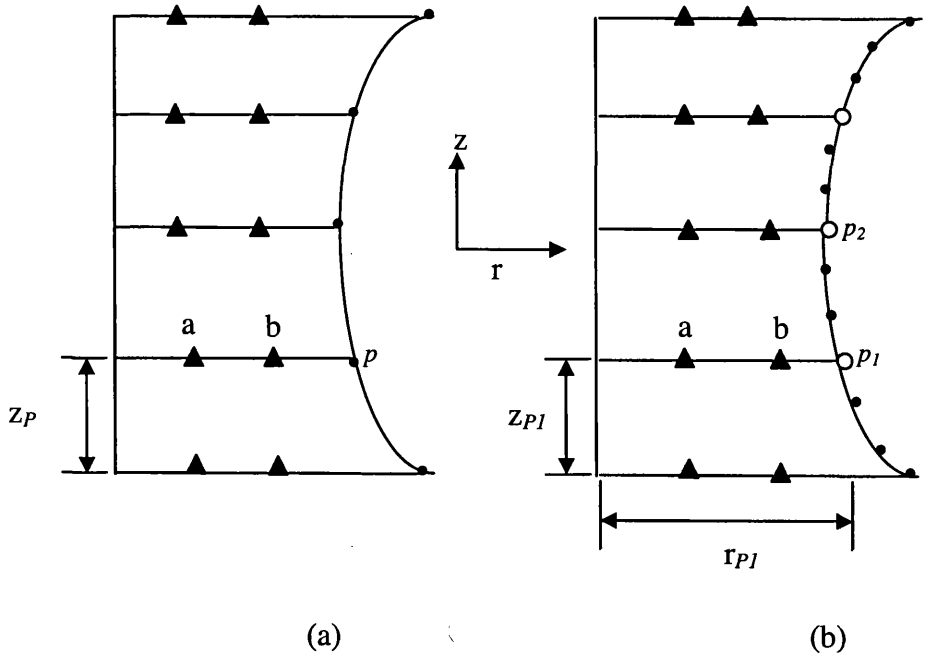

Fig 3.1 Schematic: internal nodes with surface particles a) aligned; (b) misaligned

The above procedure is applicable to particles aligned with mesh nodes as in Fig. 3.1a. Further adjustment procedures are required (see Fig. 3.1b) for surface particles, misaligned with mesh-lines and nodes. For such a contingency, the pseudo-particle location (o) on the free-surface must first be located via assessment of the point of intersection between the surface and the horizontal mesh lines connecting the interior nodes. Interpolation along a surface line segment can provide a good estimation for the velocities of the particles lying between two such neighbouring pseudo-particles (p_1) and (p_2). Therefore, the order of axial-oriented interpolation (linear/quadratic) controls the resultant nature of the free-surface movement and accordingly, its curvature. Linear interpolation provides linearity in shape, whilst quadratic interpolation is less restrictive. The quadratic option chosen allows greater freedom of independent particle movement, hence permitting more general surface-curvature capture.

3.2.2 Sub-cell finite volume stress discretisation

To update the nodal solution, cell-vertex *fv*-schemes are utilised for stress which distribute control volume residuals based on an upwinding technique (fluctuation distribution). Rewriting and rearranging the stress constitutive equation (2.35) in terms of flux (**R**) and source (**Q**), yields:

$$\frac{\partial \boldsymbol{\tau}}{\partial t} = -\mathbf{R} + \mathbf{Q}, \tag{3.22}$$

$$\mathbf{R} = \boldsymbol{u} \cdot \nabla \boldsymbol{\tau}, \tag{3.23}$$

$$\mathbf{Q} = \frac{1}{De}(2\mu_1 \boldsymbol{d} - f\boldsymbol{\tau}) + (\boldsymbol{L}\cdot\boldsymbol{\tau} + \boldsymbol{\tau}\cdot\boldsymbol{L}^{\dagger}) - \xi\{\boldsymbol{d}\cdot\boldsymbol{\tau} + \boldsymbol{\tau}\cdot\boldsymbol{d}\} - \frac{\alpha}{\mu_1}\boldsymbol{\tau}\cdot\boldsymbol{\tau}. \tag{3.24}$$

Each scalar stress component, τ, is assumed to act over an arbitrary volume of Ω, whose alteration is controlled via flux and source component fluctuation, R and Q; respectively, as below,

$$\frac{\partial}{\partial t}\int_{\Omega}\tau d\Omega = -\int_{\Omega} R d\Omega + \int_{\Omega} Q d\Omega . \tag{3.25}$$

Based on the strategy of choice, the flux and source alterations are evaluated over each finite volume triangle, and distributed the same to its three cell vertices. The update to a given node l is obtained by summing contributions from its control volume Ω_l, which is composed of all *fv*-triangles surrounding node l, as in Fig. 3.2, see [10]. Flux and source residuals may be evaluated over different control volumes. Namely, over the fv-triangle $T(R_T,Q_T)$ and/or the median dual cell (*mdc*), associated with a given node l within the fv-cell $T(R_{mdc},Q_{mdc})$. Median-dual-cell zones are non-overlapping regions defined per node l, an area one-third of the base triangular cell over which it is constructed (see Fig.3.2 once more).

Taking eq. (3.15) into account, a consistent distributional approach, exposed in Webster et al. [10], may be expressed in a generalised form, for stage 1b with $\Delta\tau_l^{n+1} = (\tau^{n+1} - \tau^n)_l$,

$$\{\Omega_{FD} + \Omega_{mdc}\}\frac{\Delta\tau_l^{n+1}}{\Delta t} = \underbrace{\sum_{\forall T_l} \delta_T \alpha_l^T b_{T_l}}_{FD} + \underbrace{\sum_{\forall mdc_l} \delta_{mdc}^T \alpha_{mdc}^T b_{mdc}^l}_{mdc}, \tag{3.26}$$

where

$b_{T_l} = (-R_T + Q_T)$, $b_{mdc}^l = (-R_{mdc} + Q_{mdc})^l$,

$\Omega_{FD} = \Sigma_{T_l} \delta_T \alpha_l^T \Omega_{T_l}$, and $\Omega_{mdc} = \Sigma_{mdc_l} \delta_{mdc}^T \Omega_l^{T_l}$.

The parameters, δ_T and δ_{mdc}^T are mutually linked and complementarily exclusive, $\delta_{mdc}^T = 1 - \delta_T$, and may be established to provide a powerful categorization of this class of schemes, see [10,31] for schemes CT_i, i=0-3. For example, $\delta_T = 1$ and $\delta_{mdc} = 0$ reverts, to a pure fluctuation distribution form, pertinent to present extension-dominated needs. This scheme is temporally modified on the *lhs*, using α_l^T area-weighting.

Fluctuation distribution coefficients α_l^T, may be provided via an appropriate choice of scheme: for example, LDB, Lax-Wendroff, or PSI. Here, we focus on a single linear version (Lax-Wendroff), satisfying the property of linearity-preservation, but not positivity. It is spatially-centred and second-order accurate in space. In addition, it contains a dissipation term, designed to control oscillations in the neighbourhood of discontinuities, thus conferring second-order accuracy in time. For this Lax-scheme, the distribution coefficients α_l^T may be expressed as:

$$\alpha_l^T = \frac{1}{3} + \frac{\Delta t}{4\Omega_T} \mathbf{a} \cdot \mathbf{n}_l^T, \tag{3.27}$$

where, Δt is a time-step size, $\mathbf{a}$ an averaged cell-advection velocity, and $\mathbf{n}_l^T$ a scaled inward-pointing normal vector to an edge of triangle T, opposing node l. Importantly, the closer the advection velocity $\mathbf{a}$ is to being parallel to a cell boundary, the larger the contribution to the downstream node at that boundary (see Fig. 3.2).

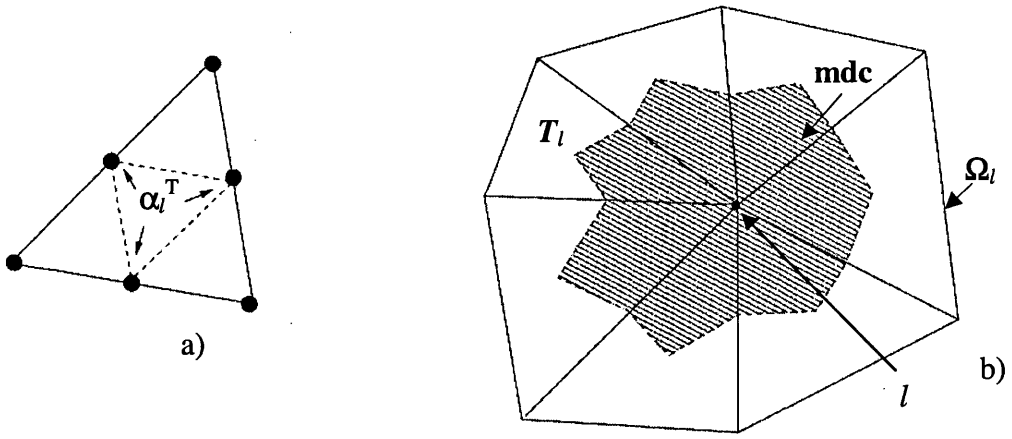

Fig 3.2: a) fe with four fV sub-cells, and b) mdc area for node l

3.2.3. Numerical discretisation for multi-mode vs single-mode

Here, a semi-implicit transient decoupled hybrid finite volume/element scheme is employed to discretise and solve the related non-linear system of field equations with appropriate initial and boundary conditions. Comprehensive discretisation detail with system and component matrices is provided in reference [61], thus only a concise summary is given here. A two-step Lax-Wendroff scheme is the base with a Taylor series approximated up to $O(\Delta t^2)$. Pressure is incremented through a Pressure-Correction strategy (TGPC) [28], rendering a three-stage scheme structure. Stress and non-solenoidal velocity fields are both updated in the first stage. Then, the pressure is updated at the second stage. At a final third stage, the velocity field is updated. Spatial discretisation of the full system is performed via a finite-element approach on a triangular tessellation with piecewise-continuous linear interpolation for pressure and quadratic for velocity. The stress equations are discretised within the velocity element, through a sub-cell finite volume method of cell-vertex form (linear interpolation). To achieve this, the pressure/velocity element is sub-divided into four sub-cells for stress. Finite volume fluctuation distribution on time and space derivatives is taken through a Lax-scheme, which confers second order accuracy in both temporal and spatial manner [61]. An algebraic system is obtained and to solve such a system a Jacobi-iterative method is employed for velocity (using mass-iterations of number three to five), and a direct Choleski decomposition scheme for pressure. Via the resulting diagonalised fv-stencil, the stress is directly evaluated, yielding explicit nodal evaluation.

3.2.3.1 ALE strategy, mesh and free-surface movement applied to multi-mode vs single-mode

For the multi-mode vs. single-mode study, advances are made as those pursued in reference [61], discarding the inferior surface height function description, h(x,t) [10]. This height function approach, which provides for purely radial free-surface movement, has been employed likewise by others [3,4]. Instead, a particle-tracking procedure for free-surface movement (an Euler scheme), with freedom of movement

in both axial and radial directions has been chosen, see section for 3.2.1.2.1. This is found to be particularly helpful in elements containing filament-plate contact.

3.2.3.2 Procedure through time for multi-mode vs single-mode

The scheme employed for single-mode simulations has been validated through a number of both steady and transient studies [10,61]. This scheme can be extended to accommodate multi-mode modelling. Two important new issues are involved here. The first is handling a range of different relaxation time-scales, for which improved time-implicitness treatment upon the constitutive equation is required. The second aspect is related to dealing with the near-Maxwellian form of the momentum equation, as solvent viscosity is largely absorbed within the individual modes. The outcome represents significant progress towards equitable time-steps for both multi-mode as well as single-mode implementations.

Some modifications are made to the single-mode procedure of [61] under the multi-mode context described below. For any single Hencky-strain step (Δt_{Hencky}), the following sequences of algorithmic steps are followed:

Step 1. Hencky-strain is updated, $t_{n+1} = t_n + \Delta t_{Hencky}$.

Step 2. Plate-boundary conditions are fixed at t_{n+1}.

Step 3. Through a single step (Δt_{Hencky}), plate locations are shifted.

Step 4. Free-surface nodes are shifted to updated t_{n+1} position [61].

Position of interior/domain nodes governed by *ALE-scheme* is readjusted, as above [61].

Step 5. First, kinematics is updated through single-mode modelling, gathering current pressure and velocity field on the shifted domain, solving fractional-stages, with dynamic boundary conditions.

Step 6. Next, the stress state is synchronously evolved forward for each mode to coincide with the kinematics.

Step 7. Finally, the pressure/kinematics is corrected, to ensure consistency with the updated total multi-mode stress.

Step 8. Stopping criteria: local time of stretch is determined; if not at terminating time, go back to Step 1 and continue.

An elliptic-mapping mesh distribution for interior nodes (Thompson algorithm mesh distribution [34]) is used for the initial mesh (t=0). On specific steps, some further detail is in order. At Step 5, pressure and velocity field solutions are determined, with frozen stress and solvent viscosity weighting ($\mu_s = \mu_0 - \mu_1$), equivalent to the single-mode context, in the ratio, μ_s / μ_0, that is some two orders larger than that in the multi-mode representation. This is performed to a specified iterative tolerance [10] over each Hencky-strain step. The extremely efficient iterative sub-time-steps demanded at this stage are termed inner-steps. They are based upon the current domain state and the intrinsic velocity-pressure solver [66,60] and are of linear time-space complexity. Through Step 6, primary variables ($\boldsymbol{v}$, p, $\boldsymbol{\tau}$) are evaluated simultaneously, so that, the total number of steps employed (M) matches the ratio of the Hencky-strain step Δt_{Hencky} to the local inner time-step Δt_{inner}. Each stress mode (i) is solved subject to its own polymeric viscosity (μ_i). At Step 7, ($\boldsymbol{v}$, p) are calculated with frozen multi-mode stress $\boldsymbol{\tau}$, employing the actual solvent viscosity ($\mu_s = \mu_0 - \sum_i \mu_i$).

3.2.4 Step-strain discretisation procedures

3.2.4.1 Field equation solution

Filament deformation occurs in the field-domain throughout the dynamic step-strain process. A hybrid *fe/fv,* time-splitting semi-implicit formulation has been employed per time-step. This formulation consists of an incremental pressure-correction scheme, defined through a pressure-term weighting factor ranging from zero to unity ($0 \leq \vartheta_1 \leq 1$) detail of which is given in section 3.2.

3.2.4.2 Free-surface tracking and ALE implementation for step-strain

In the step-strain study, the filament undergoes two different stretching modes. Throughout the first phase, the filament is continuously stretched by retracting the end-plates under a controlled scenario say exponential rate) the details of which are discussed in section 3.2.1.1. During a second phase, the plates undergo a sudden halt, and filament is subject to radial thinning as time evolves. An *ALE*-technique with an Euler particle tracking procedure is applied on the domain to trace out the free-surface path. In the next time-step (t^{n+1}), the surface-particles and their associated nodes are shifted, depending on their local nodal velocities, to updated locations for which the details are described in section 3.2.1.1.

During continuous stretching, the mesh and fluid move simultaneously, so, axial extension and inward radial compression are carried out via an *ALE* approach. On all boundaries, $\boldsymbol{u}_m=\boldsymbol{u}$ and $\boldsymbol{u}_c=\boldsymbol{0}$. Nevertheless, applied directly this may stimulate premature mesh-folding as a result of imposing the fluid velocity ($\boldsymbol{u}_m=\boldsymbol{u}$) on interior nodes close to the filament foot-zones (filament-plate contact zone). To avoid such undesirable mesh-folding, internal mesh redistribution adjustment is deployed based on a re-projection of internal/free-surface nodes onto pure lubrication lines. Firstly, the free-surface movement is determined via the local fluid velocity. Secondly, filament centreline nodes are shifted according to pure lubrication fluid velocity. Then, the intersections lie between the horizontal lubrication lines, emerging across the filament through newly positioned centreline nodes, and the free-surface segments. Free-surface nodal attributes are adjusted as forward time-step position and velocity are updated. Likewise, projection of interior nodes takes place onto these pure lubrication lines, generated by the centerline axial fluid velocity (u_z). Radial movement occurs uniformly on each time-step, being consistent with the mid-plane radial fluid velocity, u_r. Due to mesh quality preservation over the time-step, the resultant mesh velocity reflects miniscule disparity from the true fluid velocity.

During phase two, in which step-strain takes place, the plates are subject to sudden halt and consequent commencement of the thinning-down process (t_0). This advances just prior to filament failure until a final time (t_f), where the least attainable filament

mid-plane radius emerges (equivalent to achieving a maximum element aspect-ratio criterion). Employing the continuous-stretching *ALE*-approaches (*full-ALE*), as described above, tending towards dominant axial shift, has been observed to perform element suction away from the mid-plane (drainage to feet). Hence, vigorous element migration towards the end-plates arises, which eventually causes larger mesh aspect-ratios in the mid-plane filament section and quality degradation of final predicted filament surface shapes. Thus, implementation of an amended procedure is demanded. This is termed radial-*ALE*. In this fashion, centreline nodes alongside their connected horizontal mesh lines (see above) may now be fixed and the axial distance between node-pairs (δz) remains unchanged. All other *ALE* schema re-projection procedures remain unaltered.

The two phases described above can be summarized as below within a single Hencky-strain step (Δt_{Hencky}):

Phase1:

Step 1. Hencky-strain is updated, $t_{n+1} = t_n + \Delta t_{Hencky}$

Step 2. Plate-boundary conditions are set at t_{n+1}

Step 3. Plate locations are moved through single step (Δt_{Hencky})

Step 4. Free-surface nodes are relocated to updated t_{n+1} position

Step 5. Position and solution are relocated at internal /free-surface mesh nodes.

Step 6. Kinematic fields (velocity and pressure) are updated over the new domain (t_{n+1}), via fractional-stages solutions to a prescribed tolerance with dynamic boundary conditions.

Step 7. Field fractional-staged equations are solved for velocity, pressure, and stress fields through prescribed inner/local steps, $M=(\Delta t_{Hencky} / \Delta t_{inner})$ time-steps.

Step 8. Hencky-strain is verified, if not termination time, go to Step 1 and continue

Phase 2:

Under the second phase, following adjustments/amendments are made in the above sequence of algorithmic steps:

Step 1. Time is updated, $t_{n+1} = t_n + \Delta t$.

Step 2. Plate velocity is set at $U_{plate}=0$.

Step 3 is skipped as there is no plate movement.

Steps 7 (M=1), 4 and 5 are performed, as of Phase 1.

Step 6 is skipped as there are no dynamic boundary conditions.

Step 8. Time is verified, if not termination time (t_f), go to Step 1 and continue.

Chapter 4

Modelling Multi-Mode Viscoelastic Flows[†]

In this chapter the transient viscoelastic response of strain-hardening fluids in filament stretching flows is analyzed. An Arbitrary Lagrangian/Eulerian temporal approach (ALE) is utilised, coupled with a particle-tracking procedure for free-surface movement and a hybrid finite volume/element method upon the domain. Findings between Oldroyd, Giesekus and linear Phan-Thien/Tanner models are contrasted and between single and multi-mode implementations. In addition, the impact that greater severe strain-hardening has in this transient flow context can be identified. By comparing single-mode solution response between a shear-thinning Giesekus and a constant shear viscosity Oldroyd-B model, rheology induced through shear-thinning contributions may be gathered. A parameteric study has been carried out on body force and surface tension effects, where the occurrence of asymmetries in the flow under certain conditions, leading to the onset and formation of bead-like structures is isolated. Hence, the specific localised influence

[†] Material of this chapter has been shaped in the paper "Modelling filament stretching flows with strain-hardening models and sub-cell approximations" by H. Matallah, M.J. Banaai, K.S. Sujatha and M.F. Webster and published in *Journal of Non-Newtonian Fluid Mechanics, Vol. 134, Iss. 1-3, pp. 77-104.*

can be shown that surface tension and gravitational forces have upon some stretching filament flows.

4.1 Introduction

There are a variety of different ways under which filament stretching can be conducted. In the present study, a liquid bridge is initially formed between two concentric circular disks, and then, extended by pulling one or both of the end-plate fixtures apart at an exponential rate. The resulting flow kinematics in the liquid column should mainly approximate ideal uniaxial elongational flow. Under such circumstances, the desired extensional viscosity as a function of time may be determined from the axial force at the end-plates and the Hencky strain applied to the material is computed from the total stretch imposed on the sample.

Free-surface deformation and non-deforming end-plates are the two aspects to which the principal practical complications arising in filament stretching are related. The balance of applied forces during the free-surface deformation leads to necking. Non-deforming end-plates at the feet of the filament, cause significant shear due to the imposed no-slip boundary conditions. This leads to filament deformation, dominated by elongation, yet with some presence of shear flow. Particular techniques specifically designed to tackle free-surface deformation under these circumstances have been developed.

In this type of work, strain-hardening like response is an issue of particular relevance. The influence of strain-hardening can be observed through some typical aspects such as: the sharp rise in tensile stress encountered; the adjustment in slope governing mid-point filament radial evolution; and the tendency towards axial uniformity in the distribution of the filament radius. All these features are detected and the form of strain-hardening behaviour predicted in the present study has been found to be in good agreement with that in the open literature.

Nowadays, many nonlinear constitutive models have been introduced to describe the rheology of interest here. The Giesekus model has been chosen as our base-case [1], in both single and multi-mode form which is contrasted against

Oldroyd and Phan-Thien-Tanner (PTT) models. Since the Giesekus model can fit both linear and nonlinear shear rheology of most concentrated polymeric solutions, it is commonly used to represent weakly strain-hardening fluids. As an example, the Giesekus model has already been used by different authors, such as Li et al. [2] and Yao et al. [3]. In their work, Li et al. employed a higher-order-discrete-elastic-viscous-stress (*hp-DEVSS*) finite element method to solve an axisymmetric stagnation flow. In contrast, Yao el al. [3] investigated the transient viscoelastic behaviour in filament stretching devices under uniaxial stretching, following the cessation of stretching via the application of a commercial software package, POLYFLOW.

In a number of instances including a variety of different approaches, the numerical solution of viscoelastic filament stretching flows has been studied, employing Lagrangian and Eulerian treatments with integral and differential constitutive laws [4-7]. For instance, Sizaire and Legat [4] considered the two-dimensional finite element simulation of filament stretching by applying a differential FENE-CR model to substantiate strain-hardening/constant shear viscosity material response in an Eulerian configuration (L^2 extensibility coefficient of 4325.5). A surface height function 'h' defined as the normal displacement to the initial surface position, has been used to determine free-surface movement. In this work, a moving grid algorithm was employed, in conjunction with a Thompson conformal mapping, to avoid distorted elements. With this approach, FENE-CR field results were presented up to Hencky-strains of 2.56, reportedly failing earlier than equivalent experiments. An alternative treatment is that adopted in the work of Hassager and co-authors [5-7], where a Lagrangian formulation is preferred, coupled to an integral constitutive relationship. Typically, in the article of Bach et al. [5], the non-linear constitutive equation was a modified form of the K-BKZ version of the molecular stress function (MSF) model of Wagner et al. [8], which describes a range of strain-hardening response. Remeshing and solution reprojection are demanded periodically in this Lagrangian approach throughout the filament evolution process. Such work is relevant to the present study through its attention to the growth of non-axisymmetric/three-dimensional disturbances in the flow (physical instability), and circumstances of both failure and non-failure within

polymeric liquid filaments. Multi-mode PTT modelling (exponential version, 5 and 9-modes) was also applied by Langouche and Debbaut [9]. Shear, dynamic and transient stretching characteristics were successfully fitted using a broad relaxation spectrum. Within a semi-analytical framework, excellent agreement was found between experimental data and predictions at moderate Hencky-strains for instantaneous extension and step-strain recovery experiments. Yet, beyond a Hencky-strain of 2.0, predictions overestimated the experimental data. Subsequently, to extend the analysis into two-dimensions, a finite element scheme was implemented. This allowed for the consideration of boundary conditions, surface tension and inertia, and succeeded in identifying the occurrence of inertial oscillations during start-up.

In the current study, we have implemented a novel hybrid finite volume/element scheme (h_y-fV) developed in [10] and employed here specifically within the transient viscoelastic free-surface context. The scheme is centred about a number of main features. First, it is a time-stepping procedure of fractional-stage form on each Hencky-strain step, combining incremental pressure-correction stages with Lax-Wendroff/Taylor-Galerkin time-splitting. Second, a *Compressed-Mesh (CM)* spatial implementation is used as opposed to that of a *Volume-of-Fluid (VOF)* scheme, as an Arbitrary-Lagrangian-Eulerian (*ALE*) treatment is preferred to a pure Eulerian alternative. Third, to determine the motion of the filament free-surface, the superiority of particle-tracking (dx/dt) over height function ($\partial h / \partial t$) methods will be discussed in chapter five. Fourth, domain spatial discretisation is based on a finite volume sub-cell approximation for stress, with finite element technology adopted for velocity and pressure. *ALE* implementations are frequently used schemes to track complex free-surface shapes that retain freedom of mesh movement. In such procedures, the mesh is relocated with a suitable mesh velocity. Noh [11] and Hirt et al. [12] introduced the *ALE*-formulation in the finite difference domain. This was further developed into the finite element domain by Hughes et al. [13] for incompressible viscous flows.

In the present work, the rheological response of a range of different models in this complex extensional flow setting of Oldroyd-B, Giesekus and Phan-

Thien/Tanner models are analysed, following Yao et al. [14]. Under the current parameter settings, the *linear* PTT version (LPTT) is useful due to its larger transient extensional response than that associated with the Giesekus model, hence reflecting the effect of this particular dynamical feature. The focus is primarily on single-mode approximations, with a Deborah number (De) chosen as 1.89, and an initial filament aspect-ratio of 0.54 (see below). Higher Hencky-strain levels above *three* and around *four plus* units have been achieved. Furthermore, the numerical scheme is extended to accommodate a multi-mode implementation, relying upon previous PTT multi-mode experience derived for steady-state wire-coating flows with three to seven-modes [15,16].

Within the larger Hencky-strain range, $\varepsilon>3.0$, the specific, competing and separate impacts may be investigated of gravitational and surface tension forces upon deformation-states and evolving filament forms. Hence, it is possible to isolate the onset of asymmetries and exhibit the growth of single to multiple bead-like structures, attributing this to the rheological properties of the fluids in question. Other researchers have observed such phenomena [17-23]. Bazilevsky et al. [18], Stelter et al. [19], and Tripathi et al. [20] reported studies via the capillary-driven thinning of a liquid filament as a rheometric device for quantifying the behaviour of complex extensional flows. The liquid bridge formed between two coaxial cylindrical disks was stretched beyond its static stability limit by being subjected to a uniaxial step-strain. Subsequently, the liquid-bridge underwent a capillary thinning process, which eventually led to break-up, as a result of the combined effects of capillary pressure, gravity, viscous and elastic stresses. The temporal mid-filament radial evolution was noted employing high-speed video imaging. Entov and Hinch [21] conducted a detailed study of the evolution of a viscoelastic fluid undergoing capillary-induced break-up. Findings, from this and the above mentioned studies, indicate that during the stretching process, there can be a period when gravitational and viscous forces are negligibly small, whilst capillary and elastic forces balance one another. During this interval, the local extension-rate in the mid-filament section of the liquid-bridge remains constant and the filament radius decreases at an exponential rate. Under such circumstances, the

characteristic relaxation time of the fluid may be determined based upon the measurement of the mid-plane filament radius thinning rate. In this regard, the data obtained by Anna and McKinley [17] employing extensional rheometers has quantitatively corroborated the observations of Entov and Hinch [21].

4.2. Problem specification

In this problem, the extensional deformation is considered of a viscoelastic filament between two coaxial plates, pulled apart in time at an exponential rate. The context is one where, in the first instance, it is reasonable to ignore the gravity effects. Inertia, represented through the Reynolds number ($O(10^{-3})$), has practically negligible impacts throughout these flows studied. Also, the problem is limited to one initial aspect ratio of $\Lambda_0 = 0.54$, following Yao et al. [3]. Tables 4.1 and 4.2 show the selected material and operating parameters for the single-mode (Oldroyd, LPTT and Giesekus), and multi-mode Giesekus, LPTT models.

3-modes			
	Mode 1	Mode 2	Mode 3
λ_i (s^{-1})	0.421	0.0563	0.00306
μ_i (Pa.s)	25.8	7.71	1.37
α_i (Giesekus)	0.3162	0.2422	0.0993
ε_{ptt} (PTT) ξ	0.035 0.13	0.035 0.13	0.035 0.13
De_i	1.886	0.252	0.014
μ_s(solvent viscosity) (Pa.s)	0.069		
2-mode			
De_i	1.886	0.252	
μ_s(solvent viscosity) (Pa.s)	1.439		
single-mode			
De_i	1.886		
μ_s(solvent viscosity) (Pa.s)	9.149		

Table 4.1: Material properties for single and multi-mode models

Re (Reynolds number)	$4.7*10^{-4}$
Λ_0 (initial aspect ratio)	0.54
R_0 (initial radius) (m)	$3.50*10^{-3}$
L_0 (initial length) (m)	$1.89*10^{-3}$
χ (surface-tension coefficient) (Nm^{-1})	$30.0*10^{-3}$
ρ (density) ($Kg.m^{-3}$)	1030
μ_0 (zero shear viscosity) (Pa.s)	34.949
$\dot{\varepsilon}_0$ (initial stretch or extension rate) (s^{-1})	4.48
Ca (Capillary number)	9.86
Bo (Bond number)	1.2

Table 4.2: Filament and fluid characteristics

The geometric domain and boundary conditions considered are illustrated in Fig. 4.1. On velocity, Dirichlet-type boundary conditions are applied on all but the free-surface. Vanishing shear stress is imposed on the filament central axis and an ambient pressure level is set on the free-surface. In addition, initial conditions are taken as quiescent, with the exception of those on the moving-plates, where the initial impulsive velocity is taken as ($V_0 = \pm L_0 \dot{\varepsilon}_0 / 2$). This provides an appropriate characteristic velocity scale, $U = V_0$, with a length scale of the initial filament length, $L = L_0$. Primarily, single-mode predictions are considered, but also with some multi-mode preliminary solutions for two Hencky-strain levels of $\varepsilon = 0.2$ and $\varepsilon = 1.0$. Hence, the consequence of drawing upon multi-mode physical representation, as implemented for the first time through the proposed *hy-fV* scheme.

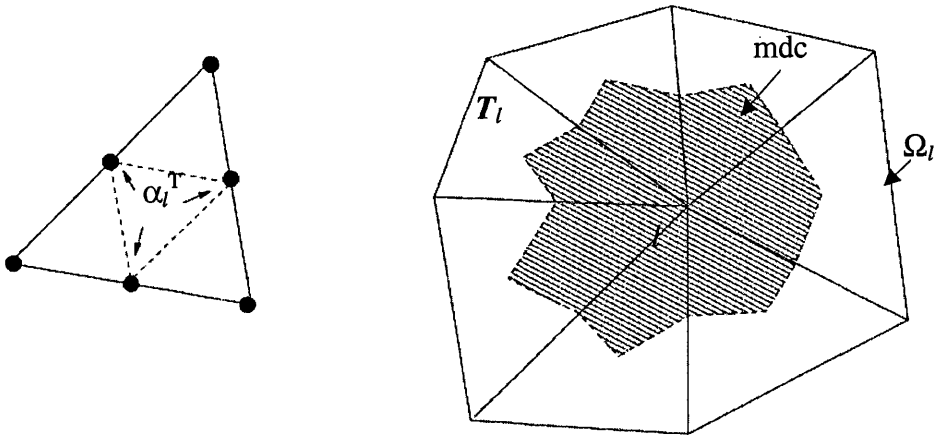

Fig 4.1a: fe with four *fV* sub-cells, and mdc area for node *l*

To perform present computations, a typical rectangular initial mesh of 20 x 100 elements, with 8241 nodes and 4000 triangular elements, is used. This mesh choice was adopted after an intensive mesh refinement study, the details of which are reported in [33]. Being stretched and

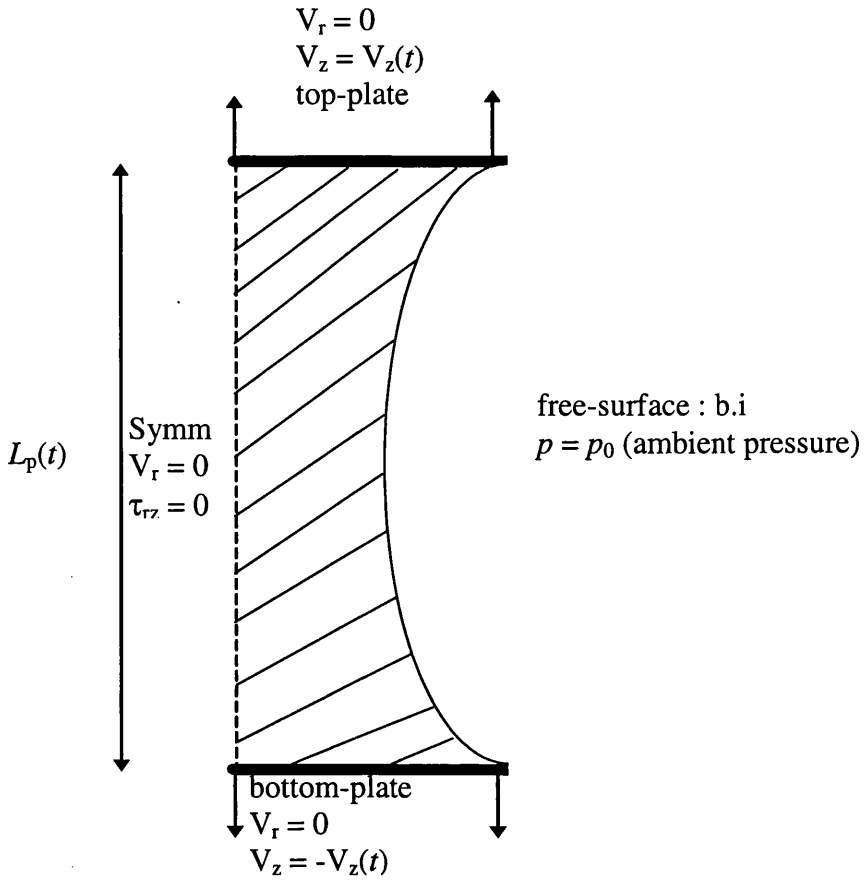

Fig 4.1b: Domain of filament, full length model with boundary conditions

distorted, the mesh movement is controlled by the time-step and remeshing algorithm and accordingly must adjust in time, see [34,10].

Calculation of the normal force (F_z) exerted at the moving end-plates is conducted through the integral of stress over the end-plate area A, viz.,

$$F_z(t) = \int_A (T_{zz} + p)dA, \qquad (4.1)$$

where $T_{zz} = 2\mu_s(D_{zz} - D_{rr}) + (\tau_{zz} - \tau_{rr})$ represents the total stress, summing viscous and polymeric components. The Trouton ratio (Tr) is defined by

$$Tr(t) = \frac{\bar{\mu}^{+}}{\mu_0}, \tag{4.2}$$

where $\bar{\mu}^{+}$ represents the extensional viscosity (type IB, as defined by Yao et al. [14]), through which the Trouton ratio is compared with corresponding experimental data. The extensional viscosity is functionally specified as,

$$\bar{\mu}^{+}(t) = \frac{F_z}{\dot{\varepsilon}_0 \pi R_{mid}^2} - \frac{\chi}{\dot{\varepsilon}_0 R_{mid}} + O(F_i, F_g). \tag{4.3}$$

Here, the notation employed implies an extension rate ($\dot{\varepsilon}_0$), surface tension coefficient (χ), and the mid-plane filament radius (R_{mid}). The term $O(F_i, F_g)$ represents correction arising from imposed inertial and gravitational forces. This term may be neglected in the present study.

4.2.1 Fluid characterization

In the present problem and following the analysis of Yao et al. [3], the data for a 5.0 wt% solution is considered of a narrow distribution, high molecular weight polystyrene. The viscometric characterization for this test fluid is described in Li et al. [2]. In Fig. 4.2a, the measured steady-state shear viscosity is plotted compared to that for the Giesekus model: covering instances of single, two and three-mode representations. It is observed that the single-mode model well predicts the experimental shear viscosity up to a shear-rate of O(10) s^{-1} (as arising in the range of filament stretching deformation rates). Subsequently, due to the large contribution of the solvent viscosity, the shear viscosity deviates to a plateau level of μ_s (see on). Such deficiency in the single-mode model may be accounted for by adopting either a multi-mode approximation, or alternatively, a single-mode White-Metzner form. We appeal to the former instance. Parameter values for the Giesekus model are tabulated in Table 1, extracted from Li et al. [2], and used by Yao et al. in the filament stretching context [3]. The single-mode model is identified by

adopting the largest of the relaxation time modes, with the corresponding μ_s absorbing the partial-viscosities of the discarded modes.

In Fig. 4.2b, steady elongation data only differentiate between Giesekus and LPTT models at large deformation-rates, where LPTT exceeds Giesekus in more excessive strain-hardening. Noting the single-mode model properties in shear, yet, one observes that this model effectively ignores the shorter relaxation times response. This will in turn, give rise to more rapid generation and initial growth in transient stress, noted in the extensional data (see on to Fig. 4.9). By contrast, the two- and three-mode models being exposed to lower relaxation time response accommodate a wider range of time-scales. This is indicated in the further moderated start-up sequence of the multi-mode instance (see below Fig. 4.2).

Li et al. [2] have commented on suitability of respective rheological models for present purposes, including Giesekus, PTT and PTT-WM. In shear, the 3-mode Giesekus model was observed to provide the best representation for both steady second-normal stress difference and flow inception. This is moderated by its inability to independently fit extensional data, being found to under-predict uniaxial extensional viscosity for shear-thinning solutions. In contrast, the PTT model offers the ability to adjust extensional viscosity predictions over a broad range of deformation rates, yet suffers from the well-known setback of the Gordon-Showalter derivative in shear flow ($\xi \square 0$). The preferred choice of Li et al. was a PTT-WM model, being adjustable for extensional data and matching shear data well, although it proves suspect in transient flow [35]. Implementation revealed that the PTT-WM model was certainly more computationally efficient than a multi-mode alternative. The present case study is intended to shed further light on both LPTT and Giesekus predictions.

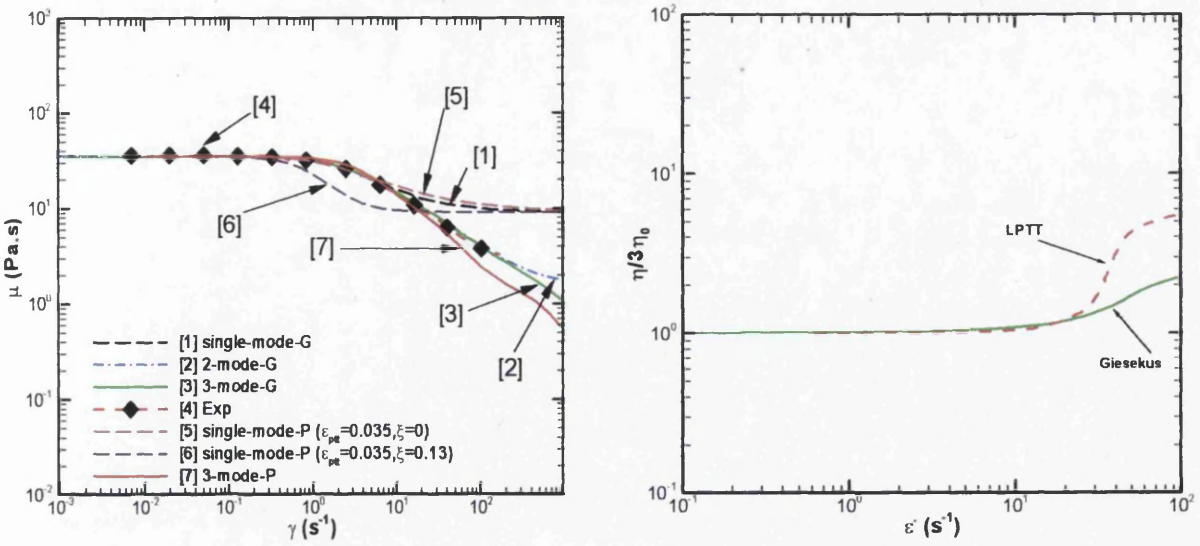

a) shear viscosity b) elongational viscosity

Fig 4.2: Steady (a) shear and (b) elongational viscosity; (G) Giesekus and (P) LPTT

4.3 Results and discussion

Computational results can be outlined for the weakly strain-hardening polystyrene solution data described above. It is clear from the shear viscometric material properties of the test fluid that the single-mode fit provides a reasonable approximation over a reduced range of shear rates. Comparative numerical predictions for Oldroyd, Giesekus and LPTT models, primarily based on the single-mode representation will be presented. Subsequently, a discussion on the implications of a multi-mode representation is presented. That is with the knowledge that in contrast to a single-mode, a three-mode Giesekus model provides an improved fit over a broader range of shear-rates.

4.3.1 Single-mode predictions

The principal comparison basis throughout this work is taken against the data of Yao et al. [14] who used two Deborah numbers (De) of 1.97 and 1.89. The single setting of De= 1.89 is adopted in this work. Also, the length scale (L_0) is chosen as the initial filament length, so that $R_0 = R_{plate} = (L_0 / \Lambda_0)$ as in Yao et al. [14]. Critical levels of Hencky-strain achieved (ε_{crit}) prior to observing numerical failure in the stretching procedure are referred to throughout.

4.3.1.1 Early Hencky-strain predictions: spatial comparison (ε=1.0)

We begin with a comparative review of Oldroyd-B, LPTT and Giesekus fluid kinematic/stress results, covering spatial plots at a specific Hencky-strain of unity (z=0). We comment that as the mobility factor α in the Giesekus fluid tends to zero, the structure of the Oldroyd-B model is recovered. By examining the kinematics along the mid-plane (scaled by R_{mid}) and centreline axes (scaled by L_p) of the filament, it is observed that the most important differences in results between the three models lie near the free-surface zone. Through the radial velocity V_r along the mid-plane in Fig. 4.3a, one may observe that velocity profiles depart around a radial value of about r=0.1 units. This has a pronounced impact on stress development, as can be seen below. V_r-maxima for the Giesekus model are larger than those for LPTT and the Oldroyd-B models (0.65 compared to 0.60 and 0.55 units). Across the three models, this position causes the most rapid compression towards the centreline under the Giesekus results. In contrast, along the centreline axis, where the axial velocity V_z is dominant, no major differences in profiles are detected among the models (see Fig. 4.3b).

In Fig 4.3c, the stress component τ_{zz} is plotted along the mid-plane of the filament. Here for the Giesekus model, τ_{zz} is elevated in value from 3.5 units to about 4.0 units for LPTT, and 5.5 units for the Oldroyd-B model. In Fig. 4.3d, the axial stress τ_{zz} is shown along the centreline of the filament. Again, across the three models trends are similar. Stress is minimal near the end-plates, increasing towards a maximum at the mid-plane of the filament, achieving values of 4.5 units for Oldroyd-B, 3.5 units for LPTT and 3.0 units for Giesekus instances, respectively. These findings are cosistent with expectation due to the differences in extensional behaviour for these respective models.

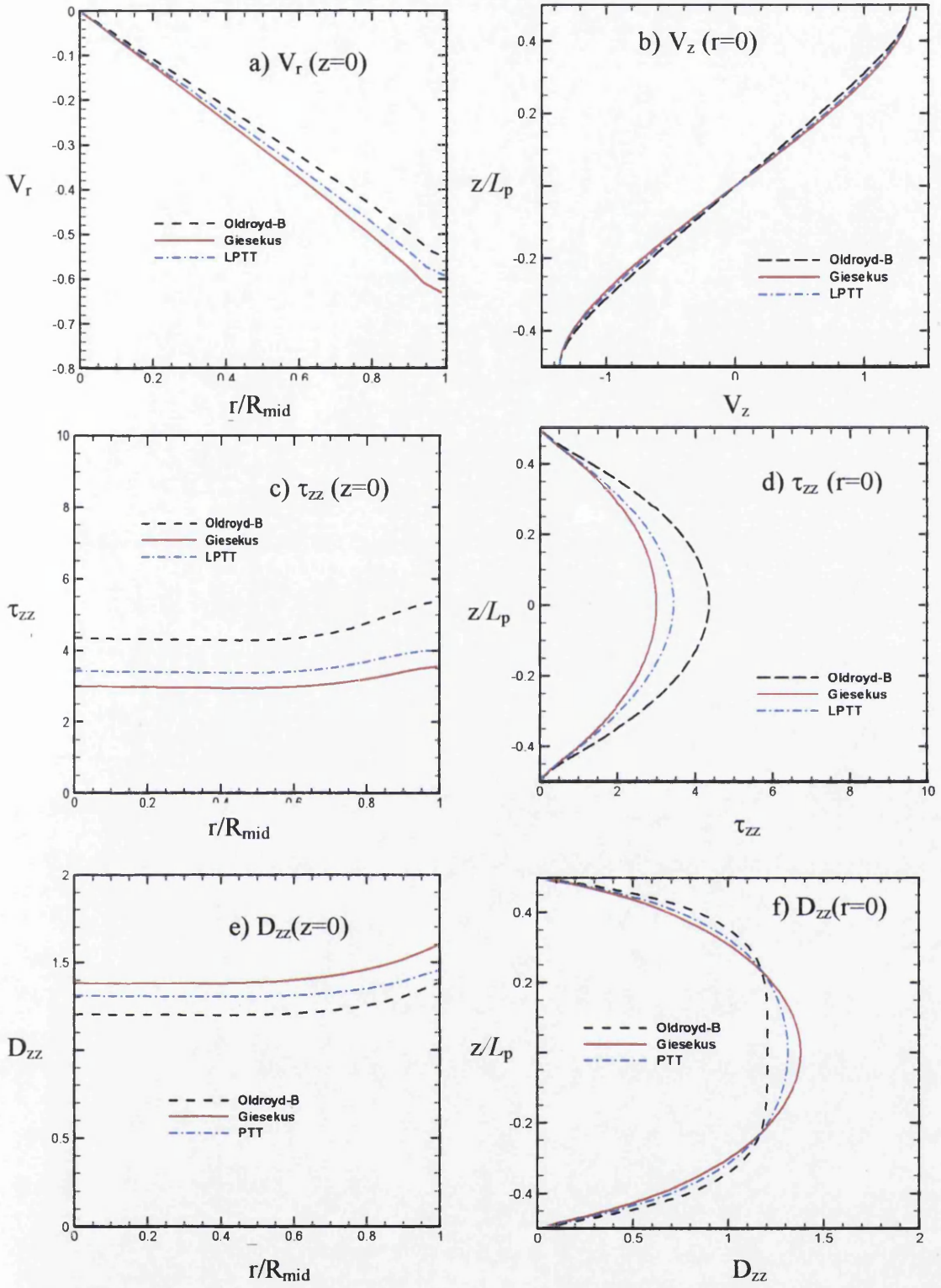

Fig 4.3: Principal axes data, Oldroyd-B, Giesekus and LPTT, ε=1: along axis (z=0) a) V_r, c) τ_{zz}, e) D_{zz}; along axis (r=0) b) V_z, d) τ_{zz}, f) D_{zz}

Once more, along the axial direction and for velocity gradient, D_{zz}, greater departure is observed between results for Oldroyd-B, LPTT and Giesekus models near the centre of the filament (see Fig. 4.3f). The more excessive flattening of the Oldroyd D_{zz}–profile lies alongside the tendency towards more uniformity and cylinder-like shape in filament column radius and greater influence of strain-hardening. Along the radial direction at the filament mid-plane, the Giesekus model generates larger D_{zz}-values than with LPTT and Oldroyd-B models (see Fig. 4.3e). This is expected, since the currently selected material parameters lead to a Giesekus fluid model with weak extensional properties. For all three models over the range $r/R_{mid}<0.5$, D_{zz} sustains a constant level (about 1.2 units for Oldroyd, 1.3 for LPTT, and 1.4 for Giesekus). Then, D_{zz} increases to reach a value of about 1.35 units for Oldroyd, 1.45 for LPTT, and 1.6 units for Giesekus at the free-surface. The reason for this is that at the filament mid-plane, axial velocity change between filament layers is faster for the Giesekus than the Oldroyd-B model. This implies that in the Giesekus form, particles at the mid-plane (particularly near the free-surface) move faster in the axial direction (z). Hence, the filament is more easily extended in the case of the Giesekus model fluid than equivalently for the Oldroyd-B representation.

4.3.1.2 Temporal predictions at larger Hencky-strains (0.2 ≤ε≤3.0)

In Fig. 4.4, the development of the mid-plane filament radius (R_{mid}) is considered as a function of Hencky-strain. The anticipated overall trend of radial decrease with filament stretch is observed. Up to a Hencky-strain of two, radial evolution for the Giesekus model overlaps that for approximate lubrication theory ($e^{-0.75\varepsilon}$ curve, Newtonian, fixed-end-plates result). Lubrication theory overestimates R_{mid} beyond this level of $\varepsilon=2$, with the true mid-plane radius decreasing more rapidly, following a non-linear-logarithmic representation. In contrast, R_{mid} for the Oldroyd-B model departs from lubrication theory ($e^{-0.75\varepsilon}$ curve) around $\varepsilon=1.2$, retarding the rate thereafter, approaching the curve representative of homogeneous deformation in uniaxial elongational flow ($e^{-0.5\varepsilon}$ curve). Similar findings were

reported by Yao et al. [14]. In R_{mid}, it has been found that up to a Hencky-strain of three, the LPTT model response is closer to that for Oldroyd-B than Giesekus, being captured between these two extremes. From Oldroyd to LPTT results, there is slight reduction noted in filament radius. Beyond $\varepsilon=3$, the pattern begins to adjust dramatically, so that R_{mid} begins to increase (reversal of decreasing trend) with local minima appearing off the centreline, a behaviour unseen with other constitutive models. This may be attributed to the larger transient elongational viscosity response attained with the LPTT model. The consequence of this rise in mid-plane radius, alongside a highly localised adjustment in filament shape thereabouts, lies in the formation of a bead-like structure in the filament.

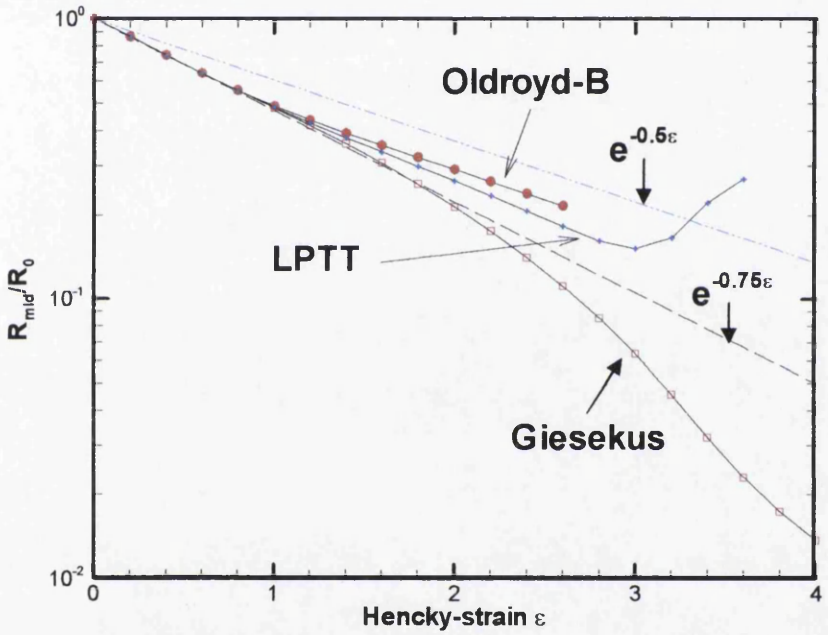

Fig 4.4: Development of R_{mid}, increasing ε, three models: curve $e^{-0.5\varepsilon}$ for homogeneous deformation, uniaxial elongation; curve $e^{-0.75\varepsilon}$ for lubrication approximation

To analyse the flow kinematics for the three models of Oldroyd-B, LPTT and Giesekus, axial profiles for velocity gradient D_{zz} along the centreline of the filament are displayed in Fig. 4.5. Barely any difference is detected across these models at lower values of Hencky-strain up to $\varepsilon=0.2$. The overall trend is that the axial velocity gradient increases from a vanishing value at the end-plates to a maximum at the filament mid-plane, where the largest axial stretching occurs. For $\varepsilon\geq1$ and in accordance with the literature, the Oldroyd-B model displays flatter

centralised profiles with less thinning at the mid-plane than arises with LPTT and Giesekus representations. This trend is reversed near the end-plates where larger extension is encountered with Oldroyd-B results. At the elevated Hencky-strain of $\varepsilon=3$, the solution for the LPTT model begins to show non-symmetric structure, and D_{zz}-maxima shift away from the mid-plane to a location in the upper-half of the filament. This response is due to the competition between opposing influences of shear-thinning and extreme strain-hardening, typical of force imbalance, commonly encountered between body force and surface tension effects, see below. In contrast, the less hardening Giesekus results retain their symmetrical form, with D_{zz}-maxima located at the filament mid-plane once again.

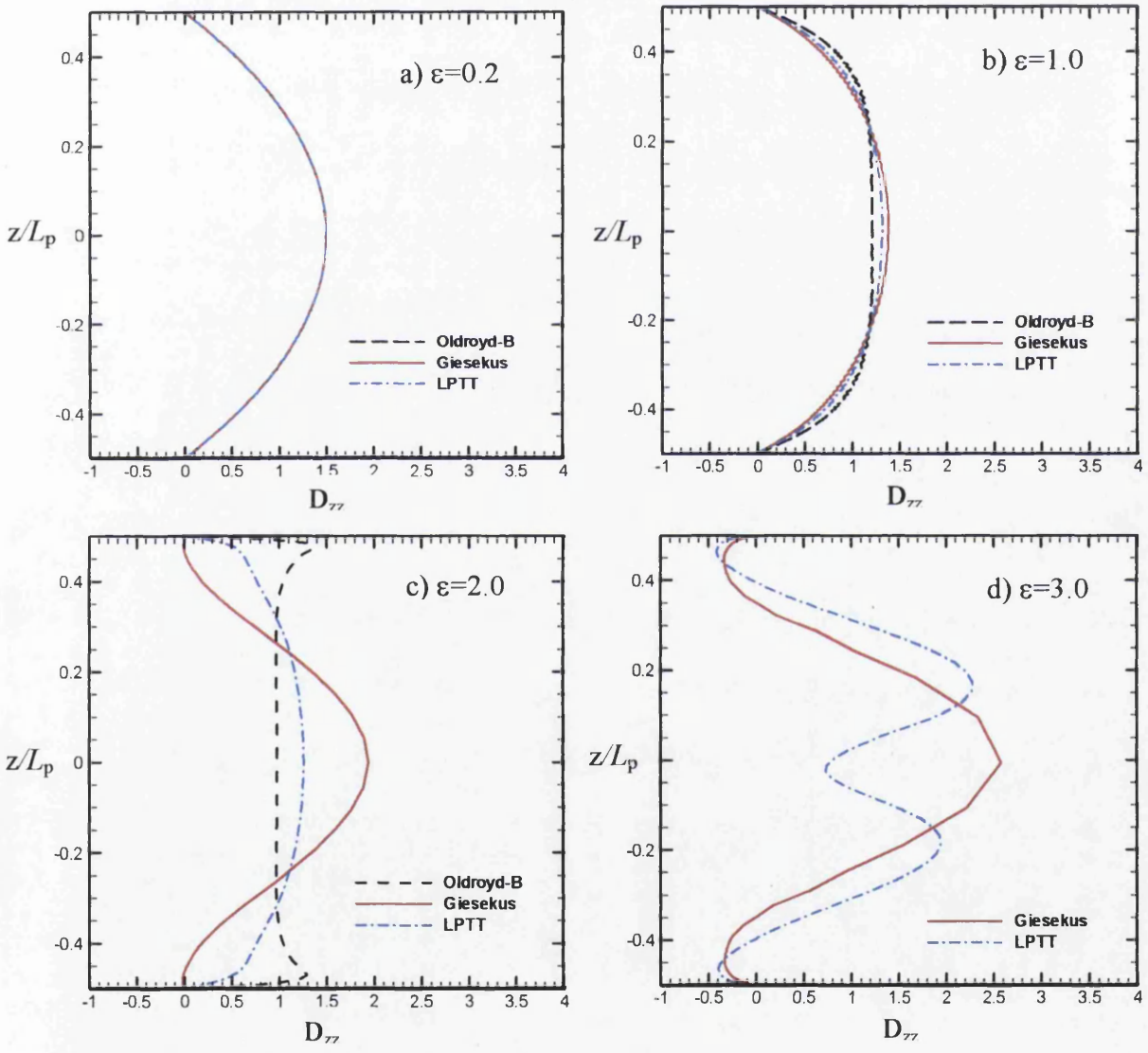

Fig. 4.5: D_{zz}- profiles r=0, rising ε, three models: a) ε=0.2, b) ε=1.0, c) ε=2.0 and d) ε=3.0

To clarify the position even more clearly, the relative axial velocity V_z/V_z^p, taken along the filament axial-centreline against plate axial velocity, V_z^p is displayed in Fig. 4.6. The overall pattern in V_z depicts minima at the bottom-plate and maxima at the top-plate, vanishing at the filament mid-plane. Around Hencky-strains of unity, discrepancy between models commences. The difference between the Giesekus result and that for the two alternative models reveals itself as the filament is subject to further stretching, whilst at this stage the symmetrical behaviour across models is sustained. However, with the LPTT model at Hencky-strains of $\varepsilon \geq 3$, symmetry is disturbed, and the axial velocity vanishes in the upper-

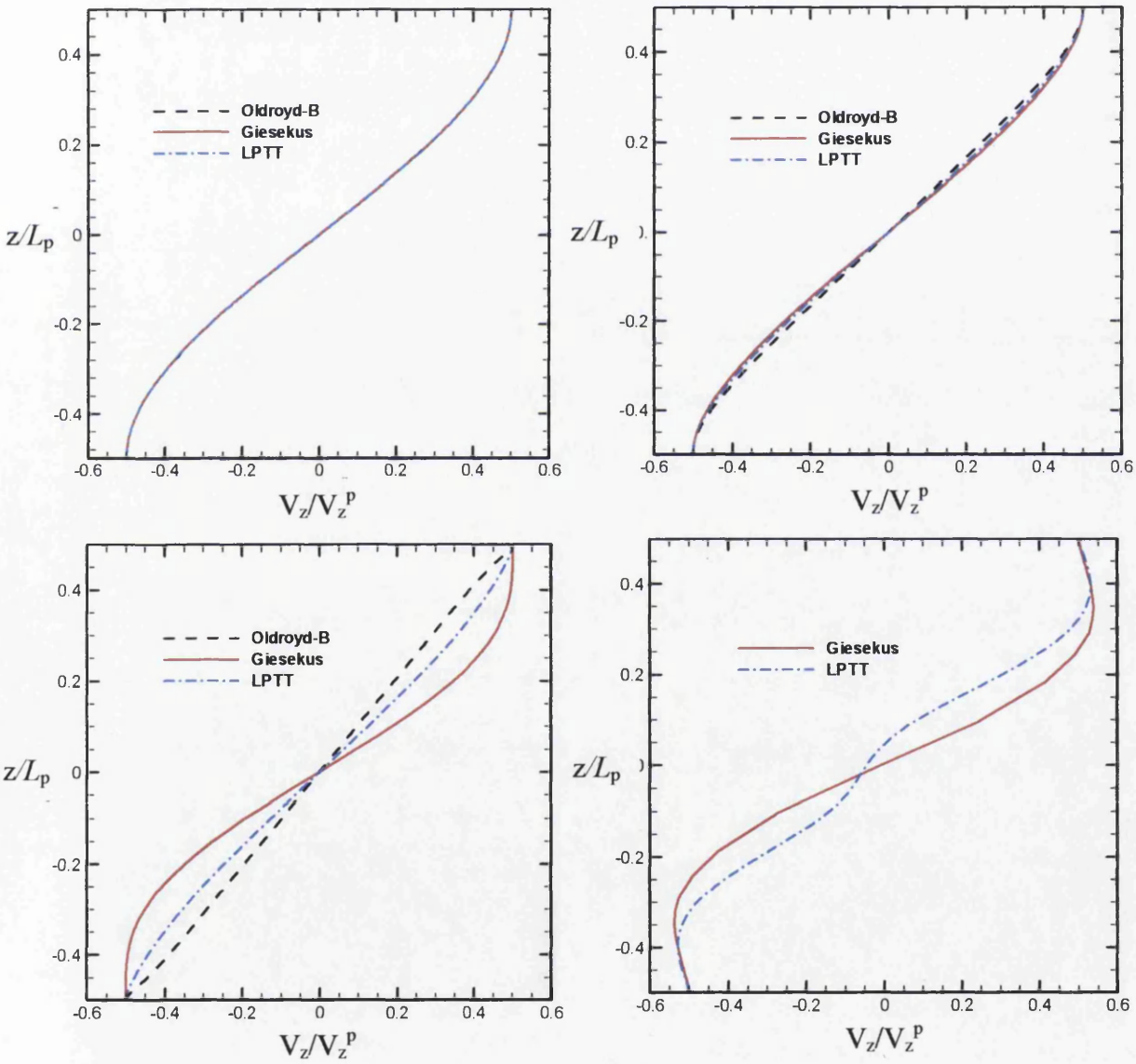

Fig. 4.6: V_z-profiles, r=0, rising ε, three models: a) ε=0.2, b) ε=1.0, c) ε=2.0 and d) ε=3.0

half of the filament instead of at the mid-plane. This does not occur in the case of the Giesekus model with the filament maintaining symmetry throughout the stretching period.

As a consequence, analysing the development of the τ_{zz} axial stress component along the filament axial-centreline for different Hencky-strain steps can be helpful. In Fig. 4.7(a-d), snapshots for $0.2 \leq \varepsilon \leq 3.0$; with $\varepsilon_{crit}=2.6$ for Oldroyd-B results are illustrated, whilst LPTT survives up to $\varepsilon_{crit}=3.6$ and Giesekus up to $\varepsilon_{crit}=4.0$. These findings are rationalised through the extremes of stress and deformation observed in each case. Overall, all models provide similar trends up to $\varepsilon=2.6$. The axial stress relaxes at the end-plates, increasing in value towards the filament mid-plane. The difference lies in τ_{zz}-maxima reached for each model. Beyond a Hencky-strain level of $\varepsilon=0.2$, the largest axial stress magnitudes are yielded for Oldroyd-B solutions, followed by those for LPTT, and finally those for the Giesekus model. This may be attributable unambiguously to the transient elongational viscosity properties for these three alternative models. In comparison to Giesekus, the LPTT model begins to demonstrate more bizarre flow structure and stress response at extreme levels of Hencky-strains, $\varepsilon \geq 3$. For the LPTT model, maxima in stress gradually shift into the filament upper-half. Then, axial stress decreases at the mid-plane, to increase thereafter in the filament lower-portion, prior to vanishing at the bottom-plate. This trend is replicated and amplified at still larger Hencky-strain measures up to $\varepsilon=3.6$. τ_{zz}-maxima range from 0.3 units at $\varepsilon=0.2$, to 100 units at $\varepsilon=3.6$ (see Fig. 4.7(a-f)). Correspondingly for the Giesekus model, τ_{zz}-maxima range from 0.3 to only 15 units. One may realise that these magnitudes are much lower than for the LPTT choice, due to the large differences in transient elongational properties between these two model forms. The Oldroyd-B model equations are computationally more complicated to solve when compared to those for the LPTT or Giesekus models. This is demonstrated through attained levels of ε_{crit}. Thus, for example, with this particular aspect ratio and solvent-polymeric ratio, and when employing an identical Hencky-strain step ($\Delta t_{Hencky}=10^{-3}$), reaching the level of $\varepsilon_{crit}=2.6$ only with Oldroyd-B has been achievable. To stretch the filament somewhat further, a smaller Hencky-strain step would be necessary.

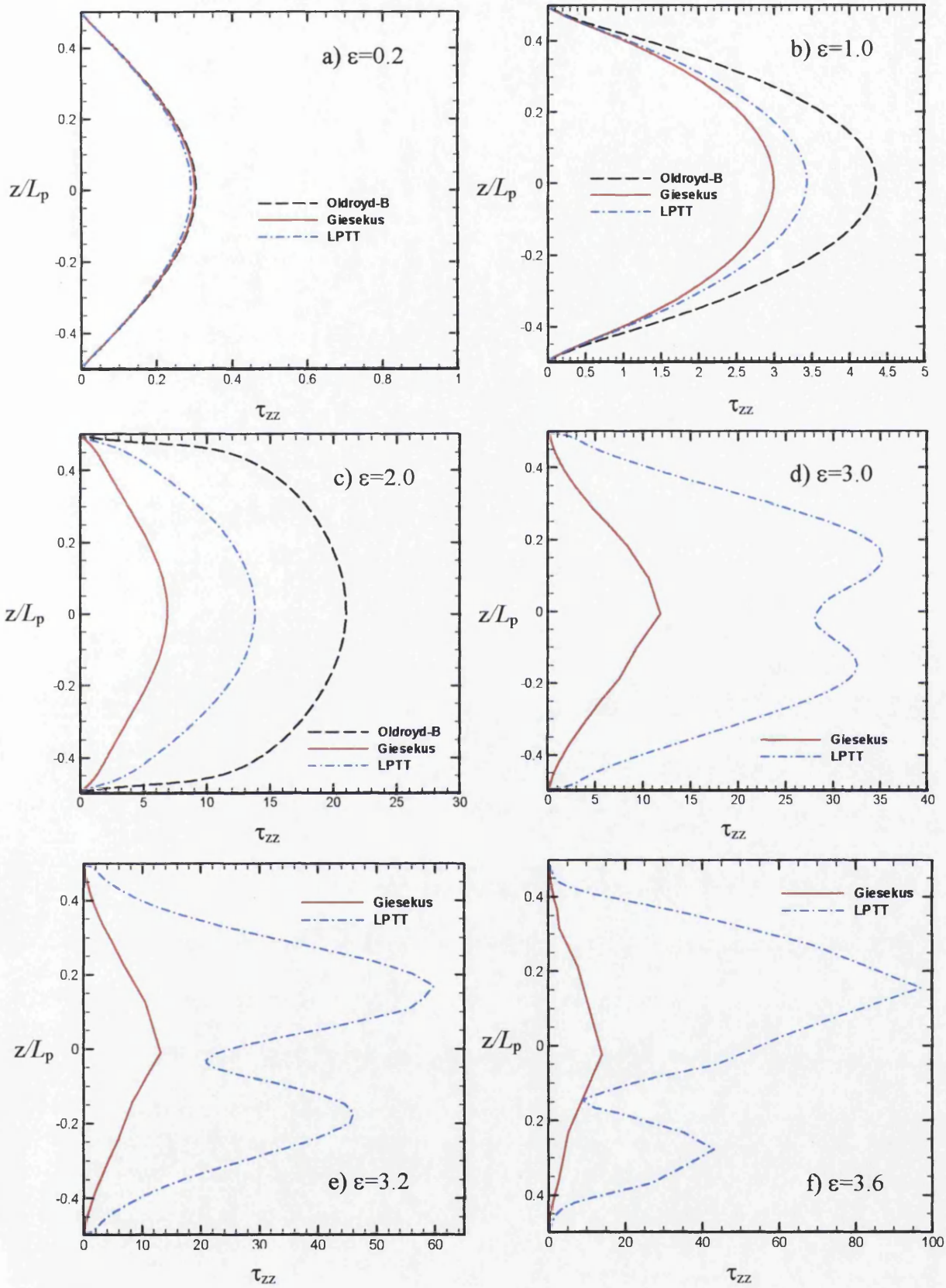

Fig 4.7: τ_{zz} profiles, r=0, three models: a) ε=0.2, b) ε=1.0, c) ε=2.0, d) ε=3.0
e) ε=3.2,f) ε=3.6

Temporal variation in stress-maxima, τ_{zz} and τ_{rz}, for Oldroyd, LPTT and Giesekus is displayed in Fig. 4.8a, the variation of deformation rates (in shear and extension) with strain (time) is illustrated in Fig. 4.8b,c. Stress fields and profiles show that the extensional component of polymeric stress τ_{zz} increases exponentially with the strain level. At any particular strain level, say for example ε=2.5, Oldroyd-B being the most strain hardening fluid provides the largest value of stress (80 units). This is to be compared to LPTT (20 units), which is followed by Giesekus results (10 units). The shear stress component, τ_{rz}, is much smaller in comparison to its extensional counterpart. At ε=2.6, τ_{rz} for Oldroyd-B is about 6%

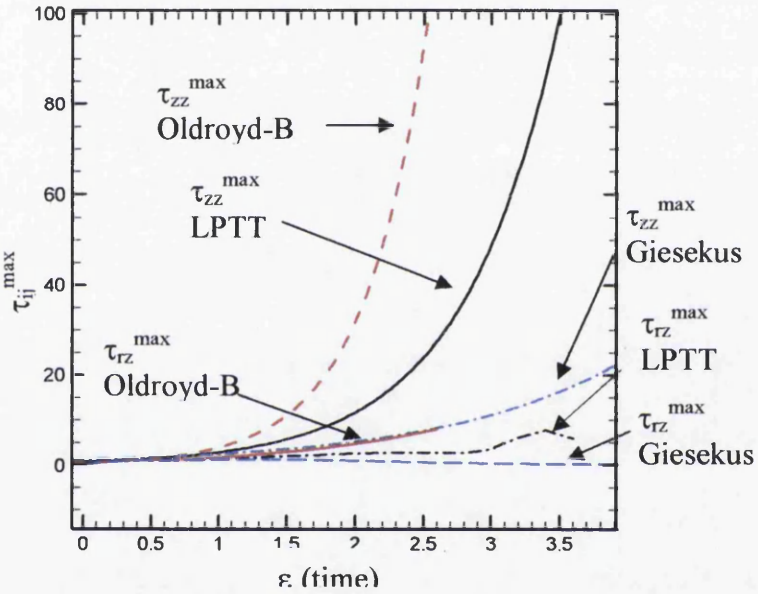

a) τ_{rz}^{max} and τ_{zz}^{max}

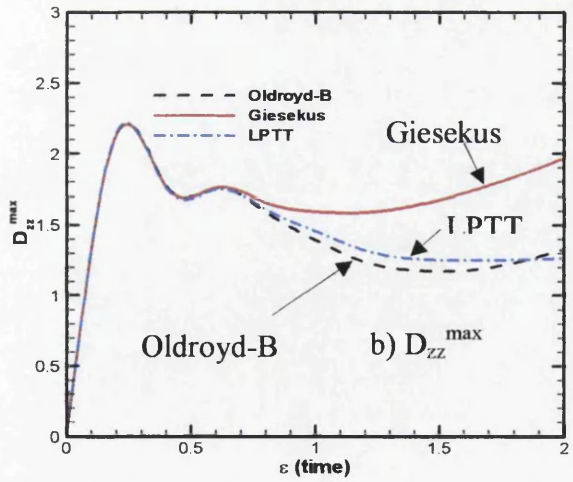

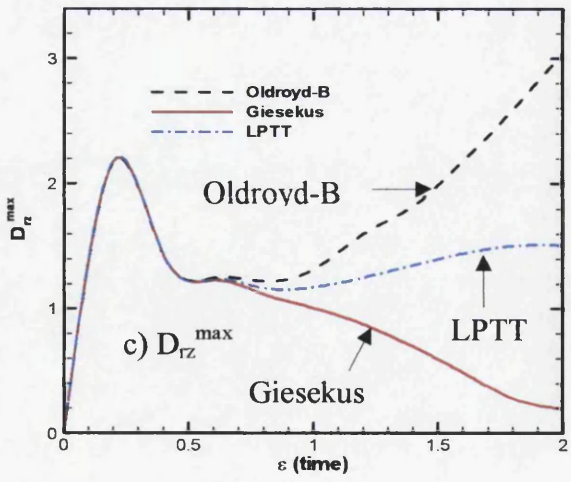

Fig. 4.8: Temporal variation in maxima, three models: Ca^{-1}=0.0, F_g=0.0;a) τ_{rz}^{max} and τ_{zz}^{max}, b) D_{zz}^{max}, c) D_{rz}^{max}

of τ_{zz}. Deformation rates D_{zz} and D_{rz} indicate similar response patterns to each other. For the Oldroyd-B fluid, D_{rz} (3 units) is larger when compared to D_{zz} (1.3 units) at a Hencky-strain of 2.0. In contrast, D_{rz} for the Giesekus model declines to small values at ε=2.0 (around 0.2 units).

In Fig. 4.9, Trouton ratio predictions are plotted against effective Hencky-strain, ε_{eff} (as by common convention, see [14] for definition), and against the available experimental and numerical data of Yao et al. [14]. The numerical results are in good agreement with the experimental data at low Hencky-strains of O(unity); this being continued likewise for the Giesekus model at larger Hencky-strain levels. The departure between Giesekus and LPTT-predictions occurs around ε=1.2, beyond which stage the LPTT-Trouton ratio rises at a greater rate than that observed for the Giesekus model. This is in accordance with the dynamic extensional properties of each model.

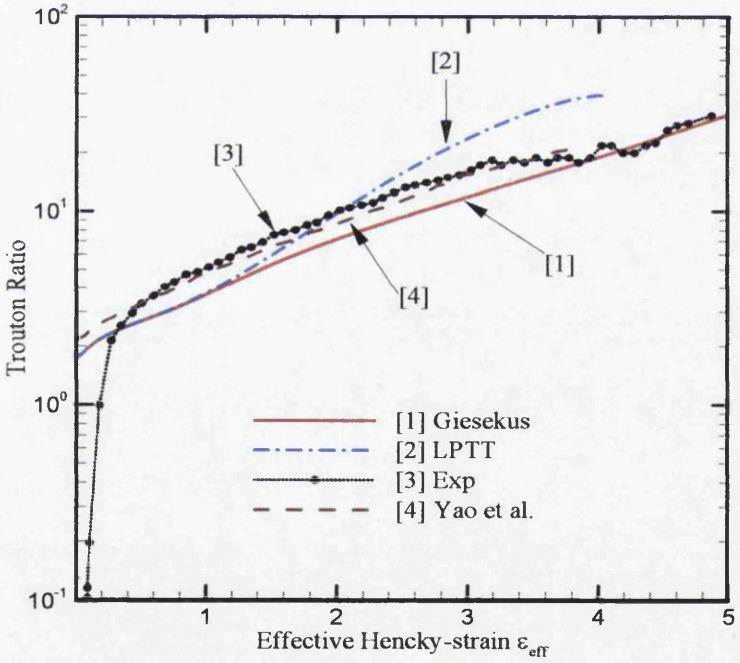

Fig. 4.9: Trouton ratios vs ε_{eff}; two models, experimental and numerical data, Yao et al. [14]

Filament shapes for the different models at ε=2.6 are plotted in Fig. 4.10 to interrogate filament structure globally and within the zone of the filament foot. In the filament-foot zone and near the end-plates the Oldroyd-B filament shape is more pinched towards the axial-centreline of the filament than is apparent for LPTT and Giesekus instances. In contrast, the Giesekus model filament-foot limits lie outside those for LPTT or Oldroyd-B; so that in this zone, the Giesekus fluid is less stretched along the centreline axis than for the LPTT instance. Yao et al. [14] reported the same trend for Oldroyd-B and Giesekus models. In contrast, at the filament mid-plane, the Oldroyd-B fluid is least stretched along the centreline axis with the Giesekus fluid being most stretched and the LPTT fluid lying in between. Once more, this finding can be attributed to the nature and differences between the elongational properties of these particular three fluids. Hence, as the elongational viscosity gets larger, it becomes more difficult to stretch the fluid along its axis, the region of largest extension where the fluid will resist compression most.

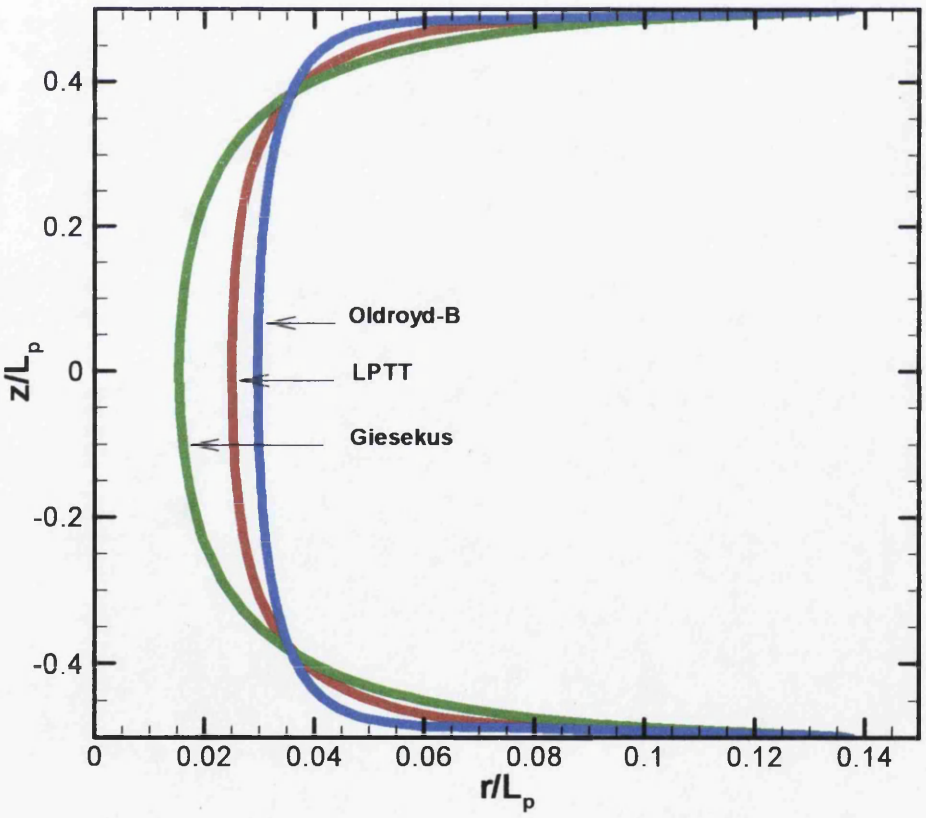

Fig. 4.10: Filament structure and foot zone: ε=2.6, three models

4.3.1.3 Quarter-domain vs half-domain problem

For the purpose of verifying mesh convergence and validating non-symmetrical results, a quarter-domain problem (half-length) was employed alongside the default half-domain case (full-length filament). Here, only a quarter of the filament domain is retained physically and solved for in a symmetric manner, effectively doubling the mesh-density of the original problem. In this case, on the filament mid-plane (now lower boundary), symmetry boundary conditions with no-shear must be explicitly imposed. Such a setting effectively removes the development of asymmetrical features in the evolving flow, and in the comparison against the full-length filament representation quantifies the numerical impact on emergence of asymmetry.

In Fig. 4.11, minimum filament radius at the mid-plane axis (R_{mid}) and filament-centre stress are plotted against increasing Hencky-strain for Oldroyd-B and LPTT models. Results are presented for Oldroyd and LPTT instances, as the former provides premature ε_{crit} <3.0, whilst the latter transcends ε=3.0 and illustrates bead-like structures with localised minima. The minimum radius in Fig. 4.11a,b for the quarter-domain problem overlaps that corresponding to the full-length case, exactly for Oldroyd-B, with slight departure noted in LPTT around $\varepsilon\approx$3.0. According to Yao et al. [14], the radius continually decreases as the filament is stretched up to ε=4, in accordance with our full-length problem Giesekus results. For the development of τ_{zz} across fluids and the two problem-domain instances, similar agreement is observed in Fig. 4.11c,d. Stress rises monotonically to a maximum for the Oldroyd-B model (ε_{crit}=2.6 full-length case, ε_{crit}=2.8 quarter-domain problem); for LPTT fluids, τ_{zz} increases to a maximum, beyond which a decline is detected thereafter (ε_{crit}=3.6 full-length case, ε_{crit}=3.4 quarter-domain problem). Such findings are in agreement with the trends observed with mesh refinement.

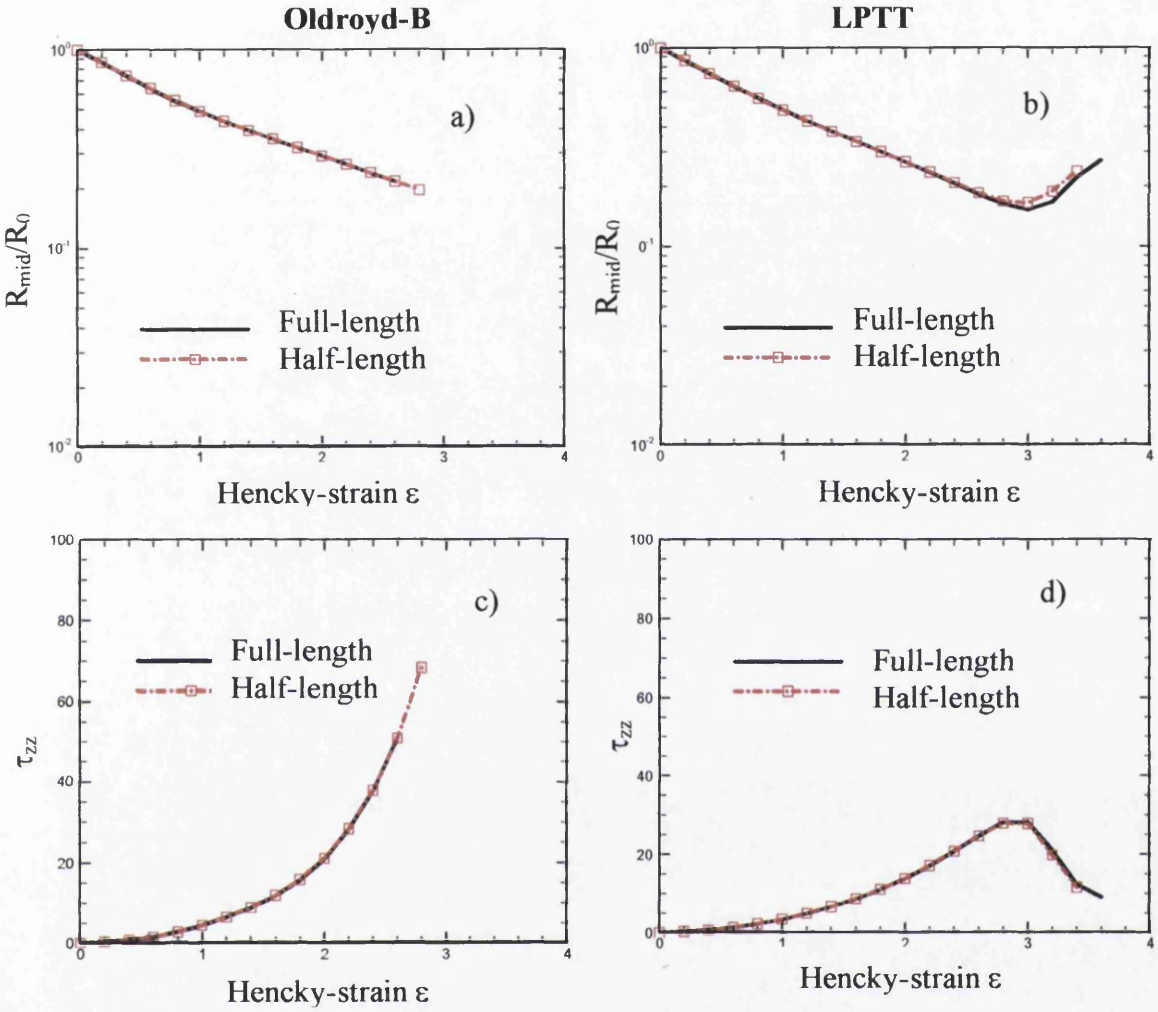

Fig. 4.11: Temporal evolution of R_{mid}, and τ_{zz} (r=0, z=0) for a,c) Oldroyd-B and b,d) LPTT models $Ca^{-1}=0$, $F_g=0$.

Quarter-domain solutions consistently report differing ε_{crit} as opposed to their full-length counterparts. The Oldroyd position would display that increased refinement has helped in elevating ε_{crit}. Under LPTT, reduction in ε_{crit} is possibly a consequence of approaching asymmetry. In specific local conditions about the symmetry mid-plane, the marginal solution discrepancies noted are subtle and their discrete treatment comes into effect. Through detailed investigation on this issue it has been revealed that reflected meshing about the filament mid-plane (to impose symmetry conditions numerically), physically retained, or virtually imposed (as with the quarter-domain problem), itself may be the cause of some numerical

anomalies. The issue here is manifested via solution (velocity-) gradient representation across such a flow station, and when treated as a domain boundary or not, as the case may be. As employed elsewhere by default [36], asymmetrical, continuous structured meshing across the mid-plane retains the discrete property of superconvergence. This is reflected in the invoked computational stencils and the high quality of velocity gradients extracted thereby. For reflected meshing which may display false local minima in normal gradients (producing a reflected oscillation in D_{zz}) the same statement cannot be disclosed on passing normally across the mid-plane. This anomaly is negligibly small in extent and natural for such a domain periphery location, where degradation in accuracy is to be anticipated in the quarter-domain problem, be an aspect often overlooked in some flow problems with symmetry boundaries, for example, in cross-slot flow or flow past a sphere. Undoubtedly, its significance is heightened along a purely extensional symmetry flow line, where steep velocity gradients are anticipated. For example, simply capping the maxima in D_{zz} with a plateau across the mid-plane corresponds to a crude finite-difference stencil approximation. In this fashion, an undershoot in D_{zz} would effectively be avoided but the true maxima will fail to be captured accurately. Nontheless, in the context of seeking representation for physical disturbances and non-symmetrical solutions, this is a point of detail to recognise, which has had influences in our inclination towards the full-length problem representation with the superconvergent choice of continuous structured meshing, non-reflective across the filament mid-plane.

4.3.2 Inclusion of gravity and surface tension (LPTT)

The influence of both surface tension and axial gravity inclusion in separate phases is plotted, noting results for LPTT by default, against which other fluids may be compared below. Low Hencky-strain predictions are discussed first.

4.3.2.1 Surface tension effects, $\varepsilon \leq 2.0$

First, with *surface tension alone*, quantified through the inverse capillary number, denoted by Ca^{-1}, covering a range of values from 0.0, 0.1, 0.5 and 1.0 (nb. Yao et al. [14] employed $Ca^{-1}=0.1$). Trends of localised τ_{zz} maxima which develop at the position of minimum radius, are demonstrated for $\varepsilon=1.0$ (see Fig. 4.12b),

whilst filament shape remains symmetrical. Local stress magnitude can be exaggerated at Ca^{-1}=1.0 by as much as 10% above that corresponding to the equivalent scenario devoid of surface tension influence. These local maxima are absent at the earlier time of ε=0.2 (see Fig. 4.12a). At larger levels of Hencky-strain of 2.0 (see Fig. 4.12c) and above, one would observe that solutions in τ_{zz}, begin to distort for capillary numbers higher than Ca^{-1}=0.5, an effect that becomes quite marked by the level of Ca^{-1}=1.0. These findings reflect the sensitive nature of the solution to this particular physical effect. Correspondingly, up to Hencky-strains of 2.0 (see Fig. 4.12d) filament shape is barely affected.

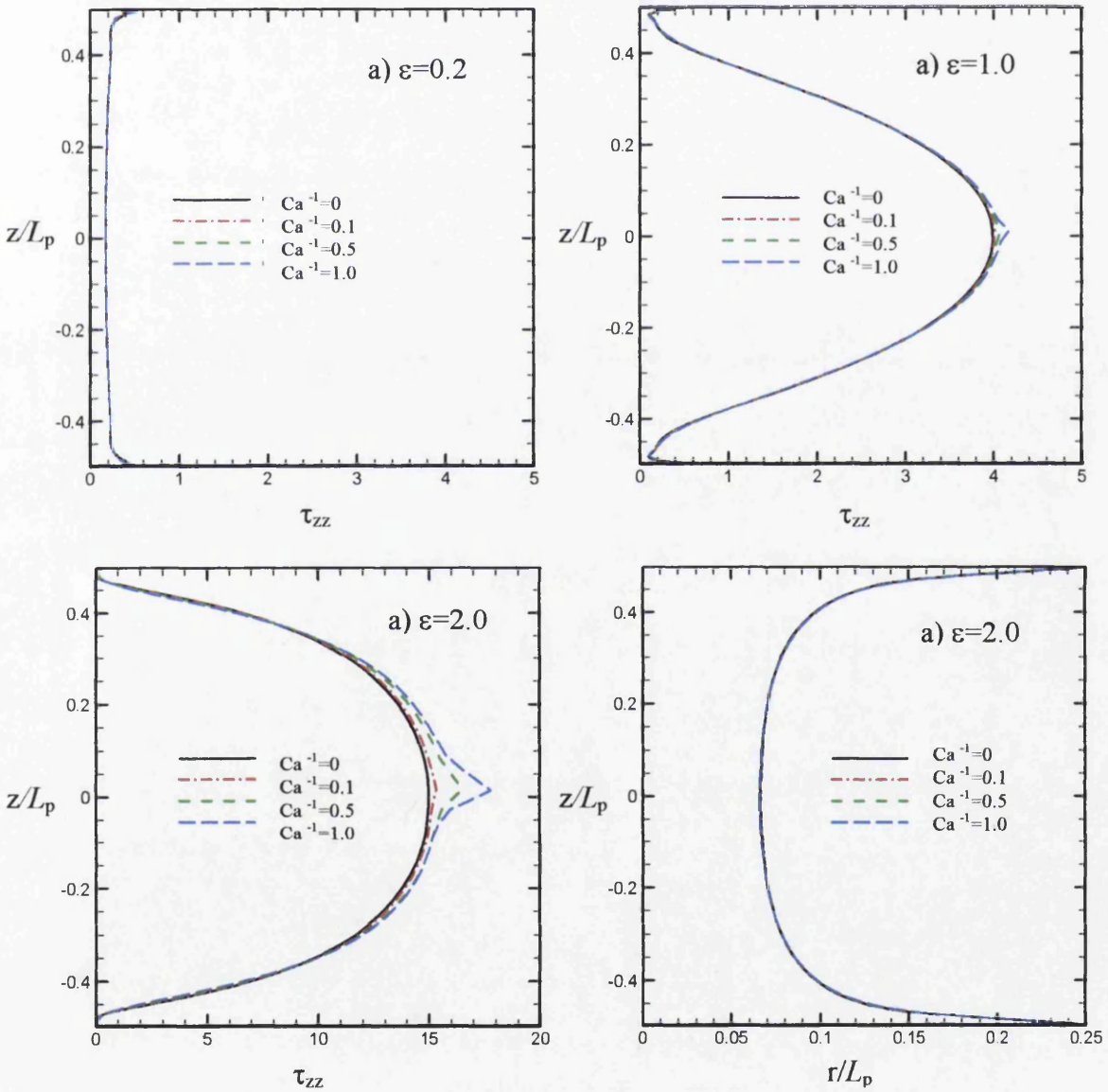

Fig. 4.12: With surface tension alone, Ca^{-1}variation: F_g=0.0, LPTT; free-surface τ_{zz} a) ε=0.2, b) ε=1.0, c) ε=2.0; free-surface shape (r/L_p) d) ε=2.0

4.3.2.2 Influence of gravity and surface tension combined, ε≤2.0

At ε=1.0 and when *gravitational forces* (imposed axially) are brought into consideration alongside surface tension effects, $0.1 \leq Ca^{-1} \leq 1.0$, with a base level of body force factor of F_g=0.122, distortion is revealed in filament shape and surface tensile stress distribution. This distortion is moved towards the lower half-filament, where the minima in filament radius and local stress maxima now are detectable (see Fig. 4.13). Once more at the more elevated Hencky-strains of ε=1.6 and 2.0 this position is observed. Here, to identify the restoring role of surface tension forces (at Ca^{-1}=0.1 level) surface tension which acts to counterbalance against

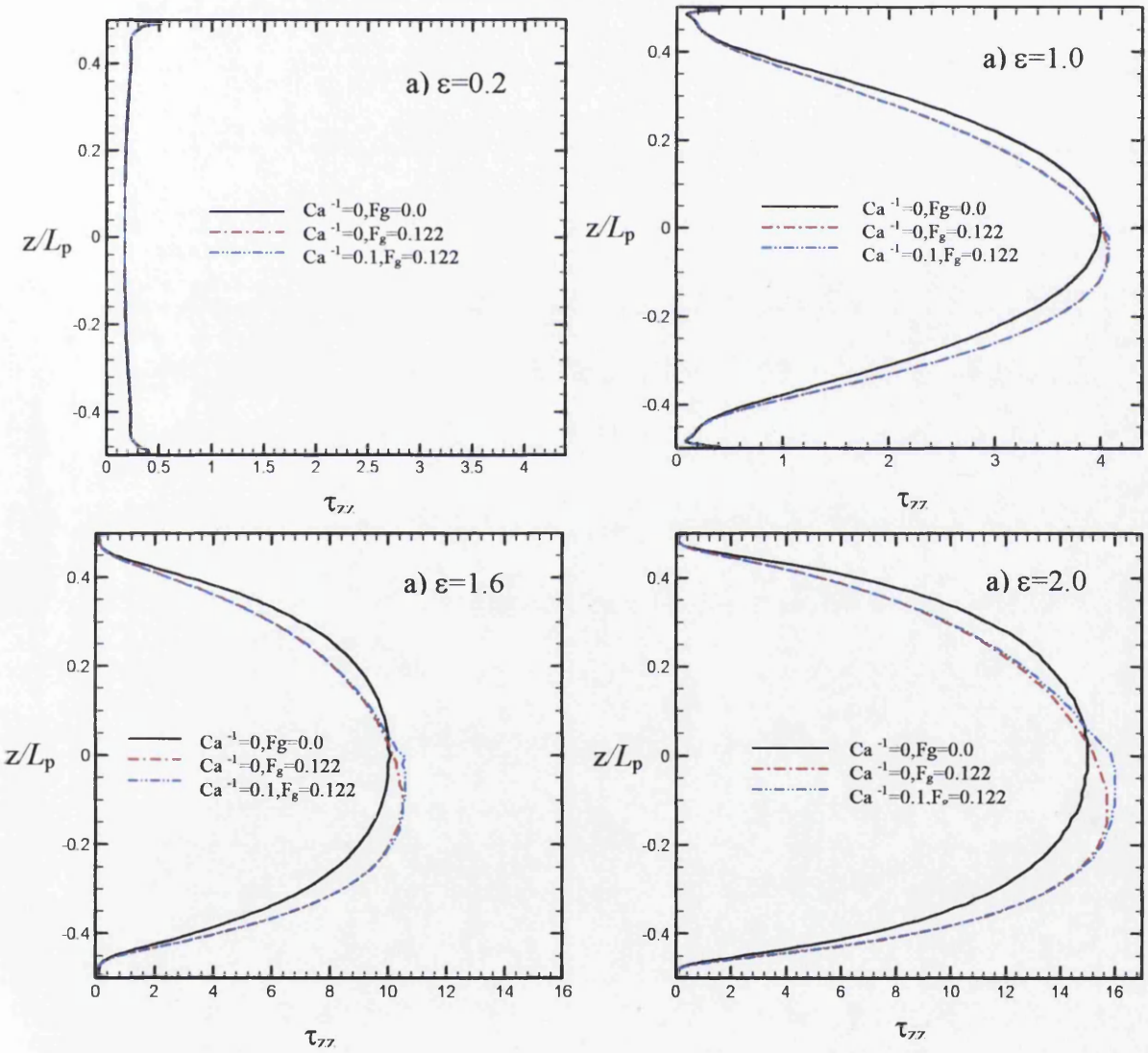

Fig. 4.13: With surface tension with/without body force: LPTT; free-surface τ_{zz} a) ε=0.2,b) ε=1.0, c) ε=1.6, d) ε=2.0

gravitational forces is removed. As such, local stress maxima are shifted backwards towards the filament centre.

4.3.2.3 Large Hencky strain results, ε>2.0

At large Hencky strains above 2.0, various conflicting influences are encountered, so that richness is observed in alternative flow structures generated, depending upon the particular configuration involved. This includes the formation of bead-like structures and asymmetries in shape, alongside redistribution and replication of local stress maxima. Filament shape can be commented on, via profiles and full filament representations, and on tensile stress (τ_{zz}) and/or axial deformation rate (D_{zz}) likewise. For the characteristic instance involving *surface tension* (at Ca^{-1}=0.1) and *gravitational forces* (with F_g=0.122), see Fig. 4.14 with the LPTT fluid, disruption in the filament shape from its symmetrical orientation above ε=2.8 is noted, so that at ε=3.0 there is a slight indentation around the

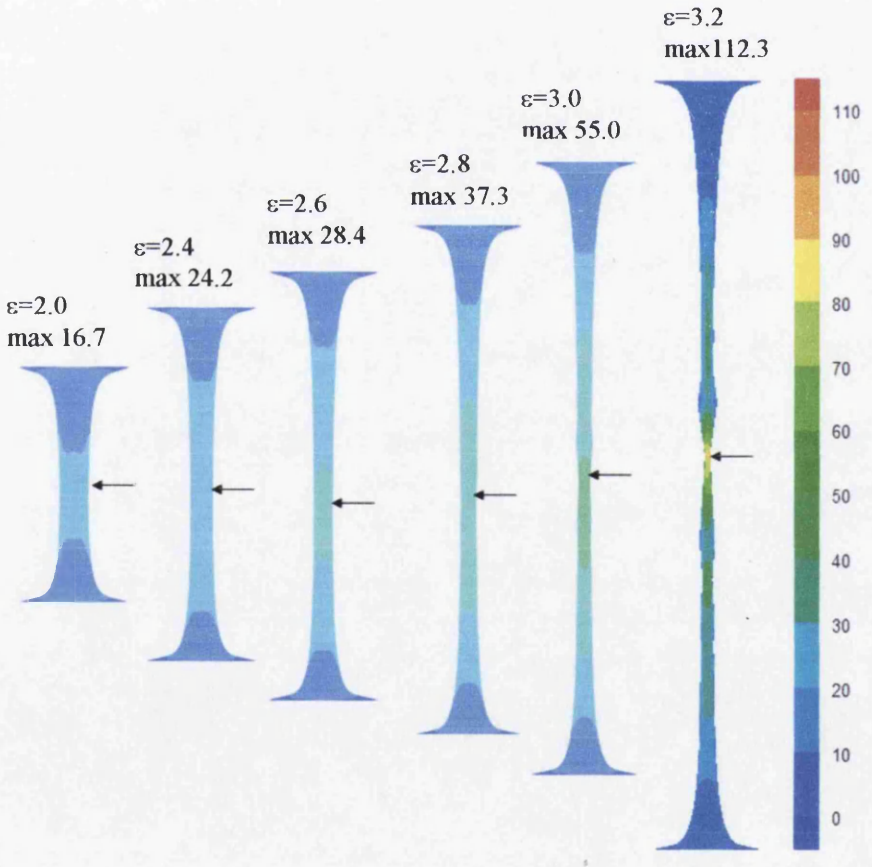

Fig. 4.14: Full filament, LPTT, with body force and surface tension, ε≥2.0: filament shapes and τ_{zz} field contours

filament centre. Further development in this trend is observed up to the critical levels of ε_{crit}=3.2 with filament mid-plane τ_{zz}-maxima of 112 units, producing two small bulges (beads) on either side of the filament mid-plane. In addition, counterpart stress patterns are demonstrated in Fig. 4.14, indicating that there are local extremes in stress corresponding to these bulges, of relative size some O(20%) of the mid-plane maxima. For Hencky-strain values of {2.0, 2.4, 2.6, 2.8, 3.0, 3.2}, the corresponding mid-plane τ_{zz}-maxima vary through values of {16.7, 24.2, 28.4, 37.3, 55.0, 112.3} units.

One would also be able to extract further information here when tracing the temporal evolution of these point-wise maxima, in stress {τ_{zz} and τ_{rz} (Fig. 4.15a)} and deformation rates {D_{zz} and D_{rz} (Fig. 4.15b)}. This is indicative of the relative dominance between extensional and shear components of stress within the system. Comparing this information against that presented earlier for the case devoid of surface tension and body force (see Fig. 4.8), it is apparent that the stress and deformation rate maxima patterns follow similar behaviour in both scenarios (stress rises and deformation rates decline with time).

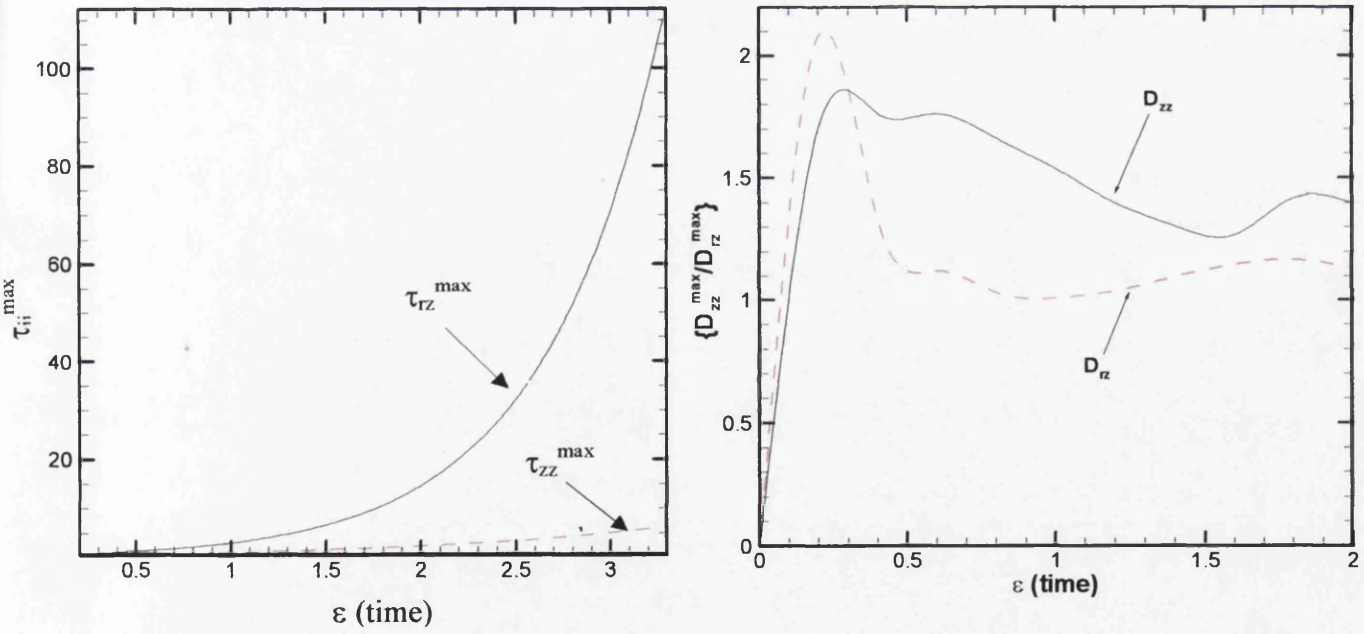

a) τ_{rz}^{max} and τ_{zz}^{max} b) D_{rz}^{max} and D_{zz}^{max}

Fig. 4.15: Temporal variation in maxima, LPTT: Ca^{-1}=0.1, F_g=0.122
a) τ_{rz}^{max} and τ_{zz}^{max}, b) D_{rz}^{max} and D_{zz}^{max}

In switching attention to the instance devoid of surface tension, and solely subject to *gravitational forces*, we are now able to advance up to a critical Hencky strain of ε_{crit}=3.4. In Fig. 4.16, with results provided up to ε=3.4, one may be able to make direct comparison against the previous configuration with surface tension. Now, only a single bulge-bead structure appears and this is shifted away from the centre of the filament towards its lower-portion. Here, compared to the instance when surface tension is present there is less radial pinching about the bulge, so that it is more disperse. The τ_{zz}-maxima of 93.4 units (see Fig. 4.16) emerges in the lower filament half with bead-extrema representing some O(30%) of this. To quantify and for Hencky-strain magnitudes once more in the range $2.0 \leq \varepsilon \leq 3.4$, the corresponding τ_{zz}-maxima vary through values of {15.8, 22.2, 25.4, 31.3, 45.0, 83.3, 93.4} units.

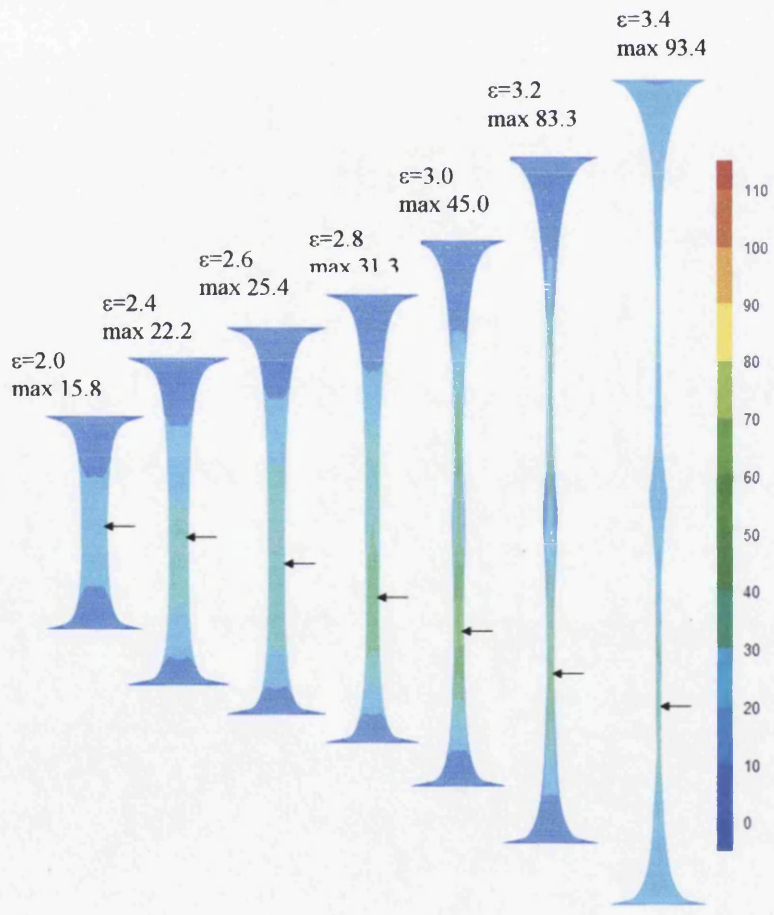

Fig. 4.16: Full filament, LPTT, with body force alone, $\varepsilon \geq 2.0$: filament shapes field contours and τ_{zz}

Within the isolated scenario of *surface tension* yet without body forces, critical Hencky strain returns to ε_{crit}=3.2; a common attainable level across all instances. The asymmetrical response appears in the formation of bead-like structure and its build-up beyond ε=3.0, switches to influence only the upper half- filament. This is in complete juxtaposition to that observed for the instance with body force alone (see Fig. 4.17). The τ_{zz}-maxima of 81.1 units emerges in the lower filament portion slightly off-centre with bead-extrema representing around 16% of this. Corresponding τ_{zz}-maxima over the Hencky-strain range $2.0 \leq \varepsilon \leq 3.2$, now vary through the range of values of {15.9, 22.6, 26.7, 31.8, 41.3, 81.1} units - following closely those for the case with body force alone.

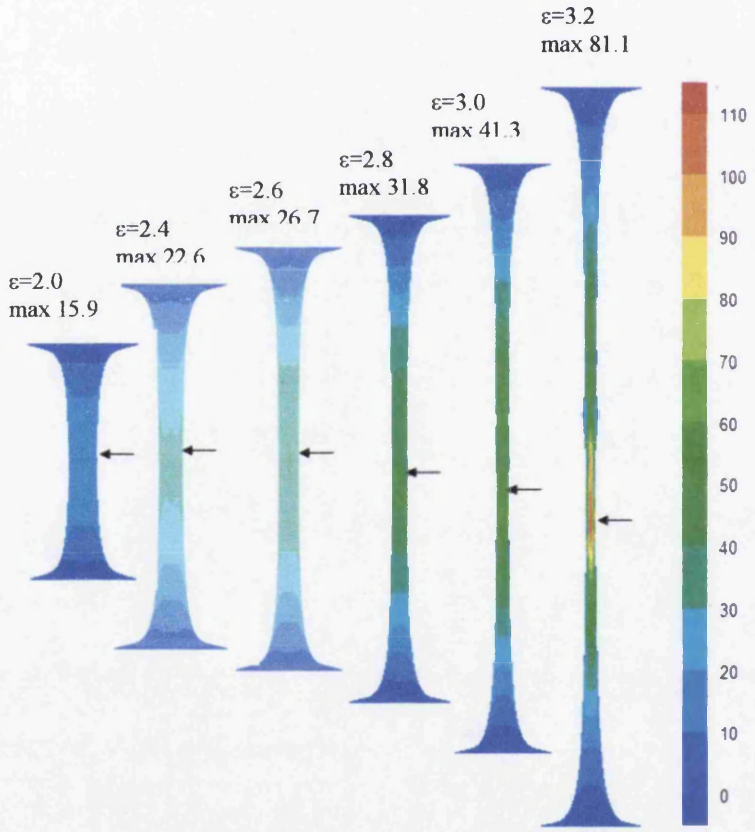

Fig. 4.17: Full filament, LPTT, with surface tension alone, ε≥2.0: filament shapes and τ_{zz} field contours

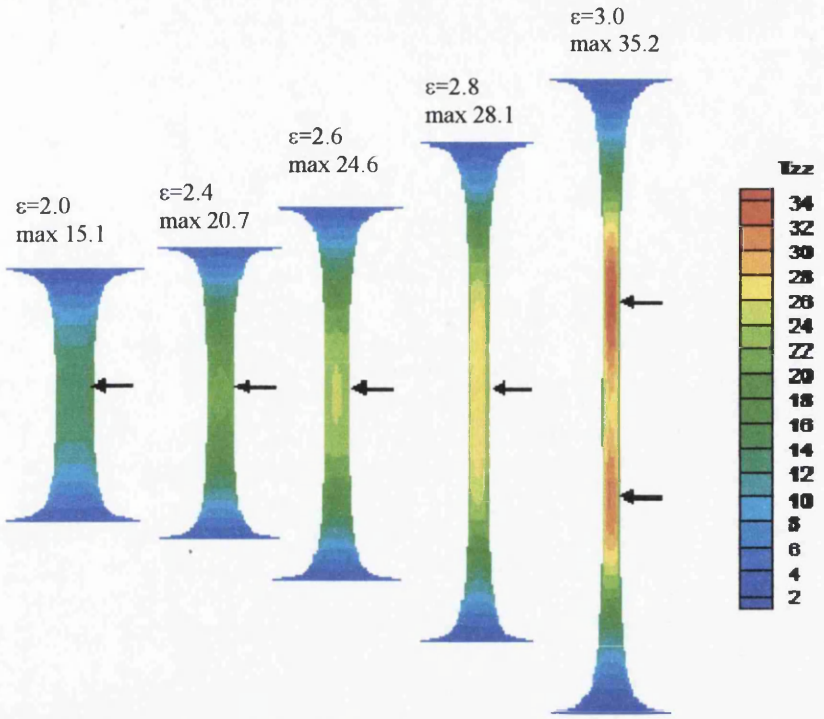

Fig. 4.18: Full filament, LPTT, without body force and surface tension, $\varepsilon \geq 2.0$: τ_{zz} field contours

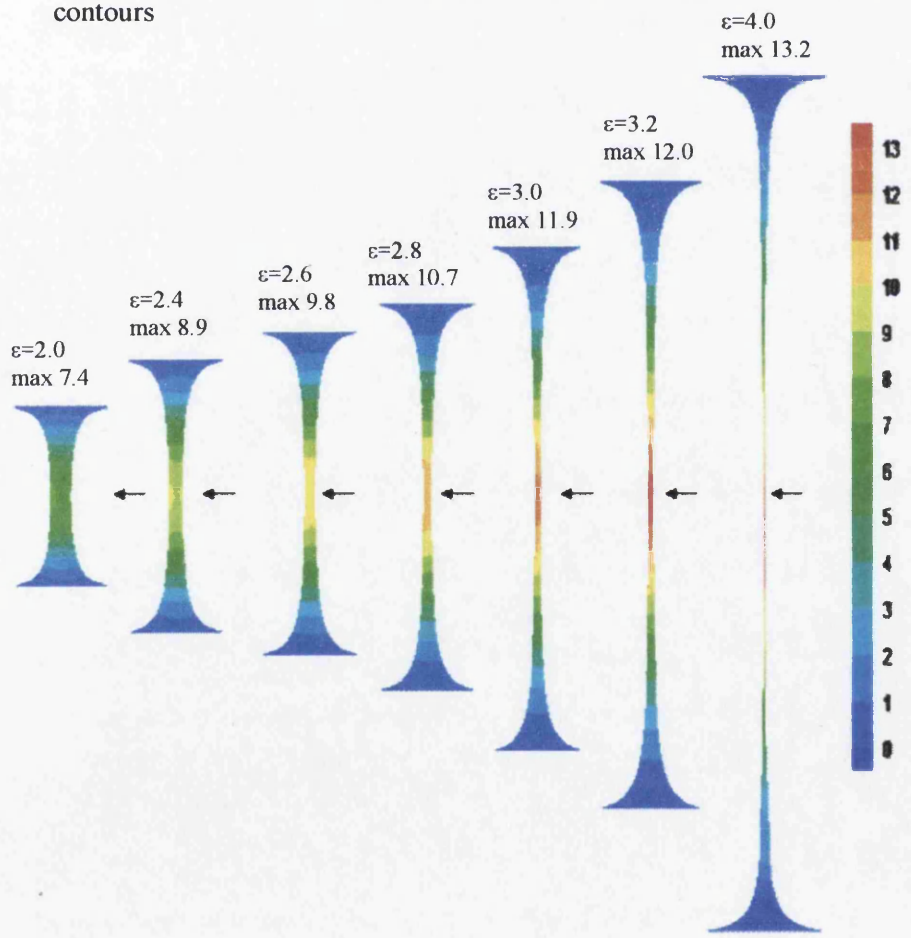

Fig. 4.19: Full filament, Giesekus, without body force and surface tension, $\varepsilon \geq 2.0$: τ_{zz} field contours

In contrast, the idealised scenario devoid of *gravitational and surface tension influences* (Fig. 4.18) retains symmetry without formation of any bead-like structure up to around ε=3.0. The significant feature is that τ_{zz}-maxima are located lower in the filament here than in the above cases at ε=3.0, only reaching values of O(35 units).

However, there are signs that stress maxima are splitting around the mid-plane area beyond ε=2.8. For example, at ε=3.0, the mid-plane value is some 26 units, being 25% lower than the actual off-plane maxima. In this scenario, the Giesekus model realised a ε_{crit}=4.0, with a τ_{zz}-maxima on the mid-plane of about 12 units, indicating no bead-like or asymmetrical features (see Fig. 4.19).

4.3.2.4 LPTT and shear-thinning adjustment, ε>3.0

The effect of adjustment in shear-thinning properties of the LPTT modelling has also been investigated by switching between LPTT (ξ=0.13) (as in Li et al. [2]) and LPTT (ξ=0). The experimental data on shear viscosity are more faithfully reflected by the adjustment to LPTT (ξ=0). At the same time, this removes the inclusion of convective derivative combinations and the complications that may be posed by the Gordon-Showalter derivative. Practically, the extensional rheology remains unchanged, if anything, with the elongational viscosity being slightly larger for the ξ=0.13 instance. In the absence of surface tension or gravitational influences and at Hencky-strains (ε<3), solution evolution is observed to be similar in trend between both LPTT-forms. At $\varepsilon \geq 1.0$, departure is noted. In particular around ε=3.0, where bead-like structures were noted above with ξ=0.13, now with delayed shear-thinning present in the model (ξ=0), these features are suppressed. With such rheological adjustment, the LPTT model reflects the solution response as previously observed with the Giesekus model, of long slender cylindrical filament shape development up to the relatively elevated value of ε_{crit}=4.4. Notably, symmetry is preserved throughout all Hencky-strain levels. This corroborates the notion of exaggerated filament foot curvature changes for the more strain-hardening LPTT over the Giesekus model and the tendency to less thinning across the filament-column span-wise. Stress maxima keep lying at the filament mid-

plane. The elevation and temporal evolution of stress maxima is such that LPTT (ξ=0.13) solutions reach O(80 units), whilst Giesekus values reach O(10 units) at ε_{crit}=4.0; equivalently, being O(100 units) for LPTT (ξ=0) at ε_{crit}=4.4. The dynamic viscometric extensional properties would bear testament to this. Here, limitation on attainable strain is not restricted so much by stress elevation as by spatial resolution (stretching of the finite element aspect ratios). Moreover, the manifestation of physical anomalies, such as asymmetries or bead-like structures, are stimulated by the interaction of more excessive shear-thinning under severe extension conditions.

The axial stress (τ_{zz}) maxima remain located at the filament mid-plane region up to a Hencky-strain of ε=3.8 under the surface tension influence alone. At this level, a bead-like structure emerges in the specified region. As the filament is stretched further, τ_{zz} shifts from the mid-plane accordingly. The symmetry of the problem is preserved at all Hencky-strain levels. Yet, with the supplementary addition of gravitational forces, symmetry is retained once more throughout all stratification levels of stretching. At ε=4, only one bead commences to form at the filament mid-plane region. Features and trends in axial stress development in this case resemble those realised under the influence of surface tension effects alone.

4.3.3 Multi-mode predictions

The aim of this section is to shed some light practically upon the departure detected between solutions predicted for single-mode and multi-mode model approximations (2-modes), ignoring the effects of body force and surface tension. Differences may arise on account of the larger solvent viscosity incorporated into the single-mode case, and the wider spectrum of relaxation times represented in the multi-mode instance. With the multi-mode representation, shorter response times will have some bearing upon the solutions obtained. The predicted Trouton ratio at the mid-plane governed by Eq. 4.3 is plotted in Fig. 4.20 to display solution response for shorter times. The Newtonian solvent component is

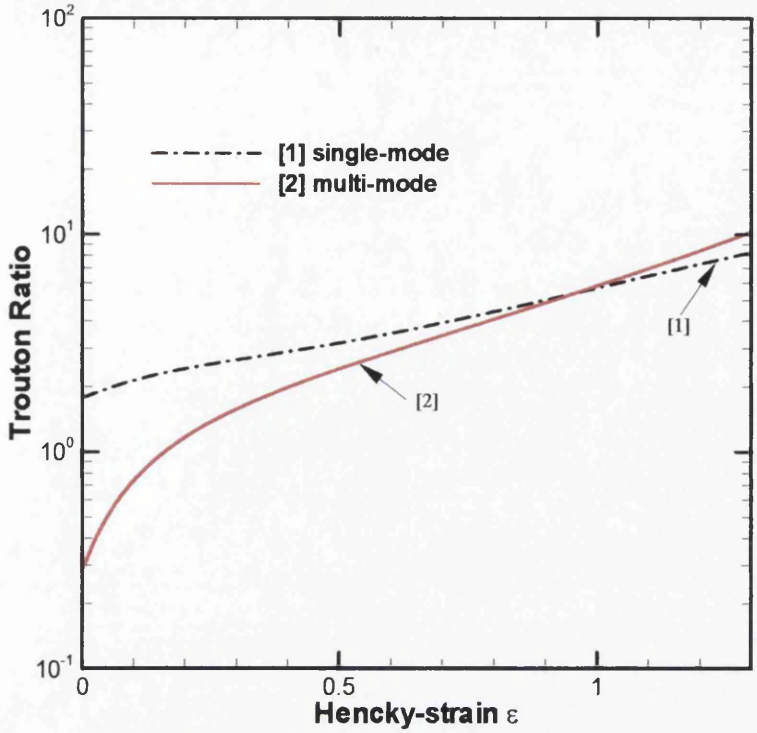

Fig. 4.20: Trouton ratio vs ε; LPTT: single- vs multi-mode results

dominant as the polymeric component is negligible at the outset of the stretching process with the single-mode model. Consequently, larger initial Trouton ratio values are generated and elevated at a constant rate thereafter upon further stretching. In contrast for a *two-mode* model, the viscous contribution is miniscule compared to its polymeric counterpart. This change in component dominance will come into view through the total stress that governs the development of the axial force, and also influences the temporal evolution of the multi-mode Trouton ratio. Here, Trouton ratio commences from a smaller initial value than for its single-mode counterpart, and rises monotonically at an increased rate over the single-mode instance, as observed also by Yao et al. [3].

4.3.3.1 Kinematic state and stress solutions

Solution profiles are plotted in Fig. 4.21 for LPTT (-P) and Giesekus (-G), single and multi-mode approximations, along the filament centreline axis at ε=0.2. At this level of Hencky-strain, barely any difference is detected in the axial velocity component of Fig. 4.21a

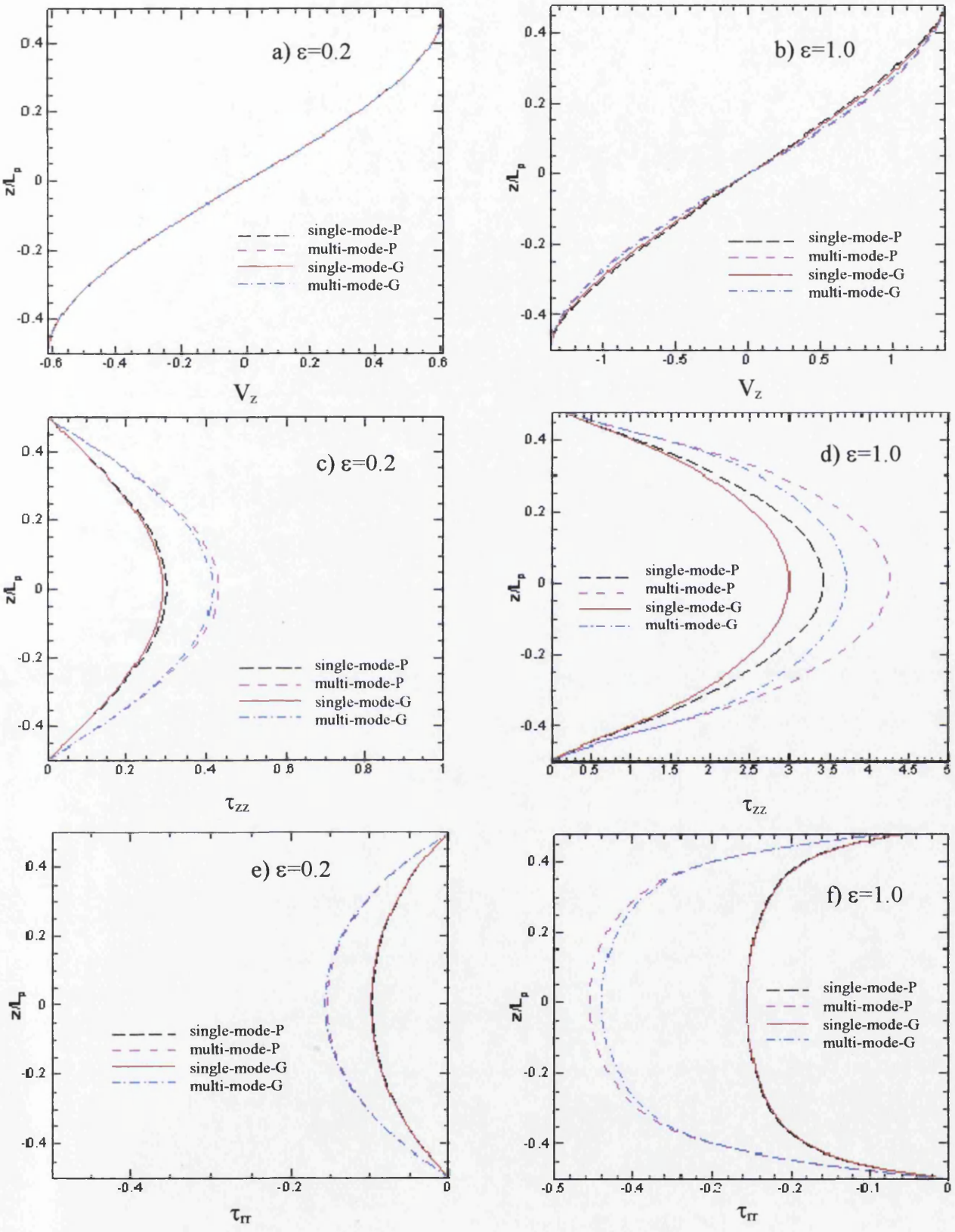

Fig. 4.21: Solution profiles, r=0, single- and multi-mode, increasing ε, LPTT and Giesekus: lhs ε=0.2, a) V_z, c) τ_{zz}, e) τ_{rr} ; rhs ε=1.0, b) V_z, d) τ_{zz}, f) τ_{rr}

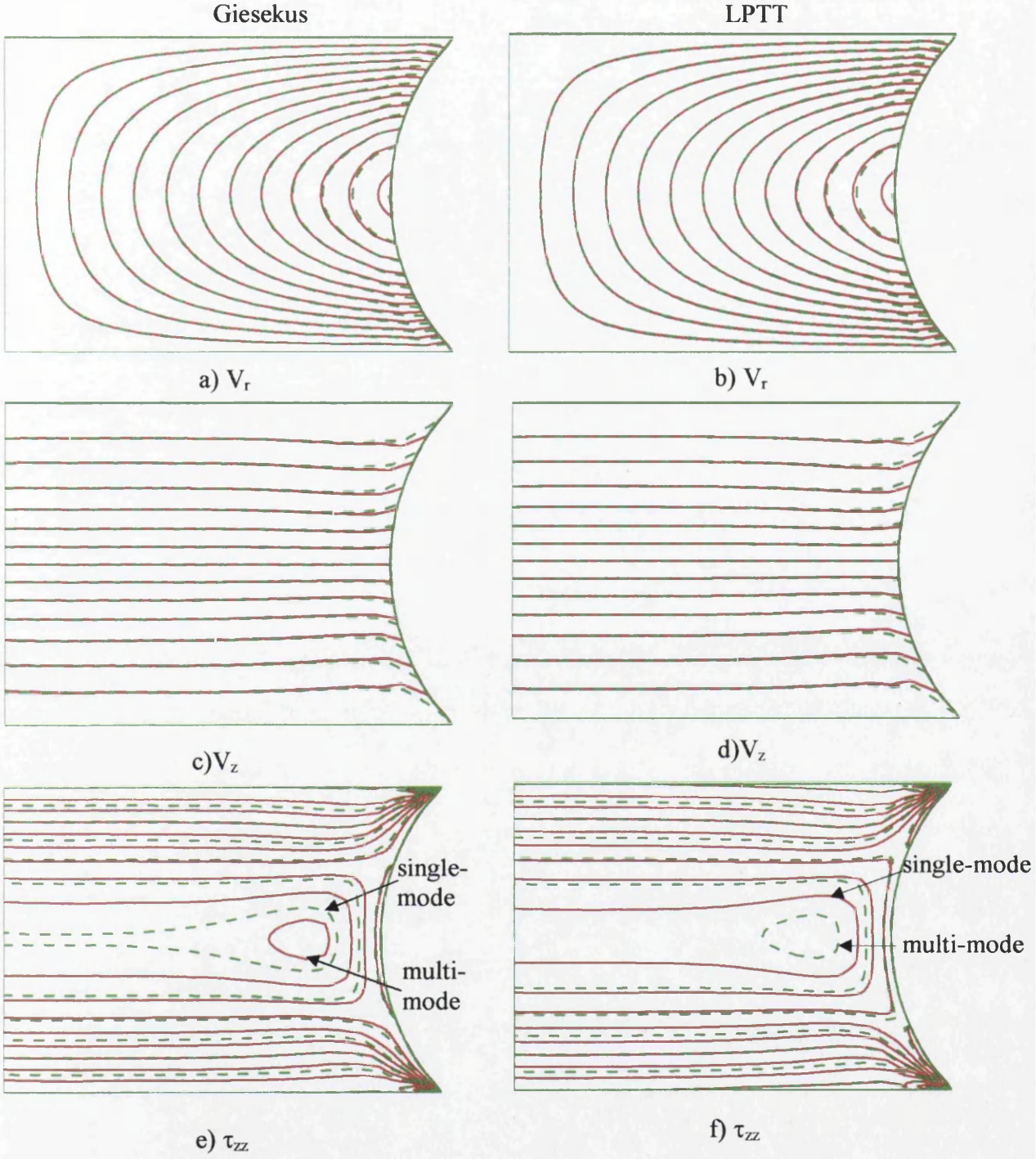

Fig. 4.22: Field contours, ε=0.2, (- - -) single- and (—) multi-mode; lhs Giesekus and rhs LPTT:Giesekus, a) V_r, c) V_z, e) τ_{zz}; LPTT, b) V_r, d) V_z, f) τ_{zz}

between the single and multi-mode velocity predictions. In contrast, the axial stress component τ_{zz} indicates signs of adjustment between the single- to multi-mode instances (see Fig. 4.21c, d). General spatial distributions in all τ_{zz} modes follow those of single-mode solutions, reaching their maxima at the filament mid-plane. As apparently shown in Fig. 4.21c, centreline τ_{zz} is subject to proportional reduction in the single-mode over the multi-mode case. In the absence of the shorter relaxation times, the total stress is dictated by the largest mode only. This in turn neglects the effect of shorter times, substantiated through the increase in multi-mode τ_{zz}. Similarly, the radial stress component, τ_{rr}, demonstrates similar behaviour to that in τ_{zz} (see Fig. 4.21c,d); yet, τ_{rr}-mid-plane maxima are reduced in comparison to that in τ_{zz}. Velocity and stress indicate minor discrepancy elsewhere throughout the domain, across single and multi-mode solutions. This state at ε=0.2 is revealed through field contours illustrated in Fig. 4.22(a-c) for Giesekus, and Fig. 4.22(d-f) for LPTT, where minimal solution differences are principally located near the free-surface region. The notation identifies comparable contour levels for direct comparison between the single- and multi-mode fields.

The departure between the single and multi-mode stress fields becomes more prominent at the free-surface region (see Fig. 4.23) when the filament is stretched further up to a Hencky-strain of ε=1.0. There, curvature adjustment is more extreme in the multi-mode form, being more stretched along the filament centreline axis than with the single-mode version. The multi-mode representation is observed to generate deeper stress penetration across the filament span-wise than in the corresponding single-mode case. Thus, at ε=1.0, higher stress levels are detected near the mid-plane and free-surface region across the domain in the multi-mode case.

The evolutionary state of deformation rates is reviewed in Fig. 4.24. At the Hencky-strain level of ε=0.2, and along the centreline axis of the filament, barely any difference is observed in the axial extension rate, D_{zz}, between single- and multi-mode representations. This holds true for both models, LPTT and Giesekus,

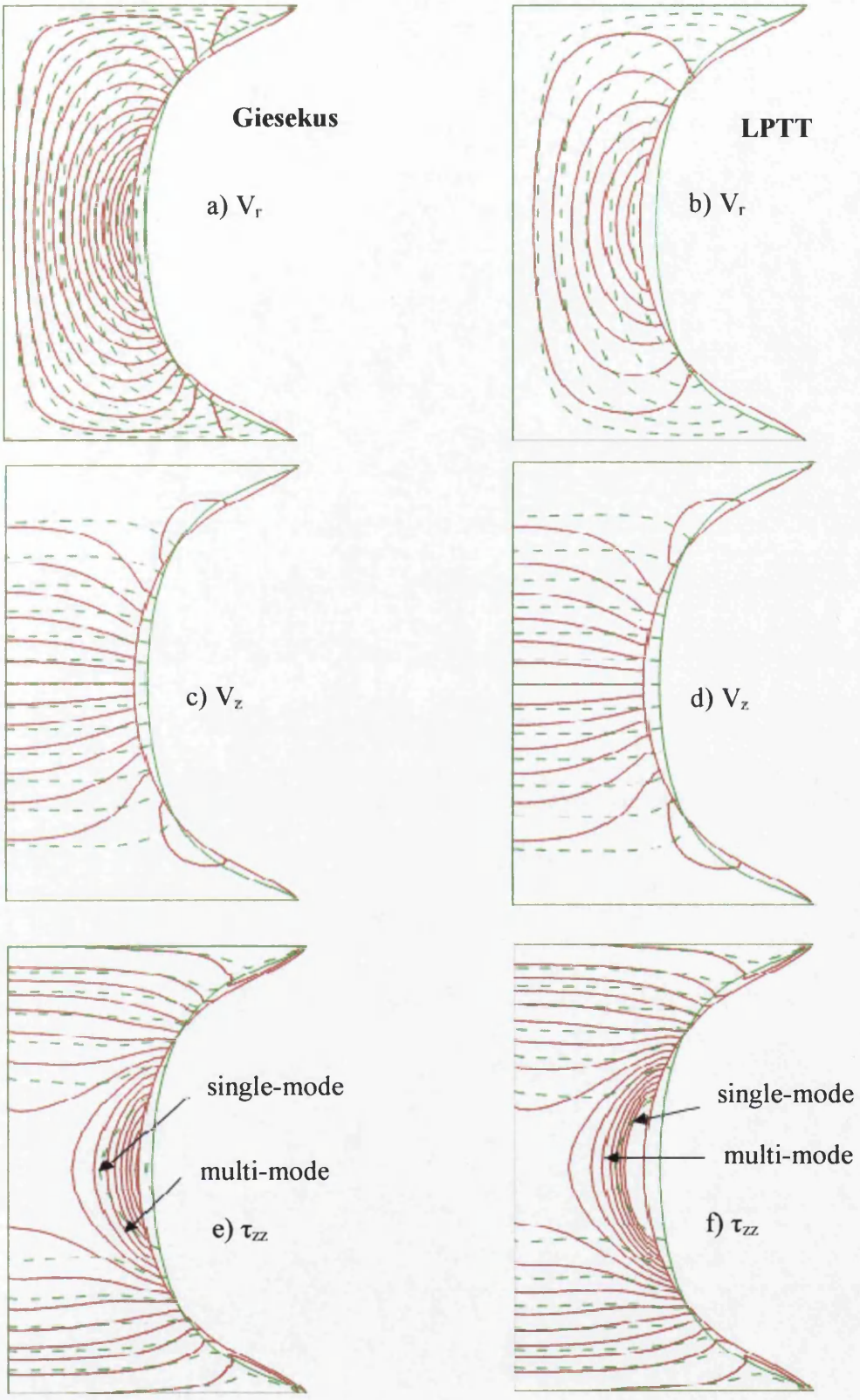

Fig. 4.23: Field contours, ε=1.0, (- - -) single- and (—) multi-mode; lhs Giesekus and rhs LPTT: Giesekus, a) V_r, c) V_z, e) τ_{zz}; LPTT, b) V_r, d) V_z, f) τ_{zz}

as shown in Fig. 4.24a. By contrast, as the filament stretching advances further and Hencky-strain rises to ε=1.0, difference in D_{zz} arises more apparently between single- and multi-mode approximations, and between LPTT and Giesekus models, see Fig. 4.24b. A slightly larger elongation rate about the filament mid-plane is yielded via the multi-mode representation than its single-mode counterpart. Regarding the discrepancy in response between LPTT and Giesekus models, the larger axial elongation rate, D_{zz}, belongs to the LPTT model. This in turn has an impact upon the axial stress component, τ_{zz} as can be seen in Fig. 4.21.

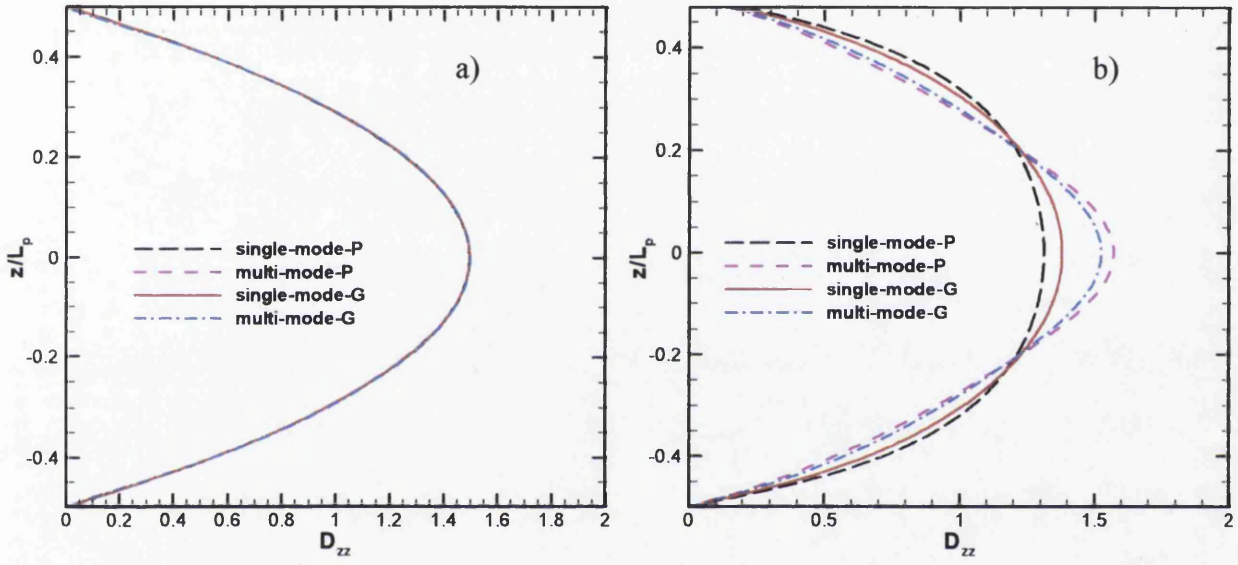

Fig. 4.24: D_{zz}-profiles, r=0, single- and multi-mode, LPTT and Giesekus: a) ε=0.2, b) ε=1.0

Generally, a better match to the material functions would be anticipated to be provided via the multi-mode representation, throughout a broader range of deformation rates up to $O(10^3\ s^{-1})$. For the present problem, however, the single-mode approximation has proved itself quite respectable, capturing the salient features of the solution; particularly as shear-rates are relatively restricted to within a range up to $O(10\ s^{-1})$ and extensional data are fairly well represented over the relevant range of Hencky-strains. This position and the computational efficiency of the single-mode implementation greatly commend its choice, as opposed to the multi-mode version.

4.4 Conclusions

The present transient filament stretching in this chapter has advanced upon the earlier work in this area in dealing with Oldroyd fluids, to consider more realistic extensional flow response through Giesekus and LPTT models. The adopted scheme of ALE-h_y-fV has proven itself quite capable in handling such a harsh numerical challenge, grasping sharp differences in filament curvature and flow structure throughout flow evolution. A single-mode approximation has proven its adequacy to represent the principal features of the flow, as they emerge and within the range of deformation rates of interest. Full filament and quarter-domain problem analyses have confirmed the quality of solutions generated. If anything, multi-mode approximation at larger Hencky-strains has revealed deeper stress penetration across the filament span and reinforces single-mode predictions for Trouton ratio (so, extensional viscosity also).

At Hencky-strain levels higher than three, bead-like formation is observed with the more strain-hardening LPTT ($\xi \neq 0$) fluid, features being absent in the equivalent Giesekus instance. Notably, the bead-like features are absent in the improved shear-thinning fit with single convected derivative form, LPTT ($\xi=0$); thus, detecting the cause of this disturbance. The Oldroyd-B fluid could not reach such large levels of Hencky-strain for the current choice of problem aspect and viscosity ratio. The effect of gravitational body force is to create a directional bias to the filament shape and to counterbalance surface tension influence. The inclusion of such forces both with and without surface tension, has been analysed for the LPTT model, to judge their relative and localised significance. Current findings reflect close agreement with the literature in measures of Trouton ratio, filament mid-plane radius and field evolution in stress and deformation-rates.

Chapter 5

ALE Methods and Free-Surface Techniques (*CM* and *VOF*)[†]

The dynamics of filament stretching for viscoelastic liquids is considered in this chapter. The consequences of utilising both *fe* and *fv* spatial discretisations are investigated within an incremental pressure-correction scheme, considering various mesh-movement and free-surface tracking techniques. For the momentum and continuity equation, finite element discretisation is implemented, whilst for the hyperbolic stress equation, a pure-upwinding cell-vertex finite volume representation is employed. Volume-of-fluid mesh procedures are outperformed by their compressed mesh counterparts. Hence, when compressed mesh procedures are coupled to an *ALE*-formulation governing mesh movement, a powerful technique to access impressively large Hencky-strains is provided. A particle-tracking approach is demonstrated to be preferable to a kinematic condition for surface-level when free-surface curvature must be determined precisely. Results of this chapter agree closely with the literature in terms of trends and Trouton ratio measures, minimum radial evolution and extensional viscosity predictions.

[†] Material of the present chapter has been shaped in the paper " Computational predictions for viscoelastic filament stretching flows: ALE methods and free-surface techniques (CM and VOF) " by K.S. Sujatha, H. Matallah, M.J. Banaai and M.F. Webster and published in *Journal of Non-Newtonian Fluid Mechanics, Vol. 137, Iss. 1-3, pp. 81-102*

5.1. Introduction

5.1.1 General background

The filament stretching is an extensionally-dominated problem, considered here under simultaneous retraction of opposing disks controlled by exponential rate movement. Over the last decade or so, the filament stretching rheometer has become known as a novel device to measure the extensional properties of liquids (Sridhar, Tirtaatmaja et al. 1991; Tirtaatmaja and Sridhar 1993) and the last few years have witnessed a rapid growth period in the development of this technique. In a typical filament stretching apparatus, a cylindrical sample of fluid is injected between two coaxial, diametrically opposed circular plates. Then, one, or both, plates are pulled apart at a preset speed usually under rate-control, either at a fixed exponential rate (providing constant extension rate) or under constant velocity (providing variable extension rate). Under the context of constant extension rate and at the filament centre, the resulting deformation approaches ideal uniaxial elongation. Engineering such kinematics is non-trivial, this being ensured by axial elongation of the sample at an exponential rate, whilst synchronously reducing the filament diameter at the mid-filament section. Nonetheless, experiments and numerical predictions practically reveal that, as a result of necking and end-effects (Sizaire and Legat 1997; Yao and McKinley 1998), significant departure away from uniaxial extension is observed. Necking directs the filament to extreme slenderness in the central region of the liquid bridge, whilst end-effects lead to significant shearing within the near-plate zones (filament-feet). Consequently, purely extensional deformation is disturbed and the predicted viscosity approximates the true extensional viscosity, commonly termed as *apparent extensional viscosity*. To overcome such experimental deficiencies, a variety of techniques have been proposed in the literature, one such being the velocity compensation technique utilised by Tirtaatmaja and Sridhar (Tirtaatmaja and Sridhar 1993). Despite these shortcomings, there is a need for a better understanding of the flow nature in such apparata, and to determine if, and when, the deformation approaches pure uniaxial elongation.

Subsequent to the recent flourishing interest in filament stretching instrumentation, much theoretical and numerical research has been performed targeting the study of complex extensional deformation experienced by viscoelastic liquids in viscometric devices. Early numerical methods applied in filament stretching flows were performed by Shipman et al. (Shipman, Denn et al. 1991) employing a finite-element method with an Oldroyd-B constitutive model. Notably, small Hencky-strain levels ($\varepsilon<1$) could only be sustained with the computational procedures adopted and available resources. More recently, higher Hencky-strain levels have been achieved via finite element methodology, invoking Lagrangian procedures with integral constitutive equations (Kolte, Rasmussen et al. 1997; Hassager, Kolte et al. 1998) and adaptive Eulerian formulations for differential viscoelastic constitutive equations (Sizaire and Legat 1997; Yao, McKinley et al. 1998; Yao, Spiegelberg et al. 2000). Alternatively, Gaudet and McKinley [42] applied a boundary element method for an Oldroyd-B model predicting the temporal evolution for the liquid interface, the resultant force on the stationary end-plates and the extensional viscosity. These predictions were tightly substantiated against the experimental results of Spiegelberg et al. [43]. Stochastic formulation has also been conducted by Grande et al. [44] utilising a hybrid Brownian-dynamics/finite element algorithm (*CONNFFESSIT*). Here, an Eulerian treatment was employed for the fixed-grid solution of the conservation equations, whilst molecular models (invoking Brownian dynamics) were used for stress and free-surface computations. Through this strategy, the basic concept of the Volume-of Fluid (*VOF*) method [12] was combined with particle tracking procedures. To corroborate algorithm correctness in [12], free-surface profiles were verified for an Oldroyd-B model against the results from the established commercial finite element software-code, "*POLYFLOW*", see [3] for example. To represent the deformation for the same model, Olagunju [45] derived a one-dimensional slender-rod theory. The results for this 1-D approximation demonstrate that radial alterations are relatively negligible, with the exception of flow near the end-plates, where two-dimensional shear flow arises on account of axial curvature and end-effects. Despite this limitation, these estimates illustrate that slender-rod equations may offer a reasonable approximation for the full filament stretching problem.

McKinley and Sridhar [46] have provided a comprehensive overview of the flow dynamics within a filament-stretching rheometer for non-Newtonian fluids. Their work encompasses fluids that display strain-hardening properties, the physics of rapid deformation in dilute polymer solutions, and the various representative constitutive equations employed to model such flows. As reported by McKinley and Sridhar [46], much work remains to be carried out to fully comprehend the dynamics of the viscoelastic free-surface instabilities that eventually lead to filament failure at large Hencky-strains. For Boger fluids, reflecting constant shear viscosity and prominent strain-hardening in uniaxial extension, the overall dynamical response within elongating liquid-filaments is now well-reported in the open literature. Regarding slenderness and breakup of filaments, a comprehensive review on the break-up phenomena in Newtonian fluid filaments and jets was presented by Eggers [47], including experimental results, numerical predictions, and similarity solutions for the approach to break-up. Later, Anna and McKinley [17] studied the transient dependence of the filament diameter and the time to break-up with variation in the molecular weight. This information is compared against the theory for failure of thin viscoelastic filaments.

5.1.2 Computational methodology

In the present work, the main focus is on the methodology to track the free-surface, which implies consideration of whether the mesh is dealt with as attached to or detached from the fluid. Hence, reviewing the recent literature on free-surface modelling is appropriate. A major motivation behind this research has been to corroborate predictions against experimental evidence for free-surface profiles computed through two alternative strategies, namely: a volume-of-fluid scheme (*VOF*), and an Arbitrary Lagrangian Eulerian, compressed-mesh scheme (*ALE/CM*). With the *VOF*-scheme, the fluid is allowed to flow over a background mesh. Alternatively with the *CM*-scheme, the mesh is tied to the fluid movement and compressed alongside the free-surface development. The *VOF*-scheme, has considerable flexibility in allowing choice over the assignment of material sample points and surface-particles method. This aids in more precise description of the physics of the problem. However under equitable comparison, the *CM*-method has

proved to far out-perform optimal *VOF*-implementation, with the capability to achieve impressively high critical Hencky-strain levels of $\varepsilon \approx O(4.4$ units). For this particular flow situation, lack of stability and poor performance of the *VOF*-scheme is shown to be attributable to the relatively poor mesh aspect-ratios experienced by elements within the plate/free-surface (solid/fluid) contact zone. Though the *VOF*-method seems suitable for general free-surface movement problems, it may prove deficient for scenarios involving both free surface and solid/fluid contact, particularly where large curvature adjustment is anticipated.

In a variety of industrial applications such as mould filling and metal forming, Eulerian methods have successfully been applied, such as the pseudo-concentration approach [48, 49], a variant of the *VOF*-method. Here, in order to track free-surface movement, a hyperbolic transport equation is solved for volume fraction. There is no specific requirement to explicitly prescribe boundary conditions because the free-surface is treated as an internal domain interface. In a conventional *VOF*-formulation, the volume fraction of liquid is considered as a step function, reflecting a value of zero in the void region and unity in the wet areas. The periphery zone of control volumes, that demarcates the boundary between wet-dry zones, is treated in various manners. Control volumes over half-full are taken as wet in its crudest (averaged) form, whilst the remainder are treated as dry. This feature will be commented upon below, with regards to hierarchical levels of improvement towards use of these periphery volume functions and accurate determination. The original *VOF*-model was formulated within the framework of finite volume method [50]; alternatively finite element variations are now available in the literature [51]. When *VOF*-type methods require fine grid resolution and higher-order interpolation [49,52], prescribed boundary conditions on the surface need to be accurate for certain applications. This occurs, for example, in situations where surface-tension effects are dominant, to capture the curvature of the free-surface accurately. To solve unsteady non-Newtonian free-surface flows, a volume-tracking method was employed by Tomé et al. [53, 54] based on the marker-and-cell (*MAC*) scheme. This utilises a finite difference technique based on staggered grids and virtual particles for flow visualisation. To illustrate and validate their implementation, a variety of free-surface problems were undertaken in this fashion.

Arbitrary Lagrangian Eulerian (*ALE*) formulations for which the freedom of mesh movement offered is appealing have now become commonplace, for many industrial flow problems with complex free-surface forms. With *ALE*- techniques, the mesh itself is moved with a mesh velocity, a suitable choice of which represents one of the major aspects involved. For instance, this technique has been employed successfully for water-wave problems. Noh (Noh 1964) and Hirt et al.(Hirt, Amsden et al. 1974) introduced the *ALE*-method in the finite difference domain. Hughes et al. (Hughes, Liu et al. 1981) also introduced finite element *ALE*-formulations for incompressible viscous flows. The free-surface falls on the boundary of the computational domain in Lagrangian or *ALE*-approaches. Hence, no additional difficulty is posed via such methods in applying complex boundary conditions. Nevertheless, these methods suffer the deficiency of requiring frequent remeshing. The choice of Lagrangian/*ALE*-method, as opposed to *VOF*-variants, is mainly based on the type of problem and degree of precision to which the resulting free-surface is to be determined.

In the context of filament stretching, viscoelastic flows with free-surfaces have been considered in a number of papers (Sizaire and Legat 1997; Yao and McKinley 1998; Rasmussen and Hassager 1999; Bach, Rasmussen et al. 2002). In these instances, simulations have been performed through Lagrangian formulations in two dimensions (Sizaire and Legat 1997; Yao and McKinley 1998) and three dimensions (Rasmussen and Hassager 1999; Bach, Rasmussen et al. 2002). In the current work, a high degree of accuracy is demonstrated in the viscoelastic scenario when employing a Lagrangian/*ALE*-scheme as opposed to a *refined VOF*-scheme to track the free-surface. In particular, findings are corroborated against the specific results of Yao and McKinley [3]. In this moving boundary problem, a free-surface tracking procedure is demanded in addition to a robust transient algorithm and an appropriate choice of constitutive model. We utilise a variety of instances of the Oldroyd fluid model and a Lagrangian/*ALE*-method, in which the mesh of the computational domain moves with the fluid-velocity. To solve the interior domain field problem, a hybrid finite element/ finite volume (*fe/fv*) scheme is adopted. This methodology comprises a time-stepping procedure that combines a finite element discretisation (semi-implicit second-order/pressure-correction) for momentum

balance and continuity equations, with a cell-vertex finite volume scheme for stress, and functional space compatibility addressed through a localised recovery scheme [15]. This effective combination is implemented as a fractional-staged formulation within each time-step. Each single, parent finite element triangular cell is divided into four finite-volume triangular sub-cells. On the parent-*fe*-cell, the interpolation is quadratic for velocity and linear for pressure. The interpolation for stress on the sub-cell is of linear form. An important aspect of the discretisation is that, with stress variables located at the vertices of the finite volume cells, no interpolation is required to retrieve finite element nodal stress values, hence this source of projection error is avoided. In the most recent advanced form of stress nodal update, a combination of fluctuation distribution contribution over the *fv*-triangle and a uniform distribution over the median-dual-cell have been proposed. This is appropriate for problems with significant non-localised shear within the flow. Various schemes may be derived ($\{CTi|_{i=0,\ldots,3}\}$, see (Aboubacar and Webster 2003; Webster, Matallah et al. 2003; Webster, Tamaddon-Jahromi et al. 2003), by combining fluctuation distribution and median-dual-cell contributions. Nevertheless, the current problem is an extensionally-dominated flow, which demonstrates some of the numerical difficulties involved in solving more generalised viscoelastic flows, where both source and flux terms may contribute equally. Yet, the extensional-domination and free-surface prohibit any consideration of median-dual-cell (*mdc*) contributions. In a previous work on filament stretching, the inclusion of *mdc*-terms was found to degrade the evolving solution, see [10]. The discrepancy was greater at the free-surface and the central region, where the velocity gradient d_{zz}, rose sharply from a constant value to a peak. In regions where such sharp change in gradient occurs, the strength of the source terms can be high and the flow can be greatly convective in character. Hence in this scenario, a pure fluctuation distribution scheme has been favoured (no median-dual-cell constructs). With a Lax-temporal construction (*fv*) that is second-order accurate in space and time, the *fv* time-term (left-hand side (*lhs*) term of the stress equation) is modified via area-weighting factors ($\alpha_l{}^T$), see (Webster, Matallah et al. 2003).

5.2. Problem description

A viscoelastic filament between two co-axial plates which undergoes extensional deformation is considered. The problem is itself extensionally-dominated, driven by simultaneous retraction of opposing plates at an exponential rate. Axial stretching, inwardly-directed free-surface progression and fluid-solid contact planes are all encompassed in the problem. In the first instance, one may disregard the effects of surface tension, inertia and gravity (considered subsequently). The plates are pulled apart consistent with the following relationships, on filament length (L_p) and plate-velocity (U_z^{plate}):

$$\textit{length:} \quad L_p(t) = \pm(L_0/2)\exp(\dot{\varepsilon}_0 t) \tag{5.1}$$

$$\textit{velocity:} \quad U_z^{plate}(t) = \pm(\dot{\varepsilon}_0 L_0/2)\exp(\dot{\varepsilon}_0 t), \; U_r(t) = 0 \tag{5.2}$$

Here, L_0 is the initial length of the filament and $\dot{\varepsilon}_0$ is an enforced initial stretch-rate. The aspect-ratio of the liquid-bridge is defined as $\Lambda_0=L_0/R_0$, where R_0 is the initial filament radius. Two settings of filament aspect-ratios, Λ_0= *{2/3,1/3}* have been chosen to be reported on, following reference (Yao and McKinley 1998). For comparison purposes, two high-polymeric/low-solvent ($\beta=\mu_2/\mu_0=0.262$) and low-polymeric/high-solvent ($\beta=\mu_2/\mu_0=0.915$) viscosity ratios described by the Oldroyd-B model together with a Newtonian fluid are utilised. The set of operating parameters are tabulated in Table 5.1.

Fig. 4.1a illustrates the boundary conditions on respective variable and fluid domain considered. Except the free-surface boundary, Dirichlet-type boundary conditions are applied everywhere. Theoretically, the extensional stress component τ_{zz} evolves on the axis, based on a pure-extension symmetry line assumption, upon which τ_{rz} may be taken to vanish. With the exception of the moving-plates, initial conditions are taken as quiescent, where an initial driving velocity is adopted of ($V_0 = \pm L_0 \dot{\varepsilon}_0/2$). Through independent scales on length ($L=L_0$), velocity ($U=V_0$), and viscosity (μ_0), non-dimensional groups of Reynolds (Re), Deborah (*De*), Bond

	High-polymeric viscosity fluid	Low-polymeric viscosity fluid	Newtonian fluid
ρ (density) (kg m^{-3})	1030	894	1006
L_0 (initial length) (m)	$12.7*10^{-3}$	$12.7*10^{-3}$	$1.27*10^{-3}$
R_0 (initial radius) (m)	$19.05*10^{-3}$	($19.05*10^{-3}$, $38.1*10^{-3}$)	$19.05*10^{-3}$
Initial aspect ratio (Λ_0)	2/3	2/3, 1/3	2/3
χ (surface-tension coefficient) (Nm^{-1})	$30.0*10^{-3}$	$28.5*10^{-3}$	
μ_2 (solvent viscosity)(Pa.s)	9.08	43.2	
μ_1(polymer viscosity) (Pa.s)	25.8	4.0	
μ_0 (zero shear viscosity) (Pa.s)	34.880	47.2	47.2
Relaxation time (λ_1) (s)	0.421	2.54	
Reynolds number (Re)	0.08	0.006	0.006
Deborah number (De)	1.89	5.08	
Ca^{-1}	0.007	0.02	

Table 5.1: Filament dimensions and fluid properties

(*Bo*) and capillary (*Ca*), are introduced. These provide dependent scales on time (*L/U*), pressure and extra-stress ($\mu_0 U/L$). Adopting a surface tension coefficient, χ, group numbers are mathematically expressed, viz.,

$$\mathrm{Re} = \frac{\rho UL}{\mu_0},\ De = \frac{\lambda U}{L},\ Bo = \frac{\rho g L^2}{\chi},\ Ca = \frac{\mu_0 U}{\chi}.$$

Under isothermal flow conditions, the governing non-dimensional equations may now be given for incompressible, viscoelastic flow, articulated as

$$\nabla . \boldsymbol{u} = 0, \tag{5.3}$$

$$\mathrm{Re}\left(\frac{\partial \boldsymbol{u}}{\partial t} + \boldsymbol{u}.\nabla \boldsymbol{u}\right) = -\nabla p + \nabla.(2\mu_2 \boldsymbol{d} + \boldsymbol{\tau}) + \boldsymbol{F}_g, \tag{5.4}$$

$$De\left(\frac{\partial \boldsymbol{\tau}}{\partial t} + \boldsymbol{u}.\nabla \boldsymbol{\tau}\right) = -\boldsymbol{\tau} + 2\mu_1 \boldsymbol{d} + De(\boldsymbol{L}.\boldsymbol{\tau} + \boldsymbol{\tau}.\boldsymbol{L}^{\dagger}). \tag{5.5}$$

Here, $\boldsymbol{u}$, p and $\boldsymbol{\tau}$ represent the fluid velocity, the hydrodynamic pressure and the polymeric extra-stress, respectively. The zero-shear-rate viscosity μ_0 consists of Newtonian solvent (μ_2) and polymeric (μ_1) contributions, so that $\mu_0=\mu_1+\mu_2$; $\boldsymbol{d} = (\boldsymbol{L}+\boldsymbol{L}^{\dagger})/2$ corresponds to the rate-of-deformation tensor and $\boldsymbol{L}^{\dagger} = \nabla \boldsymbol{u}$, the

velocity gradient. Below, total stress (**T**) is referred to as the sum of polymeric and solvent contributions, where $\mathbf{T} = \tau + 2\mu_2 \boldsymbol{d}$. F_g represents the ratio of gravitational to viscous forces given by $\boldsymbol{F_g} = (0, F_g) = (0, \frac{\rho L^2}{U\mu_0} g)$, the axial component equivalently can be expressed as $F_g = Bo/Ca$.

Both material and spatial references are dynamic, there being a constant state of motion in both temporal and spatial domains. Hence, the material time derivative of any physical property Φ within the reference configuration may be expressed as

$$\frac{D\Phi}{Dt} = \frac{\partial \Phi}{\partial t} + \boldsymbol{u}_c . \nabla \Phi,$$

$$\boldsymbol{u}_c = \boldsymbol{u} - \boldsymbol{u}_m . \qquad (5.6)$$

Where $\boldsymbol{u}$, $\boldsymbol{u}_c$, and $\boldsymbol{u}_m$ are the fluid velocity, the convective velocity and the mesh velocity, respectively. The Arbitrary Lagrangian/ Eulerian formulation is defined based on the choice of mesh velocity. The framework is Eulerian if $\boldsymbol{u}_m$=0; if $\boldsymbol{u}_m$=$\boldsymbol{u}$, it is Lagrangian; hybrid configurations are defined via alternative choices. In the present study, an *ALE* interpretation is adopted, for which $\boldsymbol{u}_m$=$\boldsymbol{u}$, and $\boldsymbol{u}_c$=0 on all boundaries. This procedure in particular, determines the forward time-step location of all exterior boundaries, including the free-surface, accounting simultaneously for both extension and compression of the overall domain. Applying the fluid velocity alone ($\boldsymbol{u}_m$=$\boldsymbol{u}$) on interior nodes was found to expose premature mesh-folding close to the exterior extremity of the filament-foot (filament-plate contact zone). This problem may be resolved out by adjusting internal mesh redistribution according to a re-projection of internal/free-surface nodes onto pure lubrication lines. The re-projection procedure is adopted as follows. First, the shift of the free-surface boundary segments between time-steps is determined by the fluid velocity. Second, the centreline shift is determined similarly for centreline mesh nodes, yet governed by fluid velocity, but now of pure lubrication nature. Then, one would be in a situation to position the intersection between the horizontal lubrication lines, drawn span-wise across the filament through updated centreline nodes, and the free-surface segments. This makes the correction to the free-surface nodal updates, in

position and velocity. Likewise, interior nodes are projected onto the pure lubrication lines (using centreline axial fluid velocity V_z), taking radial movement over the time steps in harmony with the radial fluid velocity along the mid-plane (maintaining uniform distribution). The corresponding mesh velocity proves to be only an insignificant adjustment to adopting the actual fluid velocity, yet mesh quality is safeguarded over the time step. Through such an implementation of the ALE-technique, one is able to correct for this adjustment by introducing another fractional stage governing correction for convection (see [28]). In practice, it is noted that such a correction step has trivial impact upon the evolving solution.

5. 3 Results and discussion

5.3.1 Results for Compressed-Mesh (ALE/CM) scheme

To verify mesh independence in the solutions generated spatial refinement has been undertaken. The employed meshes, M1, M2 and M3, are illustrated in Fig. 5.1(a-c). Simulations are conducted for a default initial filament aspect-ratio of Λ_0=2/3 on an Oldroyd-B fluid (β=*0.915*). Between solutions in any variable across two consecutive refined meshes a discrepancy of one percent is tolerated. The detailed mesh characteristics, alongside stress maxima, critical Hencky-strain achieved, ε_{crit}, and filament minimum radii, R_{min}, obtained (at ε=1.0 units) are recorded in Table 5.2. The adequacy of mesh quality is checked by the solutions captured, even on the coarser mesh (M1). Nonetheless, premature termination of computations upon mesh-M1 and mesh-M2 has been observed, at Hencky-strains of ε=1.6 and 2.8 units, respectively. This was believed to be caused by the larger mesh aspect-ratios encountered near the filament mid-plane region. In contrast, Mesh-M3 has proved to tolerate relatively high Hencky-strain levels, up to a critical value of 4.4 units, in close agreement with the observations reported by others (Yao and McKinley [3]). Hence, mesh-M3 is chosen below.

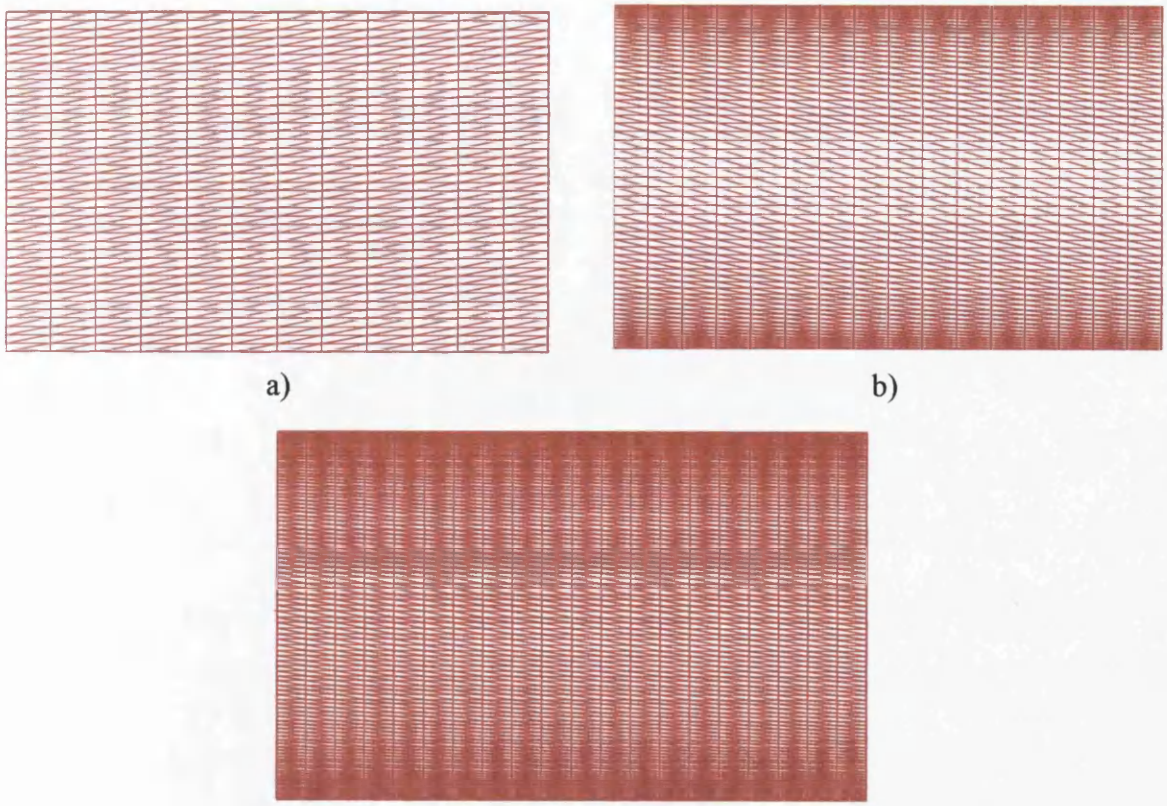

Fig. 5.1 Mesh refinement: a) Mesh-M1; b) Mesh-M2; c) Mesh-M3

Meshes	Elements	Nodes	τ_{zz}	ε_{crit}	R_{min}
Mesh-M1	960	2025	0.2955	1.6	0.724
Mesh-M2	1920	3993	0.2951	2.8	0.721
Mesh-M3	4000	8241	0.2948	4.4	0.721

Table 5.2: Mesh refinement: τ_{zz}-max, ε_{crit} and R_{min}

5.3.1a $\partial h / \partial t$ ***vs*** **dx/dt** ***results and free-surface profiles***

Findings under the employment of two different methods for tracking free-surfaces are compared with one another. The first procedure ($\partial h / \partial t$) utilises the kinematic condition, via a height function, h(**x**, t) of Eq. (3.33). Particle tracking methodology termed d**x**/dt of Eq. (3.34) is employed in the second approach. Free-surface profiles depicted in Fig. 5.2a correspond to a typical Hencky-strain level of unity, utilising both ($\partial h / \partial t$) and (d**x**/dt)-procedures. In contrast to the literature, these results apparently show that ($\partial h / \partial t$)-profiles degrade in the plate-zone near

the filament feet, for which filament volume has risen considerably. The additional volume under the ($\partial h/\partial t$)-employment is O(20%), whilst correspondingly the (d**x**/dt)-technique would seem to preserve the volume naturally (O(1%) gain). Therefore, under the ($\partial h/\partial t$)-approach greater care is demanded to sustain filament volume. An approach to achieve this is performing a global volume conservation check, by invoking ($\partial h/\partial t$)-recalibration repeatedly until filament volume is preserved. The drawback to this procedure is its tendency of exaggerating the necking process and subsequently yielding overestimates for the minimum filament radius declination rate (R_{min}). There is an alternative procedure termed "local-disc movement" [10], through which filament volume over each local sub-section is conserved. This procedure aids in conserving volume and maintaining accuracy via R_{min}-control. However, here once more at higher strain levels, say $\varepsilon \geq 1$, solution quality is degraded, but now in the filament-foot zone (see Fig. 5.2b). Thus, clear preference is established upon the (d**x**/dt)-choice, for which close agreement is observed with the literature in free-surface profiles at selected Hencky-strain levels, as demonstrated in Fig. 5.2a.

In the following sections, the detailed discussion employs the preferred choice of the scheme, ALE (d**x**/dt). One of the important features in a filament stretching

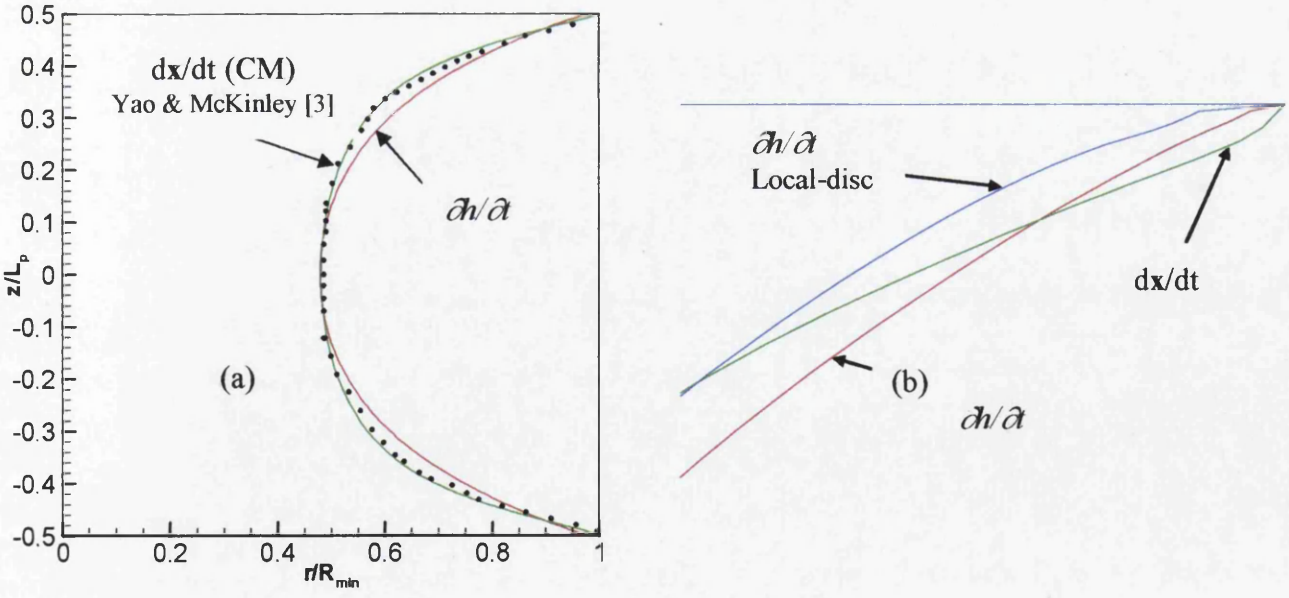

Fig. 5.2 Free-surface profiles, ε=1; d**x**/dt, $\partial h/\partial t$ and Yao & McKinley [3];
a) full plot, b) zoom of profiles at filament foot

rheometer, is the progression and adjustment of surface curvature. The free-surface deforms noticeably during the stretching history as a result of the pinning conditions at the end-plates.

In Fig.5.3 for the default initial aspect-ratio $\Lambda_0 = 2/3$, typical filament shapes are comparatively illustrated with free-surface deformation histories for a high-solvent content Oldroyd-B fluid (β=0.915, lower) and a Newtonian fluid (upper).

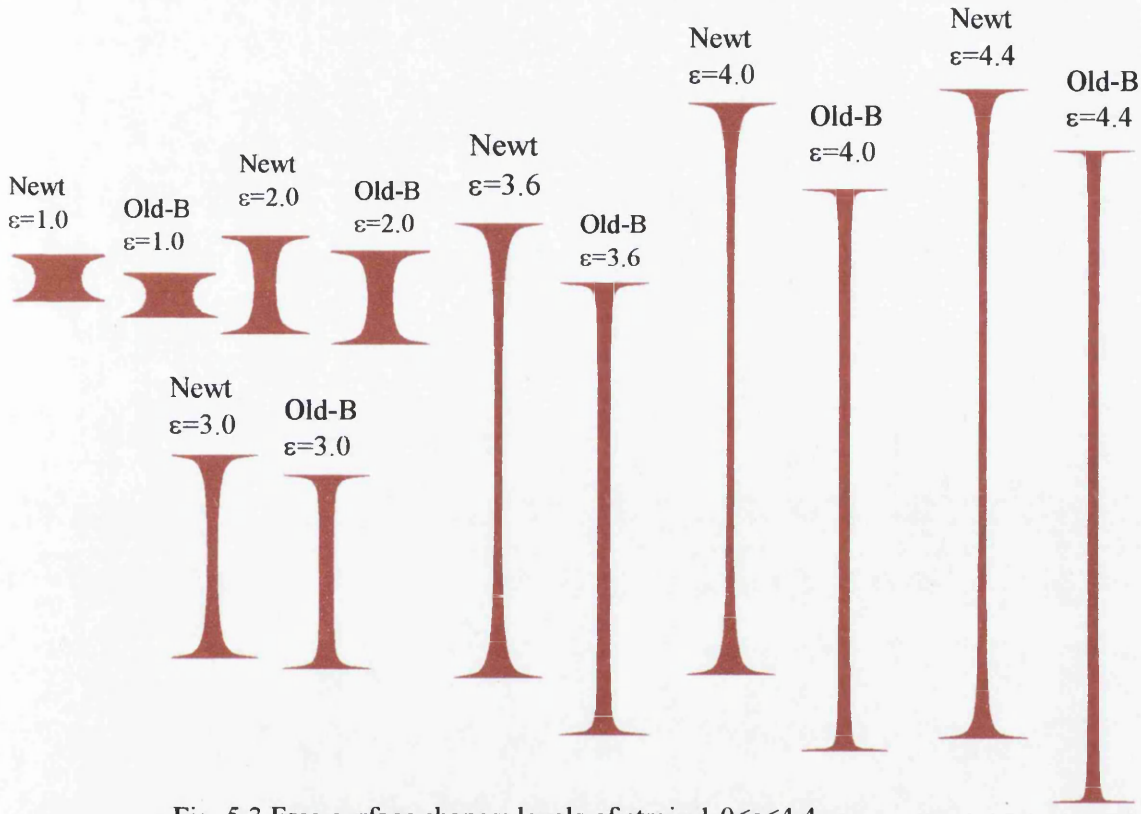

Fig. 5.3 Free-surface shapes: levels of strain 1.0≤ε≤4.4,
CM/ALE (dx/dt), Newtonian v Oldroyd-B

Beyond a certain level of Hencky-strain of about ε=2.0 units, the Oldroyd liquid bridge begins to exhibit considerable strain hardening. Hence, necking in the central part of the filament is delayed and this leads to uniform cylindrical filament-shape (constant diameter). Having reached the Hencky-strain of ε=3.0 units (see Fig.5.3), this phenomenon has become visibly perceptible in qualitative agreement with the experimental data of Tirtaatmaja and Sridhar (Tirtaatmaja and Sridhar 1993), and quantitative conformity with the numerical findings of Yao and McKinley [3]. Up to ε=2.0 units, free-surface orientation reflects no major

disparity between Newtonian and viscoelastic fluids; yet subsequently, the departure is severe (see Fig.5.3). Critical Hencky-strain magnitudes are ε=5.2 and ε=4.4 units for the Newtonian and the Oldroyd fluids, respectively. For the Newtonian fluid the filament diameter decreases along the filament length from the plate to mid-plane region. This phenomenon is particularly pronounced in the filament foot-zone near the end-plates. There, at larger strain levels, greater pinching arises for the Oldroyd fluid compared with its Newtonian counterpart. The zoomed illustration of Fig. 5.4a for this region indicates such subtle structural differences.

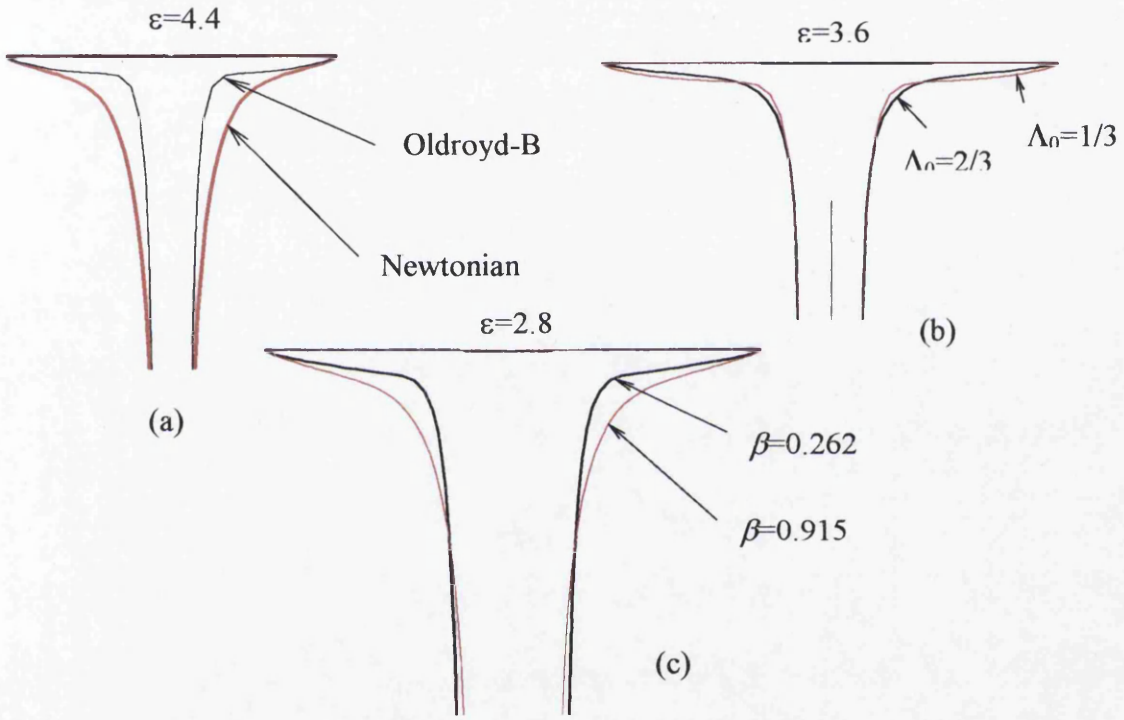

Fig. 5.4 Filament feet curvature, a) Newtonian v Oldroyd-B;
Oldroyd: b) two aspect ratios, c) two viscosity ratios

Similar observations on filament-foot curvature can be made for solutions covering polymeric:solvent viscosity ratios (β) variation and shorter:taller initial filament shapes (Λ_0) (see Fig. 5.4b and Fig. 5.4c). At the early Hencky-strain of ε=2.8 units, such curvature for the high-solvent/low-polymeric Oldroyd fluid, compares somewhat to that for a Newtonian fluid at ε=4.4 units. The more extreme the pinching effect encountered at the feet, the harder it becomes to elongate to longer times. This event corresponds to larger polymeric stress levels across the

foot-zone, circumstances that cause premature numerical termination. Such dynamics leads to slender boundary layers with sharp gradients over which further fineness of meshing is demanded. For the shorter initial filament of low aspect-ratio (Λ_0=1/3, ε_{crit} =3.7 units) which encounters relatively larger curvature at the feet than occurs with the taller/higher aspect-ratio (Λ_0=2/3, ε_{crit} =4.4 units) similar comments can be made.

5.3.1b Rate of deformation, stress and velocity development

It is informative to trace the temporal evolution in velocity components, along the free-surface (Γ_0) in u_r and along the central filament-axis (r=0) in u_z. The patterns taken up by u_r on Γ_0 (Fig.5.5a) are seen to give the filament free-surface shape, so

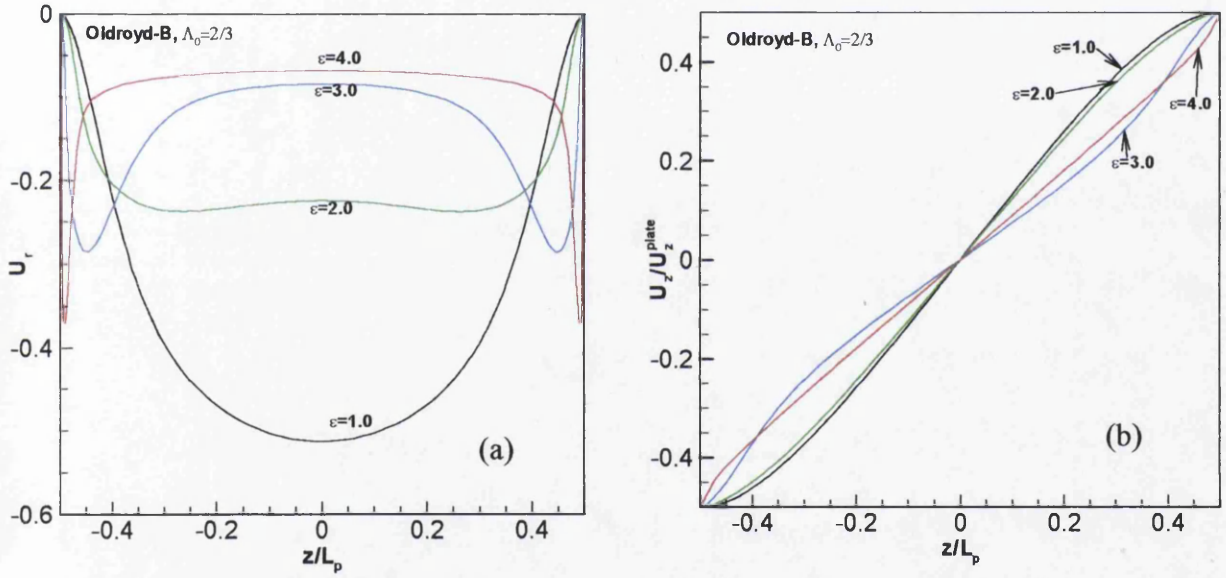

Fig. 5.5 Velocity profiles: a) U_r along Γ_0; b) U_z along r=0 axis

that by ε=2.0 units, at left and right-hand ends, a foot-shape has emerged that becomes rather thin by ε=3.0 units and above. The flattening of the u_r-profile from ε=2.0, is a sign of the onset of strain-hardening. Employing suitable common scaling, one would observe the evolutionary structure in u_z along the central filament-axis in Fig.5.5b. An additional turning/inflexion point in the profile of the upper-half of the filament between $2.0 \leq \varepsilon \leq 3.0$ is gathered, and this causes a complete reversal by ε=4.0 units about the 45° line-of-slope.

The deformation history of the liquid bridge can be characterized through extensional strain and shear-rate experienced by the fluid-elements. Figs. 5.6-5.8 display typical spatial and temporal variations of d_{zz} and d_{rz} for the Newtonian and Oldroyd-B models. For the Oldroyd-B model (see Fig. 5.7), extensive non-homogeneity

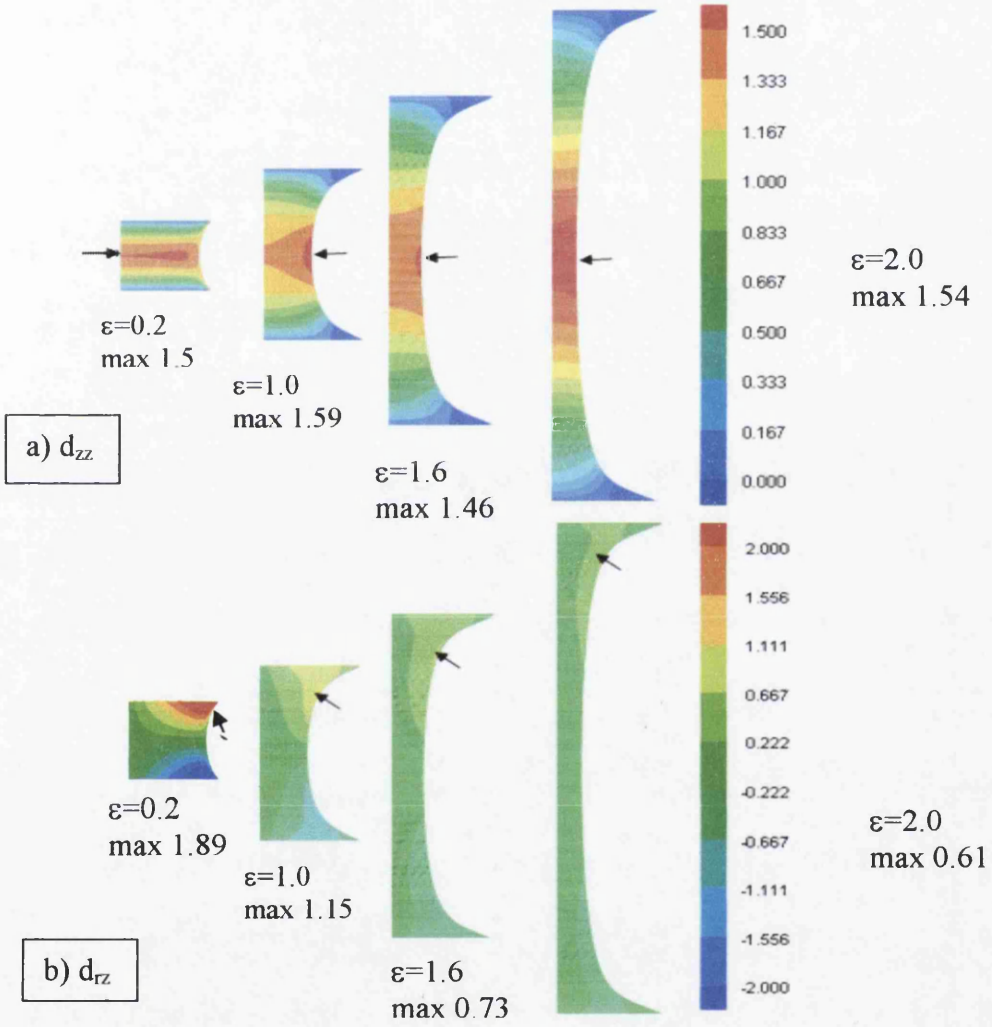

Fig. 5.6 d_{zz} and d_{rz}-field evolution: Newtonian; $0.2 \leq \varepsilon \leq 2.0$

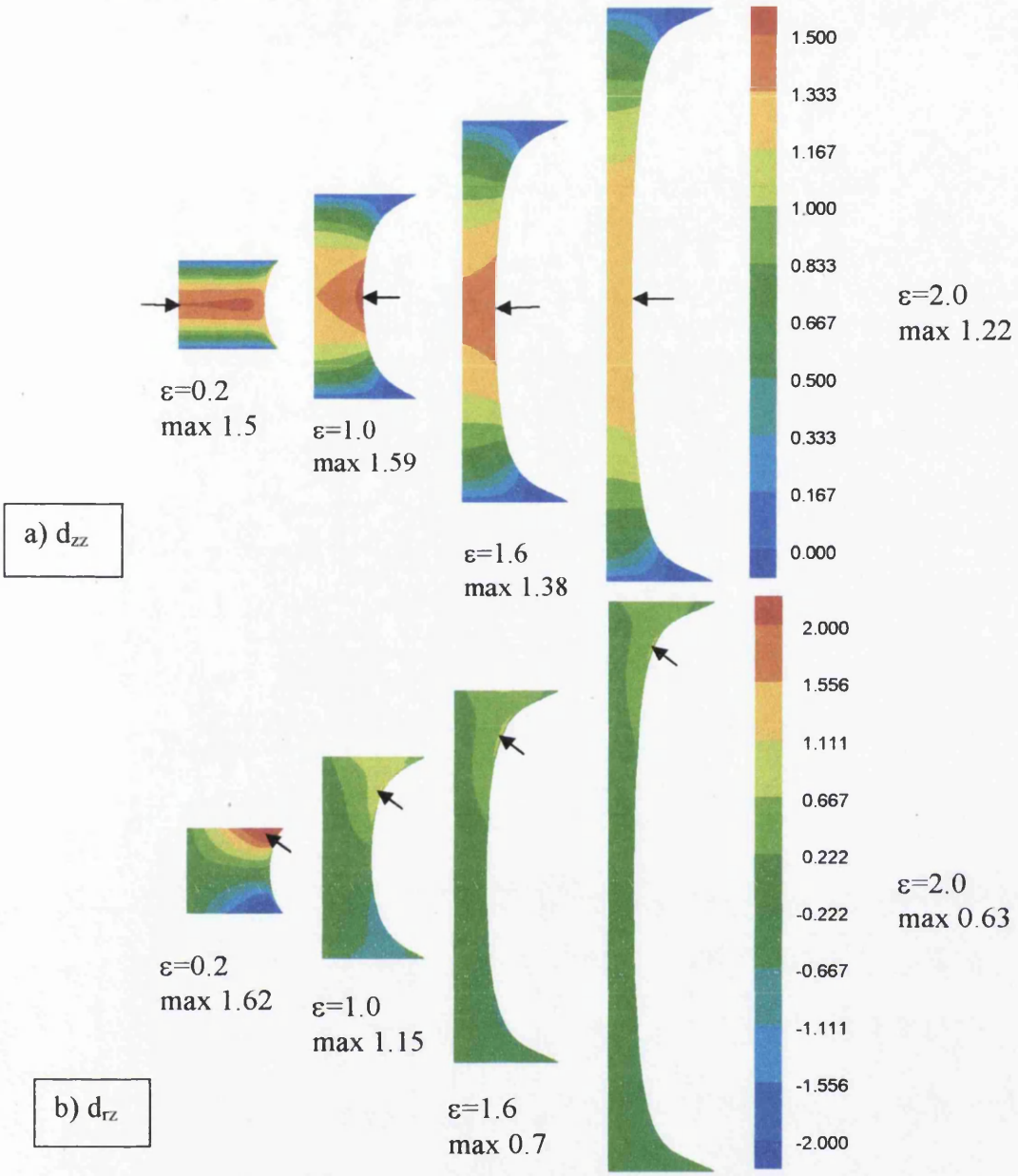

Fig. 5.7 d_{zz} and d_{rz}-field evolution: Oldroyd; $0.2 \leq \varepsilon \leq 2.0$

is detected in strain-rate throughout the liquid bridge and over the early stretching stage, at Hencky-strain levels as low as ε=0.2 up to ε=1.0. Nevertheless, the non-homogeneity gradually disappears as strain grows and by ε=2.0 units a homogeneous deformation zone is established at the central section of the filament. This homogeneous deformation zone expands continually towards the outside and subsequently upon further stretching towards the two end-plates, as strain-hardening commences to take effect. The contours of d_{rz} illustrate that significant shearing is generated at small strain levels. In the central region of the filament, the shear rate is negligible, being largest near the pinned surface at the end-plates.

These plots also exhibit that the d_{rz} decays rapidly with increase of strain (time), and more so than in d_{zz}, see ahead to Fig. 5.13a. From ε=0.2 units, maxima-d_{rz} and d_{zz} are of the same order of O(1.5), but as time advances strain-rates dominate, becoming twice (for Oldroyd) to three times greater (for Newtonian) at ε=2.0 units.

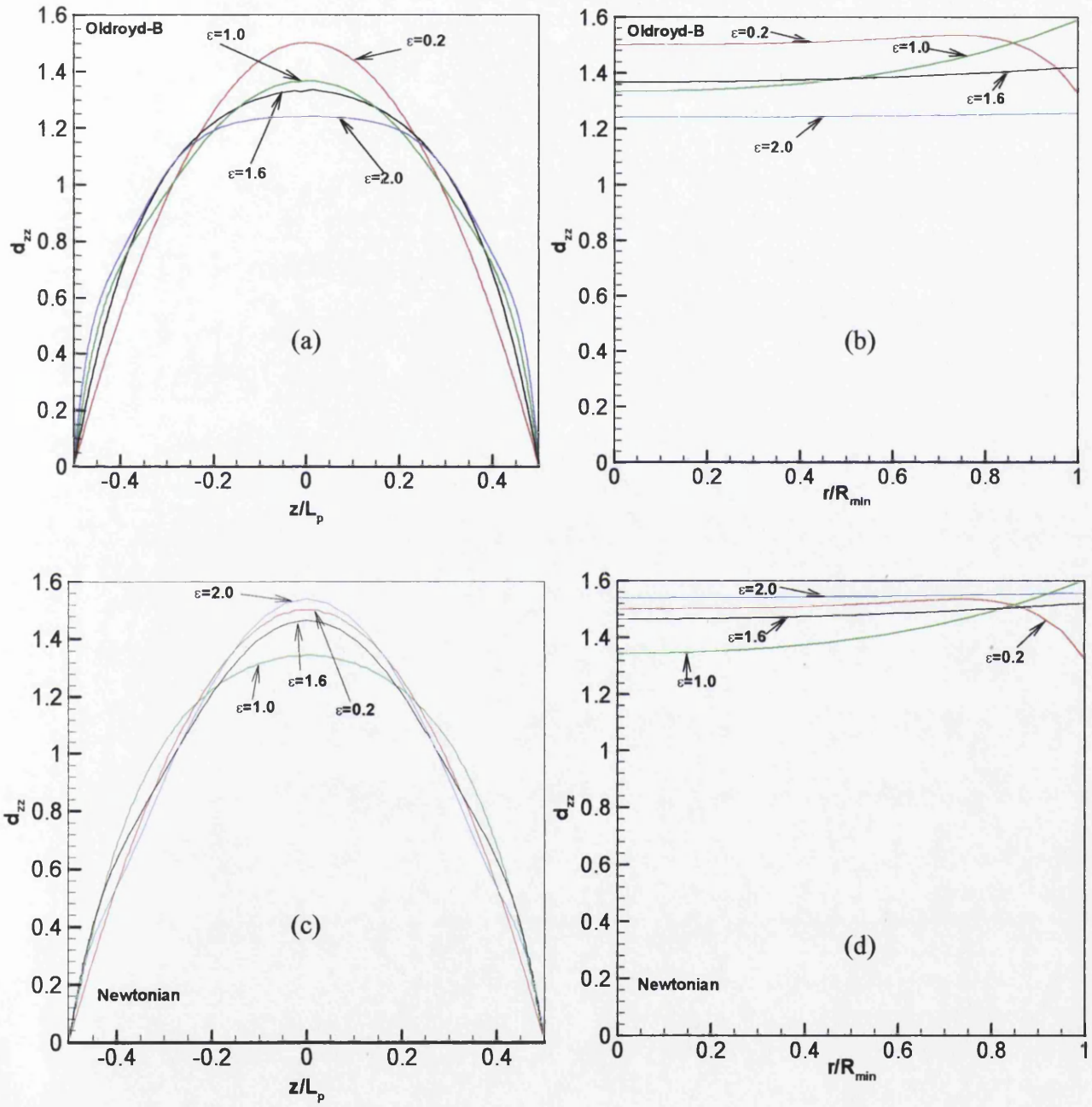

Fig. 5.8 d_{zz}-profiles, increasing ε, 0.2≤ε≤2.0: Oldroyd v Newtonian;
r=0 axis(a),(c); (z=0) axis (b),(d)

Contrasting Newtonian to Oldroyd fluid deformation fields at equivalent levels of Hencky-strain up to ε=2.0 units in Figs. 5.6 and 5.7, one realises that shear

patterns in d_{rz} are practically identical, both in peak values and distribution. Correspondingly, up to Hencky-strains of unity in extensional deformation (d_{zz}), such patterns are almost impossible to be discerned, noting the lack of uniformity in profile patterns across the filament mid-plane (width, z=0 axis). Beyond this time, differences appear with maxima spreading across the filament central-span in a uniform manner, see also profiles of Fig.5.8. Along the filament axis (r=0), Oldroyd maxima monotonically decline from 1.5 at ε=0.2 to 1.22 at ε=2.0 units, with attendant flattening of the profile. The Newtonian centreline maxima nonlinearly decrease from 1.5 at ε=0.2, to 1.3 at ε=1.0, reversing to 1.46 at ε=1.6 and rising further to 1.54 at ε=2.0 units. No profile flattening is apparent here, so that Newtonian centreline magnitudes (1.54 units) surpass their Oldroyd counterparts (1.22 units).

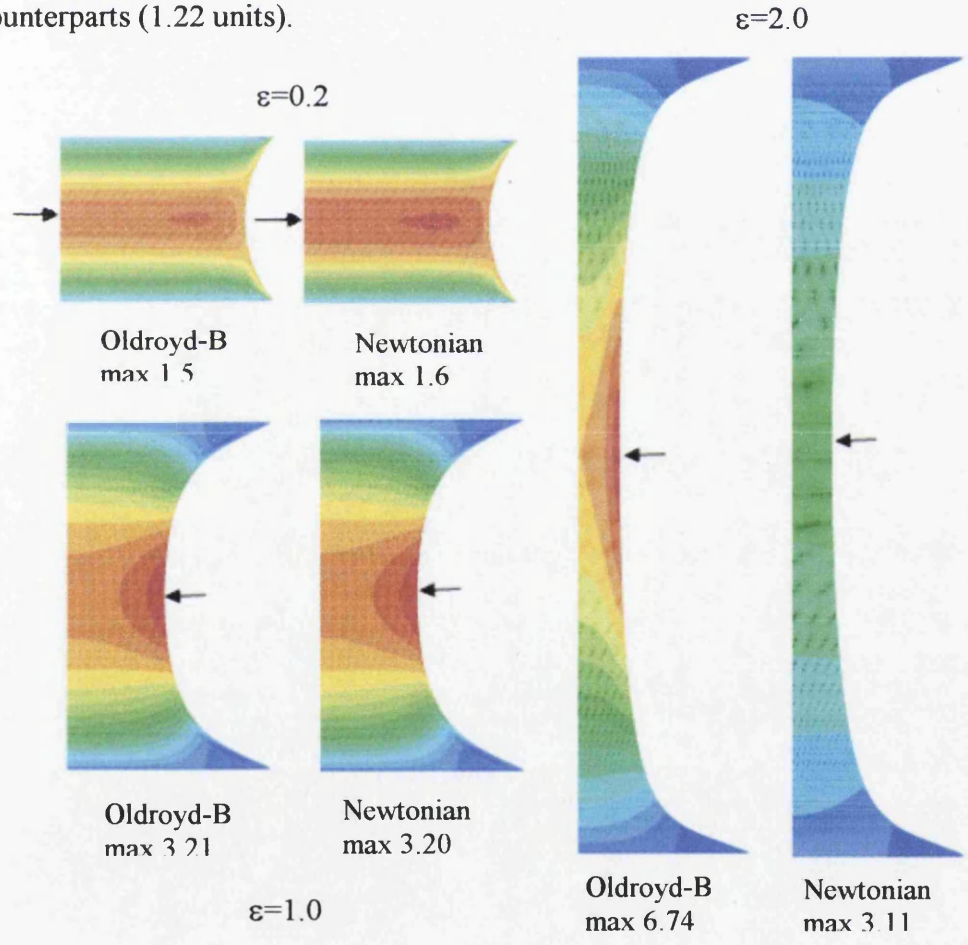

Fig. 5.9 T_{zz}-field evolution: Newtonian vs Oldroyd-B; ε=0.2, 1.0 and 2.0

Such dynamics is mirrored through total stress fields of Figs. 5.9 and 5.10, and profiles in Figs. 5.11 and 5.12, so that stress (T_{rz} and T_{zz}) between Newtonian and Oldroyd fluids is practically indistinguishable up to ε=1.0 units. Here, we may gather that solvent contributions entirely dominate polymeric counterparts. As extension increases, roles reverse and polymeric stress dominates. This behaviour is evident in Fig. 5.13a,b. Even though d_{zz} (Fig. 5.13a) reduces slightly as strain rises, T_{zz} maxima (Fig. 5.13b) increases sharply due to polymeric contributions. By means of relative demonstration at ε of unity, maxima in T_{zz} are O(3.2 units) and T_{rz} are O(1.2 units). Beyond unity in Hencky-strain, Oldroyd-T_{zz} maxima increase exponentially to O(98 units) at ε=4.0 units, whilst Newtonian values idle about O(3 units) level (see Fig.5.12). In a quantative fashion, stress and deformation patterns up to ε=2.0 units match those displayed in Yao and McKinley [3], noting the obvious difference in shear data (Fig. 5.7b) owing to their single-plate movement procedure.

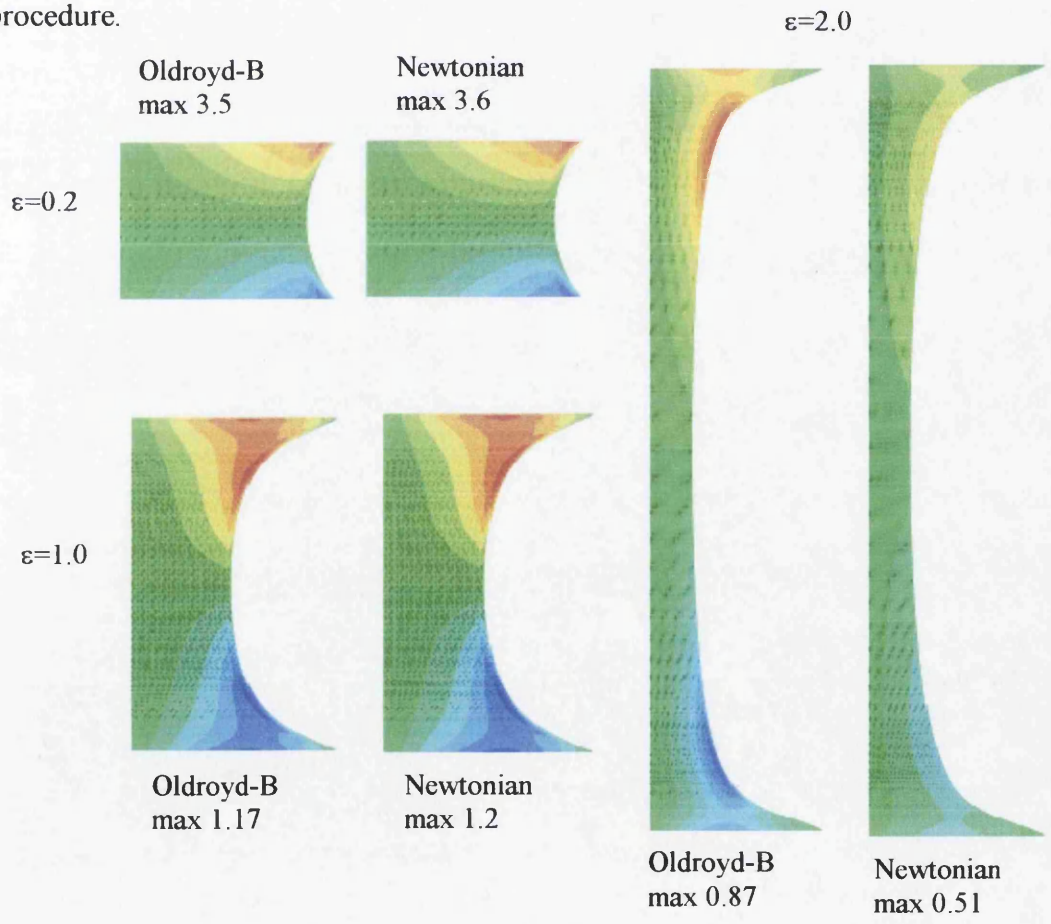

Fig. 5.10 T_{rz}-field evolution: Newtonian v Oldroyd-B; ε=0.2, 1.0 and 2.0

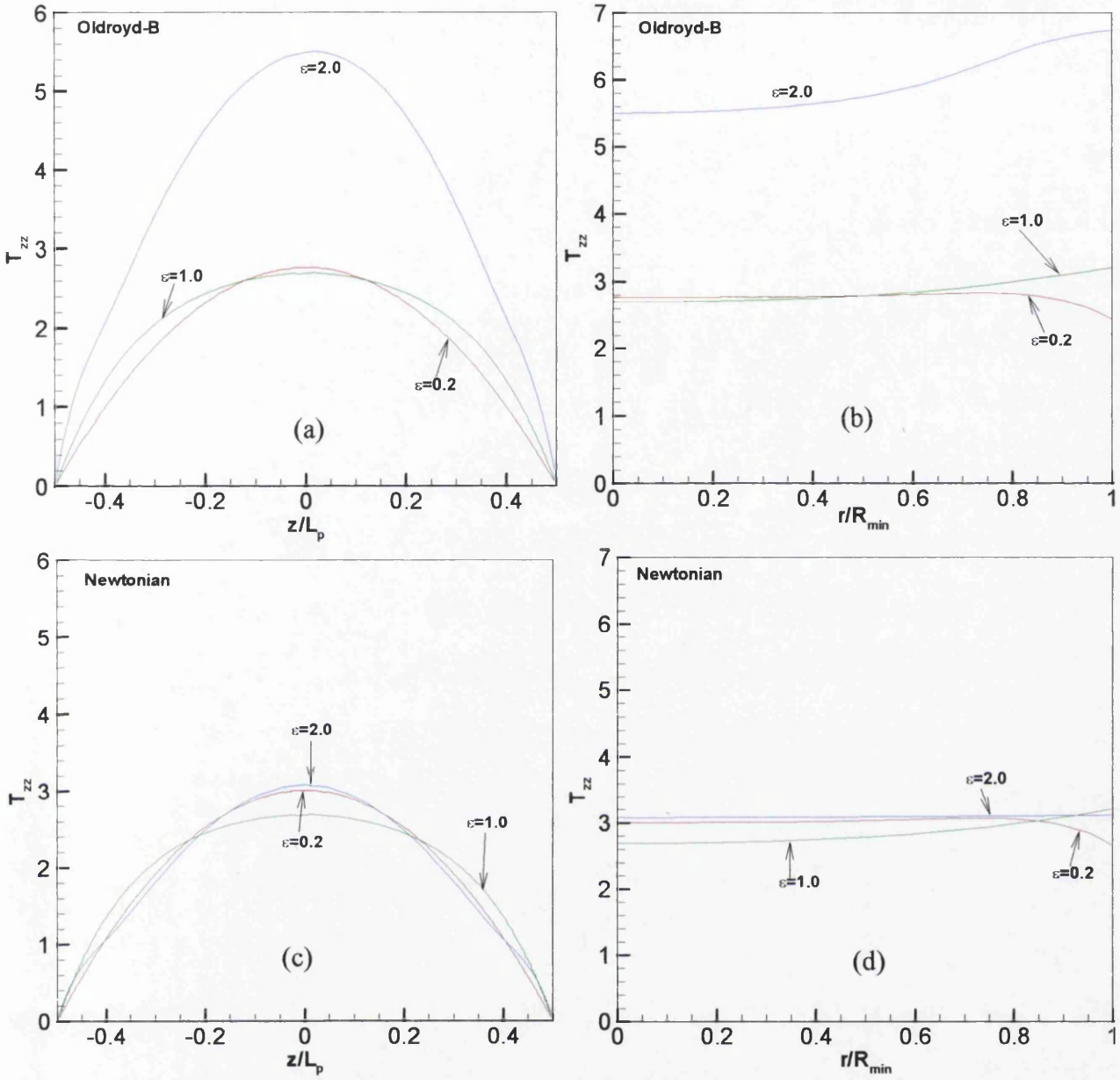

Fig. 5.11 T_{zz}-profiles, increasing ε, $0.2 \leq \varepsilon \leq 2.0$: Oldroyd v Newtonian, r=0 axis(a),(c); z=0 axis (b),(d)

In Fig. 5.14, the stress T_{zz}-profiles, along the principal axes at the high Hencky-strain level of ε=3.8 units, show the extreme differences in solution response across the different instances of *initial filament aspect ratio*. Greatest impact is observed along the filament mid-plane (z=0) and over the sector tending towards the free-surface. Such values in T_{zz} vary from 50 units for (Λ_0=1/3) to 215 units for (Λ_0=1/3) at the free-surface itself. Hence, there is some four-fold difference. Steep stress boundary layers build up at the plates in the short-height initial aspect-ratio instance (Λ_0=1/3) along the alternative filament central-axis

(r=0). Yao and McKinley [3] reported similar graphical data by providing direct validation of present solutions,

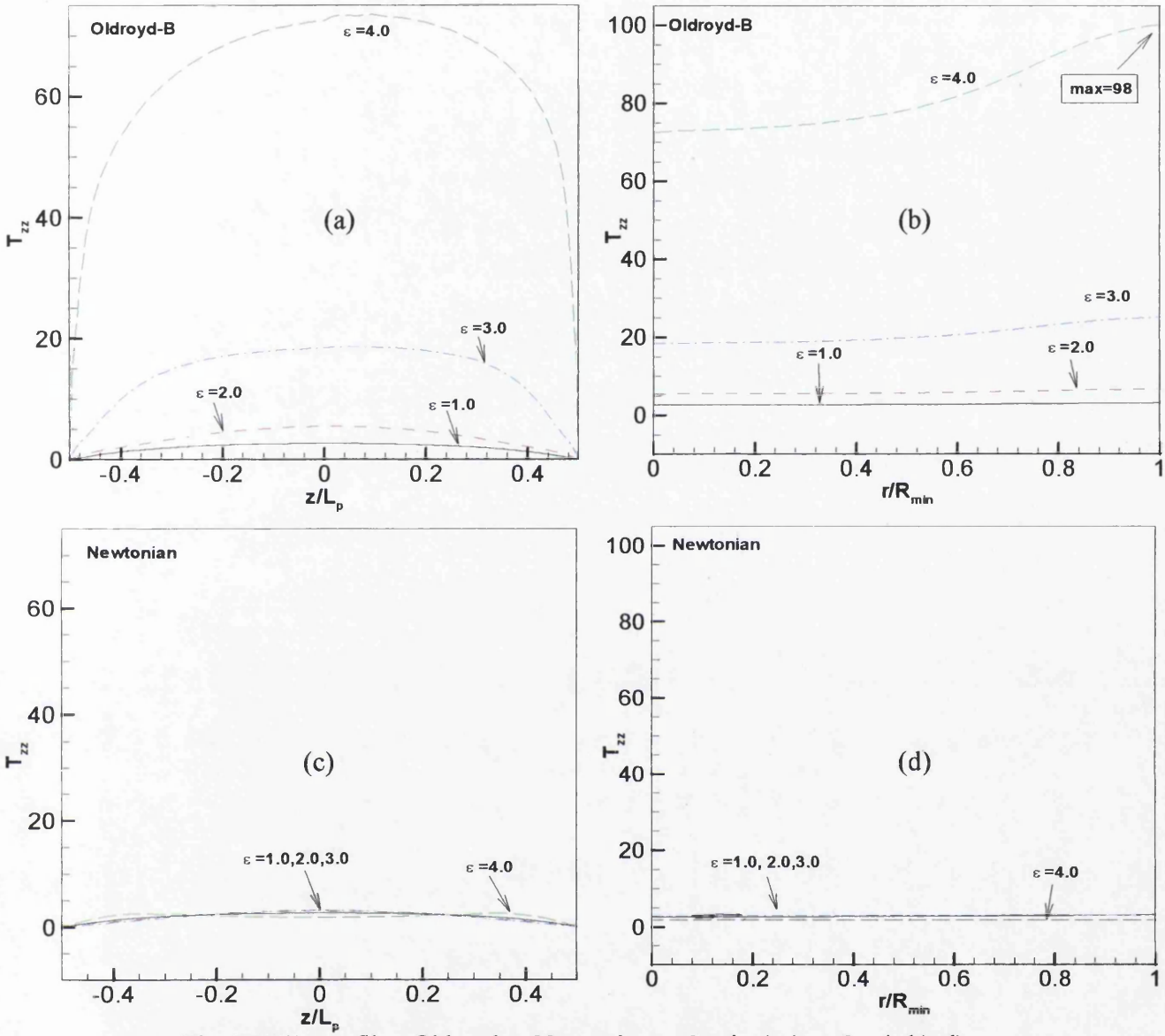

Fig. 5.12 T_{zz}-profiles, Oldroyd vs Newtonian; r=0 axis a) c); z=0 axis b), d)

both in values and trends. This also extends to temporal data for Newtonian and Oldroyd fluids across Hencky-strains of ε={0.2, 2.0, 3.8} units for the aspect-ratio (Λ_0=1/3), see Fig. 5.15(a-c). There is close quantitative agreement between Newtonian and Oldroyd data overlapping at low Hencky-strain levels of ε=0.2 units. By ε=2.0 units, maxima in Oldroyd -T_{zz} (5.5 units) have nearly doubled those for Newtonian-T_{zz} (2.8 units). At ε=3.8 units, Oldroyd -T_{zz} maxima increase to (48 units), whilst Newtonian-T_{zz} remain around O(3 units).

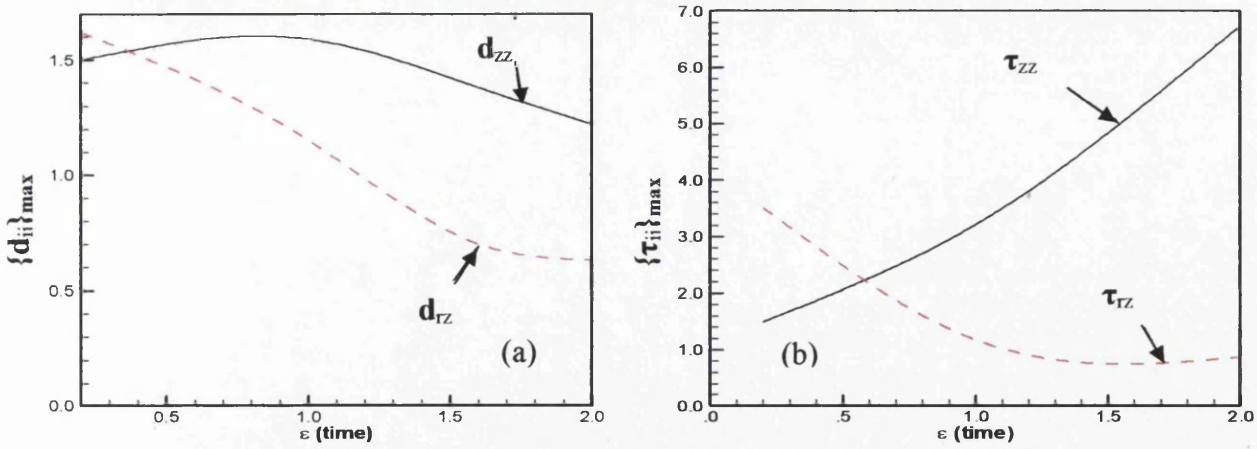

Fig. 5.13 Temporal profiles, Oldroyd-B: a) $\{d_{zz}/d_{rz}\}_{max}$; b) $\{\tau_{zz}/\tau_{rz}\}_{max}$

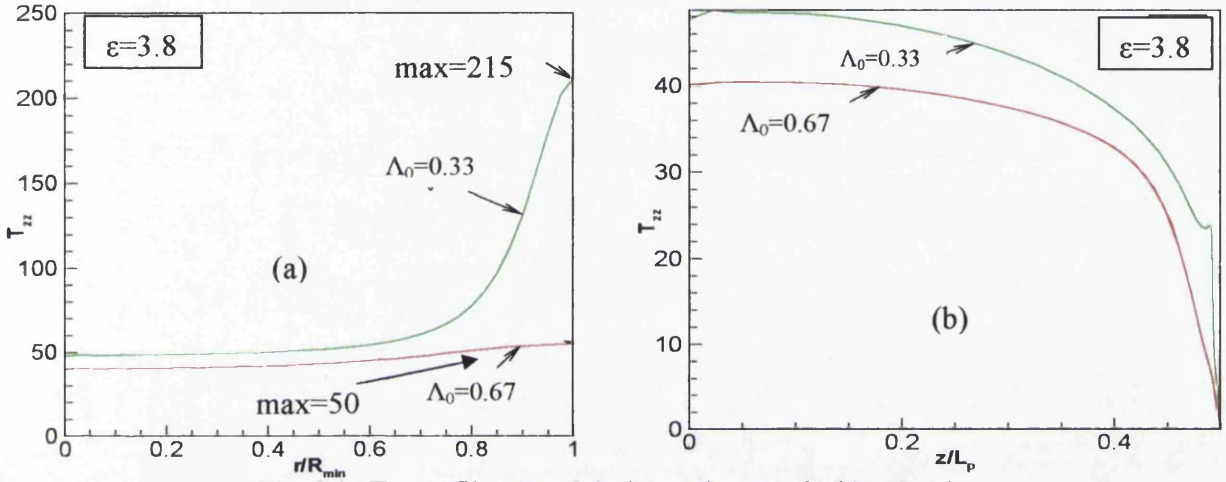

Fig. 5.14 T_{zz}-profiles at ε=3.8 along: a) z=0 axis, b) r=0 axis

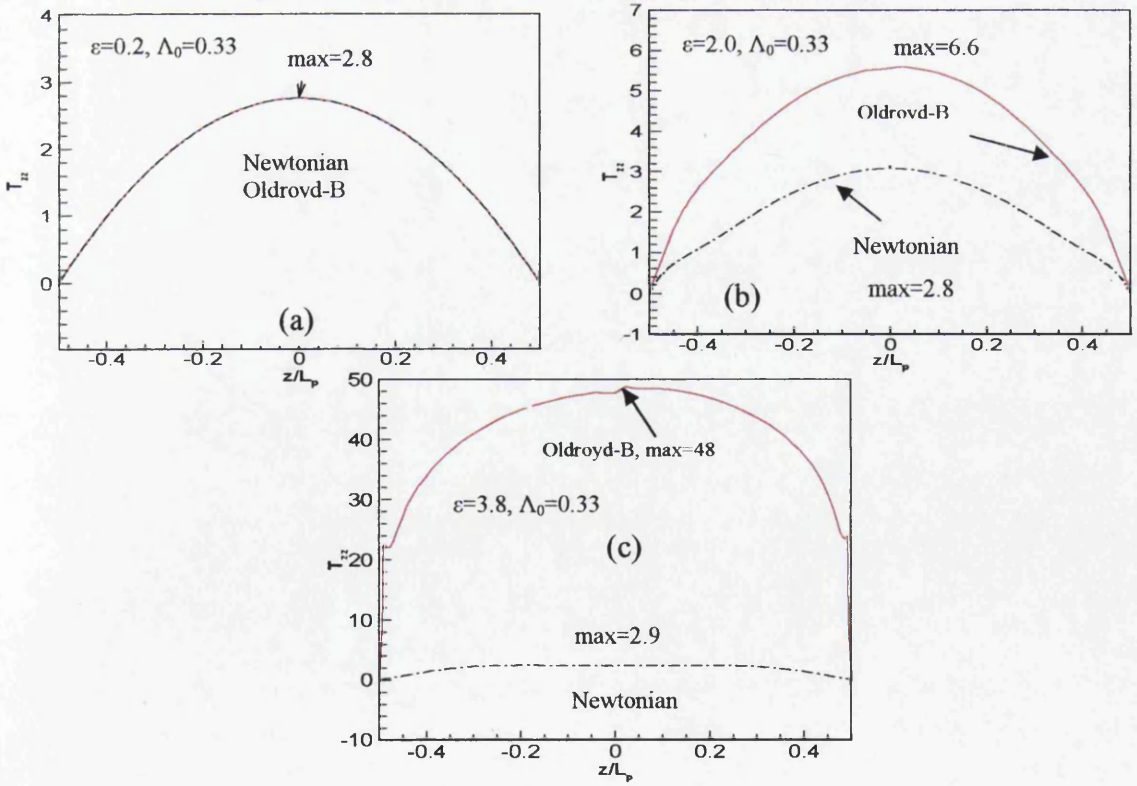

Fig. 5.15 T_{zz}-profiles, r=0 axis: Newtonian vs. Oldroyd-B; a) ε=0.2, b) ε=2.0 and c) ε=3.8

5.3.1c R_{min} estimation and Trouton ratio evaluation

Temporal development of the minimum filament radius as a function of Hencky-strain is illustrated in Fig. 5.16a. Apparently, in figure of $R_{min}(t)$ (scaled with initial radius R_0), there are two obvious regions. Since the slope of the curve is greater at lower strain levels (ε<1.75 units), the filament undergoes significant necking during this period. In the subsequent region (ε>1.75 units) and due to strain hardening, the filament radius declines more gradually. This response reflects close agreement with observations made by others [3]. Trends for approximate lubrication theory with fixed end-plates ($e^{-0.75\varepsilon}$, Newtonian solution) and ideal uniaxial elongation ($e^{-0.5\varepsilon}$) provide a window between which the response is clear for the two aspect-ratios in question.

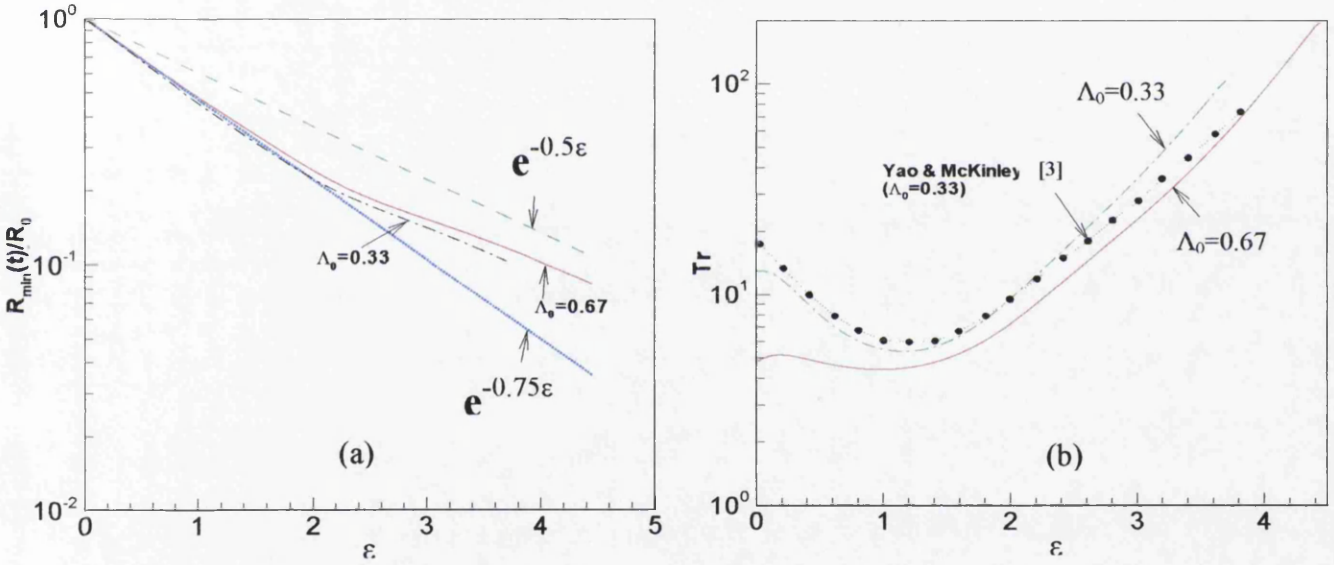

Fig. 5.16{R_{min}, Tr} variation with ε; Oldroyd-B (β=0.915),
a) R_{min}, b) Tr

One of the main targets in operating the filament stretching rheometers is estimation of extensional viscosity (η_e). Calculation of this quantity is conducted based on the force applied on the end-plate, F_z. Accordingly, Trouton ratio (Tr), which is a function of η_e, may be expressed [3] as,

$$Tr = \frac{\eta_e}{\eta_0} = \frac{F_z}{\eta_0 \dot{\varepsilon}_0 \pi R_{mid}^2} - \frac{\chi}{\eta_0 \dot{\varepsilon}_0 R_{mid}} + O(F_i, F_g). \qquad (5.7)$$

Here, R_{min} denotes the minimum filament radius at the mid-plane axis, and χ represents a surface tension coefficient. The last term of Eq. (5.7), which accounts for correction terms due to inertial (F_i) and gravitational (F_g) forces, is taken to be negligible in this work. The force on the plate, F_z, may be represented via,

$$F_z(t) = \int_A [T_{zz}(r, z_{plate}, t) + p] dA = F_v + F_e + F_p \qquad (5.8)$$

where A is the area of the end-plate and $z_{plate}=L_p/2$; F_v, F_e and F_p are the viscous, elastic and pressure forces, respectively.

In Fig. 5.16b, Tr is compared against the results reported by Yao and McKinley [3], as a function of time for the Oldroyd-B fluid. Close agreement is extracted between these and our predictions. The transient extensional viscosity of the Oldroyd-B fluid tends to infinity at large strain levels, and the Trouton ratios calculated for both aspect-ratios reflect this trend (1/3and 2/3).

5.3.2 Results for Volume-of-Fluid (VOF) scheme

Under the *VOF*-scheme, wet and dry regions are set apart, based on the assigned material property of viscosity, as relevant for momentum determination. The viscosity vanishes for a dry node, and hence the solution is null. The fraction of wet area is calculated through the number of active quadrature points (in the wet zone, simplex Gauss rules considered) for part-filled elements. Typical free-surface profiles at $\varepsilon = 0.2$ units, obtained when employing seven, four and one Gauss quadrature point (gp) options are displayed in Fig. 5.17. Based on surface particle movement (dx/dt) as described above the free-surface is determined. These findings are compared against the results of Yao and McKinley (Yao and McKinley 1998). It is implied from the

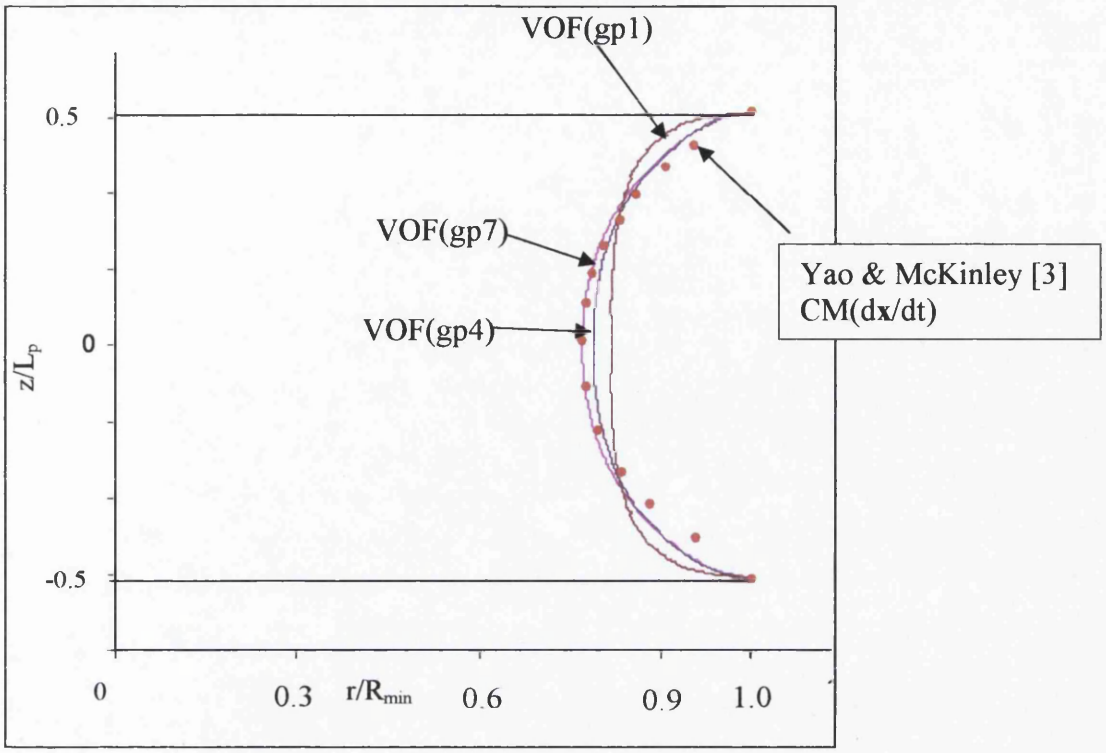

(a) ε=0.2

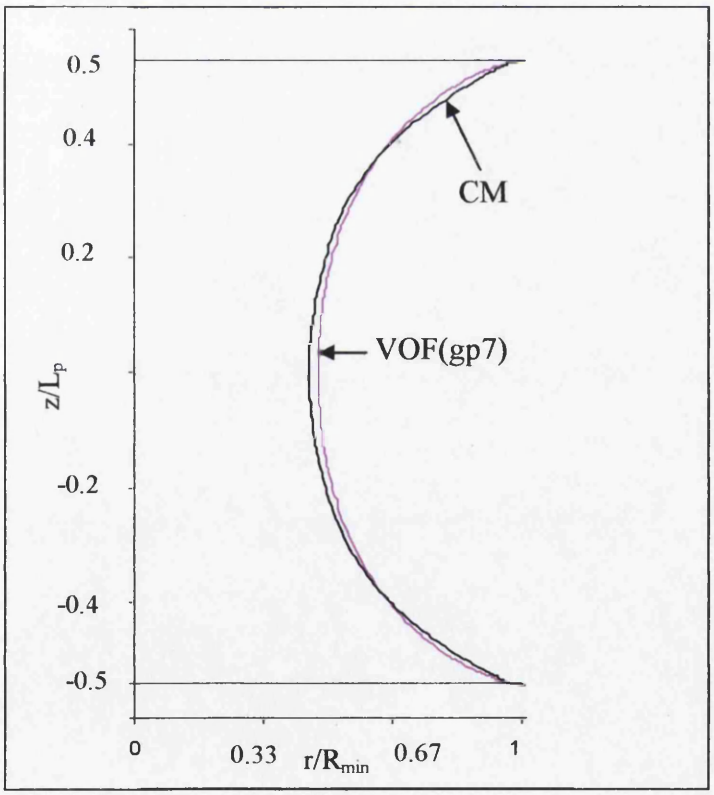

(b) ε=1.0

Fig. 5.17 Free-surface predictions, a) ε=0.2; various sample point cases;
b) ε=1.0; VOF v CM-schemes

figure that material property assignment through one Gauss point (piecewise-constant on the element, equivalent to a conventional *VOF*-implementation) accuracy degrades and the highest achievable level of strain with this setting is $\varepsilon = 0.2$ units. The Gauss point is located at the diametrical centre of the triangular element in the one gp-form. Thus, as with the original *VOF*-scheme, if the element is half or more filled, it will be considered as wet; otherwise dry. There are schemes in the literature which are governed by perimeter element nodal point control and closed Newton-Cotes quadrature rules (*fv*-discretisation), see [53,54]. Our experience shows that enhanced precision may be obtained through increasing material assignment sample integration points from one, to four, and up to seven-gp. Close agreement on R_{min} is observed between the seven-gp option and the literature [3]. No practical difference has been found through enrichment (say, to gp=15) with further sample points.

A comparison between *VOF* and *CM/ALE* free-surface profiles at Hencky-strain levels of 0.2 and 1.0 units is demonstrated in Fig. 5.17a,b. At low Hencky-strain levels, where mesh aspect-ratios are comparable, there is barely any difference between *VOF* and *CM*-solutions, except near the plates. In fact, *VOF* and *CM*-solutions are observed to be visually identical in the central part of the filament providing close agreement on R_{min} at $\varepsilon = 0.2$ units (see Fig. 5.17a). At the higher strain level of unity (Fig. 5.17b), the discrepancy between *VOF* and *CM*-solutions becomes more pronounced. The *VOF*-method apparently degrades the solution at contact-point interfaces (fluid-solid contact) where greater curvature arises. The major cause for this discrepancy may be attributed to the difference in mesh aspect-ratios generated there by the *VOF* and *CM*-procedures. The mesh aspect-ratios generated near the plate and filament centre with each method, at ε=0.2 and 1.0 units are displayed in Fig. 5.18a,b. At low Hencky-strain of ε=0.2 units, mesh aspect-ratios do not greatly differ (factor of 3.8 at top-plate and 1.0 at filament-centre). However, by ε=1.0 units, differences in aspect-ratio commence to broaden (6 at top-plate and 2.6 at filament-centre). For a typical sample point near the solid-fluid contact point, Fig. 5.19 exhibits the percentage error in departure for

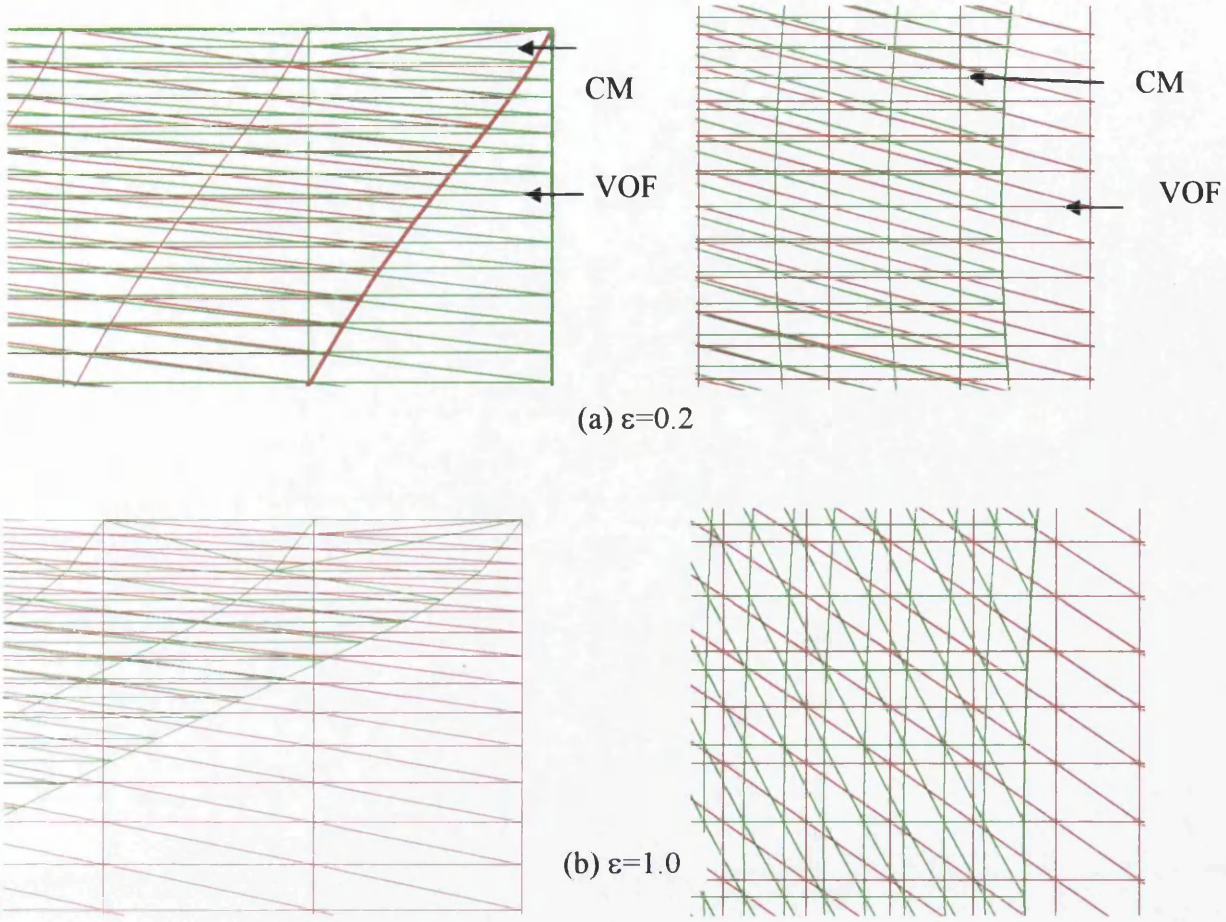

Fig. 5.18 Mesh aspect ratios at top-plate and filament centre: a) ε=0.2, b) ε=1.0

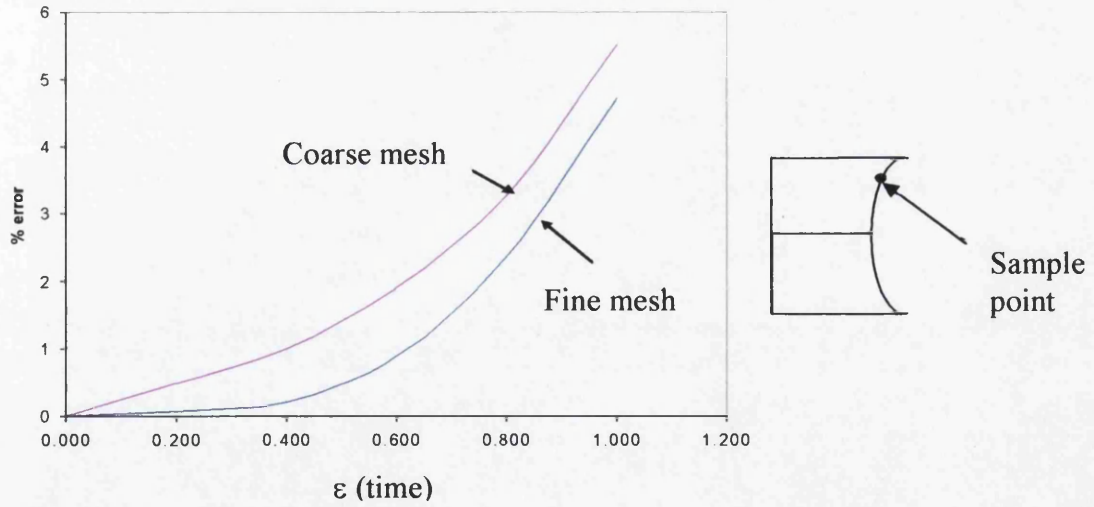

Fig. 5.19 Percentage error as a function of time at typical sample point, coarse mesh vs fine mesh

VOF-results from those for the *CM*-method. At low strain levels, the percentage error is smaller, and rises *exponentially* in time, in accordance with actual aspect-ratio growth. Mesh refinement improves the situation at low Hencky-strain levels. This reveals the deficiency of the *VOF*-method and the fact that for this particular problem of spatial stretch, exponential error growth is to be anticipated.

Apart from mesh aspect-ratios, another aspect that may contribute towards discrepancy between *VOF* and *CM*-solutions, is the difference in treatment of imposed boundary conditions on free-surfaces. Within the *VOF*-method, no explicit traction conditions are applied on such surfaces. Instead, boundary conditions are incorporated by assigning suitable material properties within associated domain integrals, via sample quadrature point evaluation.

5.4. Conclusions

The present filament stretching study establishes large Hencky-strain solutions for Oldroyd-type fluids, illustrating constant shear viscosity and vigorous strain-hardening. On the numerical side, an effective comparison has been made between a compressed-mesh approach and a Volume-of-Fluid alternative. The *CM*-approach, with *ALE*-formulations ($\boldsymbol{u}_m \approx \boldsymbol{u}$) has proved to be superior to that for the VOF-scheme in terms of both solution quality and levels of ε_{crit}. In particular, high levels of Hencky-strain of O(4 units) are realised with the full *ALE/CM*-strategy combined with d**x**/dt free-surface tracking. It is the relative mesh aspect-ratios that are mainly responsible for this.

We have also been able to severely contrast free-surface discrete treatments. In this respect, the sensitivities and deficiency of employing the kinematic condition $(\partial h / \partial t)$ to determine surface level *h(z,t)* has empirically been demonstrated. The particle-tracking technique (d**x**/dt) which is more flexible allows for less restriction of free-surface movement, and as such, captures zones of larger curvature adjustment with improved precision. This is most pronounced in the shear boundary layer near the plates at the feet of the filament. Employing the *ALE/CM*-strategy with particle-tracking yields quantitative measures via Trouton ratio, extensional viscosity, minimum filament radius, deformation rates and stress which are in close agreement with the literature. Here, we have managed to retain stability

and provide viscoelastic field data up to Hencky-strain levels as large as 4.4 units.

In this work a robust numerical procedure has been established. In the companion work of chapter six, the impact of alternative forms of rheological response is identified for the finest mesh studied here and under the particle-tracking approach (dx/dt). There, we report upon the impact of both surface tension and body force influences on single-mode and multi-mode representations covering the three viscoelastic models discussed in chapter four.

Chapter 6

Single vs Multi-Mode Modelling for Filament-Stretching Flows[†]

The subject of this chapter is computational investigation of filament stretching at high Hencky-strains. Previous predictions are extended on the multi-mode side through advance in Hencky-strain and single-mode predictions via rheological variation, with the additional consideration of linear versus exponential-stretching configurations under Oldroyd modelling. The focus is on strain-hardening polymeric solutions and broadening the application range of an ALE-formulation hybrid finite element/volume scheme. Computational predictions are validated against theoretical solutions and through discrete refinement for consistency. For such strain-hardening fluids, dominance of tension-thickening over shear-thinning properties is established. Shear effects are amplified for a Giesekus model, and greater foot pinching results with filament mid-plane thickening, as a consequence of hardening reduction and less extension at the filament centre. This has led to more exaggerated filament thinning. The importance of each mode has been addressed by comparing and contrasting single- versus multi-mode modelling (multi-timescale). The influence of multiple modes reveals itself through the

[†] Material of this chapter is based upon the paper "Single and Multi-mode Modelling for filament stretching flows", by H. Matallah, K.S. Sujatha, M.J. Banaai and M.F. Webster, and published in *Journal of Non-Newtonian Fluid MechanicsVol. 146, Iss. 1-3, pp. 92-113 .*

developing components of stress generated and their impact on filament shape. At large levels of Hencky-strain, the emergence of bead-like structures has been explored. These structures are absent in either Giesekus or linear Phan-Thien/Tanner(ξ=0) solutions up to Hencky-strains as large as 5 units. In contrast, at sufficiently large Hencky-strains beyond 3 units, the presence of such structures is detected with the linear Phan-Thien/Tanner (ξ=0.13) option.

6.1 Introduction

Extensional flow of polymeric fluids has application within numerous industrial processes, such as film blowing, fibre spinning, and extrusion of polymeric materials. These processes are largely influenced by extensional modes of deformation. Extensional flows are also involved in applications such as coatings, enhanced oil recovery, lubrication, turbulent drag reduction and atomization. Filament-stretching is a common example of such an extensional flow with a broad spectrum of application in the study of polymer solutions and melts. In addition and particularly following the pioneering work of Sridhar and co-workers [37], filament stretching has become a well-established rheometric technique for the measurement of elongational viscosity. In a number of polymer processing operations, the accurate calculation of extensional viscosity is of prime importance. The fluid sample undergoes extensional deformation, and subsequently a uniaxial extensional flow at the filament-centre is established. In a *FISER*-type (Filament Stretching Extensional Rheometer) rheometer, plate-retraction is often constrained to an exponential-rate, which imposes an exponentially increasing velocity upon the fluid filament and is accompanied by a constant stretch rate. Constant plate velocity and variable stretch rate is an alternative configuration. In the course of thinning and necking down, whilst the filament is progressing ultimately towards rupture, calibration is performable by monitoring the subsequent evolution of the mid-plane filament radius, or force measurement on the end-plates. Due to mechanical constraints and elastic instabilities, such filament-stretching experiments are practically difficult to conduct. Additionally, quantitative measurement of extensional viscosity is recognised as a challenging task to perform for highly mobile liquids, further exacerbated here by the presence

of shearing effects at solid-fluid boundary interfaces. Therefore, particularly at large strain levels, the need arises for guidance and precision through accurate modelling and prediction of such extensional flows. For suitable background information, a thorough review of the flow dynamics is provided in the article of McKinley and Sridhar [46] covering filament-stretching rheometers. Matta and Tytus [56] who allowed the lower plate to fall under gravity, were the pioneers in introducing filament stretching device, conducting constant force experiments. In this instance, the authors reported that the liquid bridge was subject to a constant extension rate when the plates were rapidly retracted. An improved form of this apparatus has been developed by Tirtaatmadja and Sridhar [38] for low viscosity liquids. In their work, to sustain a constant stretch rate at the filament centre, the disks were pulled apart at an exponential rate.

Some general observations may be made regarding the literature on bead-formation under extensional deformation. Bead formation is a typical viscoelastic phenomenon under elastocapillary thinning, in which a uniform liquid filament collapses into a series of sphere-like drops connected by thin liquid threads, forming the so-called beads-on-string structure. The thicker regions of fluid are termed beads, interconnected by axially-uniform ligaments. In threads, molecules are highly stretched and viscoelastic stresses dominate, whilst in beads, molecules relax and surface tension dominates. The formation of a beads-on-a-string morphology occurs as a result of interplay between inertia, viscous, capillary and elastic forces in a nonlinear dynamic process. Such structures have been observed in both jets and stretched filaments of polymeric liquids in air. Goldin et al. [57] studied bead formation in viscoelastic and Newtonian liquid jets. Linear theory for infinitesimal disturbances captured the initial fast growth of axisymmetric wave disturbances in viscoelastic jets when compared with Newtonian fluids of equal viscosity. Yet, such linear theory was unable to describe the retardation of filament break-up in viscoelastic filaments (ultimate slow growth of disturbances), that is caused by the build up of extensional stresses. As such, viscoelastic filaments prove more stable to break-up compared against their Newtonian counterparts. In addition, the generation of beads at repeated times, termed 'iterated stretching' was

studied by Chang et al. [58] for viscoelastic FENE and Oldroyd-B fluid jets. This analytical work was conducted via simplified long-wave theory and through simulation. To quote Chang et al., the beads may be described as accumulators and transmitters of noise from the surrounding fluid that trigger recoil dynamics, without being affected themselves by recoiling and consequent formation of secondary filaments. Through some more recent experiments, Oliveira et al. [59] studied iterated stretching and periodic formation of 'beads-on-string', concluding that this provides a means for probing transient extensional response even for very low viscosity polymer solutions.

With regards to predictive modelling, a number of computational studies have been conducted, aimed at predicting the development of viscoelastic fluid ligaments under various forms of filament stretching. In this respect, a number of alternative numerical techniques have been proposed to overcome the rigorous computational challenges involved: dynamic configuration, moving free-surface with solid-liquid contact, mixed mathematical equation type, and inclusion of surface tension and body forces. To model such flows, appropriate constitutive equations are sought that realistically reveal particular forms of fluid response. For example, the current interest is centred on strain-hardening polymeric solutions. Consequently, numerous integral and differential constitutive models have been considered [4-7], of both single-mode and multi-mode description. The FENE-CR (Chilcott-Rallison) model was implemented by Sizaire and Legat [4] in the single-mode category to predict strain-hardening/constant shear viscosity material response. This involved a two-dimensional finite element solver within an Eulerian configuration (with the FENE-CR L^2 extensibility coefficient of 4325.5). Bach et al. [5] in contrast, used a pure Lagrangian formulation alongside an integral constitutive model of minor modification to that of K-BKZ. Yao et al. [3] under multi-mode modelling, studied the stress evolution in Giesekus filaments under uniaxial elongation and stress relaxation following the cessation of stretching. Yao et al. utilised the commercial software package "POLYFLOW", adopting an Eulerian Galerkin finite element discretisation of classical form, with a Thompson transformation remeshing technique and a height function to track free-surface

deformation. Contrasting both multi- and single-mode solutions, the specific role of the fluid relaxation spectrum was investigated to identify the discrepancies in predicted viscoelastic response across the individual modes. Langouche and Debbaut [9] introduced a multi-mode Phan-Thien/Tanner model (exponential version EPTT, five and nine-modes) with a broad relaxation spectrum ($O(10^{-3}) \leq \lambda_i \leq O(10^2)$), under which shear, dynamic and transient stretching characteristics were all well-fitted. There, within a semi-analytical framework, close agreement was observed between predictions and experimental data at moderate Hencky-strains (up to 2 units), both for instantaneous extension and step-strain recovery experiments. Yet, predictions overestimated experimental data beyond a Hencky-strain level of 2.0 units. Then, to extend the analysis into two-dimensions, a finite element scheme was employed. This allowed for the additional considerations of force inclusion and boundary conditions, through inertia and surface tension, and during the early phase of instantaneous recovery tests succeeded in identifying the occurrence of inertial oscillations.

There are several nonlinear constitutive models available today capable of describing the rheology of interest. In the present work, a Giesekus model has been chosen as the base-reference [37], under both single and multi-mode representations, to contrast our findings against those for Oldroyd and PTT models. The Giesekus model is chosen for its suitability to fit both linear and nonlinear shear rheology for the majority of concentrated polymeric solutions, and is commonly used to represent weakly strain-hardening fluids, see for example Yao et al. [3] and Li et al. [2]. A higher-order discrete-elastic-viscous-stress (*hp-DEVSS*) finite element method was utilised in the work of Li et al.[2] to solve an axisymmetric stagnation flow of mixing-separating type [82,83]. This work is useful as it describes the viscometric characterisation of the test fluid in question, together with comments on the appropriateness of the various candidate rheological models under consideration.

The numerical algorithm employed in the current work is that of an *ALE*-formulation hybrid finite element/volume scheme (h_y-fV). This scheme, as already

described in detail in the literature [82,83], is centred on several novel and advantageous features. Here, it has been developed and employed specifically within the context of transient viscoelastic free-surface flows. Elsewhere, it has effectively been applied for steady and transient inflow-outflow viscoelastic problems under static meshing and within enclosed domains [11]. The outstanding characteristics of this scheme are as follows. On each Hencky-strain step, it embodies a time-stepping algorithm of operator-splitting/fractional-stage structure, which takes a combination of incremental pressure-correction stages with Lax-Wendroff/Taylor-Galerkin time-splitting procedures [12]. The dynamic nature of the problem (mesh movement) is cast into an Arbitrary-Lagrangian-Eulerian (*ALE*) technique [31], as opposed to a pure Eulerian formulation. Furthermore in reference [19], the superiority of a *Compressed-Mesh (CM)* radial implementation is displayed in preference to that of a *Volume-of-Fluid (VOF)* scheme, along side improved free-surface procedures that favour particle-tracking (dx/dt) over height function $(\partial h/\partial t)$ schemes. The major signature to the scheme, comprising hybrid finite element and finite volume contributions, with a finite volume *cell-vertex sub-cell* approximation for stress, and a finite element treatment for velocity and pressure [31,12] is provided through the precise form of spatial discretisation employed. The principle behind the *ALE*-technique is to permit freedom of mesh movement, under a prescribed mesh velocity in a Lagrangian dynamic frame of reference, and to track the associated adjustment of complex free-surface shape in the evolving flow. Noh [11] and Hirt et al. [12] first introduced this approach in the finite difference domain. Then, Hughes et al. [13] further extended it into the finite element domain for incompressible viscous flows. The character of dynamic filament stretching well matches this description, being mainly the deformation of uniaxial extensional form. In Ref. [43], the distinct benefits are established of the present schemes under single-mode modelling to achieve high Hencky-strain solutions (three units and above), to capture fine structural definition at filament feet (solid-fluid boundary interface), and to include capillary and gravitational forces.

The current chapter is split into two sections, the first one dealing with fresh aspects of detail under single-mode modelling and the second one covering multi-mode solutions. In consideration of single-mode modelling, the prior work in [31] has been expanded to consider three different strain-hardening models, inclusion of body force and surface tension effects, and both exponential and linear plate-retraction for Oldroyd fluids. Under the multi-mode section, only exponential-stretching is considered and comparison between three-mode Giesekus and linear-version PTT (denoted LPTT) models is provided. Attention was given to a two-mode representation in [31], where preliminary results were gathered at low to moderate Hencky-strain levels (up to 1 unit). Therefore, in the present chapter, the focus is extended to a three-mode approximation and a widened strain regime. At the same time, this facilitates the study of the influence of a spectrum of relaxation times ($O(10^{-3}) \leq \lambda_i \leq O(10^{0})$), and indicates how high Hencky-strain levels (above 3 units) may numerically be reached. The broader spectrum of relaxation times and viscosity weightings demand some modifications to the single-mode algorithm, in particular, tackling the smaller solvent viscosity contributions. The linear-stretching configuration, under constant and simultaneous plate retraction-rate, has also been studied by Foteinopoulou et al. [24] and by Koplick and Banavar [25]. The principal focus of the work of Foteinopoulou et al. was on predicting the growth of bubbles within the stretched filament between the end-plates. Koplick and Banavar [25] conducted a study on the atomic scale, examing the interfacial breakup of the liquid bridge, under variable exerted force that fluctuated throughout the course of stretching.

The next section proceeds to outline the numerical modelling procedures used and predictions they generate.

6.2 Problem specification

In the present flow problem, a viscoelastic filament is considered as contained between two coaxial circular discs, which are parallel to one another. The discs are simultaneously retracted to elongate the liquid bridge at a controlled rate. Both linear and exponential-stretching configurations are considered for the single-mode

approximation, in the presence of gravity and surface tension. Under multi-mode (three-mode) prediction, only exponential-stretching, with/without surface tension effects is considered. Throughout this work, the strength of inertial influence, reflected through the Reynolds number ($O(10^{-3})$), has negligible effect in practice.

To address consistency under the multi-mode version, spatial and temporal refinement is performed. Mesh-refinement is tackled in two axial and radial directions. Three initial meshes of generalised rectangular (triangular element-pairs) element description (100x20), (150x20), (200x20) are utilised for the axial direction; two meshes of (150x15 and 150x20) are taken radially. Under the context of single-mode simulations, the single (100x20) mesh is employed, as appearing in [31,12]. In order to allow for emerging asymmetries and on the arguments presented in reference [31], a full filament mesh discretisation has been selected. That is without enforcing symmetry conditions on the filament mid-plane, or in the spatial discretisation (griding) above and below the mid-plane (but with centreline symmetry).

In all field variables, initial conditions are taken as quiescent and a base-reference of ambient surrounding pressure level on the free-surface is assumed. No-slip boundary conditions are considered along the interface between the liquid filament and end-plates imposing axisymmetry along the filament-central axis (axial) and a local force balance at the free-surface, as exhibited in Fig. 6.1 (t=0 and t>0), where a natural boundary integral (b.i.) is enforced. Velocity, $V_z(t)$, and length, $L_p(t)$, are imposed on the moving-plates, viz.,

a) exponential-stretching:

$$V_z(t) = \pm(\dot{\varepsilon}_0 L_0 / 2)\exp(\dot{\varepsilon}_0 t),\quad V_r(t)=0,\quad L_p(t)=\pm(L_0/2)\exp(\dot{\varepsilon}_0 t),$$

b) linear-stretching:

$$V_z(t)=\pm(\dot{\varepsilon}_0 L_0/2),\quad V_r(t)=0,\quad L_p(t)=\pm(L_0/2)(1+\dot{\varepsilon}_0 t),$$

where $\dot{\varepsilon}_0$, L_0 denote an imposed initial stretch-rate and the initial filament length, which provide an appropriate characteristic velocity scale, $U = V_0 = \dot{\varepsilon}_0 L_0$. The initial filament aspect ratio is defined as $\Lambda_0 = L_0 / R_0$, taken here as 0.54 following reference [3] (yet with alternative data provided in [21]) with initial filament radius R_0.

Stretch-rate may be defined with generality for the two stretching configurations, as

$$\dot{\varepsilon} = \frac{1}{L_p(t)} \frac{dL_p}{dt}$$

so that the Hencky-strain is defined as $\varepsilon = \int_{t_0}^{t} \dot{\varepsilon} dt = \ln(\frac{L_p(t)}{L_0})$. Thus, across configurations of stretching and at *equivalent filament lengths*, *equivalent Hencky-strains* will be established. Under numerical solutions reported, critical values of Hencky-strain, referred to below, equate to the maximum sustainable levels (time) to which stable solutions may be computed, prior to numerical divergence or breakdown. This provides for a constant stretch-rate under exponential stretching, and a dynamically decreasing stretch-rate under the linear stretching configuration.

In the presence of surface tension and along the liquid-gas free-surface interface, the following boundary condition is applied as derived from a localised force balance

$$\boldsymbol{\sigma} \cdot \boldsymbol{n} = -p_a \boldsymbol{n} + Ca^{-1}(\frac{1}{R_1} + \frac{1}{R_2})\boldsymbol{n},$$

where p_a denotes the ambient surrounding pressure level, R_1 and R_2 are the principal radii of curvature of the free-surface [43,66], and $\boldsymbol{n}$ represents the free-surface normal vector. This condition is incorporated via a natural form boundary integral that is provided through the finite element method.

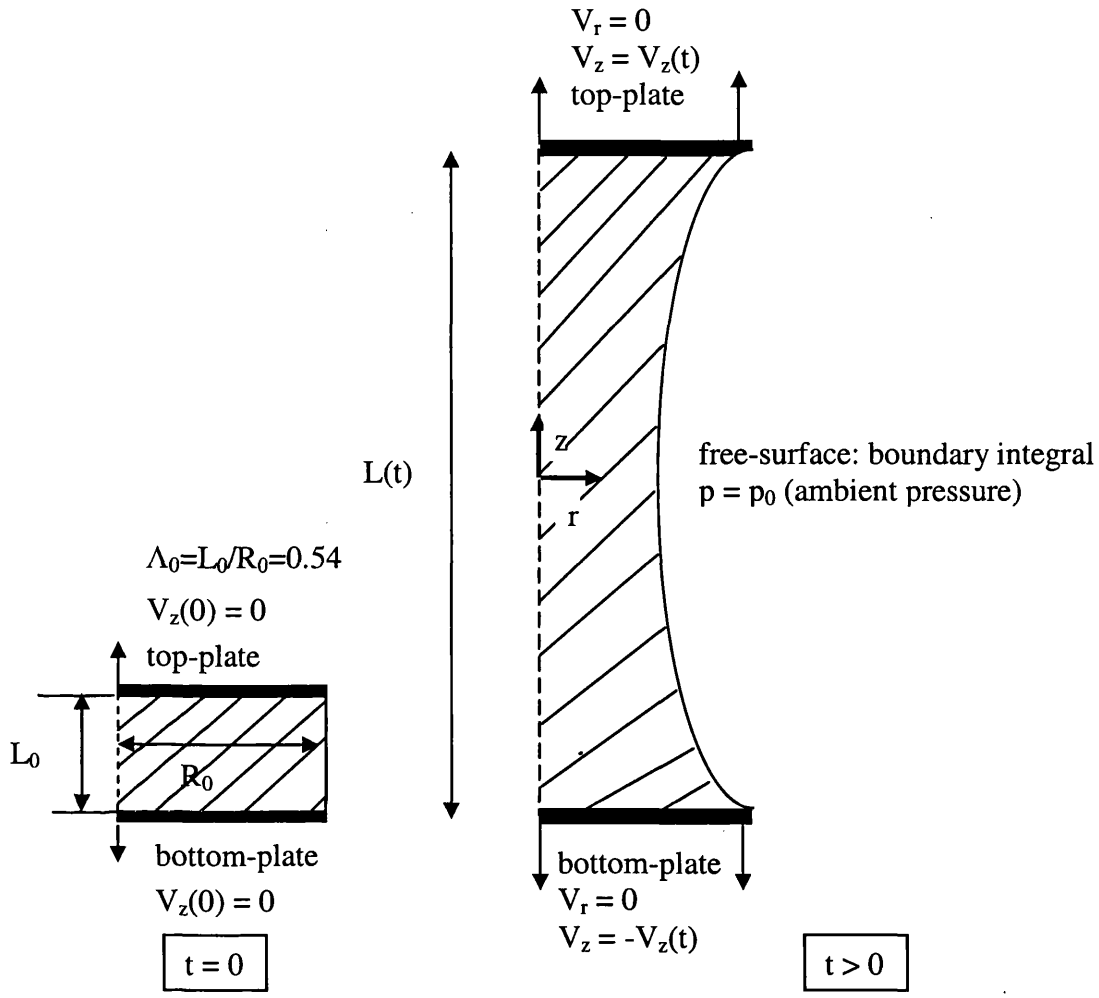

Fig 6.1: Problem domain with boundary conditions; t=0, t > 0

Based on the force balance arguments developed in [4,33,34] the relevant transient Trouton ratio is defined in the present context neglecting inertial terms as,

$$Tr = \frac{\bar{\mu}^{+}(\varepsilon, \dot{\varepsilon}_0)}{\mu_0} = \frac{F_z}{\pi R_{mid}^2} - \frac{1}{CaR_{mid}} - \frac{Bo}{2Ca}\left(\frac{R_0}{R_{mid}}\right)^2. \qquad (6.1)$$

Above, $\bar{\mu}^{+}(\varepsilon,\dot{\varepsilon}_0)$ is the apparent extensional viscosity (Type IB of Yao et al. [3], relevant for experimental data comparison), and F_z is the force exerted on the area (A) of the moving-plates given through the surface integral,

$$F_z = \int_A \{-p + 2\mu_s d_{zz} + \tau_{zz}\}\, dA.$$

6.3 Results and discussion

Results are reported under two sections: the first deals with single-mode and the second with multi-mode modelling. The first section covers a choice of rheological models and alternative stretching configurations (exponential and linear), with consideration of surface tension and body force effects. Alternative rheological properties are incorporated via modelling of various fluids by adjusting the LPTT parameters (ε_{ptt}, ξ) and Giesekus mobility factor (α) . In this fashion, the prevailing influences of shear-thinning, strain-hardening, and external forces may separately be taken into consideration. (ε_{ptt}, ξ, α)-values are selected for the single-mode approximation, as those for the largest mode (1^{st} mode in Table 6.1). Similarly, the single-mode relaxation time is evaluated by neglecting the influence of the shorter modes, preserving only the largest. All polymeric viscosities of the discarded modes are taken to accumulate into the solvent viscosity, which aids numerical stability via the stronger semi-implicitness applied to the momentum equation. In the second multi-mode section, three-modes are used, accounting for surface tension effects. There, at a specific Hencky-strain of ε=1.8 units, consistency through theory and mesh refinement is corroborated for the Giesekus model.

6.3.1 Exponential-stretching: single-mode results

The results reported for the single-mode approximation with (μ_s/μ_0=0.262), are an extension of findings of Ref. [31].

	1st mode	2nd mode	3rd mode
λ_i (s)	0.421	0.0563	0.00306
μ_i (Pa s)	25.8	7.71	1.37
α_i (Giesekus)	0.3162	0.2422	0.0993
ε^i_{ptt} (LPTT)	0.035	0.035	0.035
ξ_i	0.13	0.13	0.13
De_i	1.886	0.252	0.014
μ_s (solvent viscosity) (Pa s)	0.069		
ρ (density) (kg/m^3)	1030		
χ (surface tension coefficient) (N/m^2)	0.03		
Single-mode			
λ_1 (s)	0.421		
α(Giesekus)	0.3162		
ε_{ptt} (LPTT)	0.035		
ξ	0.13		
De	1.886		
μ_s (solvent viscosity) (Pa s)	9.149		
μ_p (polymeric viscosity) (Pa s)	25.8		

Table 6.1: Material properties for single and multi-mode models

6.3.1.1 Effect of surface tension and body forces: LPTT (ξ=0.13)

To assess the effect of both capillary and gravitational forces, separately and combined, axial stress contours for the LPTT (ξ=0.13) model at elevated Hencky-strain levels beyond three are depicted in Fig. 6.2[†]. The situation for body force (F_g=0.122) and surface tension (Ca^{-1}=0.1) combined is shown in Fig.6.2a for the specific choice of parameter setting, following Ref. [31]. Overall, the maximum axial stress is observed within the central zone of the filament, declining towards the moving end-plates, almost doubling in value from around 42 units at ε=3 to 80 units at ε=3.2. There are signs of the onset of bead generation, slightly off-set from the mid-plane with stress-maxima splitting at ε=3.2 units. The combined effect of

[†] Contour scales in this case vary over each Hencky-strain level, to provide direct comparison.

body force and surface tension is translated to greater extension experienced at the filament mid-plane, so that at ε=3, the axial stress increases to 42 units, compared to its counterpart devoid of body and surface tension forces that yields about 35 units (see Fig. 6.3d for direct comparison). In both cases at ε=3 units of Fig. 6.2a,b, with/without surface tension but inclusive of body force, similar internal stress distribution and filament shape is extracted.

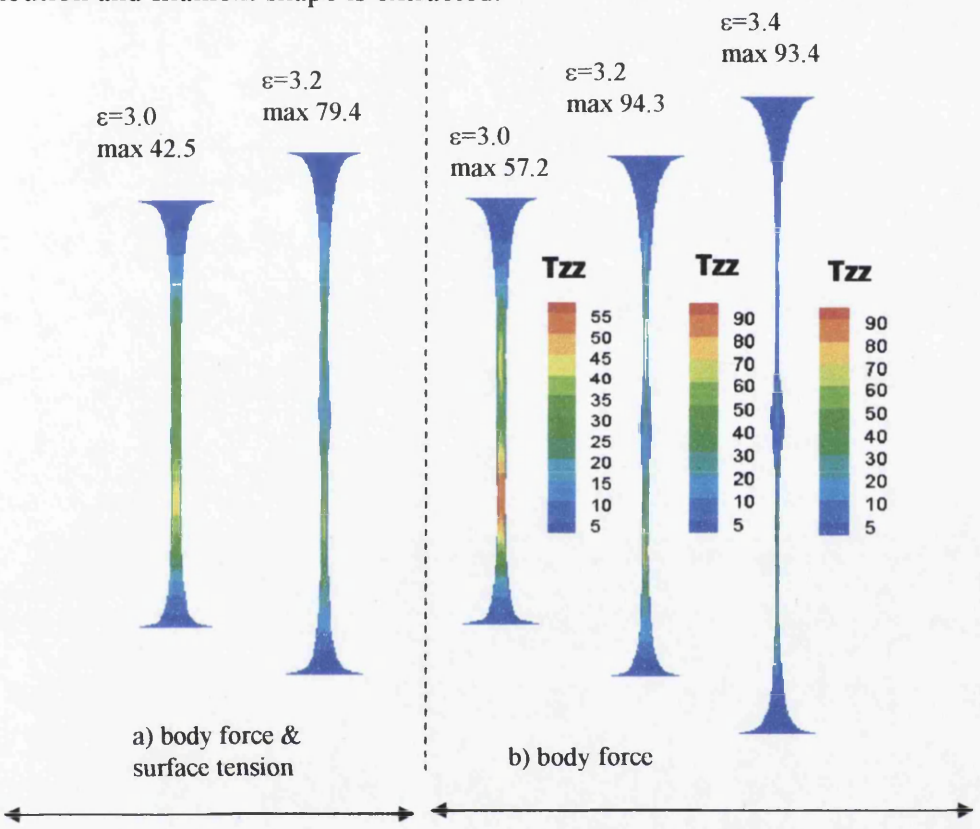

Fig 6.2: Axial stress component τ_{zz}; single-mode, LPTT (ξ=0.13);
a) Ca^{-1}=0.1, F_g=0.122, b) Ca^{-1}=0, F_g=0.122

The position of removal of capillary forces can be investigated. For ε<3 units, axial stress maxima are located at the filament mid-plane, irrespective of body force or surface tension influences. With gravitational force alone (Fig. 6.2b), beyond a Hencky-strain level of three and up to a critical level of 3.4 units, these stress maxima commence to shift slightly off-centre, supporting a single bulge. Stress maxima plateau at Hencky-strains of 3.2 units and above at around 94 units being larger than when capillary force is included. Yet overall, there is an impression of almost symmetrical shape to the elongating filament.

6.3.1.2 Comparison of Giesekus (α=0.32) and LPTT (ξ)

To analyse the influence of variation in shear-thinning and extensional properties, attention is paid to alternative model choices to LPTT (ξ=0.13), and neglect the surface tension and body force effects. Fig. 6.3(a,b) displays the results for LPTT(ξ=0) and Giesekus models. These two models reflect similar shear-thinning behaviour. In relation to this material response, the LPTT (ξ=0.13) model exhibits the onset of shear-thinning at shear-rates $O(10^{-1})$, a decade earlier than LPTT(ξ=0) and Giesekus (O(1)) alternatives. On the contrary, both LPTT(ξ=0.13)

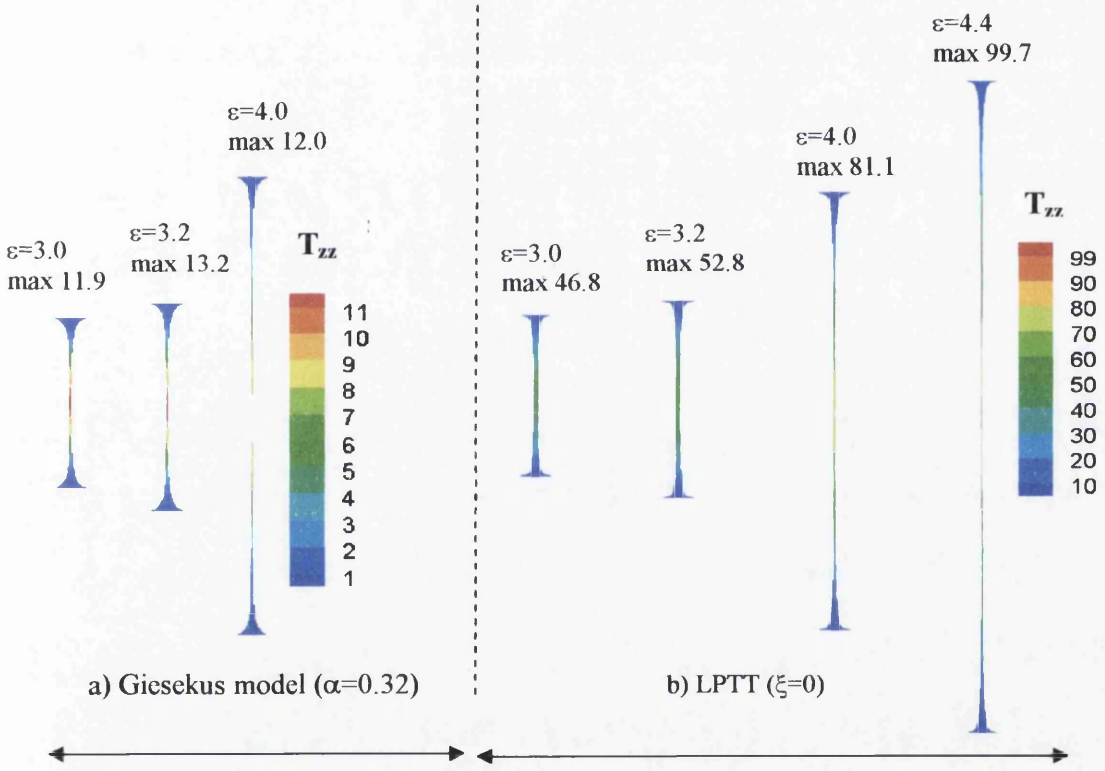

Fig 6.3: Axial stress and foot shapes; single-mode, $Ca^{-1}=0$, $F_g=0$:
a) τ_{zz} Giesekus (α=0.32); b) τ_{zz} LPTT(ξ=0)

and LPTT(ξ=0), indicate exaggerated extensional properties corresponding to those for the Giesekus model (see Refs.[2,3,31] for the relevant viscometric data).

Direct comparison is provided in Fig. 6.4a via filament shape, through foot and filament central regions, across models and at a selected Hencky-strain of ε=2.6 units. The comparison is made across models of Oldroyd-B, LPTT(ξ) and Giesekus, and the dominance of strain-hardening over shear-thinning is illustrated, both at filament feet and filament centre – (see Fig.10 of Ref. [31]). This is most

pronounced in the filament foot zone, where the LPTT(ξ) models practically line up, between the Oldroyd and Giesekus results, so that adjustment in shear-thinning has an insignificant effect upon the LPTT(ξ=0.13)-solution. The thickest filament centres match the more strain-hardening models, compensating for adjustment at the feet, with Oldroyd being thickest, followed by LPTT models, and Giesekus being thinnest. These findings agree with the observations of others in the literature [3,69].

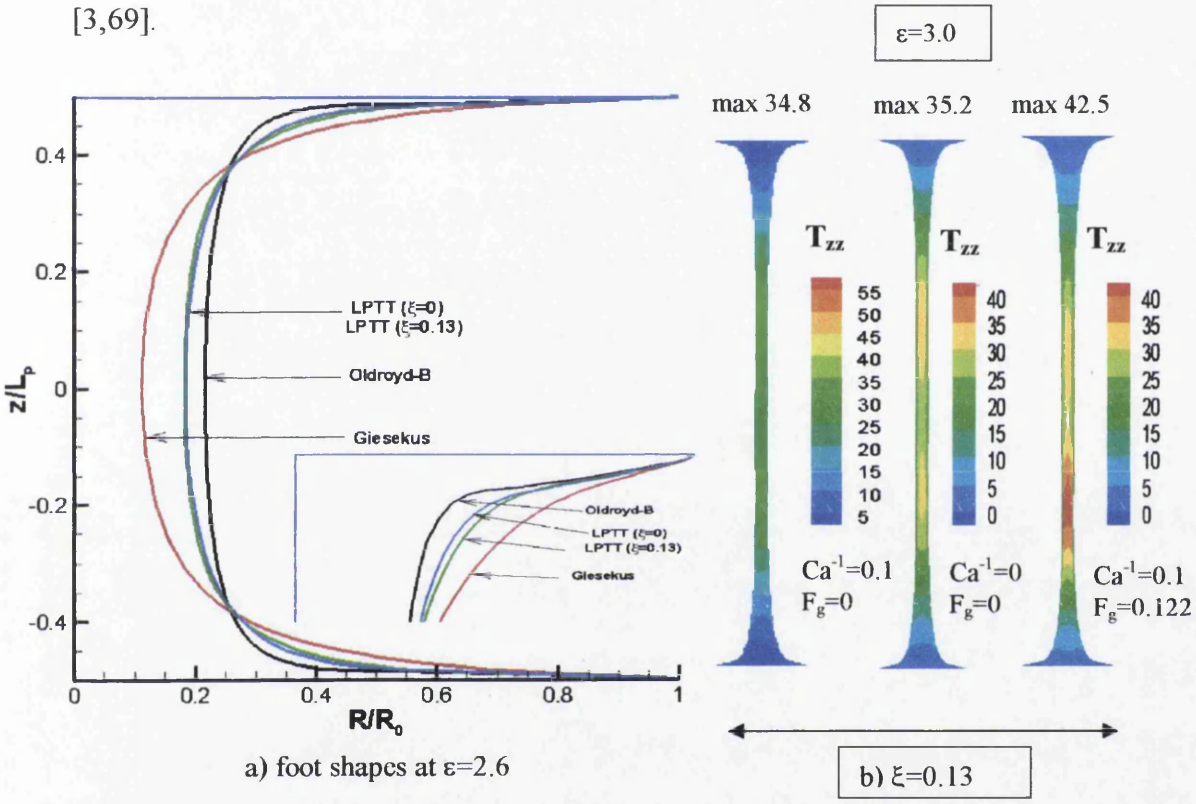

Fig 6.4: Axial stress and foot shapes; single-mode: a) foot shapes, various models, ε=2.6, Ca^{-1}=0, F_g=0; b) τ_{zz} LPTT (ξ=0.13), ε=3.0, [Ca^{-1}=0.1, F_g=0], [Ca^{-1}=0, F_g=0] [Ca^{-1}=0.1, F_g=0.122]

Present results indicate that in the presence of the ξ-parameter within the LPTT model, non-symmetrical stress patterns at high Hencky-strains (ε>3 units) may be generated, under certain circumstances. This position is examined by cross-checking results for $\varepsilon \geq 3$ units with LPTT (ξ=0) and Giesekus(α=0.32) in Fig. 6.3a,b. It is observed that the LPTT (ξ=0) model yields similar solution trends to its Giesekus counterpart, yet noting the distinct departure in the levels of stress maxima extracted. Just long slender cylindrical filaments develop, with no bead-like structures or asymmetrical features present. From this, two observations may

be made. First, since the Giesekus(α=0.32) model supports a non-zero second-normal stress difference to similar order as LPTT(ξ=0.13), see Ref.[26], this cannot be identified as a main cause of asymmetry. Second, neither can the upper-convected stress derivative terms, as all solutions possess these terms. Quantitative data in Fig. 6.3a indicate that the Giesekus model attains a critical Hencky-strain of ε_{crit}=4.0 units, with τ_{zz}-maxima on the central-plane of {11.9, 13.2, 12} units at ε of {3.0, 3.2, 4.0}. In contrast, the LPTT(ξ=0) model (Fig. 6.3b) achieves ε_{crit}=4.4 units, with τ_{zz}-maxima of 81 units at ε=4 units, compared to some 12 units for the Giesekus model. This is a substantial demonstration of the increased strain-hardening supported by the LPTT model. In Fig. 6.4b and for LPTT (ξ=0.13), three solutions at the fixed Hencky-strain of ε=3 units are contrasted. Both inclusion and exclusion of surface tension and body forces are covered through various options. The onset of symmetry breaking through the τ_{zz} fields and splitting of the stress-maxima is illustrated for the solution with body force.

6.3.1.3 Strain-hardening effects: Giesekus model ($0\leq\alpha\leq1$)

To study the strain-hardening behaviour of the Giesekus model (see stress field contours of Fig. 6.5), the mobility factor is adjusted throughout an appropriate range. The Oldroyd-B model is recovered when this factor vanishes, which represents the limiting situation in maximum strain-hardening under Giesekus modelling. By increasing the mobility factor, in contrast, the model reduces its level of strain-hardening and one expects less axial stress development. Thus, the problem becomes more tractable to numerical solution. According to Larson [26], the solution loses physical meaning beyond the limit of α of unity. The corresponding critical Hencky-strain declines as α decreases: so, ε_{crit} is {2.69, 4.20, 4.40, 4.80} for α of {0.0, 0.32, 0.5, 1.0}. Across the range $0.0\leq\alpha\leq1$, there is a consistent rising trend in critical Hencky-strain. As demonstrated in Fig. 6.5a-d shear stress is dominant near the region of the moving-plates (filament foot zone),

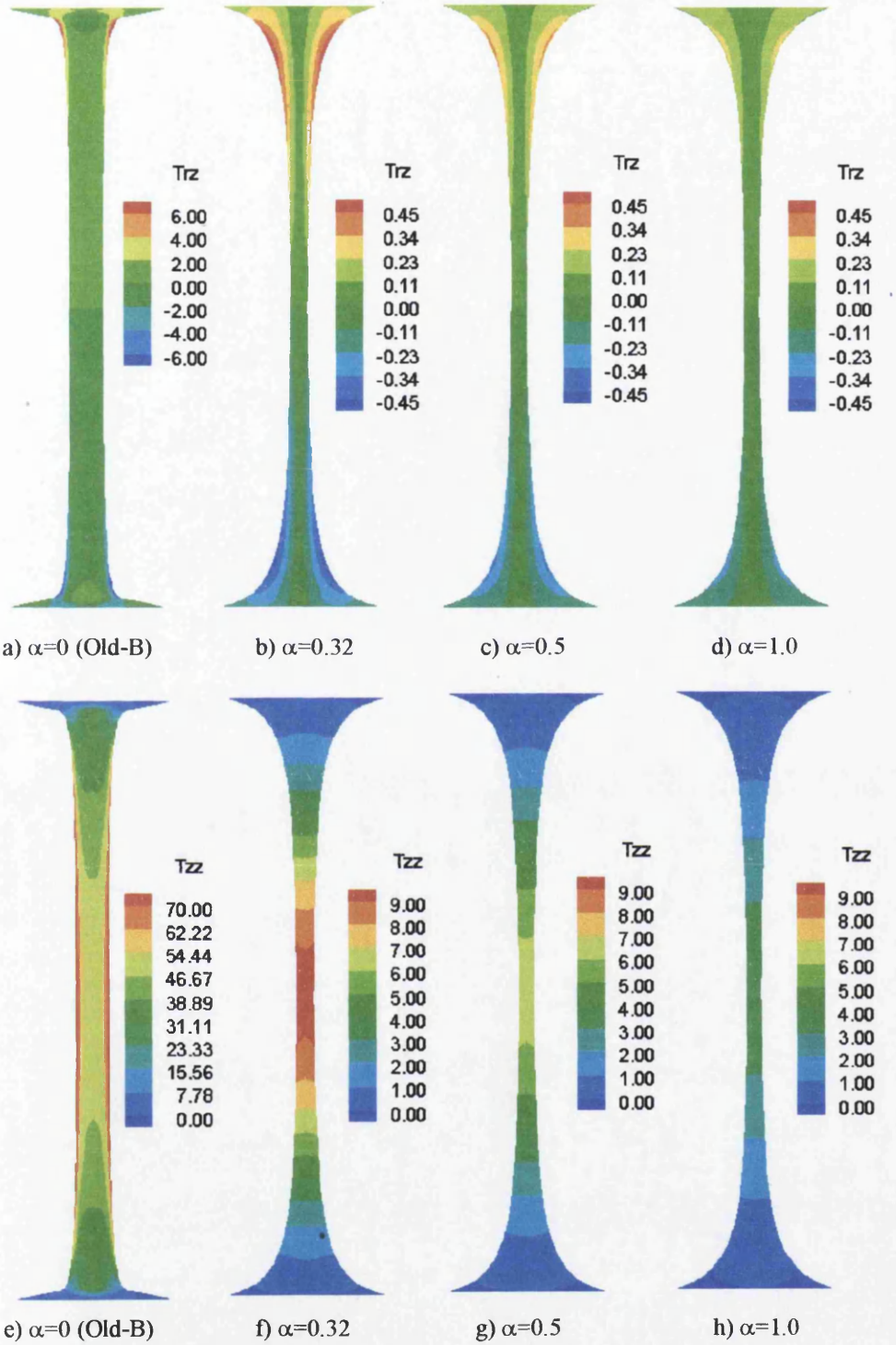

a) α=0 (Old-B) b) α=0.32 c) α=0.5 d) α=1.0

e) α=0 (Old-B) f) α=0.32 g) α=0.5 h) α=1.0

Fig 6.5: Shear and axial stress contours at ε=2.6, α-variation, Giesekus single-mode: τ_{rz} (a-d); a) α=0, b) α=0.32, c) α=0.5, d) α=1.0; τ_{zz} (e-h); e) α=0, f) α=0.32, g) α=0.5, h) α=1.0; Ca^{-1}=0, F_g=0

at the common Hencky-strain of ε=2.6, and as the mobility factor α declines this shearing influence increases. In terms of axial stress, greater extension is dominant in the filament mid-section, yet this also falls with rise in α. At ε=2.6 in each instance of α, quantitative data on shear/axial-stress maxima of Table 6.2 reveal magnitudes of: (8.11;80.0), (0.51;9.77), (0.37;6.69) and (0.28;3.65) at α=0.0, 0.32, 0.50 and 1.0, respectively. As $\alpha \rightarrow 0$ and shear stress intensifies locally in the neck of the filament foot, the foot gets pinched, whilst the filament mid-section becomes thickened. Contrary to the situation with increasing α ($\alpha \rightarrow 1$), lesser extension experienced at the filament mid-plane causes greater thinning in filament mid-plane radius (exaggerated filament thinning – see Fig. 6.5e-h). So, as V_r rises in absolute value and reaches its minima close to the plates, the fluid there becomes further pinched, being drawn more towards the centre of the plates. This is explained through changes in V_r^{min}, with $-0.28 \leq V_r^{min} \leq -0.23$ for $0.0 \leq \alpha \leq 1.0$ (see Table 6.2).

α	ε_{crit}	τ_{rz}^{max} (ε=2.6)	τ_{zz}^{max} (ε=2.6)	V_r^{min} (ε=2.6)
0.0	2.69	8.11	80.0	-0.28
0.32	4.20	0.51	9.77	-0.26
0.5	4.40	0.37	6.69	-0.25
1.0	4.80	0.28	3.65	-0.23

Table 6.2: Variation of mobility factor (α)

6.3.2 Exponential- vs linear-stretching: Oldroyd-B

This section is intended to compare and contrast predictions for Oldroyd-B fluids under the linear-stretching mode against those for the corresponding, exponential configuration, whilst adopting similar discrete approximations. The advantage of exponential-stretching is that the stretch-rate remains constant and this is helpful in the direct study of such physical properties as Trouton ratio and extensional viscosity [38]. From a computational point of view, the benefit of linear-stretching, with variable stretch-rates but constant plate-retraction rate, is that longer filament lengths and stretch times may be computed. In addition, this has some impact on temporal adjustment of minimum-maximum element aspect-

ratios. Comparison between these two stretching configurations is taken at equivalent lengths (equal Hencky-strain levels) to analyse axial stress, normal force, Trouton ratio and radial velocity.

To provide some validation for Oldroyd solutions, the exponential-stretching polymeric stress solution is plotted in Fig. 6.6. This is performed at the centre of the liquid bridge against various theoretical solutions under increasing strain measures.

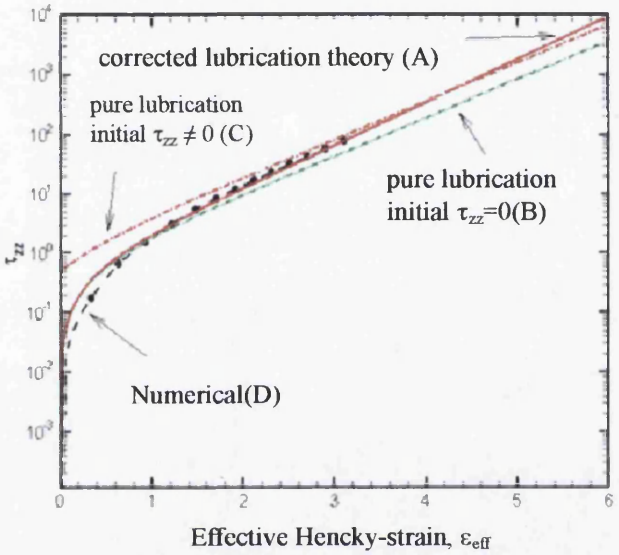

Fig. 6.6a) Exponential stretching, axial stress vs effective Hencky-strain at (r=0, z=0): Oldroyd-B, Ca^{-1}=0, F_g=0

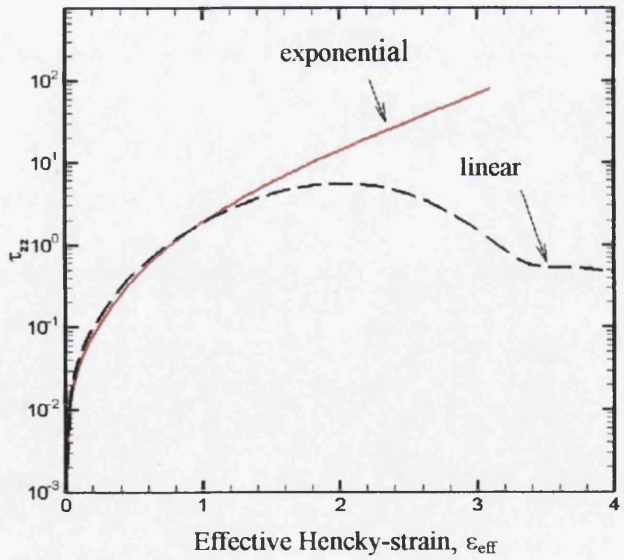

Fig. 6.6b) Exponential vs linear stretching, axial stress vs effective Hencky-strain at (r=0, z=0): Oldroyd-B, Ca^{-1}=0, F_g=0

Following the arguments of McKinley [69], we utilise the more representative effective mid-plane radial Hencky-strain measure, $\varepsilon_{eff} = 2\ln[\frac{R_0}{R_{mid}(\varepsilon)}]$, (see on to multi-mode Giesekus solutions). Such Oldroyd solutions are in close agreement over a broad range of strains with the corrected lubrication theory solution (A) of the form,

$$\tau_{zz} = \frac{3\mu_p \dot{\varepsilon}_0 \lambda_1^{-1}}{3\dot{\varepsilon}_0 - \lambda_1^{-1}} \left\{ exp[(3\dot{\varepsilon}_0 - \lambda_1^{-1})*t] - 1 \right\}.$$

This theory takes account of simultaneous plate-retraction (origin at filament centre), no-slip end-plates conditions, but not free-surface influence. Large strain behaviour (above 3 units) adopts an exponentially rising form (linear in log-plot of gradient $(3\dot{\varepsilon}_0 - \lambda_1^{-1})$). The two ideal lubrication theory solutions of McKinley et al. [39,69], offer upper and lower bounds for the mid-to-large strain numerical data (1-3 units). These two forms of theoretical solution cover: the circumstances of diminishing initial filament stress (B) on the one hand (matching low strain numerical data (O(1)) and lying below the large strain numerical data (O(3)); and alternatively, an assumed prescribed level of initial residual filament stress (C) (in particular, lying above the large strain numerical data). At the larger strain levels above unity, taking into account no-slip end-plate correction has brought prediction better into line against the theory. Slight departure from the theory below this level may be associated with the non-homogeneity of the kinematics, both spatially and temporally. This is further pronounced at early Hencky-strains below unity where free-surface curvature and its influence on the filament centre are larger. In fact, for Oldroyd data, the filament adopts extended thin cylindrical shape at higher levels of strain beyond O(1) (see Fig. 6.10). This position more closely reflects pure lubrication theory.

In contrast, one may also compare Oldroyd solutions in axial stress under both stretching configurations. Here, it is observed that the stress solution for the linear stretching mode increases more sharply than for its exponential counterpart up to a

strain measure of 1.0 unit, at which they intersect with the linear case going through a maximum at 2 units. Beyond this strain level, the linear-mode stress gradually declines whilst the exponential-form continues to rise. The eventual decline in stress is to be anticipated due to the dynamic decrease in stretch-rate, see Fig. 6.6b.

	ε =0.2	ε=1.0	ε =1.8	ε =2.6
exponential →	(a)	(b)	(c)	(d)
linear →	(e)	(f)	(g)	(h)

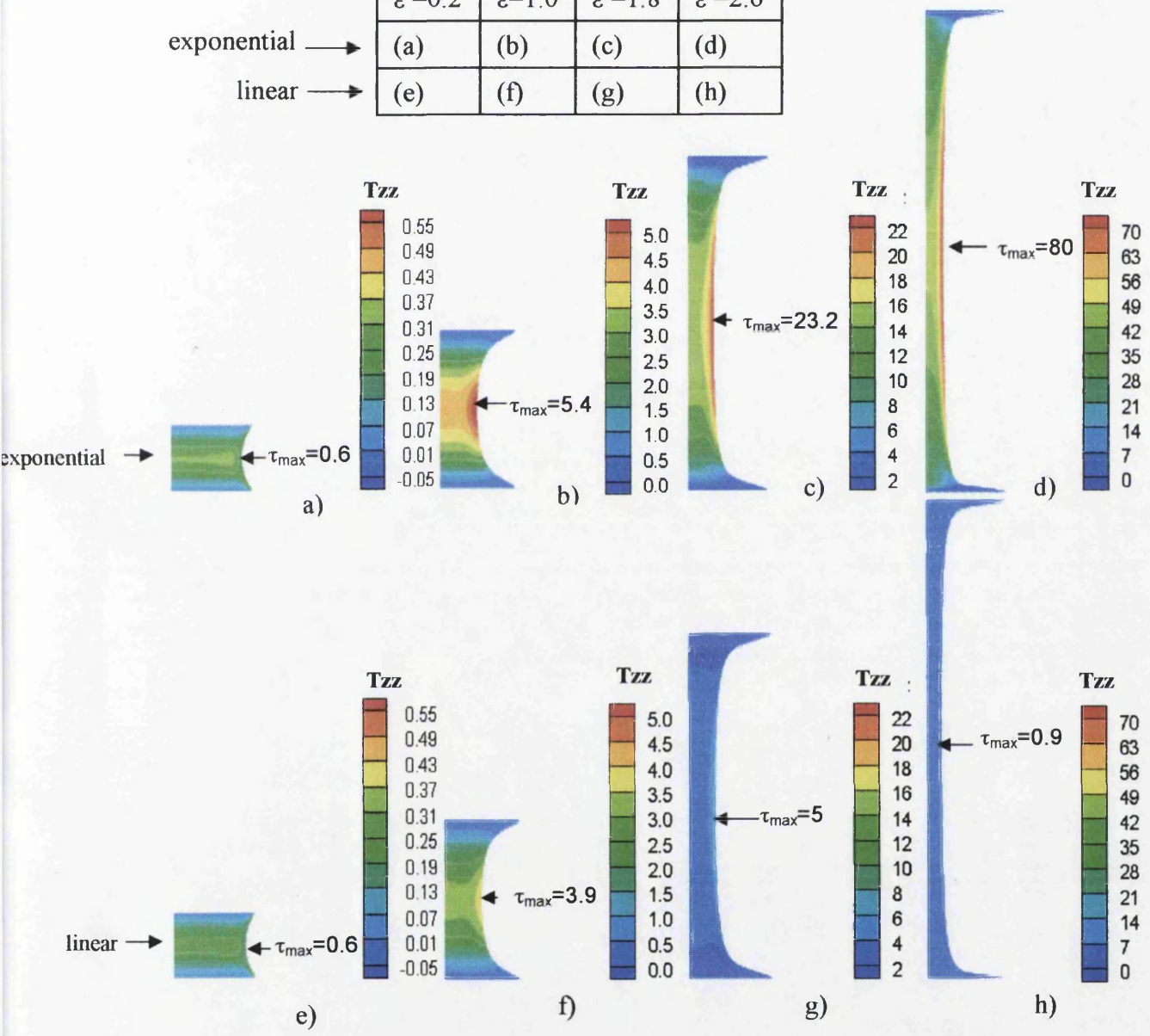

Fig 6.7: Exponential vs linear stretching, axial stress, τ_{zz} at equivalent Hencky-strains: Oldroyd-B, $Ca^{-1}=0$, $F_g=0$

6.3.2.1 Comparison at equitable lengths (equivalent Hencky-strains)

A number of solution features are plotted to perform comparison across the stretching modes at equivalent lengths. The development of extra-stress under both stretching modes is shown in Fig. 6.7 through contour field plots. Under exponential-stretching motion, extra-stress mid-plane maxima rise continually from ε=0.2 to ε=2.6 units. Whilst under linear-stretching mode, τ_{zz} demonstrates an increasing trend up to ε=1.8 units; it declines thereafter, so that τ_{zz} at ε=2.6 closely approximates its value at ε=0.2 units. The discrepancy between solutions under linear and exponential modes broadens as stretching advances. At ε=0.2 units, there are barely any differences in τ_{zz}; yet at ε=2.6 units, exponential-stretching predictions are O (10^2) times greater than their counterparts under the linear-mode. As noted above, since stretch-rate is declining under the linear-stretching motion, this causes the decrease in stress. Such disparity in stress development between the two contexts permits the longer period of stretching under the linear-case.

The development of Trouton ratio (Tr) versus Hencky-strain is illustrated in Fig. 6.8a, where the trend is one of monotonic rise under exponential-stretching mode. Under linear-stretching, Trouton ratio barely increases above the Newtonian level of three. There is miniscule rise up to $\varepsilon\approx$1.5 units (to a level of 4.6), with decline thereafter for $\varepsilon\geq$3.0 units, to a vanishing limit. Normal force on the moving-plates (F_z of Fig. 6.8b) declines initially up to $\varepsilon\approx$1.0 under exponential-stretching and subsequently rises in exponential fashion. The trend in normal force under linear-stretching is one of monotonic decay, lying consistently below values for exponential-stretching at equivalent Hencky-strains. These trends, along with those in R_{mid} (ε) of Fig. 6.8c discussed below, indicate the relative domination of F_z and R_{mid} upon Tr, over the early Hencky-strain period (ε>1), and subsequently beyond. There is slight variation in Tr between the stretching modes up to Hencky-strain measures of O(1). Only beyond this phase, does the normal force commence to dominate under exponential-stretching. Trouton ratio may also be determined by sampling the predicted solution at the filament centre through the expression, $Tr=(T_{zz}-T_{rr})/(\mu_0 * d_{zz})= N_1/(\mu_0 * d_{zz})$. The localised deformation-rate (d_{zz}) may be estimated from the initial stretch-rate ($\dot{\varepsilon}_0$) in three alternative forms: as in ideal

lubrication theory without end-plate correction *(estimate1);* or, as $(1.5\dot{\varepsilon}_0)$ with end-plate correction *(estimate2;*, or, directly from the locally predicted kinematics *(estimate3).* Such calculations have been performed under exponential retraction to find that the "force-on-the-plate" estimate is located between the two lubrication approximations with closer proximity to estimate 2. Typical values at ε=2.5 units are {*estimate1, plate-estimate, estimate2*}={70.68, 54.0, 46.64}, see Fig. 6.8a.

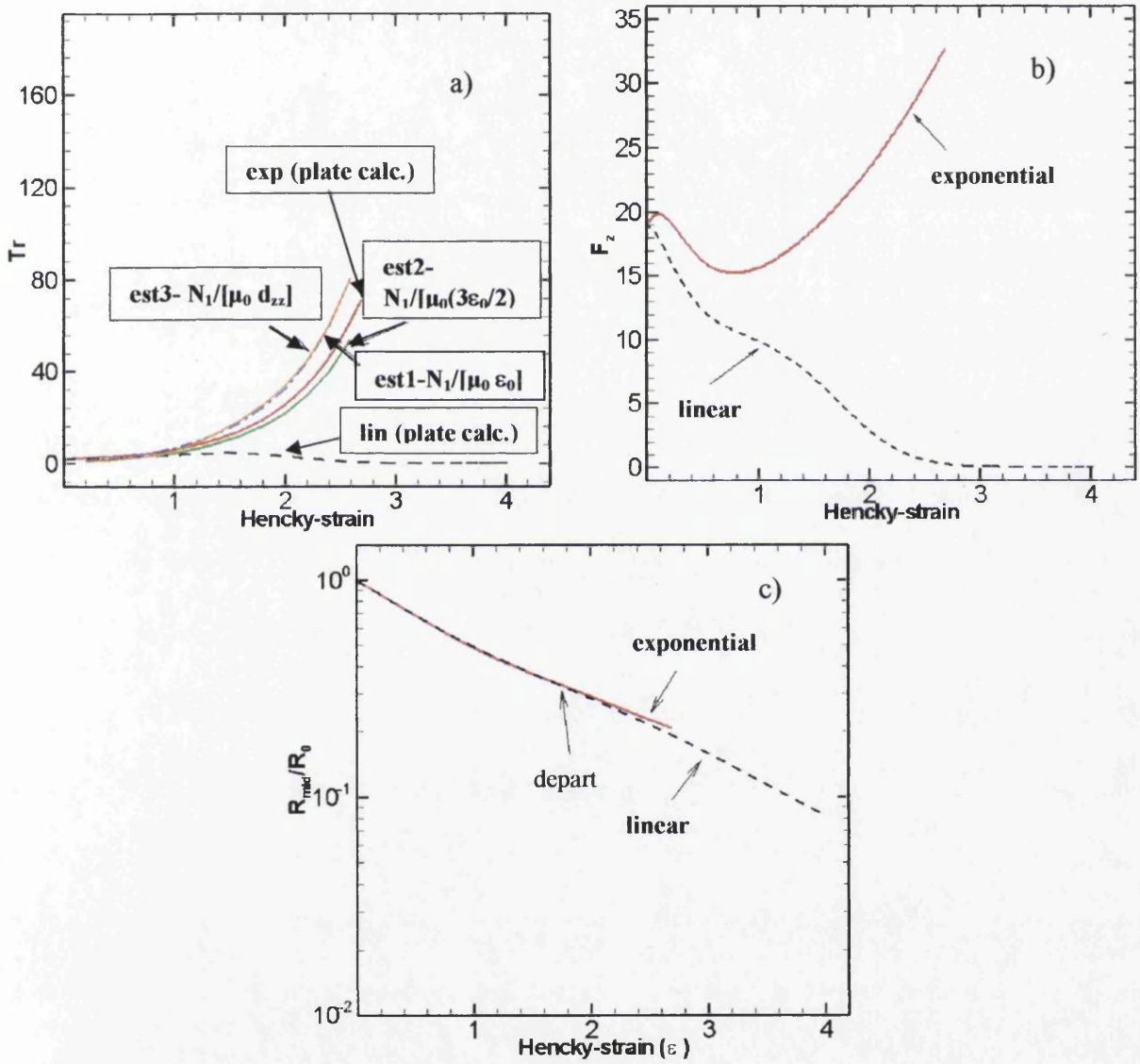

Fig 6.8: Solution variation vs Hencky-strain; (a) Trouton ratio (Tr), b) normal force, F_z on moving plates, (c) mid-plane filament radius, $R_{mid}(\varepsilon)$: Oldroyd-B, $Ca^{-1}=0$, $F_g=0$

Estimate1 substantiates a 30% elevation from the *plate-estimate*, whilst *estimate2* represents a reduction of around 12%. The local predicted kinematic calculation

(estimate3) proves to line up almost identically with *estimate1*. This corroborates the overestimation of stress anticipated at the filament centre; see Yao and McKinley [39].

In Fig. 6.8c, the corresponding mid-plane radial evolution, R_{mid} (ε), is displayed as a function of Hencky-strain (ε). Numerical predictions under constant

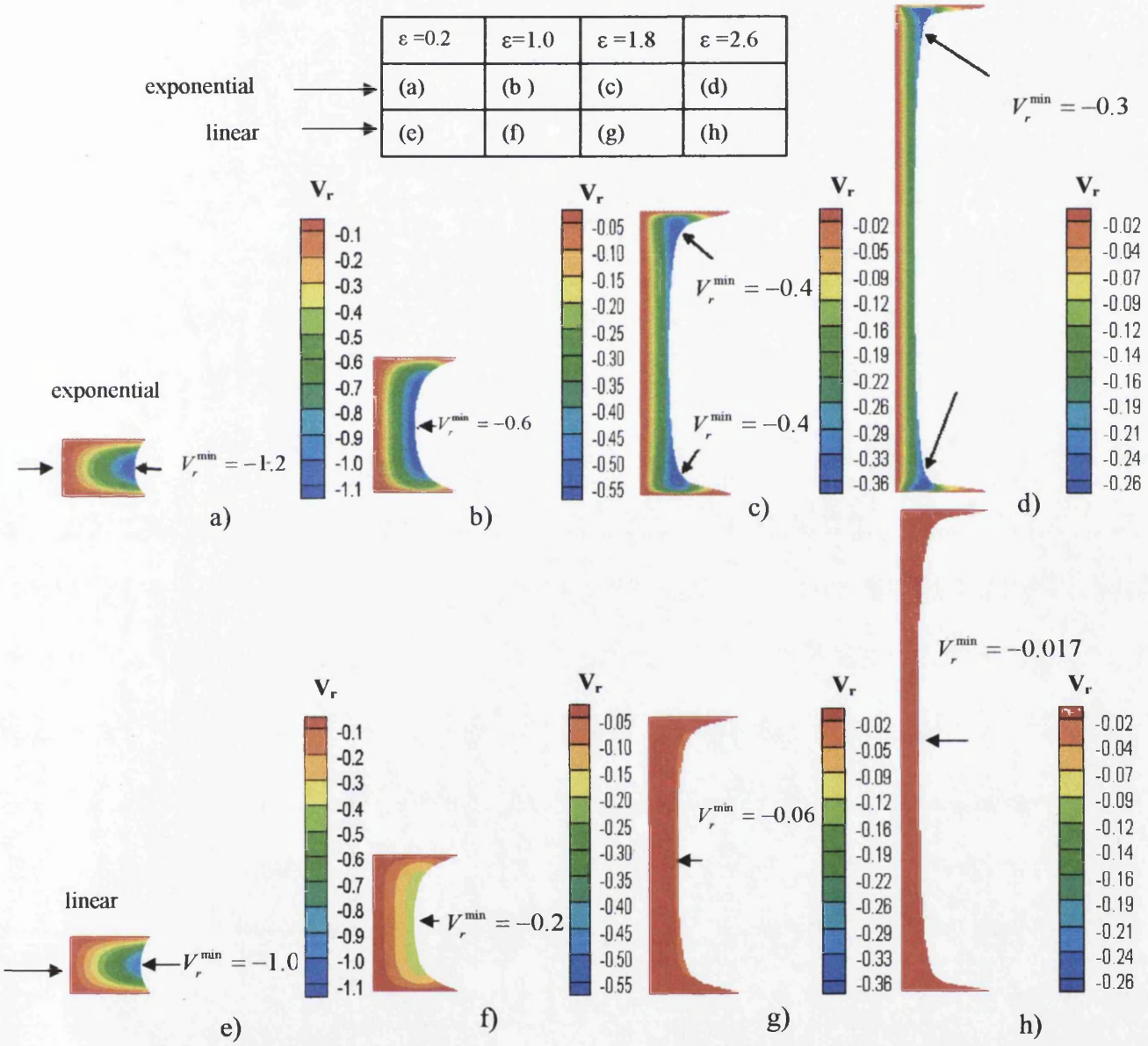

Fig 6.9: Exponential vs linear radial velocity fields, equivalent lengths (Hencky-strains): Oldroyd-B, Ca^{-1}=0, F_g=0

plate-retraction rate concur closely with those for the exponential alternative, up to Hencky-strains close to 1.6 units, around which point departure begins. So, conspicuously beyond ε>2.0 units necking is slightly greater with the constant V_z-

plate alternative. This response produces the much longer elongation times allowed under linear-stretching. For example, to reach ε=2.4 units the time for linear-stretching is t≈10 units, whilst under exponential-stretching this is only around t=2.4 units. This is slightly greater than a four-fold difference, which well compensates for the radial velocity adjustment that is typically three-times larger under exponential-stretching. For direct comparison, velocity field data are shown in Fig. 6.9 under both stretching-modes in question.

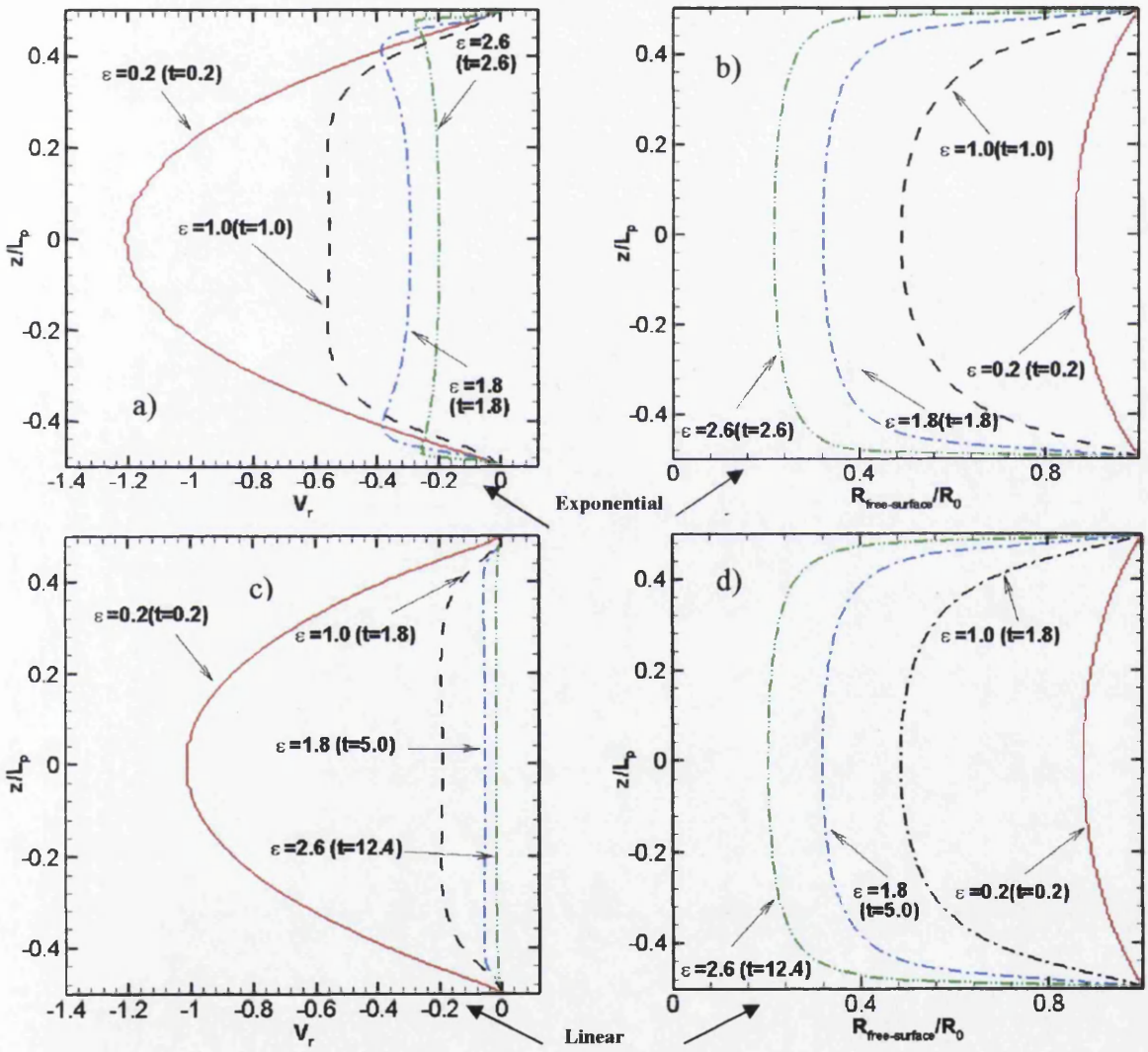

Fig 6.10: Free-surface radial velocity distribution and surface profiles; ε= [0.2, 1.0, 1.8, 2.6]; (a,b) exponential stretching, (c,d) linear stretching: Oldroyd-B, Ca^{-1}=0 F_g=0

To appreciate the position, free-surface profiles and velocity distributions are presented comparatively in Fig. 6.10 at sampled Hencky-strain levels. At the equivalent Hencky-strain of ε=1.8 units (see Fig. 6.10a,c), linear-stretching mode

radial velocity minima at the mid-plane prove substantially lower than those under exponential-stretching. We note the tendency to retard the migration of radial velocity minima towards the plate-region in the linear-stretching case over its exponential counterpart. Even at the greater Hencky-strain of ε=2.6 units, plate-zone values have not exceeded those at the centre under linear-stretching, whilst this has obviously occurred under exponential retraction. Notwithstanding such disparity in radial velocity at high levels of strain, free-surface profiles of Fig. 6.10b,d exhibit close correspondence between the two stretching modes, from low (0.2 units) to high (2.6 units) strain measures. This is indicated in the temporal variation of radii at different locations along the filament. The low strain position is not unanticipated (ε<1.0 units), where close agreement is observed in radial velocity profiles. At greater levels of strain (ε>2.0 units), this finding is in agreement with the observations of McKinley et al. [68]. Such Oldroyd-B fluid filaments tend to adopt long slender cylindrical form under ideal uniaxial extensional flow (everywhere but close to the plates), reflecting a progressively growing parity between axial and radial Hencky-strain measures. On this basis, similar radial thickness would be expected, and thus, accounts for the resemblance in surface profiles between exponential and linear-stretching modes over greater regimes of strain.

6.3.3 Multi-mode results: exponential-stretching

Here, in multi-mode representation for Giesekus and LPTT models only the exponential-stretching configuration is considered with a three-mode representation for each model. The relevant selected parameter values of (α_i, ε^i_{ptt} and ξ_i) are tabulated in Table 6.1 for each model, and as proposed in Li et al. [2], (ε^i_{ptt} and ξ_i) are held constant across the various modes. First, theoretical comparison and mesh refinement are considered with restriction to a single model of the Giesekus model. The refinement analysis is constrained to a moderate Hencky-strain measure of ε=1.8 units and is performed both axially and radially. Three meshes (100x20, 150x20 and 200x20) cover axial refinement (z-axis), and two meshes (150x20 and 150x15) cover the radial refinement (r-axis). Once consistency has been confirmed, the rheological consequence is considered of the multiple relaxation times

involved, where comparison is made to the literature to corroborate findings. In particular, the influence of shorter modes is explored, in contrast to solutions based on a single mode (the longest).

6.3.3.1 Comparison against theory for Giesekus model

In Yao and McKinley [39], theoretical solutions are reported for both *ideal flow kinematics in uniaxial elongational flow* (ignoring end-plate effects), and *corrected lubrication theory* assuming no-slip of the end-plates. Here and for the

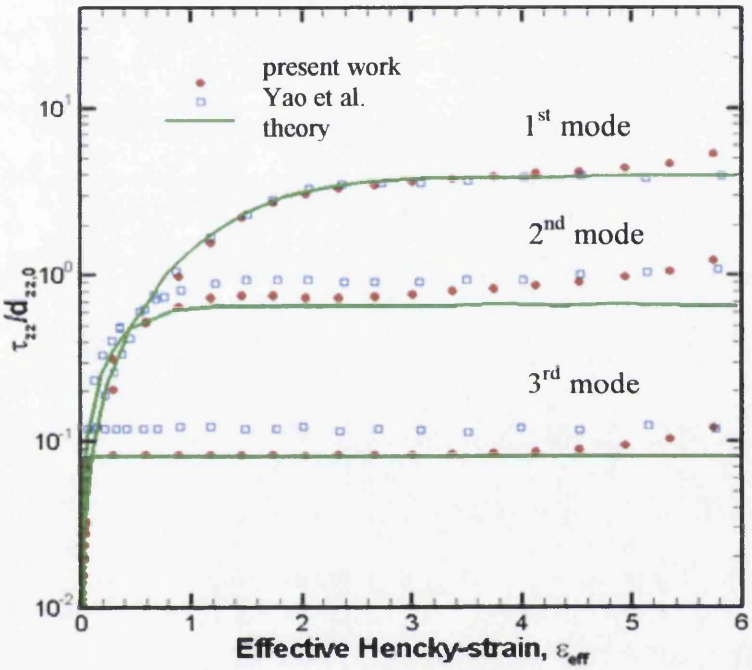

Fig 6.11: Stress development, ($\tau_{zz}/d_{zz},0$), at (r=0,z=0); multi-mode Giesekus $Ca^{-1}=0$, $F_g=0$

purposes of direct validation, we refer to the form taken up in Yao et al. [3], that of ideal flow kinematics in uniaxial elongational flow and provide comparison of our predicted data against their theoretical and predicted stress evolution data in Fig. 6.11. Such data correspond to the time history for the axial component of the polymeric stress per mode with the same Giesekus fluid, sampled at the centre of the liquid-bridge (r=0, z=0). As stated in Yao et al. [3], the closer agreement to lubrication theory is attained by interpreting data against the effective Hencky-strain measure (ε_{eff}, determined radially at mid-plane [14,39]) and with stress-

scaling consistent with the strain-rate at the liquid-bridge centre (to overcome any non-homogeneity). Beyond the early Hencky-strains (unitary), differences and similarities are discernable, yet broadly, strong correlation may be gathered. The largest (first mode) results tend to correspond rather closely with the theory to ≈ 5 strain units (around 4.6); on the second largest mode, our data lie consistently closer to the theory than that of Yao et al., as far as 5 strain units (with slight departure ≈ 6 units). The same comment applies on the smallest (third) mode data, but with close approximation to the theory from low Hencky-strains up to 4 strain units, where departure begins.

6.3.3.2 Time-discretisation for Giesekus model

Robust numerical procedures are required to discretise the constitutive equations of the relevant viscoelastic models to analyse transient behaviour in the multi-mode context. One may apply either the explicit stress time-discretisation developed earlier (see Ref. [31]), or invoke the alternative semi-implicit approach to meet both requirements of smaller time-steps, and concurrently, the occurrence of low and high relaxation times (two-three orders variation). With the semi-implicit scheme, a product factor ($2De_i+\Delta t$) is provided. This factor has dependency upon both the time-step (Δt) and the Deborah number (De_i), emerging from a Crank-Nicolson time-splitting stencil for the τ-term. This accommodates the $De_i \rightarrow 0$ context, under the scenario of larger non-trivial De_i-values. In this manner, solution for the multi-mode Giesekus model is sought, utilising a single mesh for convenience, mesh (150x15), at ε=2 units with conventional explicit and semi-implicit procedures. The corresponding axial stress (τ_{zz}) and velocity (V_z) contour plots are displayed in Fig. 6.12a,b. Close agreement is established between the two solutions generated in both components throughout the whole field (graphically no disparity).

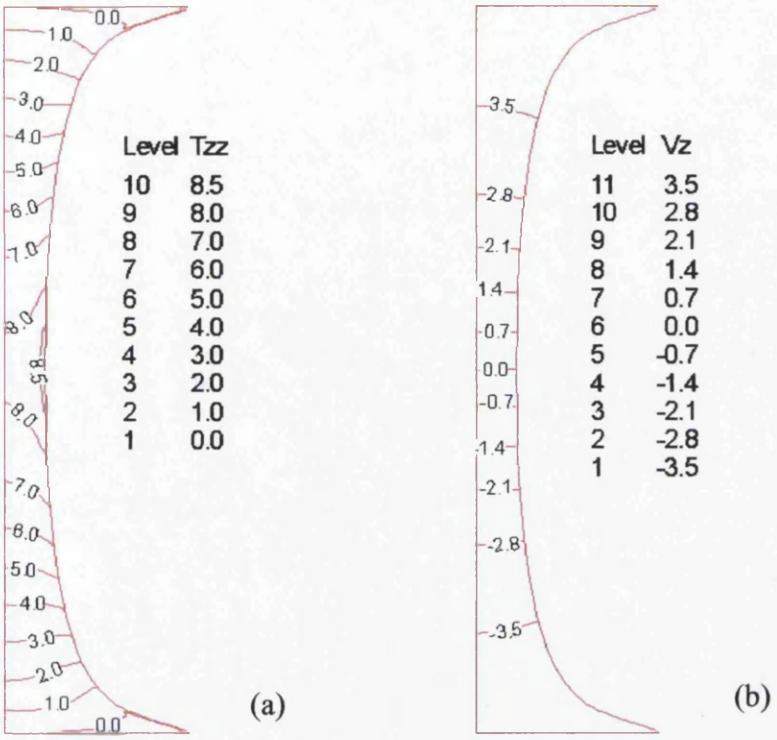

Fig 6.12 a,b): Semi-implicit and explicit time-stepping solutions; multi-mode Giesekus, $Ca^{-1}=0$, $F_g=0$, $\varepsilon=2.0$; b) τ_{zz}, c)V_z

6.3.3.3 Mesh refinement for Giesekus model

Axial refinement is demonstrated through stress field contour plots of τ_{zz}, at $\varepsilon=1.8$ units in Fig. 6.13a. These data reflect complete agreement between the solutions on the three axially refined meshes (100x20{solid}, 150x20{dashed} and 200x20{dashdot}). The contours are exhibited from 0.0 to 8.0, in steps of 0.5 units. As in the single-mode case, the axial stress reaches its maxima at the filament mid-plane region consistently across all meshes, spreading and reducing in magnitude towards the plates. In Fig. 6.13b, V_z contour data are plotted from -3.0 to +3.0 units in steps of 0.5 units. Again, the axial velocity is visibly overlapping across the three meshes, with evident symmetry around the filament mid-plane (vanishing there) with maxima (absolute value) located towards the moving-plates. Likewise, agreement in profiles may be gathered from Fig. 6.15c,e, covering (τ_{zz} and V_z) along the filament centreline.

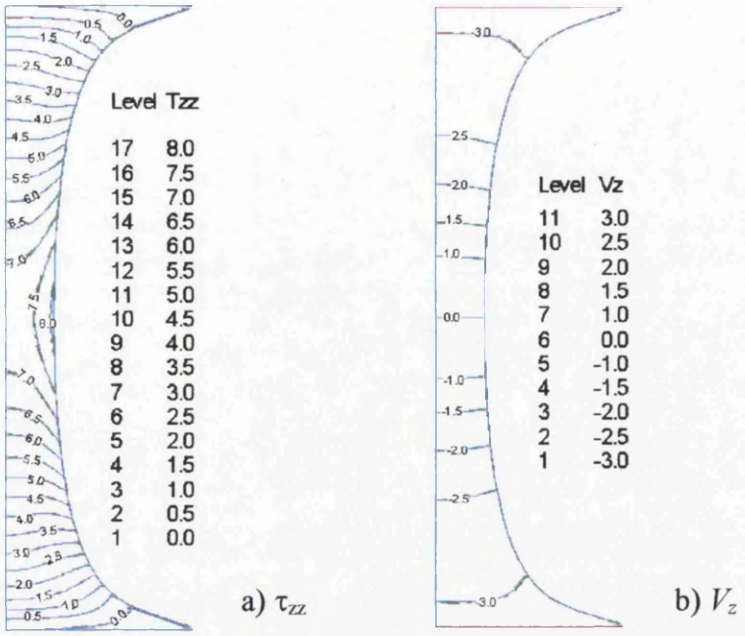

Fig 6.13: Axial refinement, multi-mode Giesekus; $Ca^{-1}=0$, $F_g=0$, $\varepsilon=1.8$; meshes 200x20 [solid], 150x20 [dashed] and 100x20[dashdot]: a) τ_{zz}, b) V_z

Radial refinement is considered at $\varepsilon=1.8$ units, in both (τ_{zz}) (Fig. 6.14a) and (V_z) contour plots (Fig. 6.14b). Again, graphically identical results are provided across the two meshes in question (150x20 and 150x15). Concentrating on the filament mid-plane region radial-axis, profiles of (τ_{rr}) and (τ_{zz}) are plotted in Fig. 6.14c,d. The overall pattern in (τ_{zz}) reflects a constant form across the filament mid-plane, with a slight rise near the free-surface. In this dominant stress component, solutions across the meshes are practically identical along the filament width (r-axis), a position repeated in the much smaller (τ_{rr})-component. The measure of the boundary layer near the free-surface stands for some five percent of the mid-plane radial span. The perturbation in (τ_{rr}) approaching the free-surface, is a signature of transition over the boundary layer, an aspect also observed in ($\partial v_r/\partial r$).

Lastly, comparison with refinement is conducted in both coordinate directions, axially and radially (data for four meshes). Radial and axial stress component profiles along the radial-axis at the filament mid-plane are plotted in Fig. 6.15b,d. Barely any disparity is detected between the different solutions, and in particular, the τ_{rr}-component displays independence of axial refinement with regard to the

free-surface boundary layer. In the same way, both stress component solutions agree under refinement when plotted along the filament centreline axis, Fig. 6.15a,c. Hence, satisfactory consistency has been established, leading to the adoption of the (100x20)-mesh in the analysis of rheological variations across the alternative models selected.

6.3.3.4 Giesekus versus LPTT (ξ=0.13 and ξ=0) comparison

In Fig. 6.16, we plot axial stress τ_{zz}-profiles for the multi-mode Giesekus model against its single-mode counterpart, along the filament centreline at different Hencky-strain levels of ε=0.2, 1.0 and 2.0 units. In this form, the difference between both single and multi-mode filament-centre solutions may be appreciated directly, a large part of which has occurred at the relatively low Hencky-strain level of ε=0.2 units. The contribution of the shorter modes to the τ_{zz}-stress is felt, in particular, through the larger value of the multi-mode solution, when compared to its single-mode counterpart. At ε=0.2 units and along the filament mid-plane where the maxima are observed, these contributions are, respectively: 0.89 units for the multi-mode case {composed of 0.3 (largest mode), 0.47 (middle mode), 0.12 (shortest mode)} and 0.3 units for the single-mode form. Similar comments apply also to the axial stress along the free-surface. Beyond ε=1.0, the τ_{zz}-largest mode contribution begins to dominate (see Fig. 6.11). From the single-mode results of Fig. 6.3, the Giesekus model exhibits symmetry in axial stress around the filament mid-plane, being preserved across all Hencky-strains up to ε_{crit}=4.0 units. The multi-mode version corroborates these findings. In Fig. 6.17, axial stress fields are depicted up to ε=4.0 units. Beyond a Hencky-strain value of ε=3.0 units, the influence of the shorter modes appears in the axial penetration of stress throughout the filament (radially uniform). Yet again, neither single nor multi-mode solutions manifest signs of bead-like formation. Under trends is axial stress-maxima across Hencky-strain levels of ε= (3.0, 3.2, 4.0), the single-mode representation yields a slight increase in the axial stress-maxima, through magnitudes of (11.9, 13.2, 12.0) units. The multi-mode representation at ε= (2.0, 3.0, 3.6, 4.0) provides axial stress-

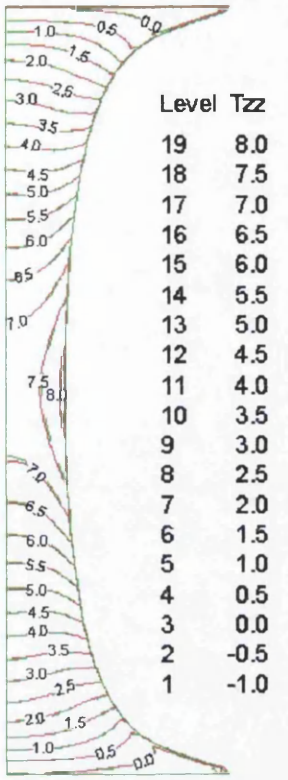

a) τ_{zz}

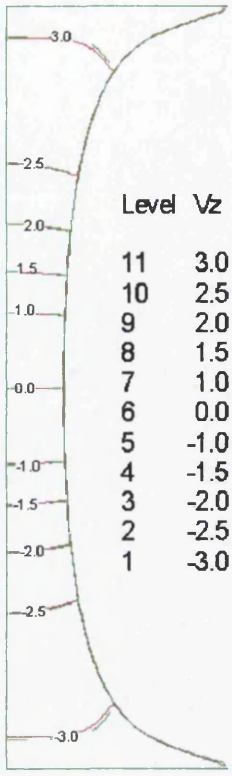

b) V_z

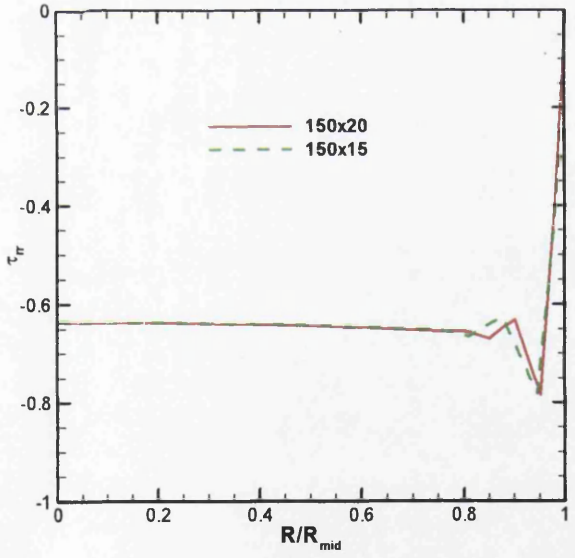

c)τ_{rr}

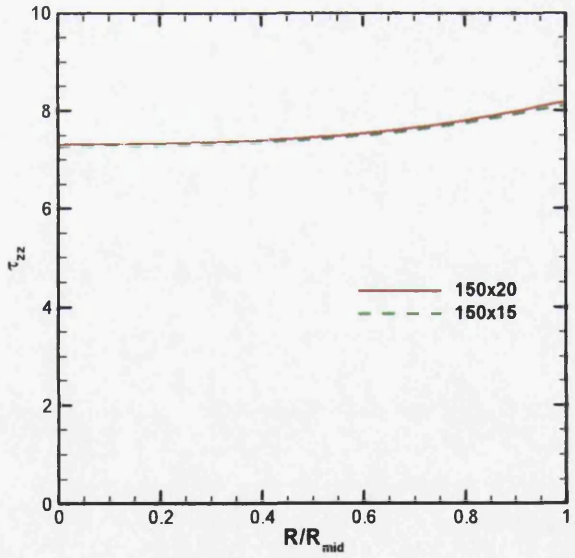

d)τ_{zz}

Fig 6.14: Radial refinement, multi-mode Giesekus; Ca^{-1}=0, F_g=0, ε=1.8; meshes 150x20 150x15: contours a) τ_{zz}, b) V_z; filament mid-plane profiles c) τ_{rr}, d) τ_{zz}

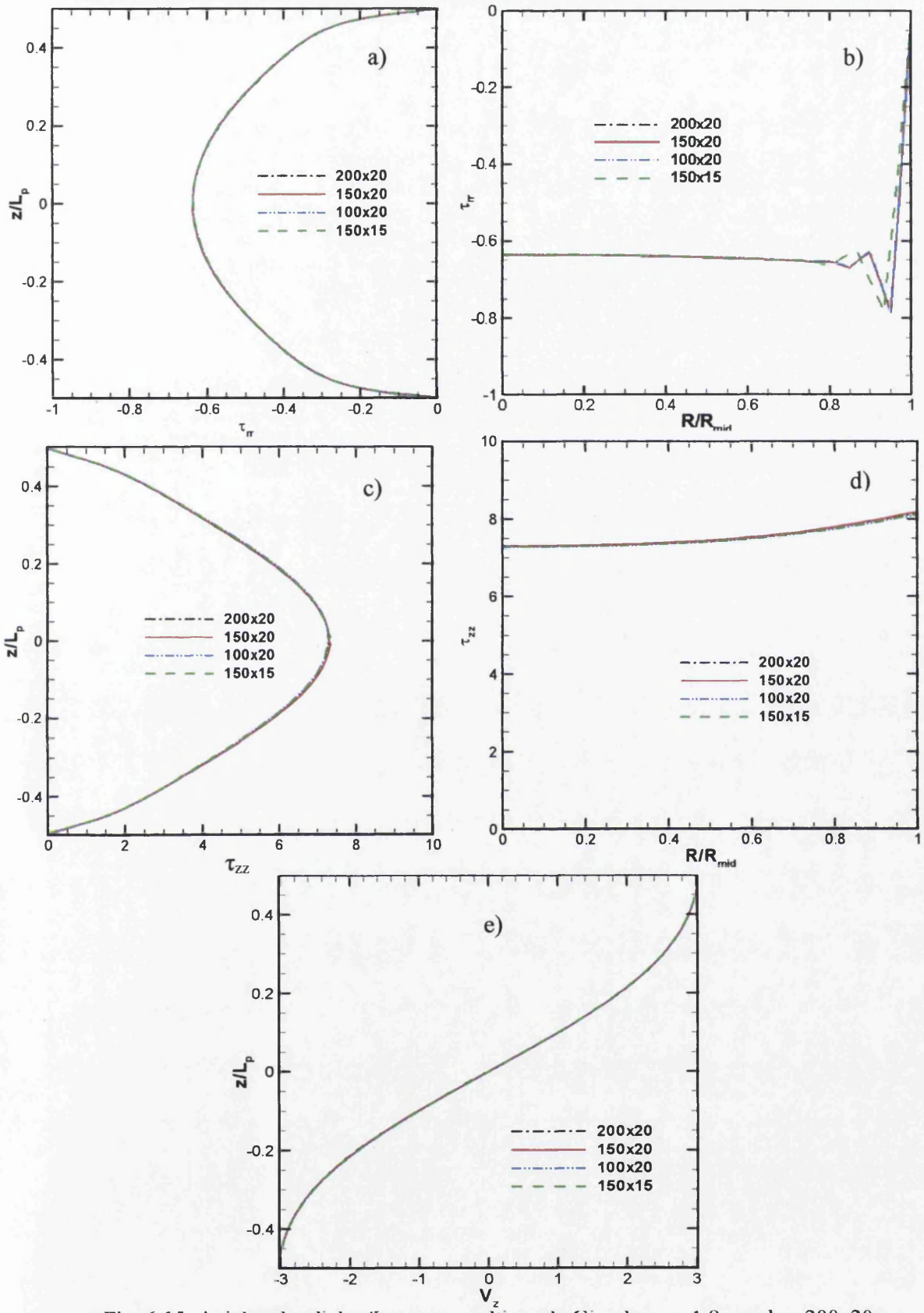

Fig 6.15: Axial and radial refinement, multi-mode Giesekus; ε=1.8; meshes 200x20, 150x20, 100x20 and 150x15; filament centreline profiles a) τ_{rr}, c) τ_{zz}, e) V_z; on mid-plane, b) τ_{rr},d) τ_{zz}; $Ca^{-1}=0$, $F_g=0$

maxima of (8.7, 12.0, 13.6, 12.0) units. This adjustment in axial stress-maxima with Hencky-strain may be interpreted as a steady limiting trend to an average plateau value of 12.5 units.

In a similar fashion to Giesekus results, symmetrical τ_{zz}-fields are also observed in the multi-mode LPTT (ξ=0) solutions. This holds true even at the high Hencky-strain level of ε=3.6 units (see Fig. 6.19 and Fig. 6.20) with the larger stresses generated in the filament over that of Giesekus solutions (see Fig. 6.17). No bead-like structure emerges for the LPTT (ξ=0) fluid. In contrast, a symmetrical bead-

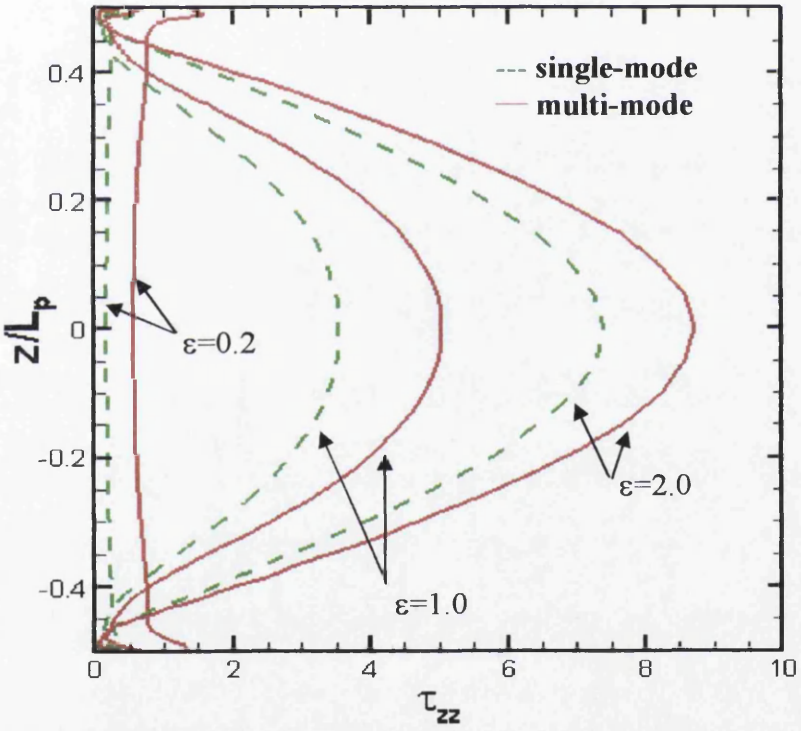

Fig 6.16: Filament centreline axial stress, τ_{zz} profiles; single and multi-mode Giesekus; increasing ε, [0.2, 1 and 2] units: --- single mode, — multi-mode; Ca^{-1}=0, Fg=0

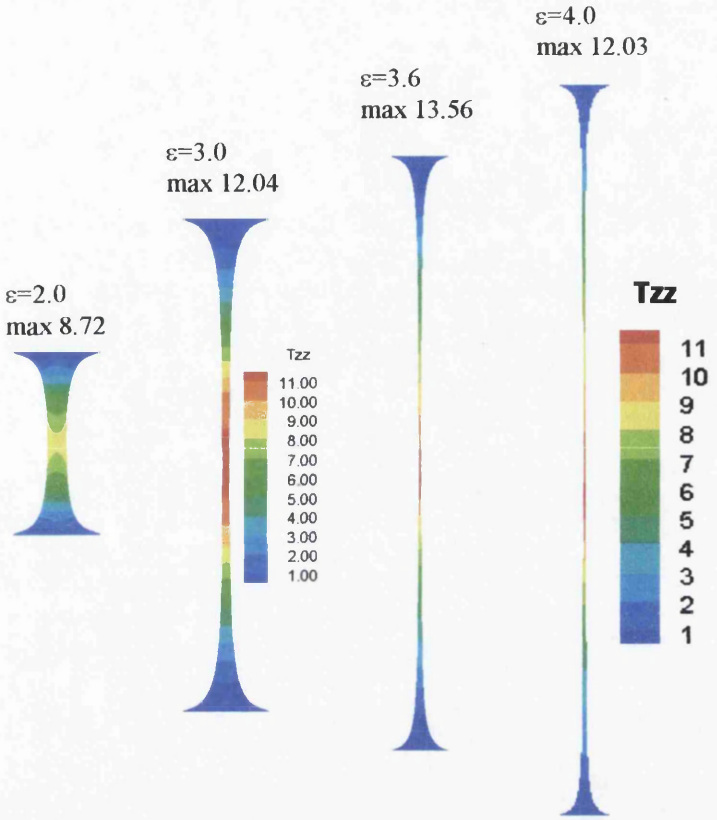

Fig 6.17: Axial stress τ_{zz}-contours; multi-mode Giesekus; increasing ε; $Ca^{-1}=0$, $F_g=0$

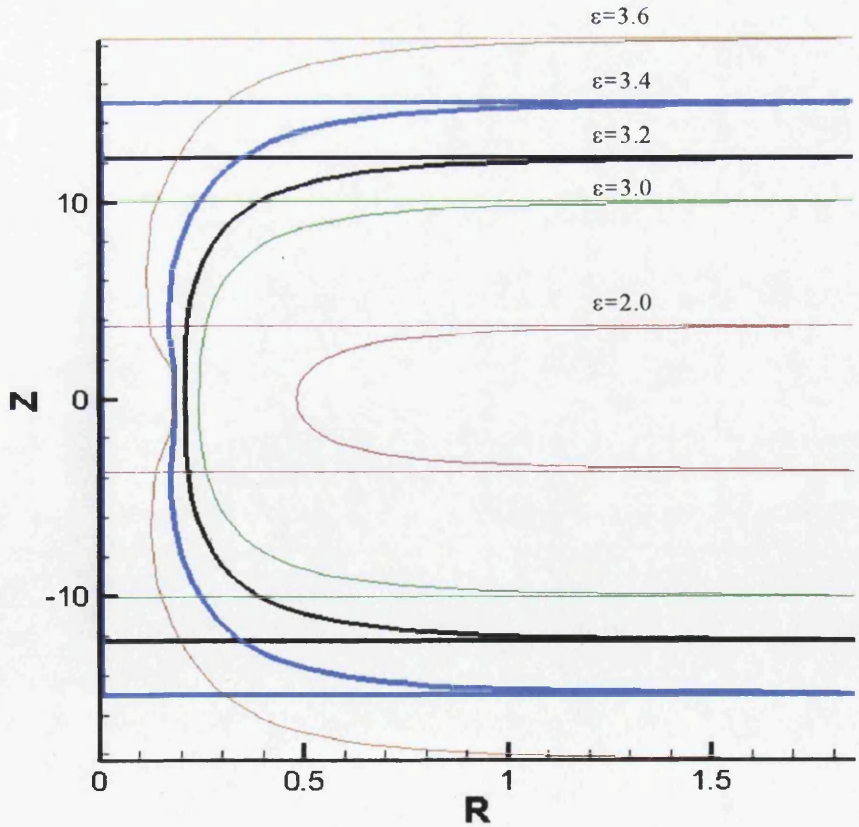

Fig 6.18: Filament shape; multi-mode LPTT(ξ=0.13); increasing ε; $Ca^{-1}=0$, $F_g=0$

structure is beginning to appear with the multi-mode LPTT (ξ=0.13) fluid for ε>3.4 units. This is absent at ε=2.6, as demonstrated through filament shapes of Fig. 6.19a, and also from Fig. 6.18 up to ε=3.4, appearing at ε=3.6 units (see also, Fig. 6.19b). For its single-mode counterpart, this bead-structure is apparent earlier at ε=3.2, the time-lag being directly attributable to the shorter modes. This is also accompanied by the splitting of stress-maxima, which generates local maxima in an off-centre position.

6.3.3.5 Comparison across relaxation-modes

In Fig. 6.20, the relative free-surface τ_{zz}-distributions across the individual modes are illustrated for LPTT (ξ=0) at ε=3.6 units. The largest mode is dominant by an order of magnitude, reaching 62.1 units when compared to 2.83 and 0.16 units for the second and third shorter modes, respectively. For $\varepsilon \geq 0.8$ units, the largest mode tends to be the main contributing factor. In contrast, at the early Hencky-strain of ε=0.2 units, the τ_{zz} is dominated by the second largest mode (see Fig. 6.11, for Giesekus model). There, maxima in τ_{zz} are equal to (0.59, 0.92 and 0.20) units, ranging from the longest to the shortest mode, respectively. In the strain range, $0.2<\varepsilon<0.8$ units, the first two modes dominate their shortest-mode counterpart and provide similar contributions.

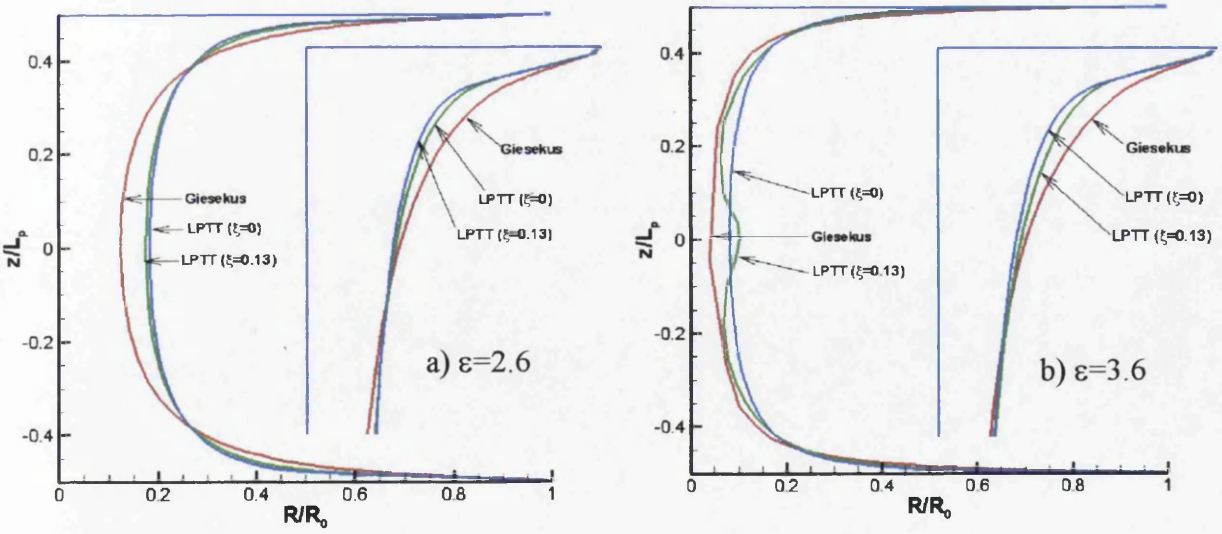

Fig 6.19: Filament free-surface and foot shape; multi-mode, various models; a) ε=2.6, b) ε=3.6; Ca^{-1}=0, F_g=0

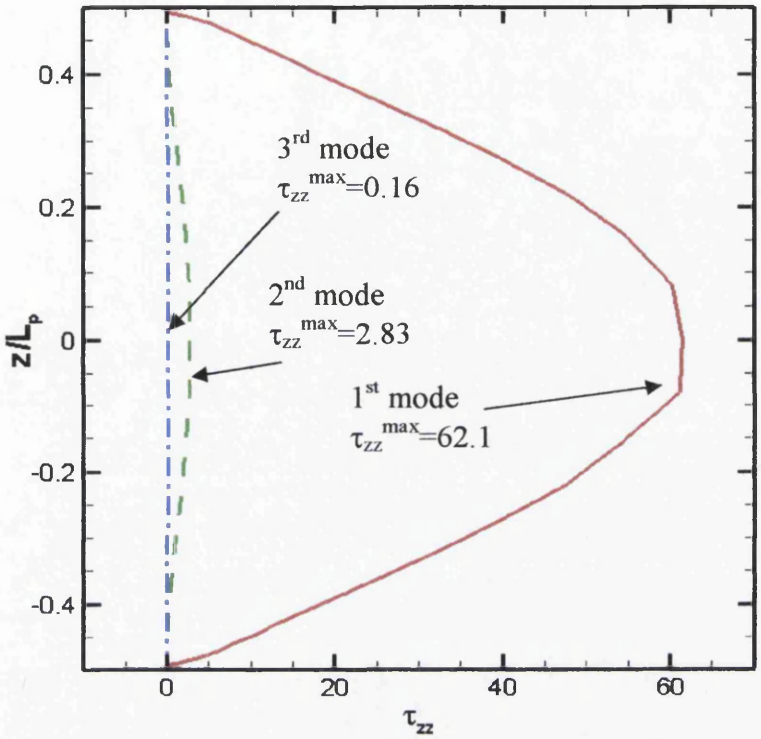

Fig 6.20: Free-surface axial stress (τ_{zz}) profiles; multi-mode LPTT(ξ=0); Ca^{-1}=0, F_g=0, ε=3.6; separate relaxation modes contribution: 1st mode, 2nd mode, 3rd mode

6.3.3.6 Comparison with inclusion of surface tension

Finally, when accounting for capillary surface tension effects, multi-mode LPTT(ξ=0.13) and Giesekus solutions are considered through axial stress free-surface profiles. The Giesekus solution of Fig. 6.21a is entirely consistent with that of insignificant surface tension forces (Fig. 6.17), demonstrating comparable stress maxima at the elevated Hencky-strains beyond 3.0 units, achieving a plateau of around 13 units. Only long slender cylindrical filament shapes are detected with the Giesekus fluid. For the LPTT(ξ=0.13) fluid of Fig. 6.21b, similar comments apply

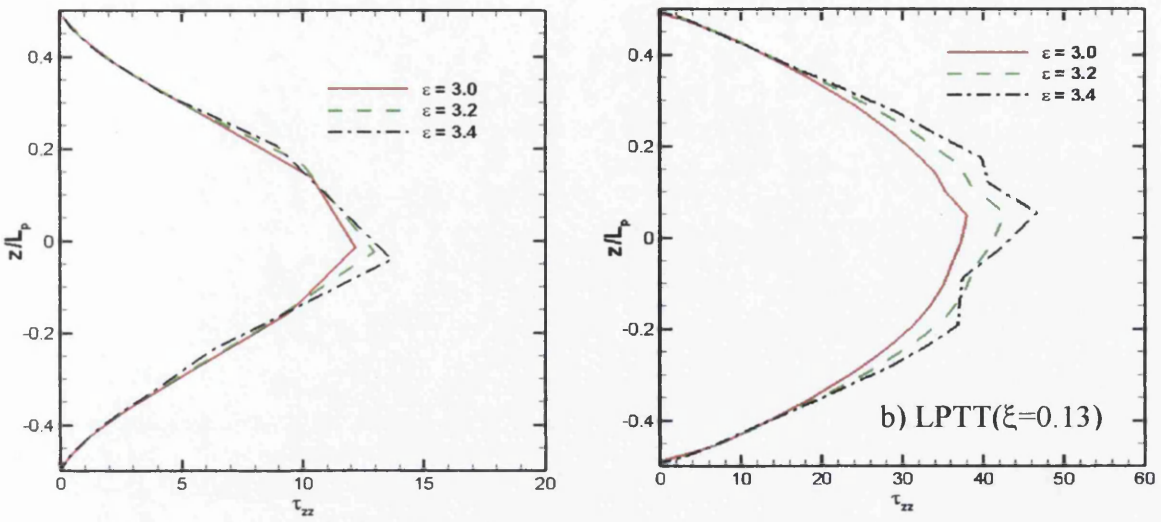

Fig 6.21: Free-surface axial stress (τ_{zz}) profiles with surface tension, multi-mode solutions; increasing ε; Ca^{-1}=0.1, F_g=0; (a) Giesekus, (b) LPTT(ξ=0.13)

when contrasting inclusion/exclusion of surface tension forces; no gross disparities are observed (see Fig. 6.18). If anything, with surface tension included, comparable but slightly larger levels of stress maxima are observed at Hencky-strains beyond 3.0 units. Stress maxima have not split *with surface tension effects included*, even at levels of Hencky-strain of 3.4 units. Once more, this would be anticipated to arise at ε≥3.6 units.

6.4 Concluding remarks

To conclude, the filament stretching problem has been studied under both a single-mode approximation and through a multiple relaxation-time spectrum representation. Prediction and validation have been performed under the strain-hardening rheology of Oldroyd-B, Giesekus and LPTT models. Numerically, two new important issues have been addressed: concurrently accommodating for values from a broad spectrum of relaxation times (small and large times, requiring improved time-implicitness); and handling near-Maxwellian form, as any solvent viscosity is mainly absorbed within a variety of individual modes. Under *single-mode modelling* and exponential-stretching, with the inclusion of body forces and surface tension for the (LPTT-ξ=0.13)-fluid, an asymmetrical bead-like structure in

the filament has emerged. Disregarding body forces/surface tension influences, the influence of variation in *shear-thinning and tension-thickening* properties has been analysed, concentrating upon comparison of results for LPTT(ξ=0 and ξ=0.13) and Giesekus models (Giesekus model, τ_{zz}-maxima=13, ε_{crit}=4 units; LPTT(ξ=0), τ_{zz}-maxima=98 units, ε_{crit}=4.4 units). Investigating filament shape, the dominance of strain-hardening is borne out for these flows, above and beyond that of shear-thinning, with the thickest filament centres corresponding to the models providing stronger hardening. Reduction in *strain-hardening* as with the Giesekus model and rising (α), renders less (τ_{zz}) development. In contrast, shear stress is dominant near the moving-plates, and by raising the mobility factor this shearing influence declines. Thus, in an $\alpha \rightarrow 0$ regime, when shearing effects are augmented, the filament foot is further pinched and the filament mid-section thickens. In contrast under the alternative regime of $\alpha \rightarrow 1$, exaggerated thinning is observed at the filament mid-section, as a result of the corresponding reduction in hardening and extension experienced there.

Linear versus exponential-stretching configurations have also been compared under an Oldroyd-B single-mode approximation, with predicted solutions validated closely against theoretical solutions. Under the linear-stretching mode, axial stress relaxes during the stretching process, hence proving less restrictive to the overall stretching period. This lies in contrast to the exponential-counterpart, where axial stress grows at an exponential rate. The dynamically decreasing stretch-rate of the linear-stretching configuration causes this decrease in stress, unlike its exponential counterpart. The trend in Trouton ratio is one of monotonic rise with Hencky-strain under exponential-stretching, whilst with linear-stretching, far lower levels of Trouton ratio are attained. Under linear-stretching, any early Trouton ratio rise is fairly insubstantial, ultimately declining to zero. Radial velocity minima (V_r^{min}) at the mid-plane prove substantially lower for linear-stretching than under exponential-stretching up to equivalent Hencky-strains of ε=1.8 units. At higher strain levels (V_r^{min}) do not exhibit a tendency to migrate towards the plate-regions (as occurs with exponential retraction). Despite such contrast for Oldroyd fluids,

and considering the arguments relating radial and axial strain measures, developing filament shapes at equivalent lengths (Hencky-strains) do not significantly differ across the various modes of stretching.

Contrasting single- and multi-mode axial stress representation at the filament-centre, discrepancy in stress local maxima appears even at the relatively low Hencky-strains of ε=0.2 units (and fully so by ε=1.0). Considering the significance of the various relaxation-modes *under multi-timescale modelling*, the impact of the shortest modes is conspicuous in the axial penetration of stress through the filament (lengthwise), whilst providing uniform radial penetration. The largest mode represents the major contributing factor to the extra-stress for larger Hencky-strain levels ($\varepsilon \geq 0.8$ units), most notably in terms of axial stress. In early stretching stages, dominance switches between the modes, with the second mode taking over by ε=0.2 units, and parity being established between first and second modes across the intermediate range ($0.2<\varepsilon<0.8$ units). In the case devoid of body/surface tension forces and under single or multi-mode approximations, both the Giesekus and LPTT(ξ=0) fluids yield similar trends. There are no manifestations of bead-like structures, retaining symmetrical filament-shapes and stress distribution patterns (axial stress), even at large Hencky-strain levels of ε>3 units. Addition of capillary forces does not alter this finding. In contrast, multi-mode LPTT (ξ=0.13) solutions, accounting for capillary force inclusion or not, provide a single symmetrical bead-like structure, but only at larger Hencky-strain levels beyond ε>3.4 units, as opposed to ε=3.2 units for the single-mode instance. At ε=3 units, the single-mode solution generates local stress-maxima, positioned off-centre, so that splitting arises in the axial stress component. This phenomenon delays its emergence in the multi-mode instance (due to shorter mode influence) until Hencky-strain levels above ε=3.4 units.

Chapter 7

Modeling Step-Strain Filament-Stretching by ALE Techniques[†]

The numerical modeling of capillary breakup extensional rheometer procedures (*CaBER*) employing Arbitrary Lagrangian/Eulerian (*ALE*) methods is discussed in this chapter. Different models, fluid viscosity ratios and aspect-ratios are studied, utilising a hybrid finite element/finite volume spatial approach. For the momentum and continuity equation, finite element discretisation is used whilst for the hyperbolic stress equation, a pure-upwinding cell-vertex finite volume representation is employed. The results are validated against equivalent experimental results reported in the literature. Viscoelastic response for some strain-hardening fluids in *CaBER*-type step-strain flows is studied through employment of various constitutive models. In this case, bead-like structures emerge for filaments with high initial aspect-ratios. In contrast, no bulges/beads appear for low polymeric viscosity Boger-type fluids (Oldroyd-B). The influence of surface tension and elastic forces upon these particular filament stretching flows is explored in this study.

[†] Material up to section 7.3 of this chapter is based upon the paper "Modeling step-strain filament stretching (*CaBER*- type) using ALE technique", by K.S. Sujatha, H. Matallah, M.J. Banaai and M.F. Webster, in press, *Journal of Non-Newtonian Fluid Mechanics.*

The chapter also explores the impact of practical implementation through examining the effect of plate deceleration at the end of the CaBER implementation. The study encompasses variation in material rheology, appealing to Oldroyd, Geisekus and Phan-Thien/Tanner type models, which display differences in shear and extensional viscosity properties (shear-thinning/extension-hardening). Two different viscosity ratio settings are considered to reflect high and low-solvent viscosity constituent components; the former representing typical Boger fluids, the latter high polymer concentration fluids. We compare and contrast results for three alternative filament aspect-ratios at the onset of step-strain. Throughout the step-strain period, we have been able to successfully capture such physical features as drainage to the filament feet, necking at the filament centre, and periods with traveling waves through the axial filament length. In addition, we have identified the suppressive influence that larger capillary forces have upon radial fluctuations, and the minor impact that gravitational forces have upon the ensuing deformation. From this study, estimates for rheometrical data have been derived in terms of characteristic material relaxation time and apparent extensional viscosity.

7.1 Introduction

Application of elongational flow of polymeric fluids arises within a number of industrial processes with the involvement of predominantly extensional modes of deformation. Examples include extrusion of polymeric materials, fibre spinning and film blowing. Extensional flows are also observed in applications such as coatings, enhanced oil recovery, lubrication, turbulent drag reduction and atomization. Filament-stretching is a common example of such an extensional flow with vast applications in the study of polymer melts and solutions. Additionally, it is a popular technique currently employed to quantify material fluid properties, via quantitative measurements of the thinning and failure within fluid filaments. McKinley and Sridhar [46] have provided a comprehensive review of the flow dynamics within filament-

stretching rheometers. The common practice in a conventional filament-stretching rheometer (type 1 - *FISER*), is to insert an exponentially increasing velocity upon the fluid formed between the two rigid plates. Typically, the subsequent evolution of mid-filament diameter is monitored during the process of necking and failure. The filament stretching rheometer may be employed for capillary-breakup trials (type 2 - *CaBER*), under a second mode of operation. In *CaBER* trials a rapid axial step-strain of prescribed magnitude is imposed, and then the 'necked fluid' sample is allowed to relax and break up under the influence of capillary forces. The viscous, elastic, gravitational and capillary forces govern the relaxation and decay of the necked sample and as with *FISER*-procedures, the evolution of the mid-filament diameter is again monitored (see [21]). In many commercial operations, such as printing, paint applications, roll-coating of adhesives, and other food processing, the associated progressive thinning and breakup of a fluid filament into numerous small beads/droplets occurs. The fluid undergoing break-up is non-Newtonian in many instances, and the transient extensional viscosity of the fluid plays a key role in controlling the dynamics and eventual break-up. This dynamical process can be extremely rapid and is dependent upon the fluid composition, viscous, elastic and inertial forces resisting the capillary forces to form droplets. Though in the study of viscous polymer solutions and melts, the conventional filament stretching rheometer has been widely used, there are practical difficulties that arise with low viscosity solutions due to the resolution of the force transducer. In addition, such filament-stretching experiments are difficult to conduct in practice as a result of limitations caused by mechanical constraints and elastic instabilities. *CaBER*-trials, can alternatively be employed to measure the extensional properties of low viscosity fluids. A *CaBER* method provides information about the relaxation time spectrum, the extent of non-Newtonian characteristics, and the time to break-up of the fluid. Within the *CaBER* experiment, the fluid dynamics of the necking process evolves with time, and understanding this process is vital to obtain qualitative material properties of the candidate fluid.

A detailed discussion on the capillary thinning and breakup of viscoelastic filaments employing a multi-mode *FENE* fluid model has been analysed and provided by Entov and Hinch [21]. In their analysis, a lengthy intermediate regime is revealed where elastic and surface tension forces balance, whilst other forces arising from inertial, gravitational and viscous effects are negligible. In this regime, capillary forces drive and viscoelastic forces resist the necking process. In order to restrain fluid molecules from relaxing, the filament must thin continuously at a rate proportional to the characteristic relaxation rate of the fluid. The predictions of Entov and Hinch [21] compared well with the experimental work of Liang and Mackley [84]. In capillary break-up rheometry, a significant amount of work has been covered in recent years since the pioneering work of Entov and Hinch [21] and Bazilevski et al. [18,72,73]. Several devices have been developed specifically to study visco-elasto-capillary thinning [18,74,75]. For example, capillary thinning of Newtonian and viscoelastic filaments through both experimental analysis and numerical simulation have been studied by Kolte and Szabo [75]. These numerical studies were performed by employing a Lagrangian finite element method and their predictions, were in close agreement with their experimental findings. They have also reported good agreement between the results obtained on the longest relaxation time and shapes and the existing theory in the literature. McKinley and Tripathi [74] have indicated that such a device can also be effectively used for measuring the Newtonian viscosity of viscous liquids. The theoretical studies of Entov and Hinch [21] and the experiments by Stelter et al. [19] have revealed that apart from the longest relaxation time, also through *CaBER*-procedures, one can measure the steady terminal elongational viscosity of the fluid. Polymer solutions have also been analysed in the work of Anna and McKinley [17], using the *CaBER* stretching device presented in Ref. [18]. In their work, it has been demonstrated how the transient elongational viscosity of a dilute polymer solution can be estimated from the mid-plane diameter evolution of the necking filament. The apparent extensional viscosity profiles obtained have been compared with

experimental measurements conducted with a rotational viscometer, and the equipment presented by Tirtaatmadja and Sridhar [38]. *CaBER* and *FISER* procedures have been shown to be complementary experiments, providing consistent measurement of the transient extensional viscosities of polymeric fluids. Moreover, the extensional rheology of other material systems, of inks and paint dispersions using capillary break-up rheometry has been studied by Willenbacher [79]. Likewise, Stelter et al. [19] have employed an elongational rheometer to measure steady terminal extensional viscosity and relaxation time at various concentrations and in suitable solvents for aqueous solutions of ionic and nonionic polymers. A method has been developed by these authors to characterise the elongational behaviour of polymer molecules and the onset of higher-order concentration impacts in elongational flows. Rodd et al. [71] have experimentally studied the dynamics of capillary thinning and break-up with polyethylene oxide (PEO) in water and glycerol for low viscosity, dilute and semi-dilute polymer solutions. These authors state that the successful operation of such a device is controllable by three time-scales and two length-scales. The two length-scales represent the initial sample size and the total stretch imposed and the three time-scales characterise the relative importance of inertial, viscous and elastic forces. By optimizing the ranges of the relevant length-scales involved, characteristic time-scales have been measured for axial stress growth for model solutions. Bousefield et al. [22] have studied the transient evolution of viscoelastic jets and the beads-on-a-string phenomenon, using a finite element method to incorporate nonlinear effects. In the literature, several studies are available that deal with the dynamics of necking threads, covering evolution to break-up. Almost all constitute similarity solutions (see, for example, Renardy [76]), utilising one-dimensional radially-averaged forms, to provide velocity fields valid for slender filaments. Eggers [47] has discussed many of these in details. Such stability analyses have been conducted to study rheological response and the ability to form stable fluid filaments and jets. Based upon the early work of Chang and Lodge [57], spinnability of viscoelastic fluids in uniaxial elongation was studied by Ide and White [83], incorporating surface tension and nonlinear extensional

rheology. Beads-on-string structure that may arise in viscoelastic threads have also been reported in detail by Clasen et al. [80]. These authors have analysed the characteristics of such a phenomenon as a function of times both smaller and larger than the relaxation time of the polymeric material. Within these *CaBER* experiments, understanding the fluid dynamics associated with the necking process is vital in order to obtain reliable material properties for the candidate fluid under study. As the fluid is allowed to relax on its own time-scale (see [71]), the fluid may reflect complex dynamical response in such a device. There are also practical difficulties in *CaBER* experiments including configuration of the desired sample loading, a low-shock step-strain stop and taking numerical derivatives from noisy data to provide the required material properties. Prabhakar et al. [191] studied the stress in the polymer in a dilute polymer solution to predict elastocapillary thinning and breakup of the solution.

In earlier chapters and to predict the dynamical response of uniaxial filament-stretching flows [33,61], a consistent hybrid finite element/volume formulation has been developed. There, under retraction of plates at an exponential rate, extensional deformation has been considered of a viscoelastic filament between two coaxial discs (plates). The base of these studies was an axisymmetric model incorporating viscoelastic behaviour, surface tension, fluid inertia and a deformable free-surface. A compressed-mesh, Arbitrary Lagrangian/Eulerian (CM/*ALE*) procedure has effectively been employed to track the flow evolution via a particle-tracking technique (d**x**/dt) utilised to capture the developing free-surface of the deforming filament. Large extensional deformation has been studied, up to impressive levels of Hencky-strain of the order of five units and above. For constant shear-viscosity fluids, Newtonian and Oldroyd-B model predictions have indicated excellent agreement against the literature. Recently, there has been noticeable progress in prediction and analysis of transient viscoelastic response of strain-hardening fluids with *shear-thinning* properties (via linear Phan-Thien/Tanner (LPTT) and Giesekus modeling) [61]. There, a parametric study varying surface tension and inertial effects has been conducted to isolate the emergence of flow asymmetries, leading to the onset of bead-like structures. The

hybrid FV scheme has proven capable in dealing with such severe computational challenges, capturing sharp differences in filament curvature and flow structure during the various phases of the flow evolution. In the present chapter, the focus lies mainly on employing this methodology in the study of capillary break-up filament rheometry, utilising three different viscoelastic models, and two polymeric viscosity ratios with alternative final filament aspect-ratios for each. For highly-polymeric fluids, three such ratios have been studied, and two further ratios for low-polymeric fluids. From the mid-filament diameter evolution, estimates may be derived for the apparent extensional viscosity and the material relaxation time. Encouragingly, such estimates of relaxation time are found to lie in close agreement with the actual relaxation time data used for the fluids in question. In addition, the trends predicted in extensional viscosity demonstrate corroboration with those in the literature.

7.2 Problem description

Capillary and extensional deformation for viscoelastic filaments between two co-axial discs is considered. First, the plates are retracted at an exponential rate, which provides a constant stretch-rate as described at section 4.2. Once the required filament aspect-ratio has been reached, the liquid bridge is allowed to relax under the action of surface tension. Two different fluid viscosity settings are studied. One fluid employed has a relatively high solvent/low polymeric viscosity ratio ($\beta=\mu_2/\mu_0=0.87$), a typical so-called SM1-Boger fluid described by the Oldroyd-B model. The second fluid is a low-solvent/high-polymeric viscosity fluid ($\beta=\mu_2/\mu_0=0.262$), which is represented through three alternative constitutive models, namely, Oldroyd-B, LPTT and Giesekus. With these latter fluids, the degree of strain-hardening varies from least in Giesekus, through to more exaggerated forms, in LPTT intermediate, to most extreme in Oldroyd. As such, the Giesekus model has been chosen to represent weakly strain-hardening fluids, providing a reasonable fit to both linear and non-linear shear rheology data for most concentrated polymeric solutions (see for example, Li et al. [2] and Yao et al. [3]). Only the Oldroyd model has a constant shear viscosity, the other

two models demonstrating some degree of shear-thinning, with onset around deformation rates of O (1) units. The fluid characteristics and filament dimensions are provided in Table 7.1, so that, the time-scales involved for the above two fluids are 0.22 and 1.0 seconds, respectively ($1/\dot{\varepsilon}$).

	High polym. visc	Low polym. visc
Re (Reynolds number)	$4.7*10^{-4}$	$3.8*10^{-4}$
L_0 (initial length) (m)	$1.89*10^{-3}$	$1.5*10^{-3}$
χ (surface-tension coefficient) (Nm^{-1})	$30.0*10^{-3}$	$37.8*10^{-3}$
ρ (density) ($Kg.m^{-3}$)	1030	1026
μ_0 (zero shear viscosity) (Pa.s)	34.949	39.2
μ_2 (solvent viscosity) (Pa.s)	9.08	34.0
$\dot{\varepsilon}$ (extension rate) (s^{-1})	4.48	1.0
Ca (Capillary number)	9.86	1.56
Bo (Bond number)	1.2	0.6

Table 7.1: Fluid properties, filament dimensions and non-dimensional numbers

Meshes	Elements	Nodes	τ_{zz}-max			R_{mid}		
			t_1	t_2	t_3	t_1	t_2	t_3
Mesh-M1 (100x20)	4000	8241	15.044	12.036	1.293	0.496	0.232	0.039
Mesh-M2 (150x20)	6000	12341	15.043	12.017	1.245	0.495	0.234	0.036
Mesh-M3 (200x20)	8000	16441	15.045	12.016	1.286	0.492	0.232	0.036

Table 7.2: Mesh refinement: τ_{zz}-max, and R_{mid} at different times.

Fluid	β-ratio	λ_{est}	λ
Fluid 1-SM1-Boger	0.870	3.12	3.70
Fluid 2- 5.0 wt% polystyrene	0.262	0.35	0.421

Table 7.3: Estimated relaxation time, λ_{est}

The problem dependent values for the above quantities are tabulated in Table 7.1.

During the relaxation process, the radial evolution of the filament midpoint characterizes the dynamics, assuming that symmetry is retained about mid-plane and the filament profiles remain spatially self-similar. The radial evolution of the midpoint is governed by a force balance on the filament, through viscous, elastic and capillary terms neglecting inertial and gravitational effects. This may be expressed as [12]:

$$3\mu_2 \dot{\varepsilon}(t) = \frac{2\chi}{D_{mid}} - (\tau_{zz} - \tau_{rr}), \tag{7.1}$$

where $\dot{\varepsilon}(t) = \frac{-2}{D_{mid}} \frac{dD_{mid}}{dt}$.

The apparent extensional viscosity, μ_{app} can also be represented as

$$\mu_{app} = \frac{(\tau_{zz} - \tau_{rr})}{\dot{\varepsilon}(t)} + 3\mu_2. \tag{7.2}$$

Combining eqs. (7.1) and (7.2) yields,

$$\mu_{app} = \frac{-\chi}{(\frac{dD_{mid}}{dt})}. \tag{7.3}$$

Here, D_{mid} is the mid-plane diameter of the filament, and χ is the material surface tension coefficient. Such *CaBER*-trials can also provide the means to determine, the principal material relaxation time (λ), and thus, an indication of the corresponding characteristic time-scale for viscoelastic stress growth under uniaxial extension. The mid-filament diameter of an Oldroyd-B fluid filament is predicted to decrease exponentially with time [18,21,22,72]. If viscous stresses are assumed to be negligible, and capillary and elastic contributions to the total force balance each other, then the mid-filament diameter is predicted to decrease according to the relationship,

$$\frac{D_{mid}(t)}{D_0} = (\frac{GD_0}{4\chi})^{1/3} \exp(-t/3\lambda). \tag{7.4}$$

Where D_0 is the midpoint diameter following cessation of stretching and G is the elastic modulus of the material and is given by $G = \frac{\mu_1}{\lambda}$.

The above relationships are deployed below upon present data to extract the relevant

material quantities in question.

7.3 Results and discussions

7.3.1 High polymeric viscosity fluids, β=0.262, various models

Here, various fluid models including Oldroyd-B, Giesekus and LPTT are employed to study the test fluid, a 5.0wt % solution of high molecular weight polystyrene dissolved in a mixture of dioctyl phthalate (DOP) and tricresyl phosphate (TCP). Li et al. [2] provide the detail on the preparation and viscometric characterisation of this fluid. A time-evolution scenario with a single LPTT fluid is illustrated in Fig. 7.1, employing two different implementations of the numerical scheme, termed *FISER-ALE* and *CaBER-ALE*. First, the liquid bridge is stretched at exponential rate to a Hencky-strain of two units and is subsequently allowed to relax. In the *FISER-ALE* instance, an *ALE* interpretation is adopted where the mesh velocity is taken the same as the fluid velocity. In this instance, it is observed that fluid migration towards the plates causes element aspect-ratios in the mid-filament region become excessively stretched (mesh sparsity). Consequently, the near-plate regions become much denser in elements. The corresponding adjustments in mesh aspect-ratio have led to degradation in the computation of free-surface curvature. To overcome this situation, adaptive remeshing strategies are required. In an alternative approach, a *CaBER-ALE* method is employed, where the length of each element is held constant in the axial-direction once plate movement has been halted. In this instance, mesh-node movement is only in the radial direction and to compensate for this difference, a correction in convection is applied after stage 3 of the fractional-stages (see ref [33]). As element aspect-ratios are now not subject to such dramatic changes, longer step-strain duration times are found for the *CaBER-ALE* instance to reach the filament break-up phase. In addition and encouragingly, the results from *CaBER-ALE* trials conducted on a low polymeric viscosity Boger fluid show close agreement in filament-shape with the experimental observations of others (Anna and McKinley [17]).

Accordingly, under subsequent simulations, we opt for this amended ALE (*CaBER-ALE*) option.

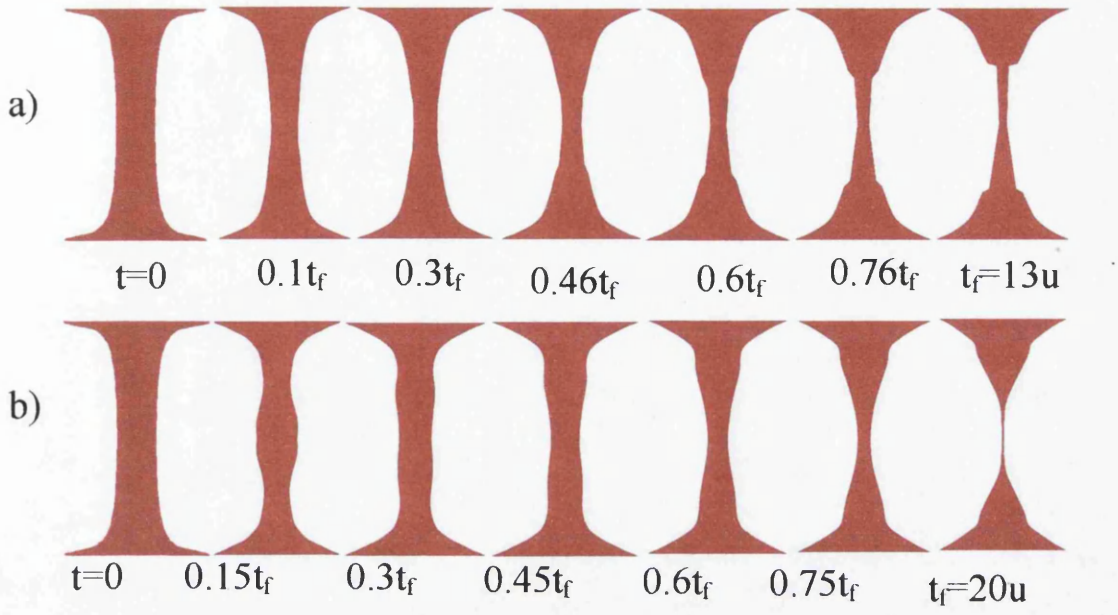

Fig 7.1 : Filament shapes, LPTT; a) *FISER-ALE* vs b) CaBER ALE; *l/d* ratio=2, Ca^{-1}=0.1, 1 time unit=0.22 sec.

A comparison across models at a starting Hencky-strain of 2 units (*l/d* ratio=2) is depicted in Fig 7.2. The Oldroyd-B fluid filament takes a longer time to reach the break-up phase, followed by LPTT, and then Giesekus filaments. Over the early stages of stretching, the Oldroyd fluid, being the most strain-hardening, demonstrates the largest level of initial mid-plane elastic stress, and consequently sustains the largest filament diameter at equivalent times (prominent over the early stages of stretching up to $0.3t_f$). Thus, it requires more strong force to neck-down. The Giesekus fluid filament develops to a thinner form much earlier at the filament mid-plane contrary to that for the LPTT fluid, and halts therefore much earlier (t_f=2.5 units). The structure in the filament feet for these various models differs significantly, as illustrated in Fig 7.2, most bulbous for Oldroyd, followed by LPTT, and then Giesekus fluids. For the LPTT

filament, a double bulge structure forms at the centre of the filament at t= 0.1 t_f. This feature is also present in a much reduced form with the Oldroyd-filament, as shown in Fig.7.5a below. This bulge subsequently shifts towards the plates in time. In contrast, for the Giesekus filament no bulge/bead emerges throughout the step-strain process.

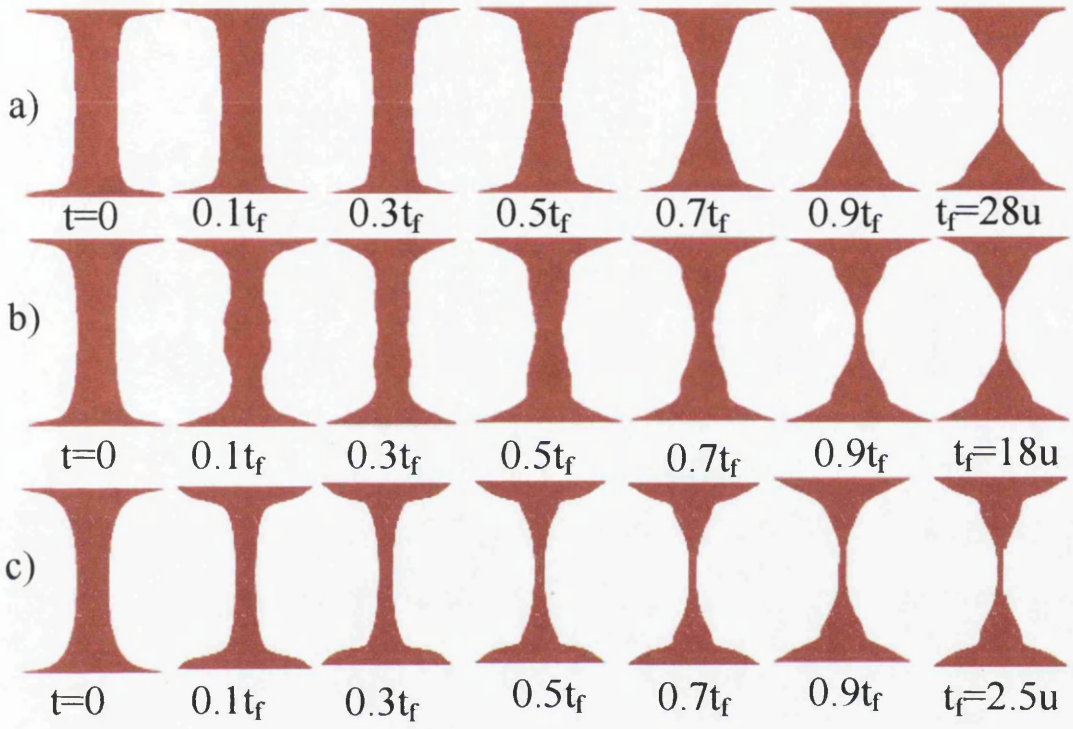

Fig 7.2: Filament shapes; a) Oldroyd-B, b) LPTT, c) Giesekus; *l/d* ratio=2, Ca^{-1}=0.1
1 time unit=0.22 sec.

At a higher aspect-ratio, equivalent to a starting Hencky-strain level of 2.4 units and *l/d* =3, comparison is made across models as displayed in Fig. 7.3. The Oldroyd-B filament reflects no signs of central thinning and fails rather rapidly as it approaches its critical Hencky-strain level (shorter time to break-up). With the LPTT fluid, a double-bead develops after one-third of the process ($0.3t_f$); and the beads subsequently move towards the end-plates.

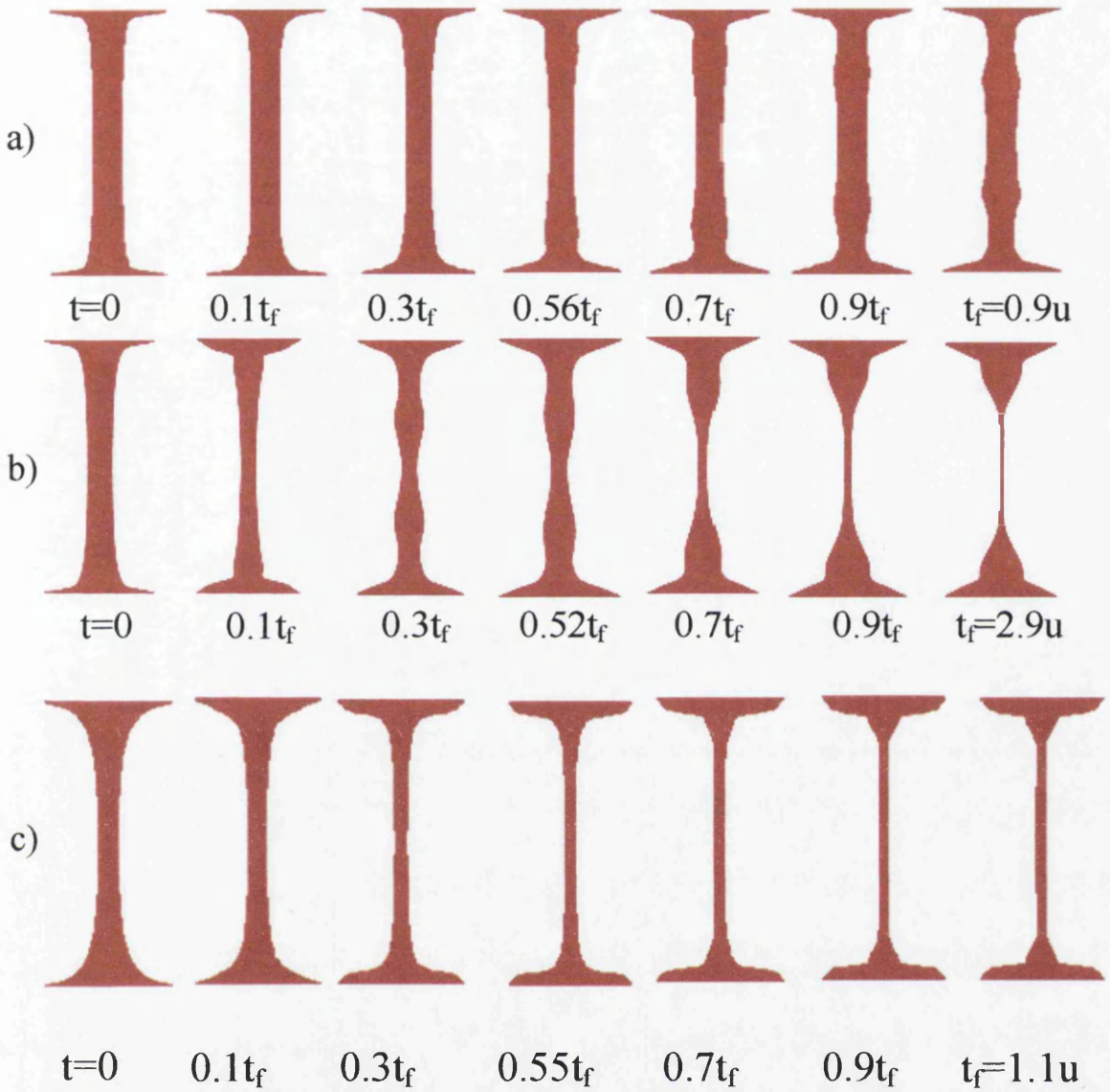

Fig 7.3: Filament shapes; a) Oldroyd-B, b) LPTT, c) Giesekus;
l/d ratio=3.0, Ca^{-1}=0.1, 1 time unit=0.22 sec.

Finally, the beads disappear and the filament thins in the central region before break-up occurs, leaving two bulges at both end-plates. In contrast, the Giesekus filament does not develop any such bulge. It has a long thin cylindrical shape at the central region, with two small triangular-like shaped swellings gradually appearing present at the near end-plate zones.

Progressive thinning of the LPTT filament at a larger *l/d* ratio of 10 is depicted in Fig. 7.4. Here, the terminating Hencky-strain at the end of phase one is 3.6 units, which is close to the critical state sustainable for this LPTT-fluid under the continuous stretching mode. In this case, symmetrical shape is maintained, no radial fluctuations or bead-like structures are formed and the filament thins down gradually until numerical failure occurs. Since the level of Hencky-strain is close to a critical state, the filament breaks-up rather rapidly at t_f=0.7 units.

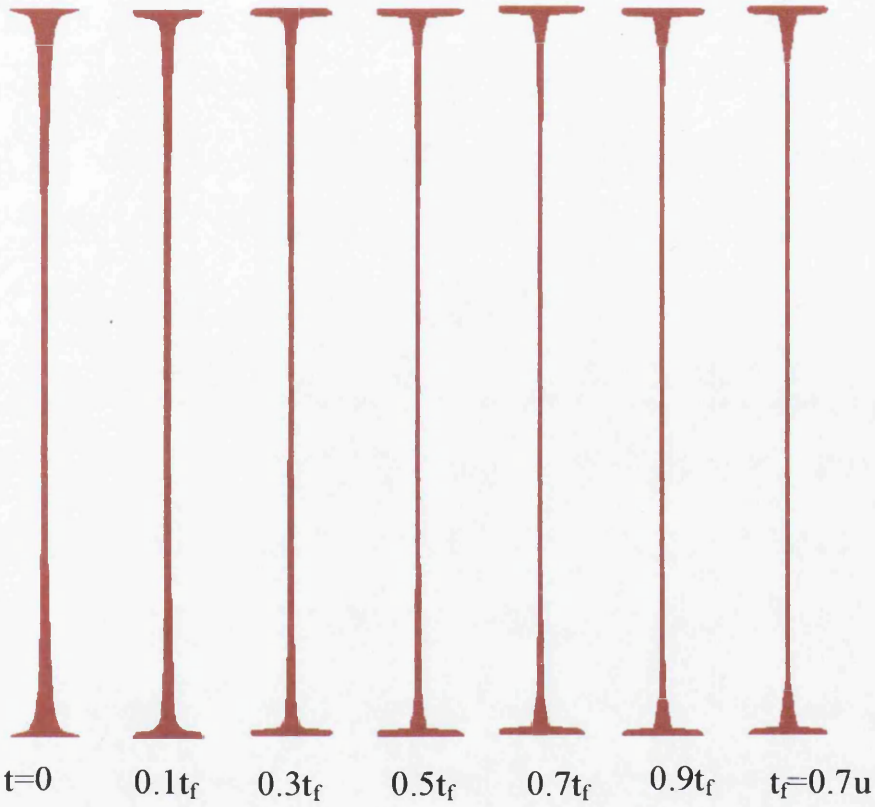

Fig 7.4: Filament shapes, LPTT (ξ=0), *l/d* ratio=10.0, Ca^{-1}=0.1, F_g=0.0
1 time unit=0.22 sec

Fig 7.5 demonstrates the variation of R_{mid} and τ_{zz}-mid-plane as a function of time for *l/d* =2. This calls upon the three models cited and the aspect-ratio of *l/d* =2, to be interpreted directly against Fig. 7.2. The state of thinning of the liquid bridge with time is apparent from this representation in correspondence with the relaxation of stress. At

earlier times, up to around t=5 units with Oldroyd and LPTT-filaments some oscillations are noticeable in both R_{mid} and τ_{zz}, but noticeably not with Giesekus filaments. This may be attributable to the formation of bulges and their shift in position at early times ($t<0.3\ t_f$, see also Fig 7.2). At longer times, the mid-plane filament diameter and stress maxima are subject to progressive decrease, until eventual break-up occurs. Approaching break-up, the stress rises rapidly as illustrated in Fig 7.5b. During the thinning of fluid filaments, elastic extensional stress resists the necking caused by the surface-tension/capillary forces. Consequently, the extensional stress in the filament grows in the local mid-filament region as one proceeds towards break-up (see [17]). The thickest filaments correspond to the most severe strain-hardening Oldroyd-B fluid, and hence take the longest time to reach their break-up states.

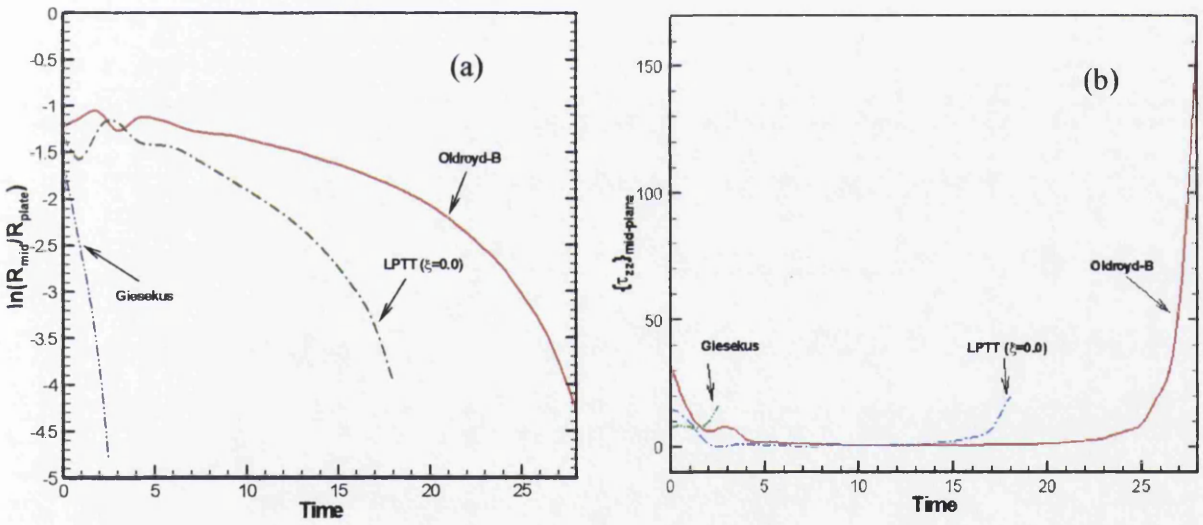

Fig 7.5: a) R_{mid} vs time; b) τ_{zz} mid-plane vs time, Oldroyd-B, LPTT, Giesekus

To demonstrate the effect of aspect ratio variation, the rate of decrease of R_{mid} for LPTT model is displayed in Fig. 7.6, for l/d = { 2, 3, 10}. The longest relaxation

period is observed for the shortest ratio. This representative data is for the LPTT (ξ=0.13) version, which reflects only marginal differences to that with ξ=0 of the alternative two aspect-ratios. For *l/d* ratios of 2 and 3, after the slight oscillations detectable at early times (t<5 units), R_{mid} undergoes a continuous monotonic decrease. The strength of oscillation and its impact upon the filament mid-plane clearly vanishes with rise in aspect-ratio. R_{mid} decreases at the steepest rate and any oscillatory behaviour is removed for the *l/d* ratio of 10. The filament has been stretched to near its critical strain level at this large aspect-ratio. Hence, the relaxation period is the shortest for this instance and numerical failure occurs due to the high stress levels achieved.

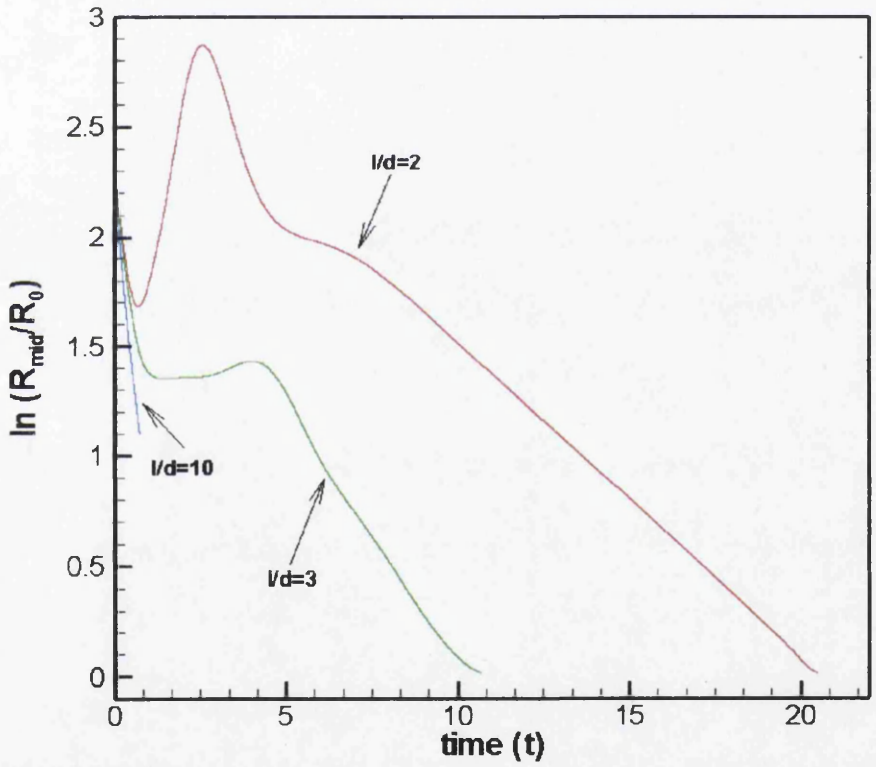

Fig 7.6: Temporal radial evolution, *l/d*=2, 3 and 10, LPTT (β=0.262)

7.3.2 Low polymeric viscosity fluids, β=0.87, Oldroyd-B, various l/d

In this instance, an Oldroyd-B fluid with low polymeric/high solvent viscosity ratio (β=0.87) is employed to match the SM1-Boger fluid as cited in Ref. [19] and for direct

comparison purposes. The evolving filament sample patterns are displayed in Fig 7.7a. These trials are conducted for a filament with *l/d* ratio of 1.36. In this instance no beads or other physical asymmetries are observed. As time progresses, filament foot structure undergoes dramatic changes, becoming more bulbous and increasingly thicker. Similar trends were reported in the experiments conducted in Ref. [17].

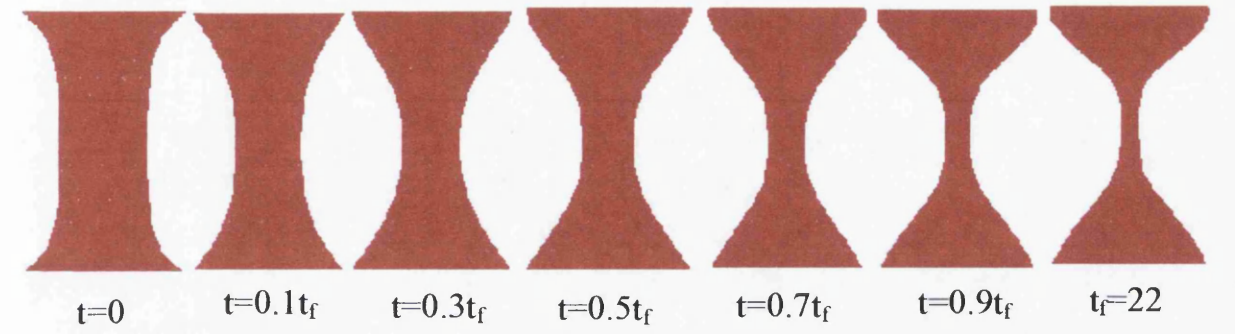

(a)

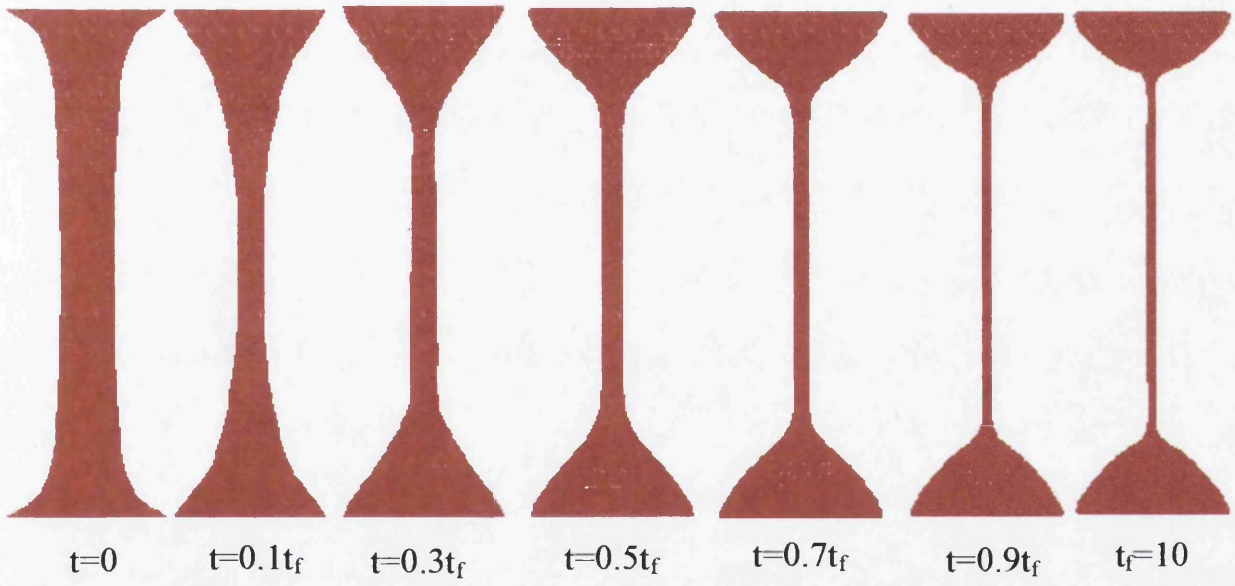

(b)

Fig 7.7: Filament shapes, Oldroyd-B(β=0.87), 1 time unit=1.0sec. a) *l/d* ratio=1.36; b) , *l/d* ratio=2.72

Fig. 7.7b displays the position for the same fluid at a larger aspect ratio (l/d =2.72). Once again, similar characteristics are observed in this instance as described above, and long, slender, uniform cylindrical shape emerges in the filament-core as time advances with feet-structure adjusting from truncated-conical to final thick hemispherical shapes. The step-strain duration times, for contiguous filaments are t_f = {22, 10} units for problems with aspect-ratios l/d={1.36, 2.72}. Mid-plane radius minima (R_{mid}) and stress maxima (τ_{zz}-max) are exhibited in Fig. 7.8a and Fig. 7.8b, respectively. From experimental results, it has been observed that in the case of capillary thinning for dilute polymer solutions, the mid-filament radius undergoes an approximate exponential decrease. The variation of R_{mid} (scaled by R_i, the initial radius at the onset of step-strain) illustrated in Fig. 7.8a provides excellent agreement with equivalent experimental results (see [17]). The lesser l/d ratio of 1.36 attracts the milder rate-of-decrease in R_{mid}, as opposed to the larger l/d ratio of 2.72. As demonstrated in Fig. 7.8b, the extensional stress increases rapidly as the filament radius decays. The higher aspect-ratio problem yields sharper and greater stress variation than the lower aspect-ratio case.

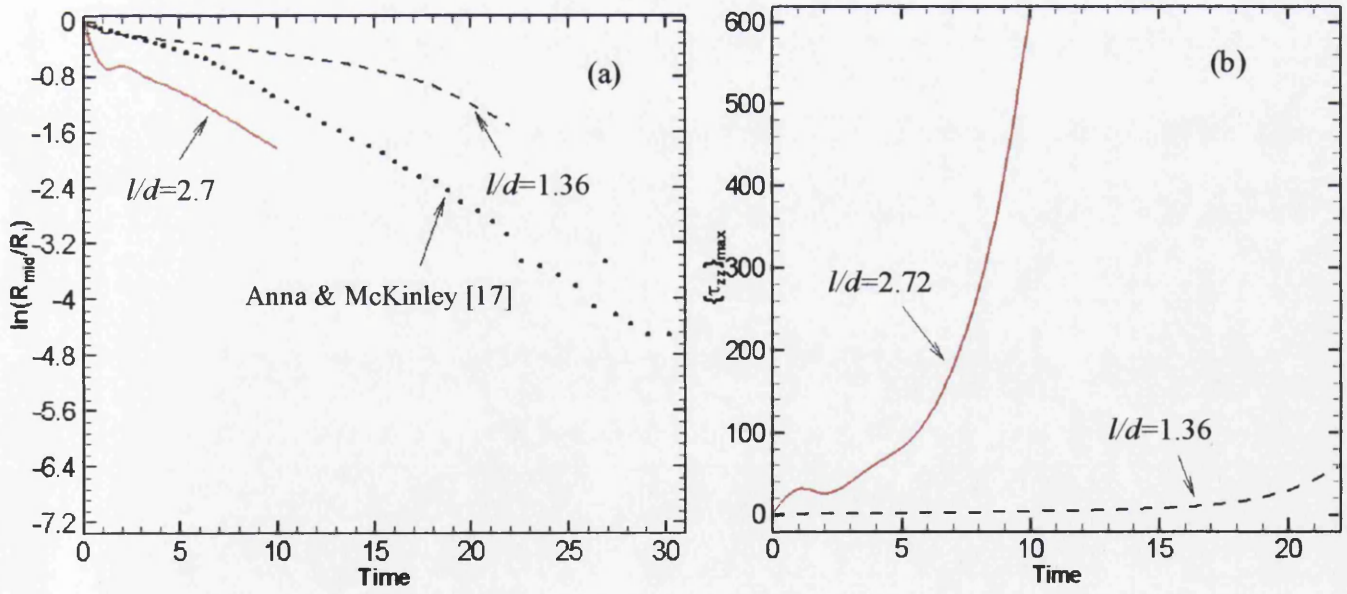

Fig 7.8: a) R_{mid} vs time; b) τ_{zz}-max vs time, Oldroyd-B, 1 time unit=1.0 sec.

Noticeably, the length of the central cylindrical ligament for l/d=2.72 represents some seventy percent of the final filament length, whilst for the l/d=1.36 instance, this length is about thirty percent.

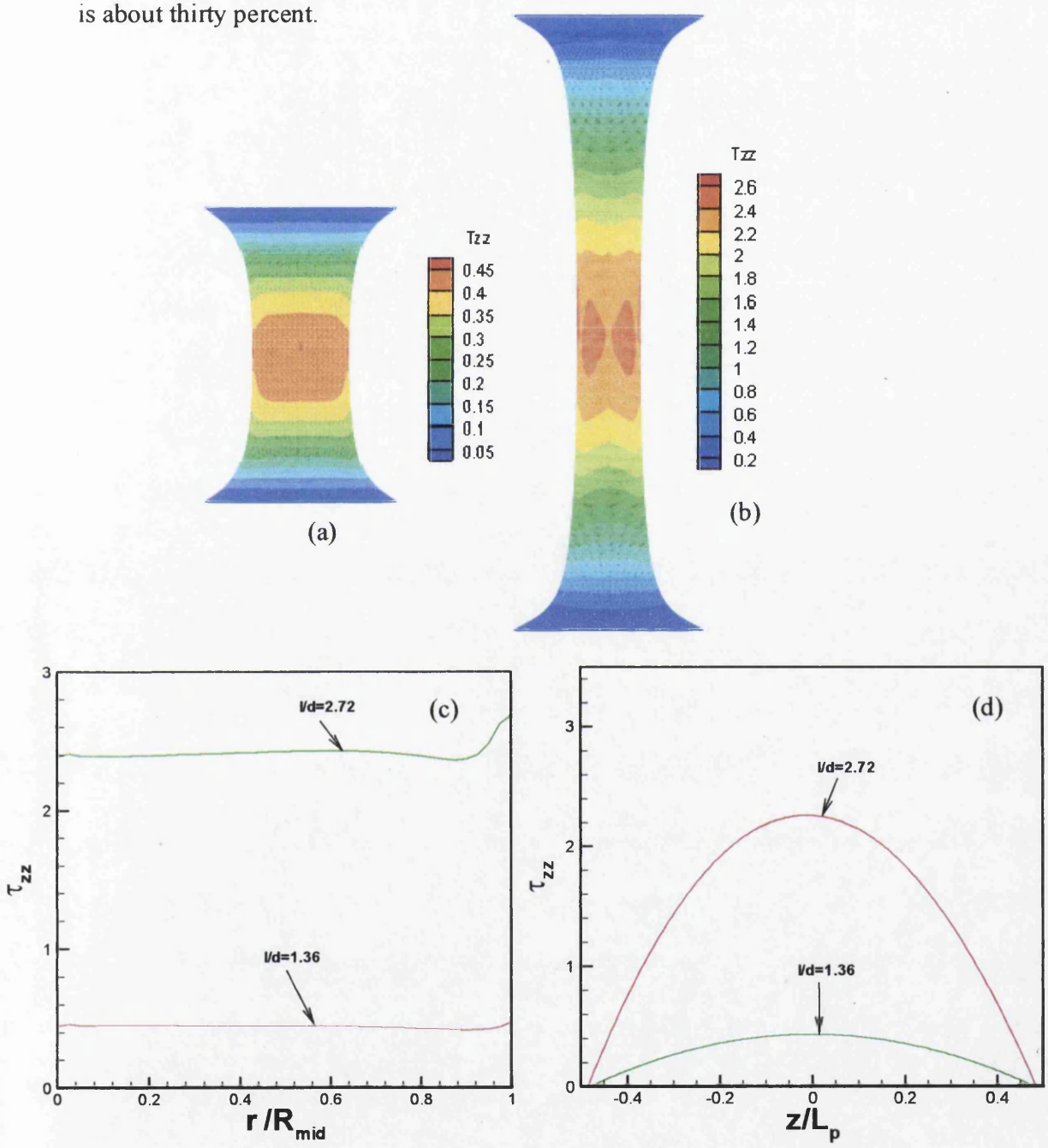

Fig 7.9: a) τ_{zz}-field contours (l/d=1.36); b) τ_{zz}-field contours (l/d=2.72); c) τ_{zz}-profiles, z=0 axis ; d) τ_{zz}-profiles, r=0 axis, Oldroyd-B (β=0.87)

Typical stress contours and profiles along principal axes for SM1-Boger fluid at two strain levels (aspect-ratios) are demonstrated in Fig. 7.9. These representative samples are chosen in the relative position at time t=0 from which relaxation commences, as a result of the step strain process. Apparently, the maximum axial stress is located about the filament mid-plane at the free-surface (Fig. 7.9c). As strain level (aspect-ratio) rises, this maximum stress increases due to the longer exposure to extension. Due to this and its associated relative decrease in filament-core thickness with rise in aspect-ratio, shortening occurs in the step-strain process period.

For both viscosity ratio fluids, the relaxation time and apparent extensional viscosity are estimated applying Eq. 7.3 and Eq. 7.4. Fig. 7.10a displays the estimated relaxation times for Oldroyd and Giesekus fluids. The data for the Oldroud fluid, the low polymeric-viscosity SM1-Boger fluid (β=0.87) is extracted from the aspect-ratio trial l/d=2.72. Similarly, the data for the Giesekus fluid, the high polymeric-viscosity 5wt % polystyrene composition fluid (β=0.262), is taken from the aspect-ratio trial l/d=2. Apparently, for both the two fluids, close agreement is observed between the estimated and actual relaxation time data. Table 7.3 indicates the averaged sampled estimates, being 3.12 to approximate 3.70 for the Oldroyd-B fluid (Fluid1-SM1), and 0.35 to approximate 0.42 for the Giesekus fluid (Fluid2). Fig. 7.10b illustrates the development of apparent extensional viscosity as a function of Hencky strain with a uniform monotonic rise for the Oldroyd (β=0.87) and LPTT (β=0.262) fluids. Here, the Hencky strain $\varepsilon(t)$ may be expressed in the form, $\varepsilon = 2\, ln\, (D_i/D_{mid}(t))$, and is radially measured at the mid-plane, in which D_i represents the initial step-strain filament diameter, see Anna and McKinley [17]. These predictions with rising trend and range of apparent extensional viscosity values reflect close correspondence with typical data reported in the literature [17,81]. The more strain-hardening Oldroyd fluid, consistently provides extensional viscosity values, one order of magnitude greater than that for the LPTT fluid, as anticipated.

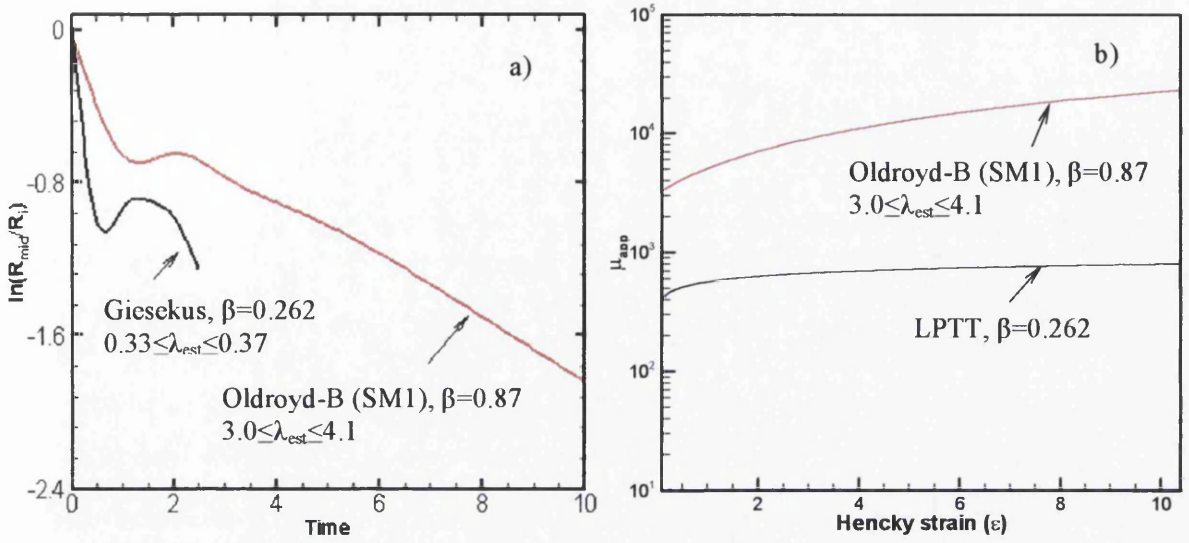

Fig 7.10: a) Estimated relaxation time, λ_{est}; b) Apparent extensional viscosity vs Hencky strain

7.4 Numerical modelling of step-strain for stretched filaments[†]

The preceding section has explored filament response under conditions where the platens are stopped instantaneously. This can not be achieved practically and therefore the focus of this section is an exploration of the impact of plate deceleration. This will be compared against the instantaneous stop model to complete the discussion in the previous section of the present chapter.

7.4.1 Computational predictions

All data are considered initially for the default filament aspect-ratio of L/D=2 and the base case of high polymeric:low solvent viscosity ratio (β=0.262), with parameters of Ca^{-1}=0.1 and F_g=0.122.

7.4.1.1 Start-up conditions

An important aspect to the current problem is the instigation of the halt condition (sudden-gradual) and to appreciate how this impacts upon the resulting dynamics in the step-strain period. For example, we have observed that commencing from various alternative start-up conditions can significantly affect the flow response. To identify this dependency, computations have been conducted for *sudden-stop* and *gradual-stop* instances with LPTT (ξ=0) model and F_g=0. Under sudden-stop, the end-plates are brought to rest instantaneously, whilst under gradual-stop, this motion is brought about only gradually over a designated period of time, just prior to the start of the step-strain phase.

Fig. 7.12a (short-time, $0 \le t \le 1$) and Fig. 7.12c (middle-time, $1 \le t \le 5$) illustrate the variation of axial fluid velocity (V_z) along the principal axis (r=0), under the sudden stop scenario. The corresponding position for a gradual-stop instance, is covered in Fig. 7.12b (short-time) and Fig. 7.12d (middle-time), demonstrating profiles when plates are brought to rest over a period of 0.2 units, prior to the (t=0)-station. Then, the

[†] Material in this section is based upon the paper "Numerical modelling of step-strain for stretched filaments", by M.F. Webster, H. Matallah, K.S. Sujatha, and M.J. Banaai and has been submitted for publication to the *Journal of Non-Newtonian Fluid Mechanics.*

time (t=0)-instance illustrates the start of the step-strain process, at which time (V_z) vanishes at the end-plates. From Fig. 7.12a-d, it is apparent that dramatic changes occur in spatial velocity variation immediately after the start of the step-strain process, confined within the early time period ($0 \leq t \leq 1$) units. Within this initial period, the magnitude in (V_z) is significantly reduced, from 3.6 units to 0.4 units (see Fig. 7.12a). Over times ($1 \leq t \leq 5$), and after the initial drastic reduction in magnitude, (V_z)-profiles display wave-like patterns whilst being anchored at both end-plates (see Fig. 7.12c). Between times 1 and 3 units, there is switch in sign of amplitude. During this secondary time period ($1 \leq t \leq 5$), velocity amplitude declines at a much slower rate. Similar comments apply for the gradual-stop instance displayed in Fig. 7.12b,d, where the magnitude of velocity (V_z) reduces considerably (halved) over that compared to its sudden-stop counterpart. Resulting filament profiles for the gradual and sudden-stop protocols are provided in Fig. 7.12e,f, where it is apparent that the setting with sudden halt captures radial fluctuations, which are largely absent under the gradual-stop protocol. There, only a relatively static filament is substantiated with insufficient dynamics to generate radial oscillations. Overall, it may be concluded that the sudden-stop protocol itself is responsible for the manifestation of radial fluctuations, and that moderation to gradual-stop tends to suppress this feature. We proceed below to consider further only the sudden-stop protocol.

7.4.1.2 High polymeric/low solvent viscosity ratio (β=0.262); Ca^{-1}=0.1, F_g=0.122, various models

We can observe temporal features in shape from the filament profiles, shown superimposed at each sample time across models (Fig. 7.13a), and separately for each model in stress contour plots (Fig. 7.13b,c). This data may be interpreted alongside that of R_{mid} profiles (Fig. 7.14a) commented upon in more detail below. First, data is considered for each model, taken comparatively across models.

Oldroyd data: In comparison to LPTT-data and prior to t=3 units, the Oldroyd profiles of Fig. 7.13a and Fig. 7.14a reflect delay in phase and about half the peak-to-

peak time-period. For $t \leq 1$ unit, these Oldroyd profiles show greater resistance to amplitude of oscillation. The Oldroyd central filament-core initially swells up to t=2 units, whilst Giesekus and LPTT filaments initially thin to $t \approx 1$ unit. There is a slight hint of a double-bulge formation at t=1 unit in the Oldroyd profiles. After t=5 units, Oldroyd profiles enter long-time behaviour up to t=28 units.

Giesekus data: Over the relatively short and early process period $1 \leq t \leq 2$, the Giesekus filament profile demonstrates the more rapid thinning and necking-down at filament-centre, with fluid drainage to the feet, which consequently become more bulbous. No temporal oscillations/fluctuations are detected with the Giesekus model, and the process terminates earlier (t_f=2.7 units, Fig. 7.14a) due to excessive necking when stress levels rise sharply. This response may be attributed to the much reduced hardening of the Giesekus model and its related properties.

LPTT data: The LPTT profiles of Fig. 7.13a line up between those of Oldroyd and Giesekus at each sample time ($1 \leq t \leq 2$) considered. A prominent double-bulge formation is observed at $t \approx 2$ units, with local minima and maxima in shape and stress, both present in the filament central zone (Fig. 7.13a-c). As with Oldroyd solutions, again there is build up of radial wave-like structures, which eventually lead to central necking-down when t>5units. Around $t \approx 3$ units, such structures are beginning to merge into a single bulge/peak, which has occurred by $t \approx 10$ units. For LPTT($\xi \neq 0$) of Fig. 7.14a, necking down suddenly accelerates around $t \approx 13$ units (t>16, ξ=0), with larger stress generation than with ξ=0. Hence, solution failure occurs earlier with $\xi \neq 0$, just beyond $t \approx 16$, and at $t \approx 18$ for ξ=0.

Examining in greater detail the R_{mid} profiles of Fig. 7.14a, we may gather further quantitative information relating to the filament centre evolution, discerning oscillatory behaviour in filament mid-plane radius for all models, bar Giesekus at early times ($t \leq 5$ units). These radial oscillations adopt the form of traveling waves transmitted axially along the filament between the plates. The variation in $R_{mid}(t)$ for LPTT(ξ=0.13) departs from that of (ξ=0) around t=4 units, yet overall, these two

LPTT-versions behave in a similar fashion. The *slightly* larger amplitude oscillation is displayed by the ($\xi\neq0$)-solution during the early fluctuation period, whilst for the ($\xi=0$)-solution, the filament-core is thicker at all times beyond t=4 units. The rheological distinction that may be drawn between these two LPTT-versions lies in the more premature shear-thinning response of the ($\xi\neq0$)-form, with onset a decade earlier at deformation-rates O(1). Hence, one might expect minor differences in solutions over regions where shearing effects are more prominent (see Fig. 7.13b,c, stress between foot-to-centre, early times $t\leq5$). The Oldroyd-B fluid filament thins at the slowest rate compared to other model alternatives. Hence, beyond the early fluctuation period (up to t=5 units), the central section of the filament is thickest for the Oldroyd fluid, leading to longer life-span of the thinning filament. One may attach this response to the larger resistive tensile stress and the most severe strain-hardening property of this model over its counterparts (as noted in Rodd et al. [71] under increased molecular weight). In contrast to Oldroyd solutions, both Giesekus and LPTT filaments neck-down earlier to a fine thread in the central region (see R_{mid} profiles of Fig. 7.14a, also filament-shape profiles and stress contours fields of Fig. 7.13a-c); most rapid is for Giesekus of t=O(2.5); then, LPTT with t=O(16-18) units. Once again, the reason for such differences in flow response may be principally attributed to the relative strain hardening properties of these fluid models. During the early stress-relaxation phase up to say $t\leq10$, the Oldroyd-fluid displays the greater extensional stress that translates to thicker filament centres (Fig. 7.13b and Fig. 7.14b). The situation reverses around the time ($t\approx10$) when LPTT-filaments enter their stress growth period and the final necking-down phase begins.

Filament foot structure: For reasons of fluid volume conservation, thicker filament centres correspond to greater foot pinching (thinner feet). Hence, when necking begins, more fluid is drawn into the filament feet, which expand accordingly. Comparing across models from Fig. 7.13a and at early times $1\leq t\leq2$, the Oldroyd-B fluid tends to generate most pinching close to the plates, followed next by LPTT solutions, whilst Giesekus solutions provide the more bulbous feet. Long-time response in LPTT

filament foot-structure reveals a more conical shape emerging, which is similar to that adopted at even longer filament duration times for the Oldroyd fluid. With the Oldroyd-fluid, the greater foot pinching at earlier times can be observed to correspond to shear stress maxima appearing in the neck of the foot (see stress contour plots up to $t \leq 5$, Fig. 7.13c). The peaks in R_{mid}, around t=2 and 5 units, provide the thicker filament centres and lead to the thinner feet formations, with these shear stress maxima. Subsequently, such stress maxima gradually shift towards the filament-centre in time, as apparent for $t \geq 10$ in Fig. 7.13c plots. For the alternative two models, such stresses are lower in magnitude and consequently there is less tendency to sharpness of foot pinching. LPTT solutions reflect a peak in R_{mid} between t=2 and 3 units, which again produces shear stress maxima in the neck of the foot over this time period. In this instance, since radial fluctuation dies away subsequently, again shear stress-maxima migrate to the filament centre for $t \geq 3$.

7.4.1.3 Influence of capillary forces, LPTT (ξ=0); L/D=2, β=0.262, F_g=0.122

The influence of surface tension is examined by varying the capillary number through the surface tension coefficient. The LPTT (ξ=0)-model is considered, with the standard case of aspect ratio of L/D=2 and β=0.262 for inverse capillary numbers of (0.1, 0.5, 1.0). This choice proves richer in solution features to analyze. By comparing temporal evolution in R_{mid}-profiles across the various parameter settings and for relative perspective R_{mid}/R_0, (Fig. 7.15a, where $R_0=R_{mid}(t=0)$), interpretation may be drawn re the overall influence of larger capillary forces upon features such as: periods of strong radial fluctuations, and also onset, rate and duration of the necking-down process. This information may be read alongside the representation of full filament patterns, sampled through the relevant time periods, providing further insight on deformation patterns and balance between the processes of necking-down (at filament centre) to gradual sucking out of fluid to the filament feet. Capillary forces have barely had time to take effect up to $t \approx 1$ unit. Beyond this time up to $t \approx 4$ units, significant radial fluctuations are observed in the (Ca^{-1}=0.1)-data, reaching troughs and peaks in

R_{mid} at t≈(1, 2.5, 4) units. Through the filament length and viewed about the mid-plane (see Fig. 7.16 for filament-profile movement), this provides localised bulges in the upper and lower portions of the filament. These structures travel axially along the filament length in time (over 1≤t≤6 units), towards the plate in each half-filament portion, before merging with the developing foot structure. With the (Ca^{-1}=0.1)-data and in comparison across the three (Ca^{-1})-instances, necking-down commences around t≈5, and continues throughout the longest time period sampled up to t=18 units. Note, that (Ca^{-1}=0.1) corresponds to the selected material surface tension coefficient, χ= 0.03 Nm^{-1}. In relative terms, the Ca^{-1}=(0.5, 1.0) data in R_{mid} reflect the increased suppression of early radial fluctuations throughout the filament, reducing this time period from O(5) for Ca^{-1}=0.1, to O(2) for Ca^{-1}=0.5. With Ca^{-1}=1, this feature has been almost completely suppressed, so that necking down begins directly after step-strain commences at the most rapid rate, terminating at t=4 units. For Ca^{-1}=0.5, necking down commences around t≈2 units, with rate-of-decline slightly less than that for Ca^{-1}=1.0, terminating at t≈6 units. In summary and as anticipated physically, the greater influence of capillary forces accelerates the rate of necking-down and reduces the tendency towards radial fluctuation. Such wave formation (undesirable experimentally) through the central core of the filament, transmits itself into greater top-bottom asymmetry in filament shape (Fig. 7.16 profiles). For Ca^{-1}=1.0, asymmetry is not appreciable, whilst with Ca^{-1}=0.5 there is only a slight hint of this in the feet formation, 4≤t≤5 units. Another noticeable feature is the gradual lengthening of the central necking filament portion as Ca^{-1} is elevated. This rises from approximately one-fifth of the filament length with Ca^{-1}=0.1, to one-third of length for Ca^{-1}=0.5, and one-half of length at Ca^{-1}=1.0.

LPTT τ_{zz}-midplane data: Alongside data on R_{mid}, the τ_{zz}-midplane data track resultant stress development over equivalent time phases. The early decay of τ_{zz}-stress is apparent only for Ca^{-1}<1.0 and up to t≈2.0 units. The final filament failure period, where there is rapid rise in stress, occurs during the last time unit prior to ultimate

termination in each case (just before filament break-up occurs). Only the (Ca^{-1}=0.1)-data yields a relatively constant mid-plane stress state over a sustained period, 3≤t≤15 units (see also Fig. 7.14b). Upon increasing Ca^{-1}, the fluid representation will display greater surface tension influence, with the same viscosity (μ_0), initial stretch-rate ($\dot{\varepsilon}_0$) and length (L_0). The greater the influence of surface tension, the sooner the fluid will break, as this forcing effect tends to dominate. The axial stress τ_{zz} is highly sensitive to decrease in capillary number (Ca^{-1} increase). For Ca^{-1}=1 and at early times (t<3 units), some oscillation in stress is apparent at the mid-plane, increasing thereafter to reach a large τ_{zz}-mid-plane value above 1200 units by t≈3 units.

7.4.1.4 Influence of gravitational body forces; Giesekus and LPTT

Giesekus data: Solutions for the Giesekus model are considered, both under the influence of body force (F_g=0.122) and without. With this model, one observes negligible impact of body forces as the step-strain period is comparably short. This is made apparent through R_{mid} (Fig. 7.17a) and τ_{zz}-profile plots Fig. 7.17b), alongside filament evolution shapes (Fig. 7.17c). Only slight differences in free-surface shapes may be inferred over 0≤t≤2.5, filament centres being consistently thinner at equivalent times for (F_g≠0)-data. With body force inclusion, the stress at the filament centre is barely changing over 0≤t≤2, with upturn and sharp rise at t≈2. This state continues up to filament failure at t≈2.5, hence, during the final one-fifth of the step-strain period. For the case devoid of body forces, filament-centre stress displays consistently larger values than when body forces are acting for t≤2.3, reversing in dominance beyond this time up to final failure. From filament evolution shapes of Fig. 7.17c, it is possible to distinguish slight asymmetry in the feet structure of (F_g≠0)-solutions through overlaid differences between the top-foot and bottom-foot. Gravitational influence is to drag the filament downwards and to swell the lower foot. The central core section is extremely thin and no shape difference can be detected there. Free-surface profiles for radial coordinate and stress of Fig. 7.18, supplement this information in a more quantitative manner. From this, we are able to detect the asymmetry in stress that emerges through

time, with off-centre maxima of 23 units for ($F_g \neq 0$). Symmetry about the mid-plane is observed for ($F_g=0$) with maxima on-centre of 15 units. Profile shapes with/without gravitational force, are almost identical. There is an interesting point of inflection that emerges in surface curvature at the throat of the filament-foot after t=1.5 (see Fig. 7.18a,c), which is clearly present by t=2 units.

LPTT data: There are some slight changes with LPTT fluids from the observations for Giesekus fluids and body force inclusion. Here, for brevity, we consider only the LPTT ($\xi=0$) instance (see Fig. 7.19). Overall, there is more of a tendency to strong and early radial fluctuation, displayed at characteristic sample time $t\approx5$ shown in Fig. 7.19c (see also, $t\approx2$ in Fig. 3, Fig. 4a with $F_g \neq 0$). In Fig. 7.19a, there is larger departure in $R_{mid}(t)$ after $t\approx3$ between instances with and without body forces. As for Gieskus above, the case with body force inclusion ultimately necks down slightly more rapidly, generating larger stress maxima for $t>12$, and terminating in solution earlier ($t\approx18$ versus $t\approx20$ in Fig. 7.19b). With respect to relaxation of mid-plane stress, both with and without body force, the initial stress value and rate of decline adjust over a similar relaxation period, $0\leq t\leq5$ units. From t=5 to around t=12 there is moderate growth, prior to the sharp necking period thereafter. Slightly greater asymmetry in filament shape is depicted by LPTT fluids with body force inclusion ($F_g \neq 0$), noting once again, the marginal top-bottom asymmetry introduced at the filament feet. In this case, the impact of body forces is practically negligible due to the dominance of viscous forces over gravitational forces. Here, the fluids considered have moderate viscosity levels of O(35 Pa s). For fluids with low-viscosity (mPa s), the problem would be quite different with large Ca^{-1}, where gravitational forces would dominate more and break-up would occur earlier. For fixed *Bo*, identical results would be achieved either by increasing Ca^{-1} or F_g, as both parameters are linearly proportional ($F_g = Bo * Ca^{-1} = \frac{gravitational\ forces}{viscous\ forces}$). In the present work *Bo* is not fixed, so some

variation is to be anticipated. For the range of Ca^{-1} considered, the largest value of unity reflects similar fluid response, with earlier thinning to break-up.

7.4.1.5 Variation in aspect ratio (L/D); Giesekus

To demonstrate the practical implications of variation in final filament aspect ratios adopted, we have investigated three choices of ratio Λ_f = for the Giesekus fluid, with β=0.262, Ca^{-1}=0.1 and F_g=0.122. Findings are reported comparatively across the three ratios at suitable sample times per Λ_f in terms of filament shapes, $R_{mid}(t)$ and profiles on the free-surface through shape and $\tau_{zz}(t)$ (see Fig. 7.20, Fig. 7.21).

Global inferences may be made from the outset. First, for low (short-fat) aspect ratios Λ_f =1, long-time relaxation periods are anticipated (10 units); there is no filament break-up (R_{mid} (t_f)>0) to observe, whilst minor asymmetry is detected in upper and lower feet formations. Second, longer aspect ratios Λ_f=2 and 3 behave in a similar fashion, showing the development of bulbous feet in a continuous monotonic fashion. The central part of the filament thins down, drawing the fluid into the feet, and excessive central thinning (necking) leads to ultimate numerical failure (as above). For the largest aspect ratio considered, the Λ_f=3 instance, the foot formation is even more bulbous than the case with Λ_f=2. Fig. 7.21 offers the quantitative description of Fig. 7.20, through free-surface profiles on shape and, correspondingly, axial stress $\tau_{zz}(t)$. This specifically covers the additional two new aspect ratios of L/D=(1, 3).

On R-surface and R_{mid}:- For Λ_f =1, there is shrinkage for t≤1, but not much adjustment thereafter. This is the only instance for Giesekus fluids, where some initial oscillation is observed (see Fig. 7.20e). With Λ_f =2, adjustment through time in the core is continuous and monotonic, yet the curvature at the filament throat displays the point of inflection as observed above in Fig. 7.18. This interferes with the central cylindrical shape that is restricted to about two-fifths (40%) of the filament. By Λ_f =3, the same behaviour of thinning at the core occurs as with Λ_f =2, but more ideal cylindrical structure is extracted, now over four-fifths (80%) of the full filament. This is the scenario to gather pure uniaxial extension conditions with cylindrical shape,

from which corresponding rheometrical data may be extracted. It would appear that ratios $2 \leq \Lambda_f \leq 3$ are preferable to establish such a position under present material considerations.

On τ_{zz} profile-data: For the low aspect ratio $\Lambda_f = 1$, there is only stress relaxation (Fig. 7.21b). This position adjusts to only stress growth at the filament core for the largest aspect-ratio considered, $\Lambda_f = 3$ (Fig. 7.21d). The intermediate case of $\Lambda_f = 2$ (in Fig. 7.18), essentially follows that of $\Lambda_f = 3$, but with some tendency to also relax in stress during the process ($0 \leq t \leq 1$, $F_g = 0$). Again, this reaffirms the positive attributes of Λ_f ratios larger than two.

7.4.1.6 Low polymeric viscosity ratio ($\beta = 0.915$); $Ca^{-1} = 0.1$, $F_g = 0.122$, various models

Next, we discuss the consequences of switching between the polymeric viscosity ratios, from high ($\beta = 0.262$) to low ($\beta = 0.915$), upon the ensuing filament deformation (Fig. 7.22-Fig. 7.26). All three fluids now more closely reflect the properties of Boger-fluids, with practically constant shear viscosity, whilst being strain-hardening to some degree. There are some obvious features that are worthy of note in the solutions predicted. First, one may comment on the impact of β-elevation upon the early-time response in the different fluid filaments. With this β-change, the level of initial mid-plane stress reduces for Oldroyd-filaments from O(30) to O(10) units (see Fig. 7.22*b*). The equivalent β-switch for LPTT-filaments yields stress reduction from O(15) to O(4) units (see Fig. 7.24*b*) and for Giesekus filaments from O(7) to O(0.7) (see Fig. 7.26*b*).

Oldroyd/LPTT-data: Correspondingly, the early-time radial fluctuations are affected differently for each fluid in turn. With ($\beta = 0.915$)-data, these are now *totally suppressed* with the LPTT-fluids, as occurs with the Giesekus filaments tested. These LPTT-fluids are observed to thin down directly from the R_{mid}-data of Fig. 7.24*a*, and from filament-shape evolution of Fig. 7.25. This would therefore also go hand-in-hand with expectation of reduction in the limiting strain-hardening plateaux for these fluids

through β-elevation. For Oldroyd-fluids likewise, there is some adjustment to these fluctuations, which occur earlier in phase, during the first two time units for (β=0.915)-data, in comparison to that for (β=0.262)-data (which are present for t≤5units, see Fig. 7.22*a* and Fig. 7.23). In addition, we can appreciate from the Oldroyd and LPTT-data that as β tends to unity (more solvent presence), there is a significant reduction in the period of duration of step-strain. This time period reduces by a factor of around one-third for Oldroyd-fluids (from 28 to 20 units), and by one-half for LPTT-fluids (from 16 to 8 units).

Giesekus-data: The time to filament break-up, or equivalently that for central column formation and breakage, doubles from t=2.5 for (β=0.262), to t=5.5 for (β=0.915). This outcome would appear to oppose that observed for the more exaggerated strain-hardening alternative two fluids. A possible explanation may lie in the underlying filament shapes (and stress) generated of Fig. 7.26. The more bulbous Giesekus feet at β=0.262, with thinner necked filament-core (see Fig. 7.17c), give rise to premature thinning and earlier termination than correspondingly for the (β=0.915)-case. The length of the central filament column at termination is also significantly different. At β=0.915, filament columns are extracted that are about half the total filament length, with correspondingly wider, less pinched feet. For β=0.262, the filament column is only about one-fifth of the final filament length.

The state of stress evolution within the Giesekus-filament, with β-adjustment from 0.262 to β=0.915 is most marked (Fig. 7.26). Over a sustained early period t≤1.5, τ_{zz}-midplane is O(0.7 units) for (β=0.915) and O(7 units) for (β=0.262); this substantiates a fourteen-fold increase. In particular, this difference in level of stressing has its impact upon the filament-foot shapes of Fig. 7.26, generating the point of inflection on the free-surface curvature of (β=0.262)-filaments, as in Fig. 7.18.

7.4.1.7 Material relaxation time (λ_{est}) and apparent extensional viscosity (μ_{app})

Apparent extensional viscosity ($\mu_{app}(t)$) and estimates of relaxation time (λ_{est}) may be taken from the $R_{mid}(t)$ data discussed above. For the high-polymeric/low-solvent base-case of (β=0.262) and L/D=2, the Giesekus data-set provides the best match to the theory and its assumptions. That is without early oscillatory disturbance to the filament structure and monotonic variation in slope of $R_{mid}(t)$-data. Other model data provide tight restriction on the time-windows of relevance, as derived from their stress growth data. The Giesekus data provides reasonable trends over time in $\mu_{app}(t)$, as gathered experimentally (see Anna & McKinley [17], English [81]), rising monotonically from $O(10^2)$ at early times, to $O(10^3)$ when approaching a time of 3 units. For the Giesekus model, when switching to the high-solvent/low-polymeric case with (β=0.915), stress levels dramatically decline and the trend in extensional viscosity follows this pattern likewise (see Fig. 7.27). The sharper rise at early times is lessened with (β=0.915), as the central filament core assumes more cylindrical form and is slower to neck down than for (β=0.262). The improved match of (L/D=3, β=0.262)-data to the necessary assumptions is also gathered from this plot, following a similar pattern to the (L/D=2)-data over the early time period up to 1.3 units, yet with a slightly more monotonic trend.

Similarly under the same assumptions, estimates of relaxation time may be gathered for any of these settings discussed with Giesekus data. For example, with (L/D=2, β=0.262)-data and taking sample times over the range $1.5 \le t \le 2.5$, one finds estimated dimensional relaxation time lies in the range $0.24 \le \lambda_{est} \le 0.21$s. Over the earlier time $0.0 \le t \le 1.5$, the estimated values are in the range $0.33 \le \lambda_{est} \le 0.35$s. Of these two estimates, the former around 0.22s is that coinciding with the final stress growth period. With (L/D=2, β=0.915)-data and the sample stress growth range $3.5 \le t \le 5.5$, the result is $0.20 \le \lambda_{est} \le 0.22$s. Earlier time estimates here would provide 0.49s. Clearly, the latter stress growth period data agree closely across the β-ratios. Encouragingly, these relaxation time estimates under either viscosity ratio yield a reasonable approximation

to the target value of 0.42s, as original material data adopted for this study (mean relaxation time measurement taken in the linear viscoelastic regime).

7.4.2 Conclusion

In this chapter, the capillary thinning (*CaBER*) step-strain filament stretching process has been simulated using an earlier established numerical procedure, a CM/*ALE* hybrid *fe/fv* method. Various fluid aspect-ratios and constitutive models (Oldroyd-B, Giesekus and LPTT) have been studied. The hybrid finite element/finite volume scheme with a problem-specific *CaBER-ALE* implementation has successfully captured sharp differences in filament curvature (beads/bulges, for example) and flow structure throughout its evolution. In high polymeric viscosity strain-hardening models with high aspect-ratio filaments, radial fluctuations and beads-like formations are observed with high polymeric-viscosity fluids and strain-hardening models. Prediction of the mid-filament radius R_{mid} evolution, and filament shape, conducted on a low polymeric Boger-type fluid (Oldroyd-B), has indicated qualitative agreement with equivalent experiments from the literature. No beads or asymmetries have been observed in such an instance. The radial fluctuations decline in magnitude as the aspect-ratio rises (from two, to three, to ten), so that they are not observed at the largest aspect-ratio of ten. At a fixed aspect-ratio, the impact of the degree of strain-hardening is an outstanding aspect. The development of radial-fluctuations is resisted by the excessive strain-hardening properties of the Oldroyd model. Whilst these fluctuations are more apparent for the intermediate-level strain-hardening LPTT model and absent for the weakly strain-hardening Giesekus model.

Considering the low polymeric Boger-type fluid (SM1-Fluid 1), with Oldroyd models and two further aspect-ratios, provides qualitative agreement with the relevant experiments recorded in the literature. This is observed in overall filament shape features, such as structures within the central core and feet. This can be concluded quantitatively via the comparison of the evolution of mid-filament radius R_{mid} through both prediction and experimental measurements. Further investigation is demanded to

resolve some deviation caused by start-up of step-strain. When the plate motion is suddenly brought to rest (impulsive step-change), yet this is difficult to approximate experimentally. In such a solvent-dominated instance with the aspect-ratios investigated, no beads-like formation or radial fluctuations are observed. Through this study on both low and high polymeric fluids, predicted estimates have been derived for apparent extensional viscosity and principal relaxation time. In this respect, close agreement has been achieved with the underlying experimental data, both on estimated relaxation time and the trend (range of values) in extensional viscosity.

This investigation has also addressed the numerical simulation of the step-strain process, using various constitutive models, final filament aspect-ratios and viscosity component fractions. A summary of our major findings may be stated as follows. The greater the effect of surface tension, the sooner the fluid will thin down, as then stronger necking (capillary) forces acts on the filament. When gravitational body force is taken into consideration, there are no significant adjustments to general observations, bar slight asymmetry in filament-shape. The case with body force inclusion, ultimately necks down slightly more rapidly, generating larger stress maxima at earlier times and terminating in solution earlier. Under various filament aspect-ratios tested, with Λ_f =1 there is shrinkage for $t \leq 1$, but not much adjustment thereafter. With Λ_f=2, adjustment through time in the core is continuous and monotonic, yet the curvature at the filament throat displays a point of inflection. By Λ_f =3, the same behaviour of thinning at the core occurs as with Λ_f=2, but more ideal cylindrical structure is extracted (more substantial length of cylinder). For the current problem, the setting ($2 \leq \Lambda_f \leq 3$) yields suitable core-filament structure, from which reasonable estimates can be made for associated rheometrical data in extensional viscosity and characteristic material time. The strain-hardening levels of the LPTT models tend to capture radial fluctuations, whilst these are damped by even greater strain-hardening with the Oldroyd model, and practically removed by much reduced strain-hardening under the Giesekus model. Such fluctuations tend to interfere with

ideal cylindrical filament shape. The shortest step-strain periods are generated by the Giesekus model, followed by LPTT, with the longest for the Oldroyd model. This is attributed to the larger tensile stresses that arise with more strain-hardening fluids, which tend to maintain thicker core to the filament to longer times. Adjustment of viscosity fractional component from high to low polymeric parts has revealed some differences in response during the step-strain period illustrated in free-surface profiles. For the more strain-hardening models of Oldroyd/LPTT, the fluid with high β-ratio displays more Newtonian-like behaviour and thins down faster compared to its low β-counterpart. The low β-ratio form yields more foot pinching, thicker filament core at all times, and consequently, a longer step-strain period. The converse is the case for the less strain-hardening Giesekus model, with the high β-ratio instance displaying the longer time to break-up. Here, it is the low β-case that provides the more bulbous filament feet, thinner core and shorter time to break-up.

Overall, this work has enabled the gathering of rheological properties and process settings to predict suitable windows for experimental operation, so that reliable rheometrical data may be extracted. In this manner, reasonable trends of increasing apparent extensional viscosity in time have been derived over acceptable ranges of values. In addition, point estimates for characteristic relaxation time are found to lie in close agreement with material data originally supplied.

Potentially fruitful directions for this work lie in the careful study of the effects of alternative modes of preliminary plate-separation (linear versus exponential), and possible variation in initial sample loadings (shapes). Such predictive knowledge would serve to aid more profound understanding of the *CaBER* procedure and its successful practical application in rheometrical measurement.

Parameter	symbol (unit)	value
Plate radius	R_{plate} (m)	$3.5* 10^{-3}$
Initial filament length	L_0 (m)	$1.89*10^{-3}$
Extension rate	$\dot{\varepsilon}_0$ (s^{-1})	4.48
Reynolds number	*Re*	$4.72* 10^{-4}$
capillary number	*Ca*	9.86
Bond number	*Bo*	1.203
Deborah number	De	1.886
zero shear viscosity, (Pa s)	μ_0	34.95
density, (kg/m^3)	ρ	1030
surface tension coefficient, (N/m)	χ	0.03

Table 7.4: Problem parameters and non-dimensional group numbers

β	Sample time	λ_{est}(s)	λ_{act}(s)
0.262	$0.0\leq t\leq 0.5$	0.35	0.42
	$0.5\leq t\leq 1.5$	0.33	
	$1.5\leq t\leq 2.0$	0.24	
	$2.0\leq t\leq 2.5$	0.21	
0.915	$0.0\leq t\leq 2.0$	0.48	0.42
	$2.0\leq t\leq 3.5$	0.50	
	$3.5\leq t\leq 4.9$	0.22	
	$4.9\leq t\leq 5.5$	0.20	

Table 7.5: Relaxation-time data; various sample time intervals; Giesekus; two viscosity ratios, L/D=2.

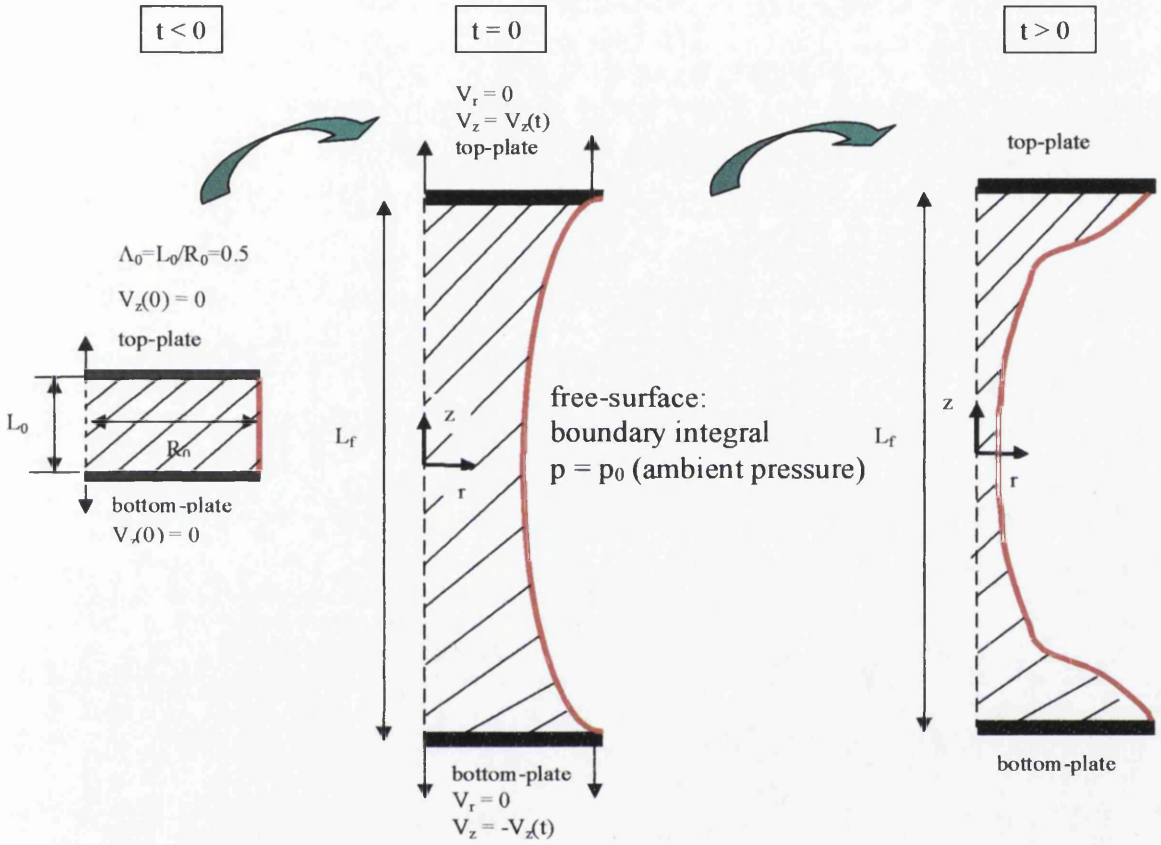

Fig. 7.11: Step-strain schematic diagram

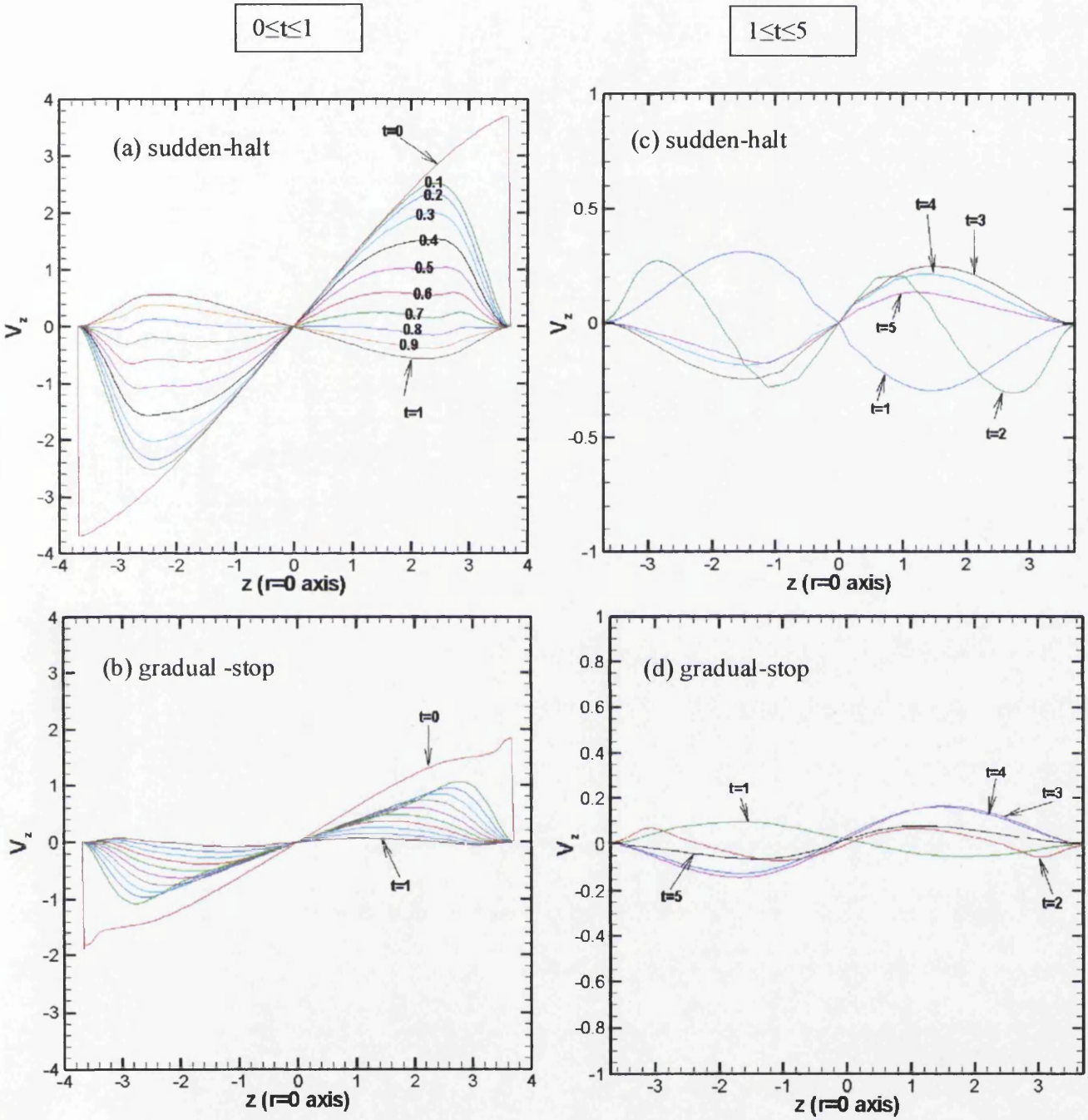

Fig. 7.12a-d: Variation stop criteria; LPTT(ξ=0); V_z(t) profiles; sudden-halt a) 0≤t≤1, c) 1≤t≤5; gradual-stop b) 0≤t≤1, d) 1≤t≤5; L/D=2, Ca^{-1}=0.1, F_g=0, β=0.262

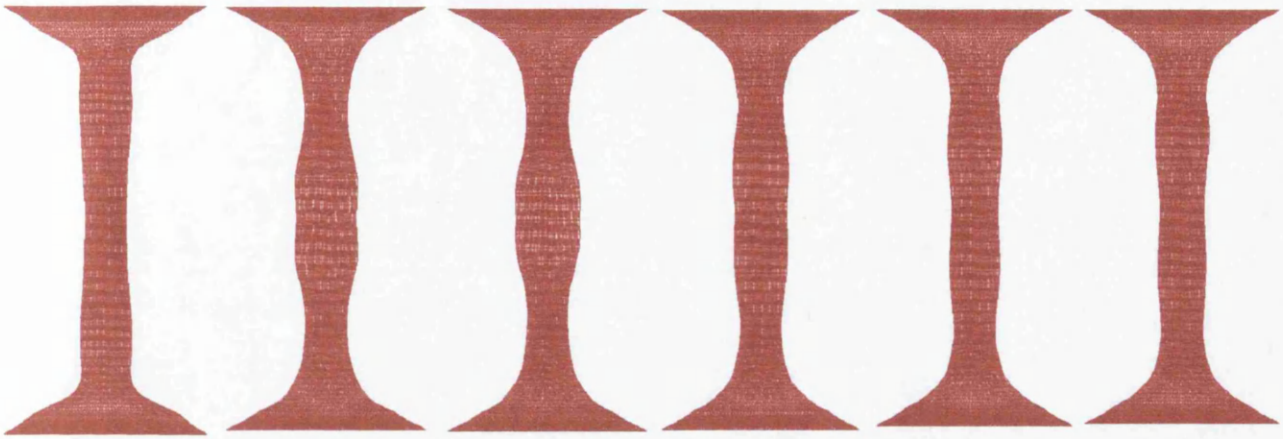

(e) Sudden-halt

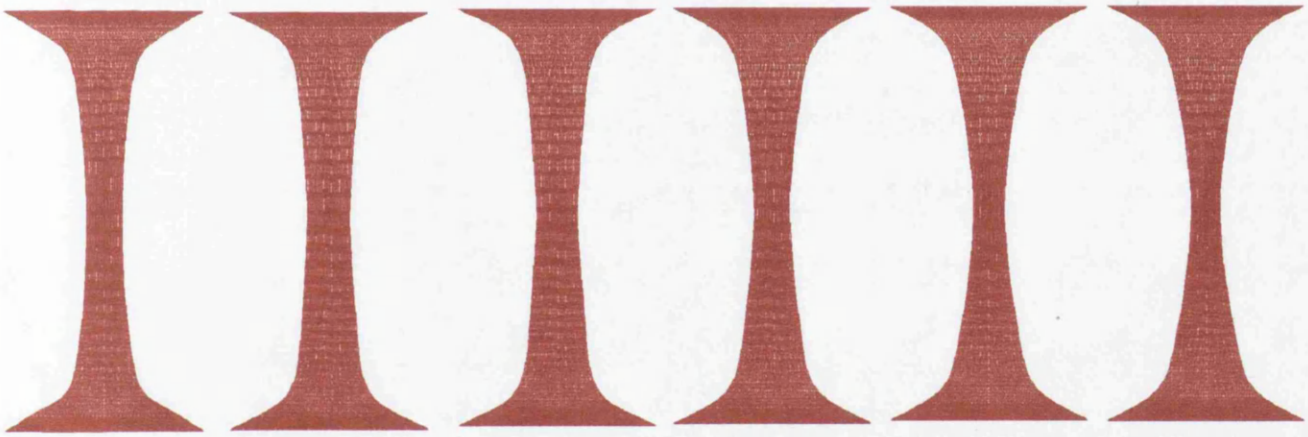

t=1 t=2 t=3 t=4 t=5 t=6

(f) Gradual-stop

Fig. 7.12e, f: Variation stop criteria; LPTT(ξ=0); e) sudden, f) gradual; filament shapes; $1 \le t \le 6$; L/D=2, Ca^{-1}=0.1, F_g=0, β=0.262

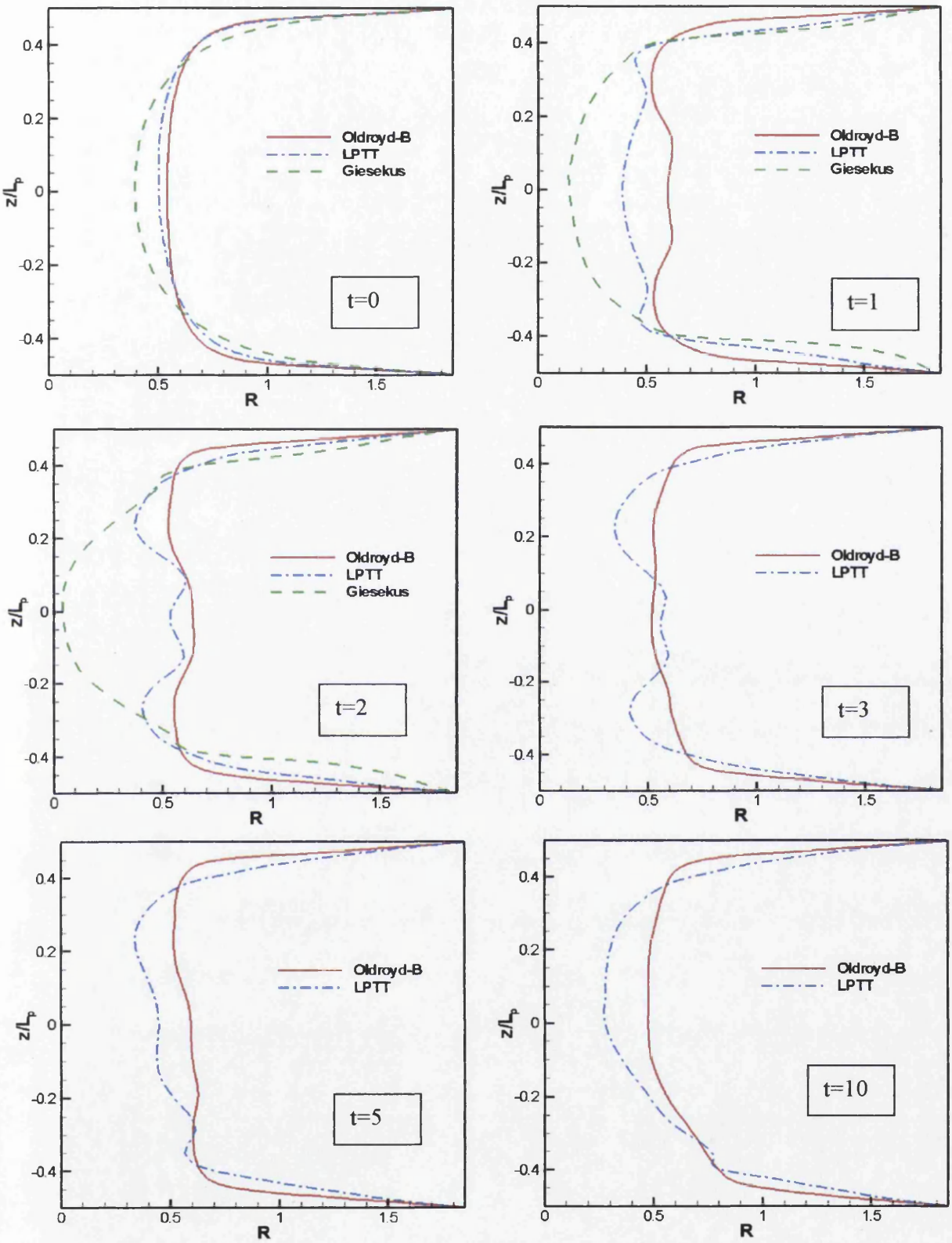

Fig. 7.13a: Filament shapes, various models (Giesekus, LPTT(ξ=0) and Oldroyd-B); $0 \le t \le 10$, β=0.262, Ca^{-1}=0.1, F_g=0.122, L/D=2

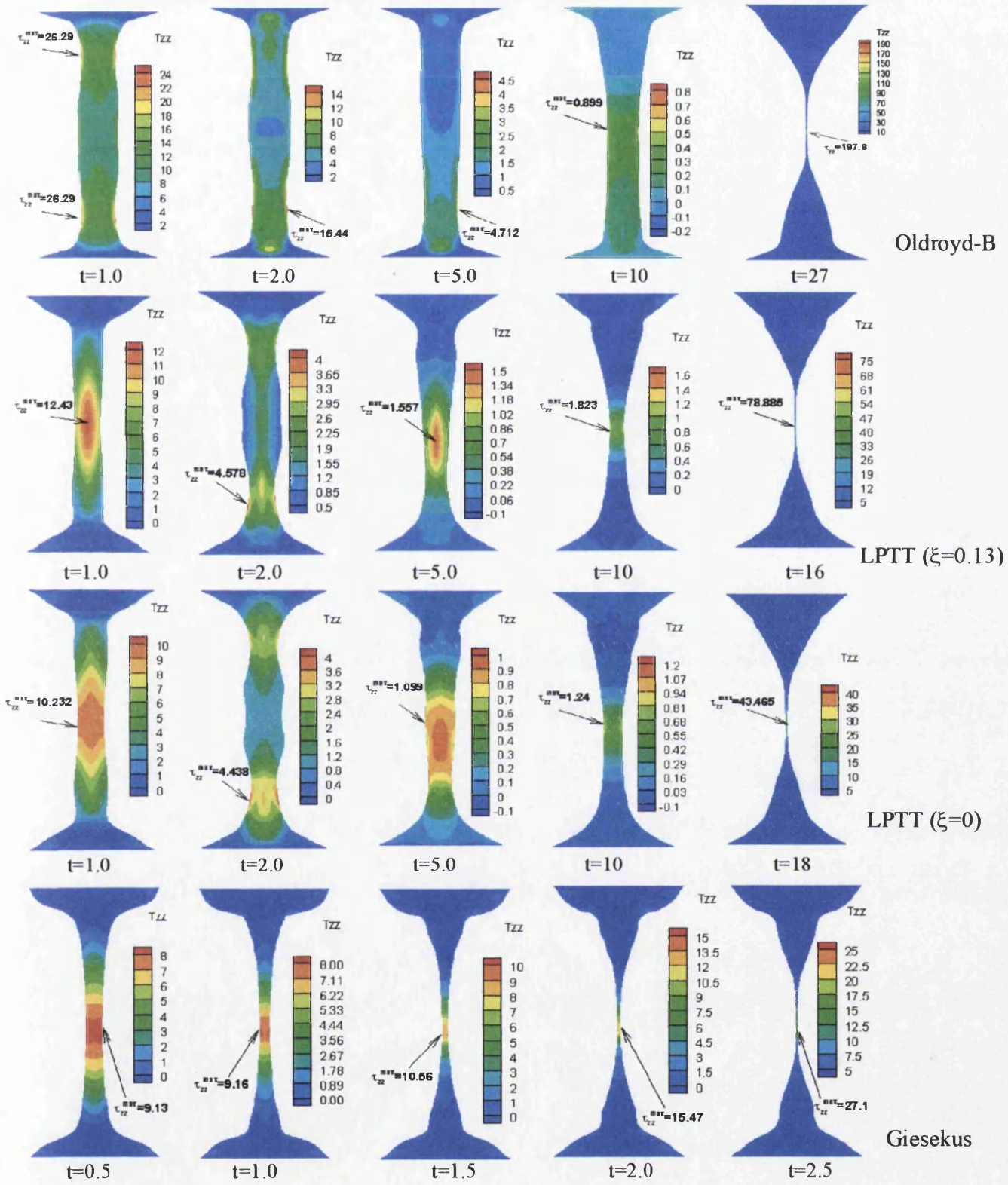

Fig. 7.13b: Filament axial stress (τ_{zz}) contours; various models, β=0.262, Ca^{-1}=0.1, F_g=0.122, L/D=2

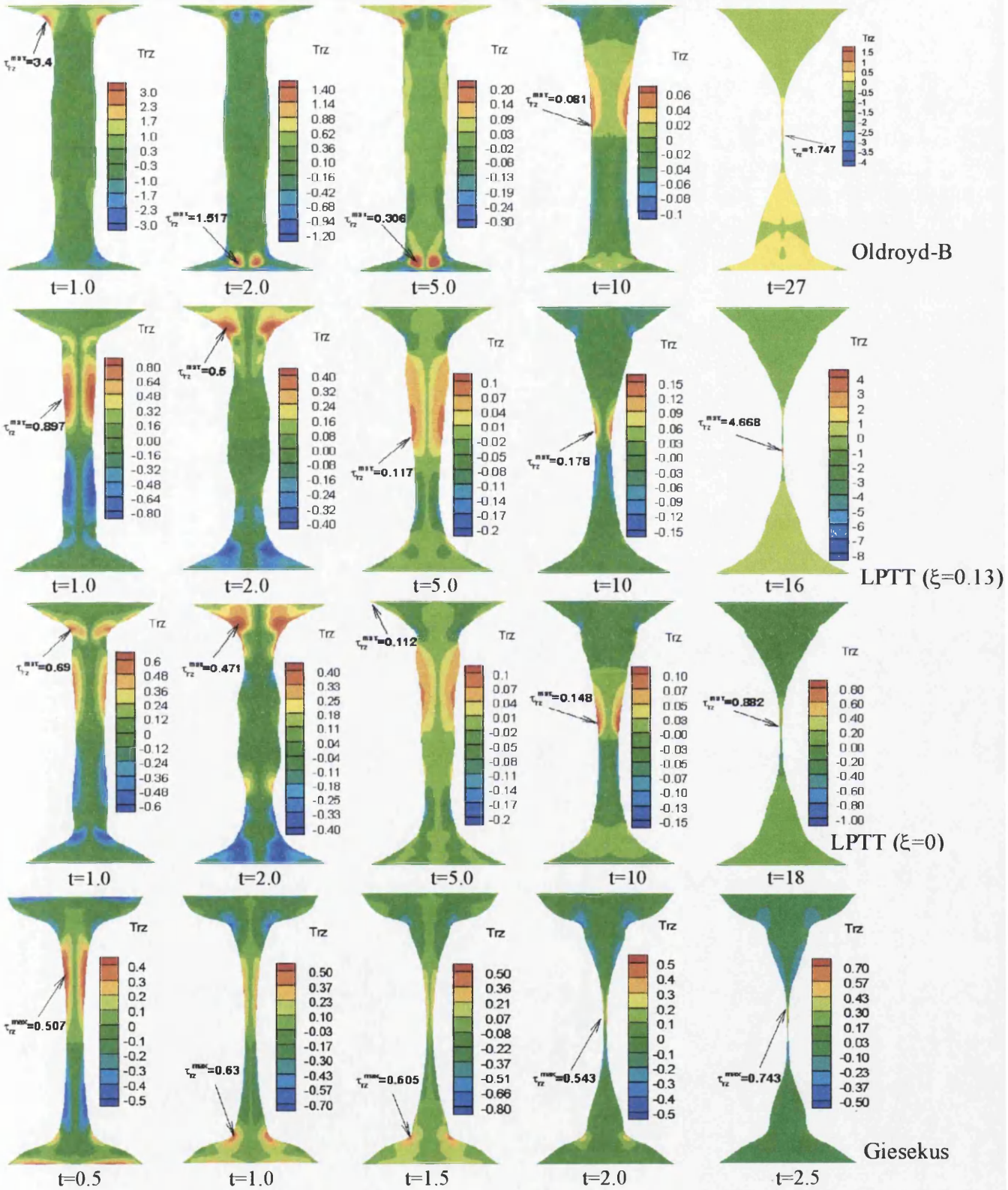

Fig. 7.13c: Filament shear stress (τ_{rz}) contours; various models, β=0.262, Ca^{-1}=0.1, F_g=0.122, L/D=2

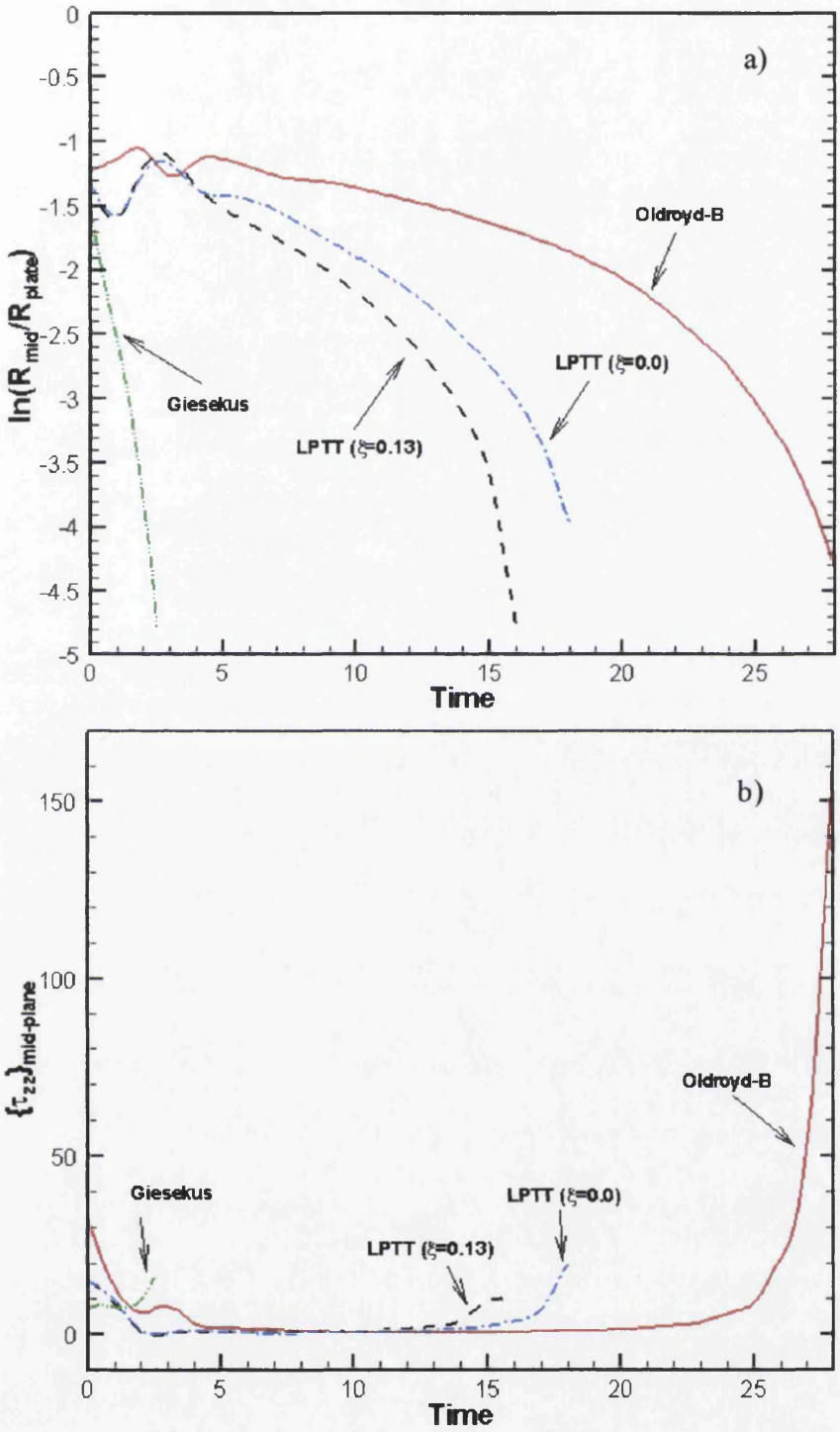

Fig. 7.14: Mid-plane axial stress and radial evolution; Oldroyd-B, LPTT(ξ=[0.13,0]) and Giesekus fluids; β=0.262, L/D=2.0, Ca^{-1}=0.1, F_g=0.122

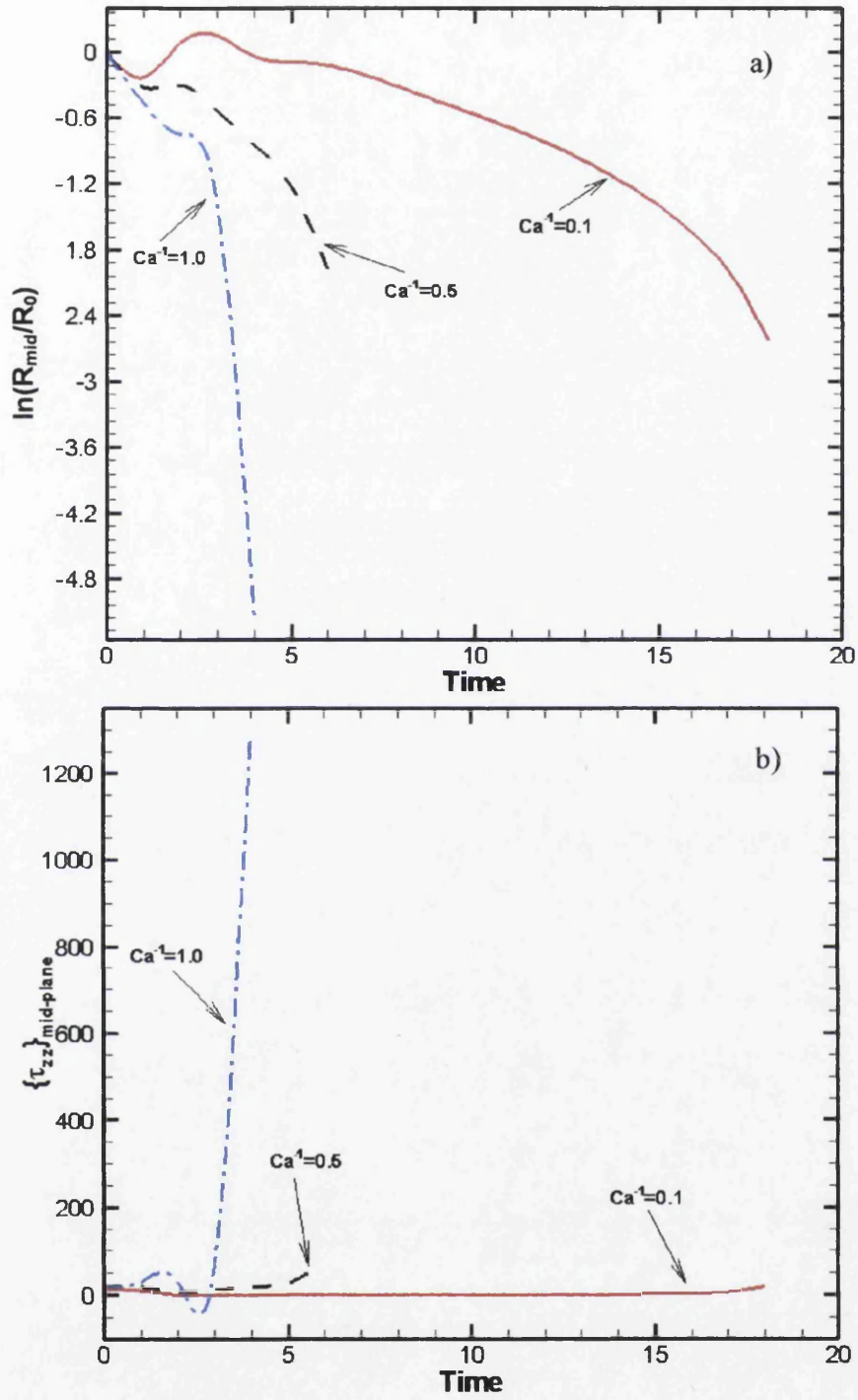

Fig. 7.15: Influence of capillary forces; LPTT(ξ=0), L/D=2, β=0.262, F_g=0.122, Ca^{-1}=0.1, 0.5 & 1; a) $\ln(R_{mid}/R_0)$, b) τ_{zz}-midplane

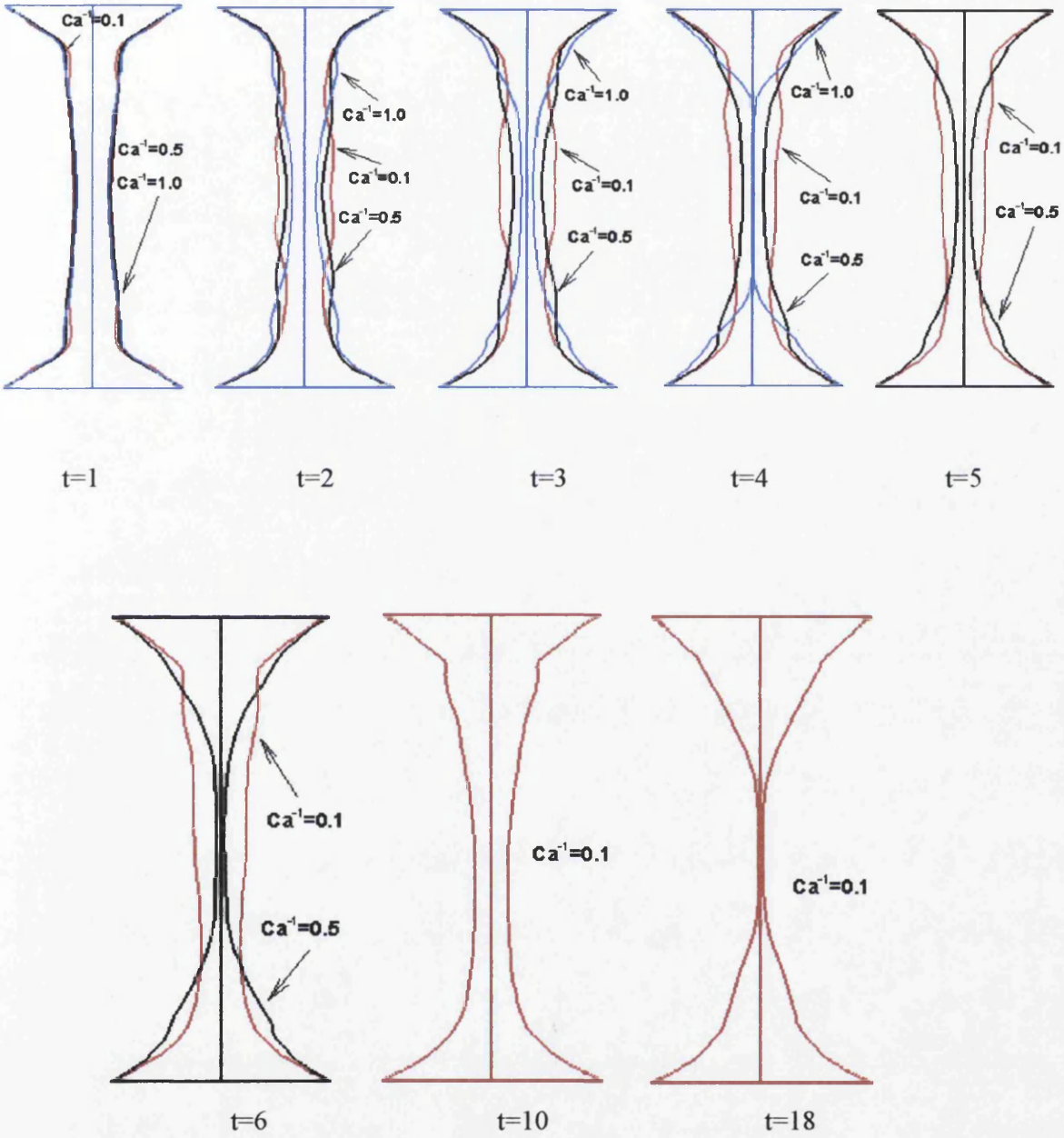

Fig. 7.16: Influence of capillary forces; deformation profiles; $1 \leq t \leq 18$, LPTT(ξ=0), L/D=2, β=0.262, F_g=0.122, Ca^{-1}=0.1, 0.5 & 1

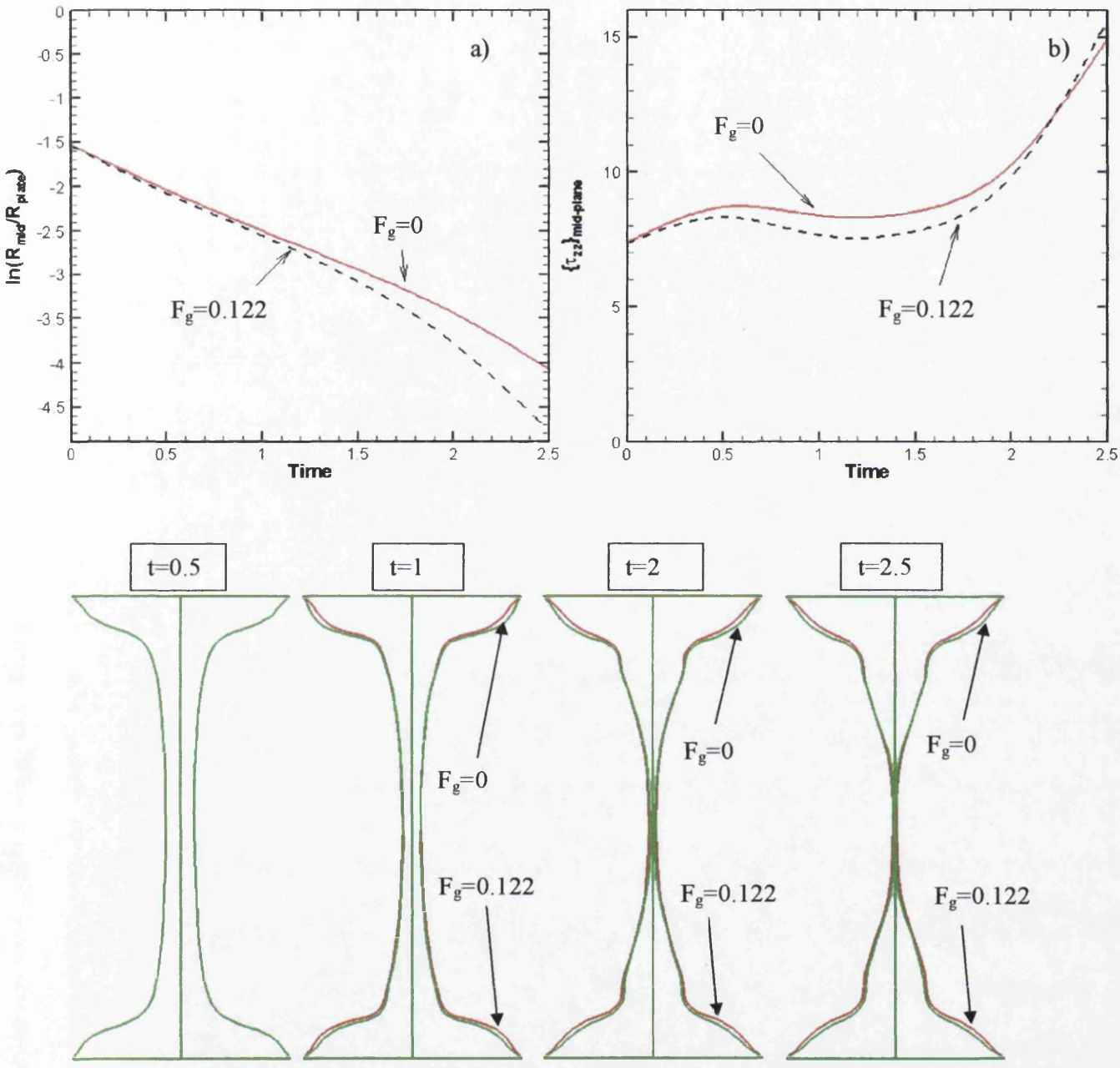

c) filament shapes

Fig. 7.17: Mid-plane axial stress and radial evolution; Giesekus; with and without body force; β=0.262, L/D=2.0, Ca^{-1}=0.1; a) R_{mid} and b) $(\tau_{zz})_{mid}$, c) filament shapes,shapes, t={0.5,1,2,2.5}

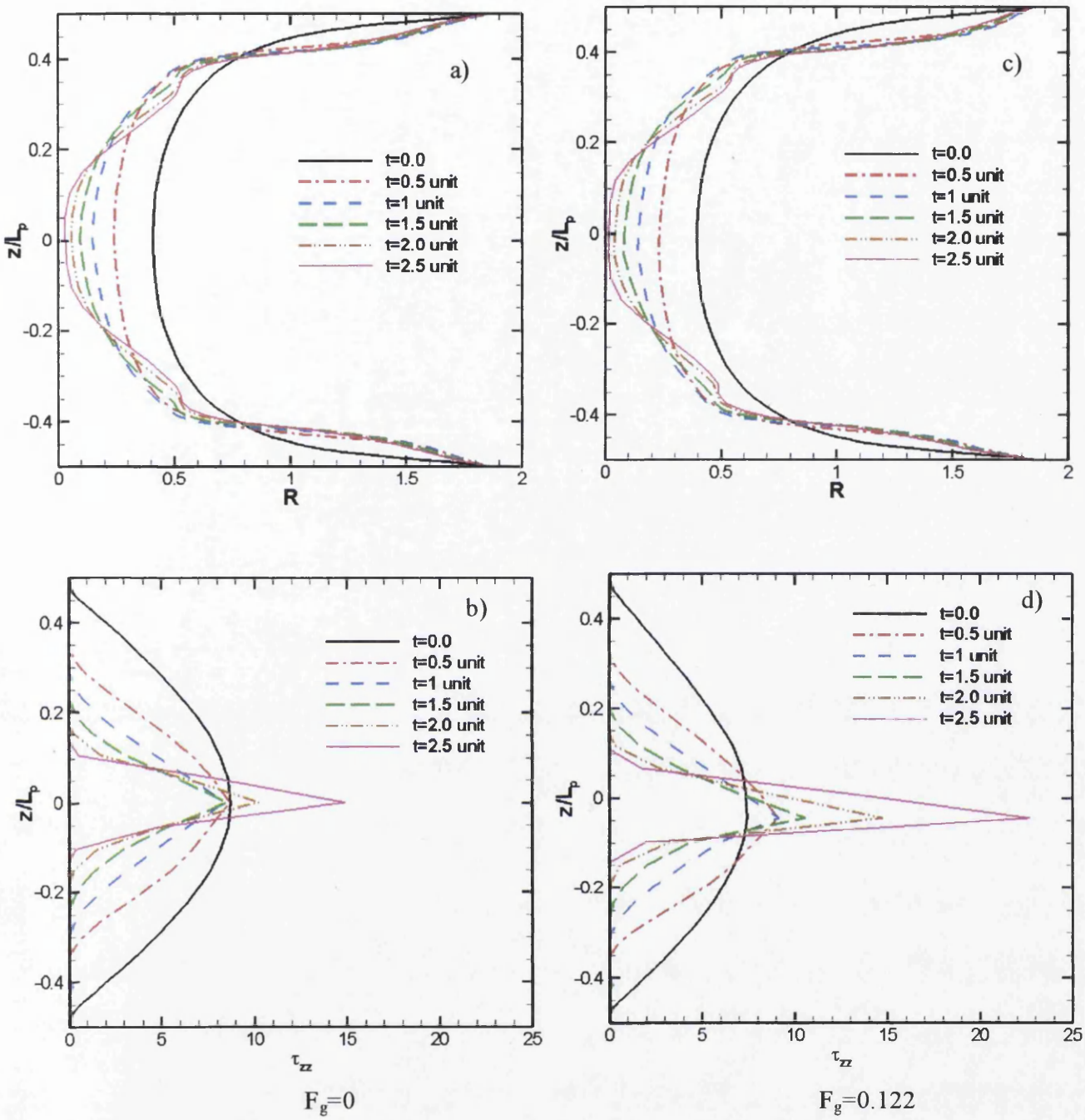

Fig. 7.18: Body force effects (F_g=0, 0.122); Giesekus; different times (0≤t≤2.5 units), L/D=2 (ε=2), Ca^{-1}=0.1, β=0.262

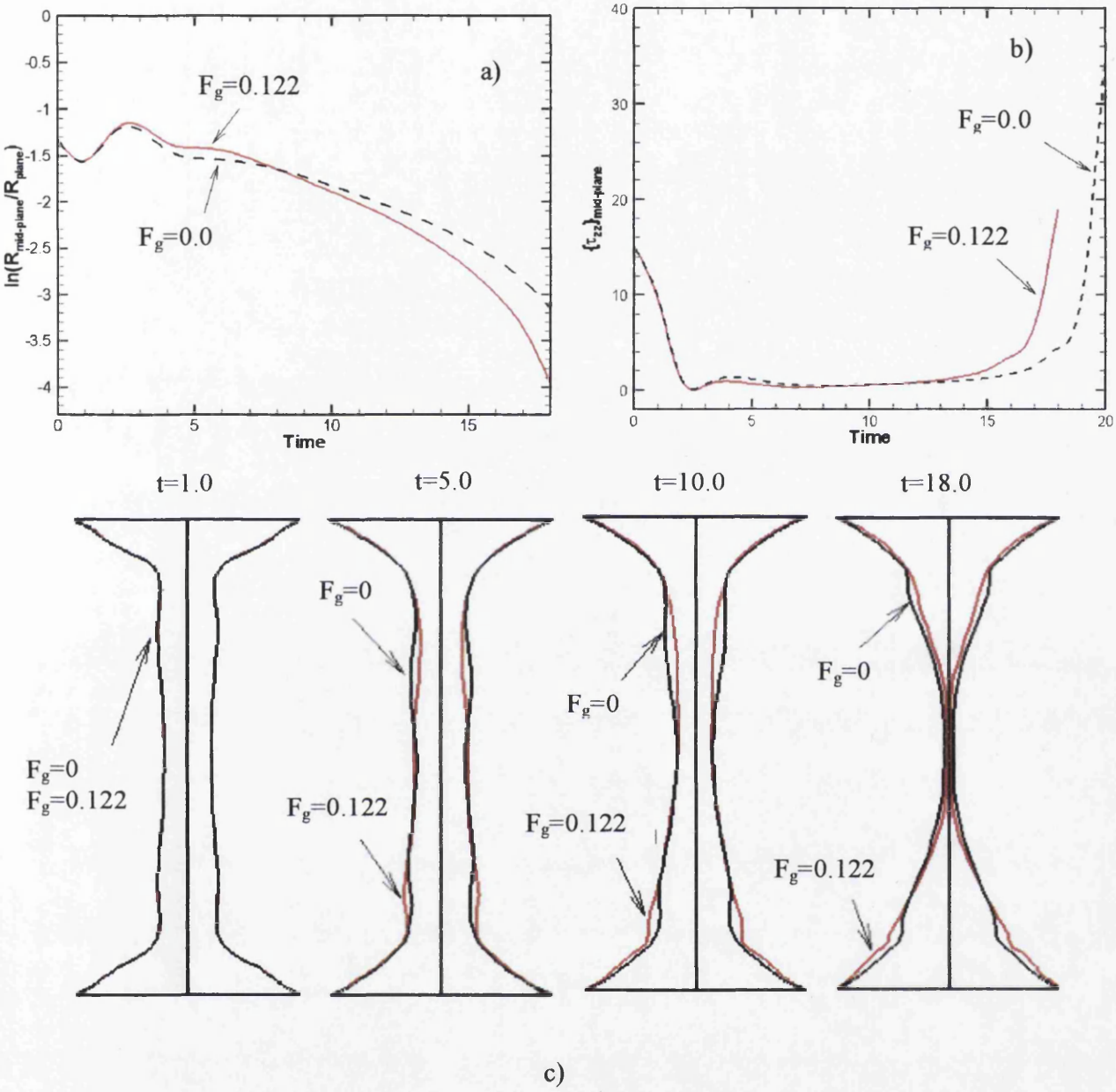

Fig. 7.19: Body force effects (F_g=0, 0.122); LPTT(ξ=0); various times ($0 \le t \le 18$); L/D=2 (ε=2),Ca^{-1}=0.1,β=0.262

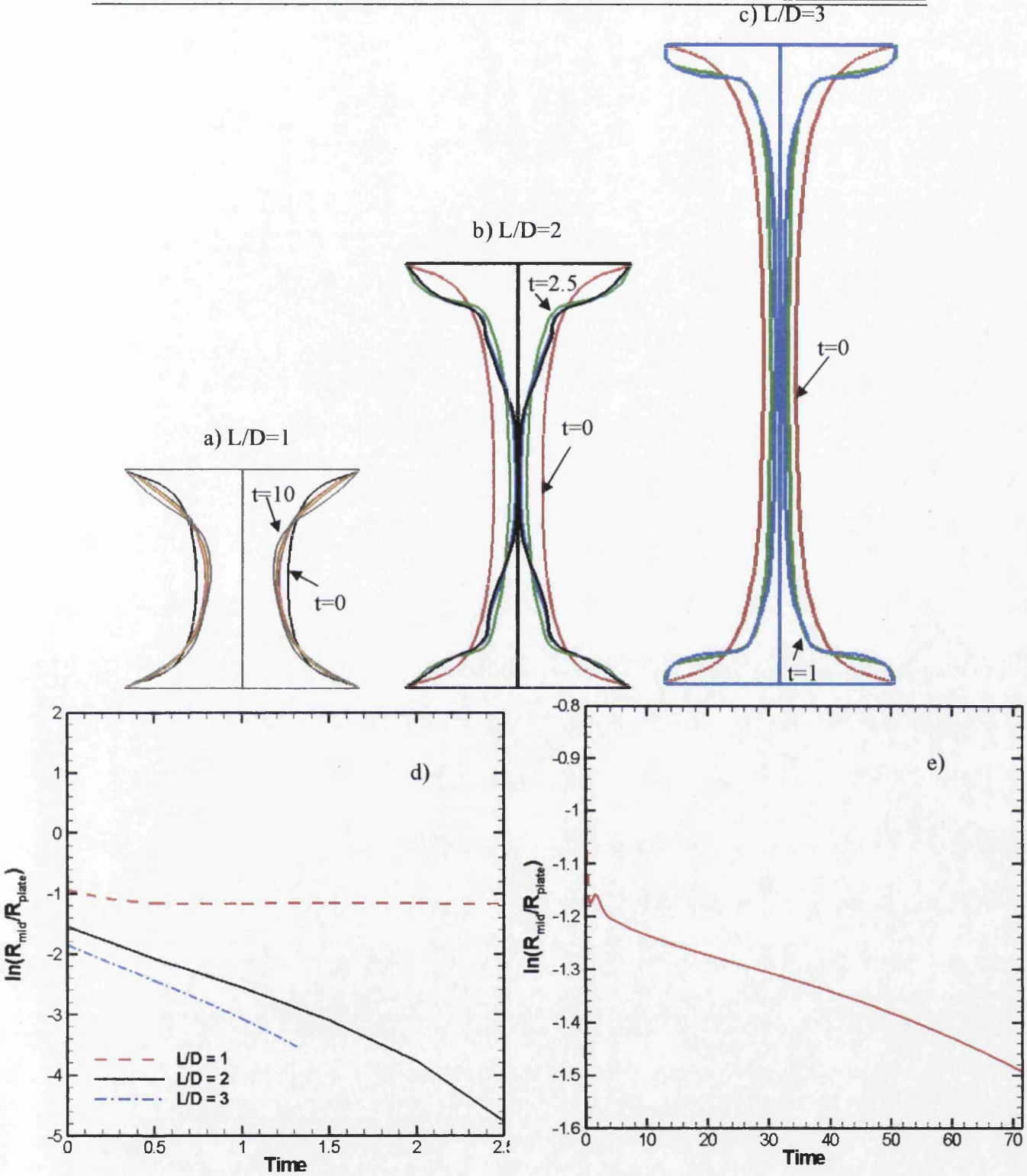

Fig. 7.20: Influence of initial aspect-ratio; Giesekus; Ca^{-1}=0.1, F_g=0.122, β=0.262: a) L/D=1, t=0, 1, 2, 3, 4, 5 & 10 units, b) L/D=2, t=0, 1, 2 & 2.5, c) L/D=3, t=0, 0.5 & 1; d) development of $R_{mid}(t)$, L/D=1, 2 & 3; e) development of $R_{mid}(t)$, L/D=1

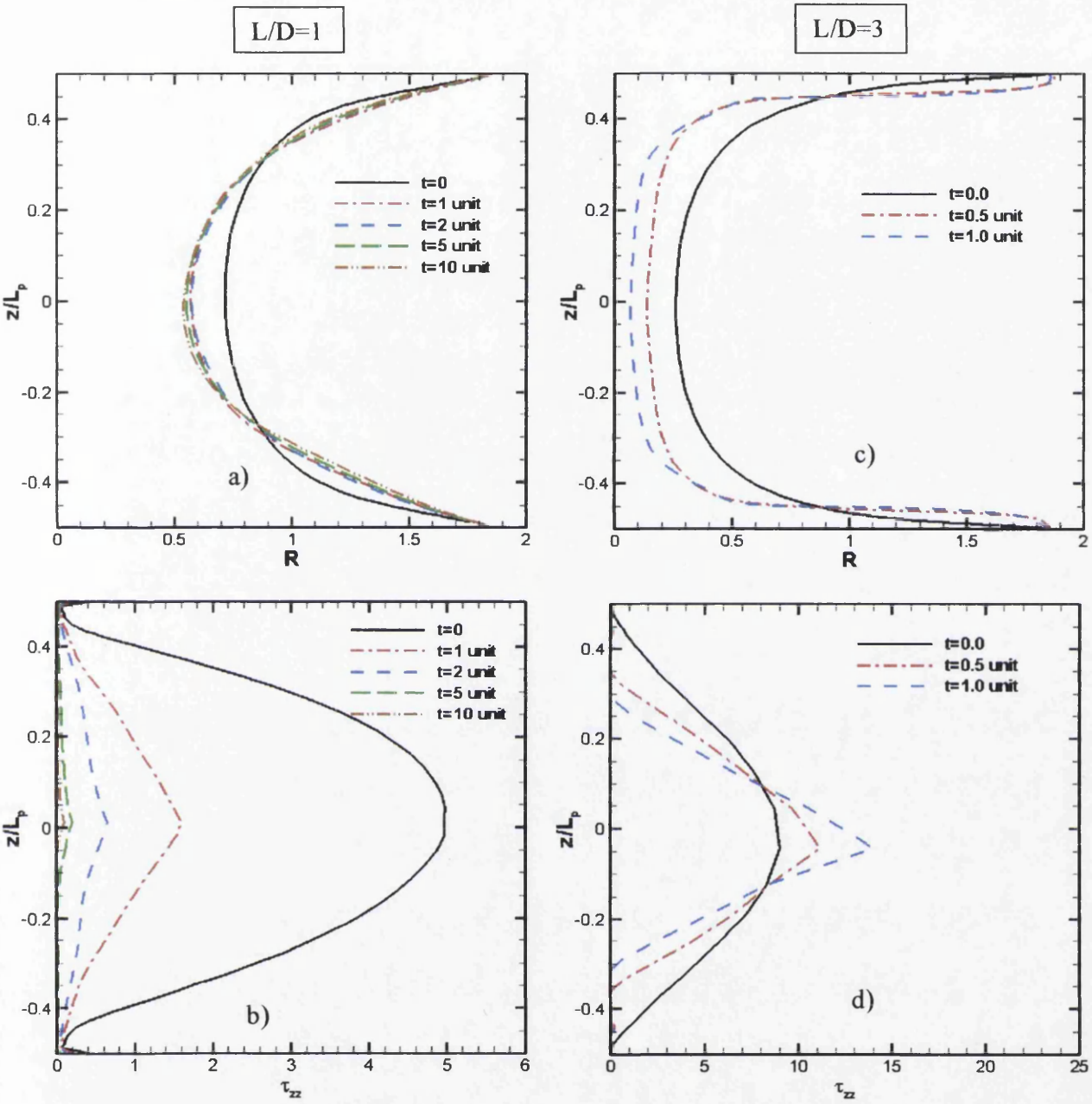

Fig. 7.21: Giesekus model, free-surface (R) and (τ_{zz}) profiles along free-surface; various times; β=0.262, Ca^{-1}=0.1, F_g=0.122; a), b) L/D=1; c), d) L/D=3

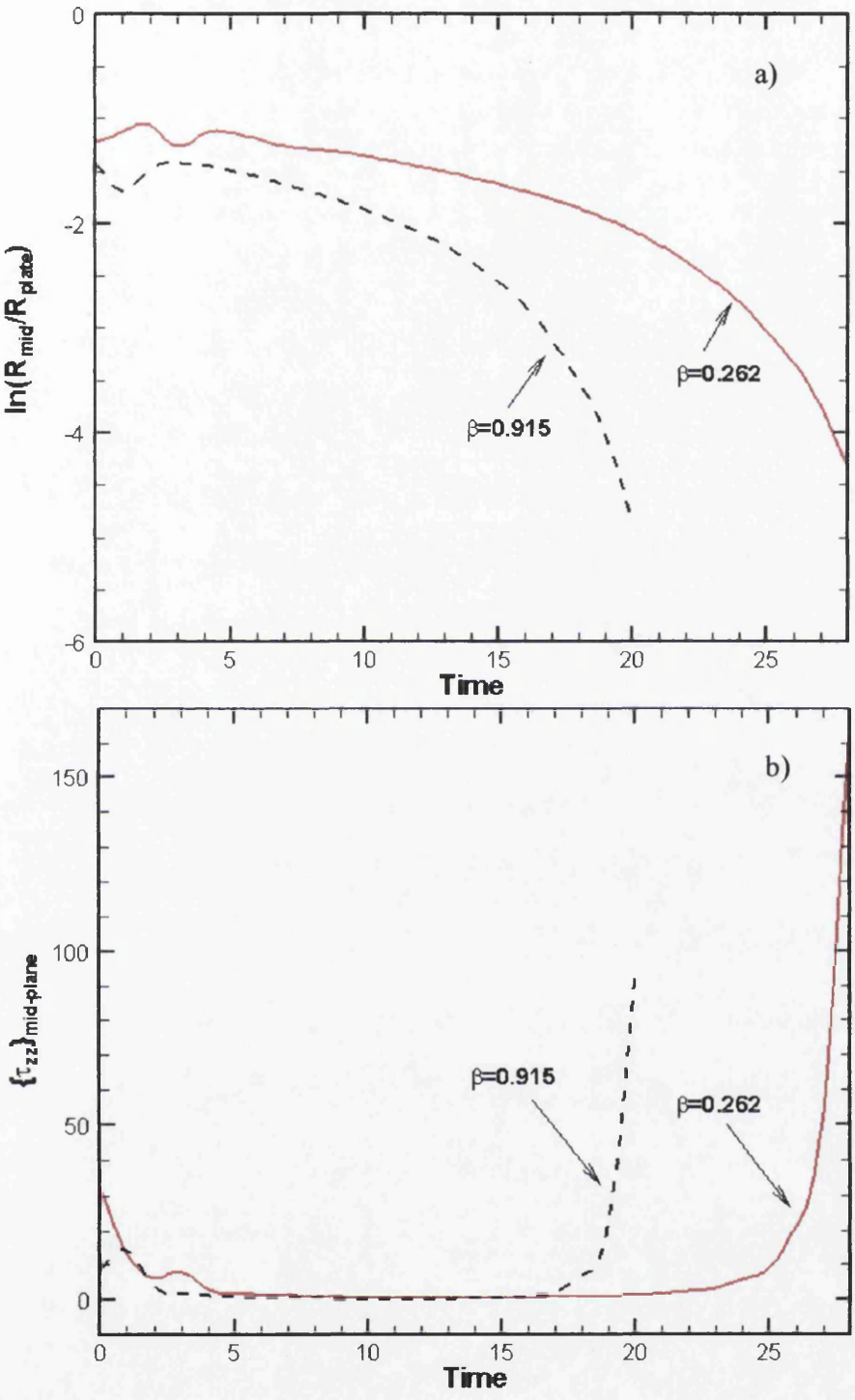

Fig. 7.22: Mid-plane axial stress and radial evolution; Oldroyd-B; β=(0.262, 0.915); L/D=2.0, Ca^{-1}=0.1, F_g=0.122

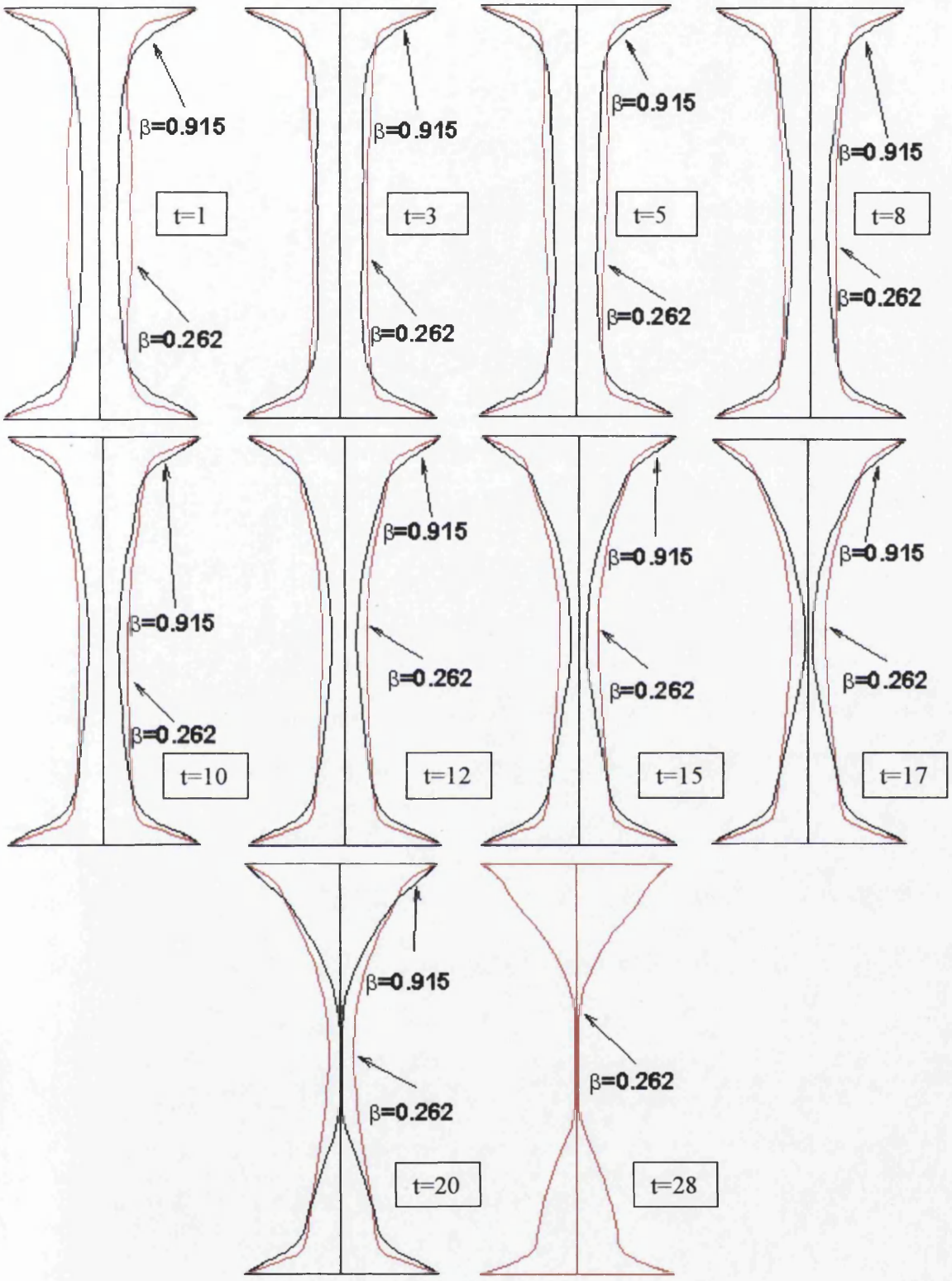

Fig. 7.23: Filament shapes; Oldroyd-B; β-ratio comparison (0.262, 0.915); $1 \leq t \leq 28$; $L/D=2, Ca^{-1}=0.1, F_g=0.122$

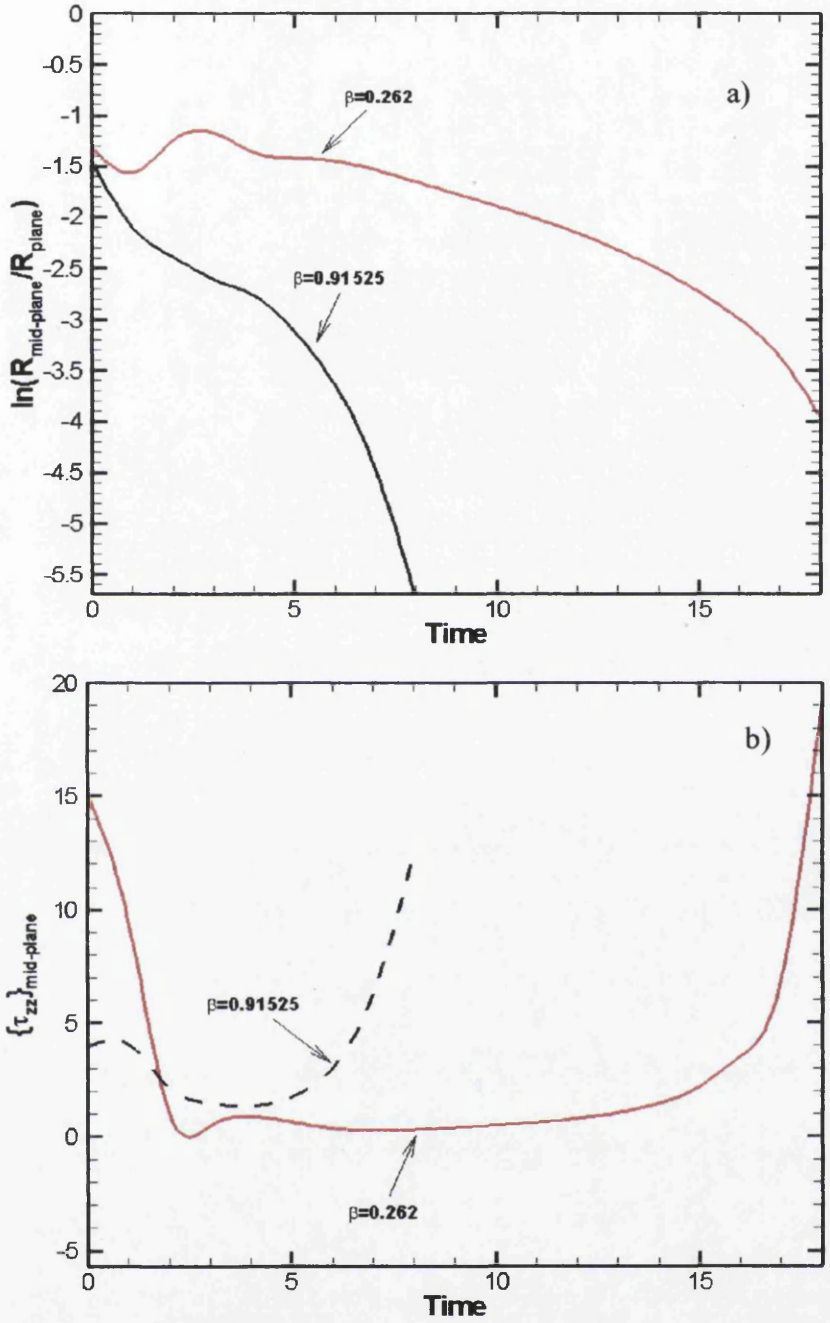

Fig. 7.24: β-ratio comparison (0.262, 0.915); LPTT(ξ=0); midplane a) R(t), b) $\tau_{zz}(t)$; L/D=2, Ca^{-1}=0.1, F_g=0.122

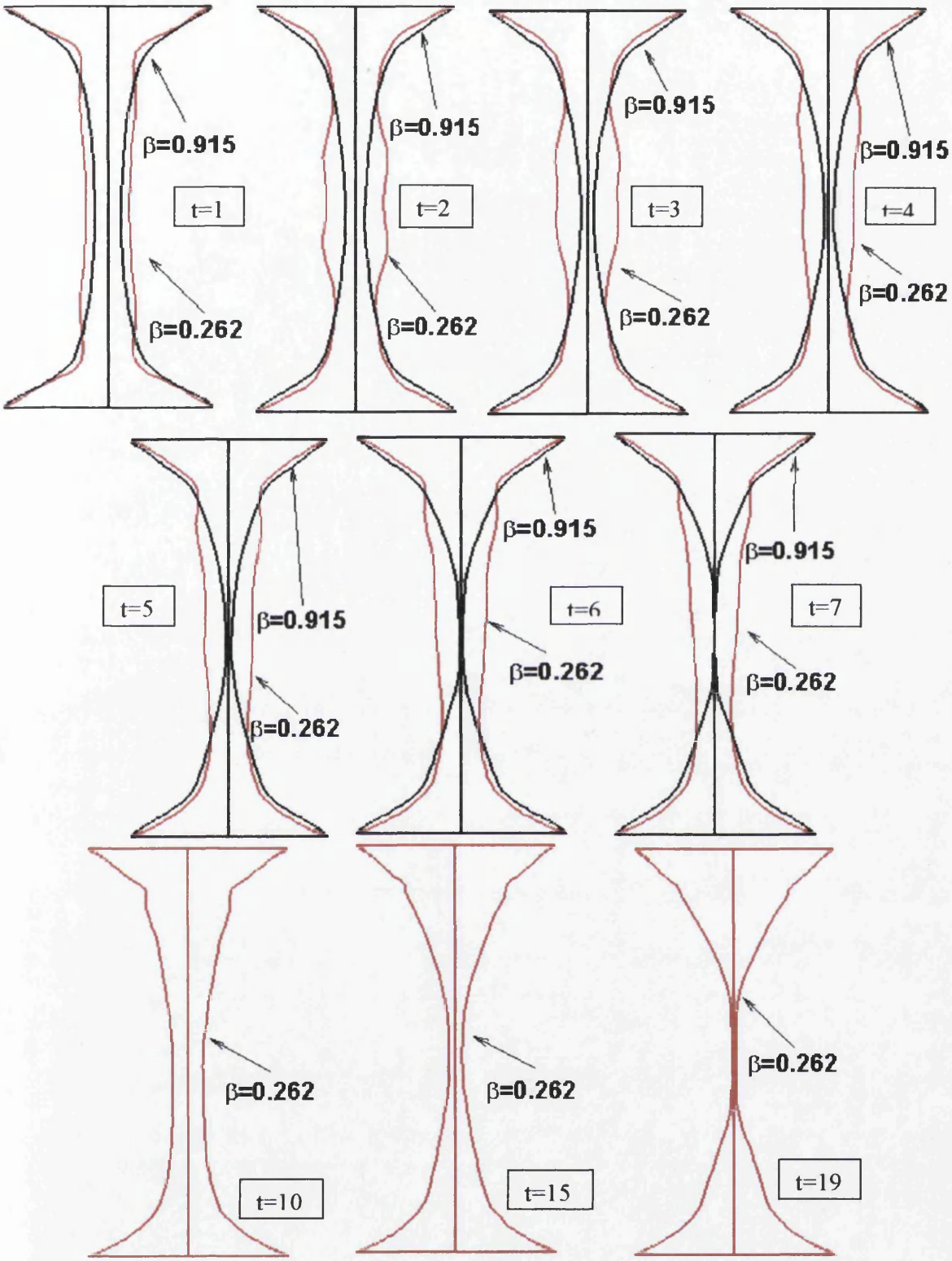

Fig. 7.25: β-ratio comparison (0.262, 0.915); filament shapes; LPTT(ξ=0); $1 \le t \le 19$; $L/D=2, Ca^{-1}=0.1, F_g=0.122$

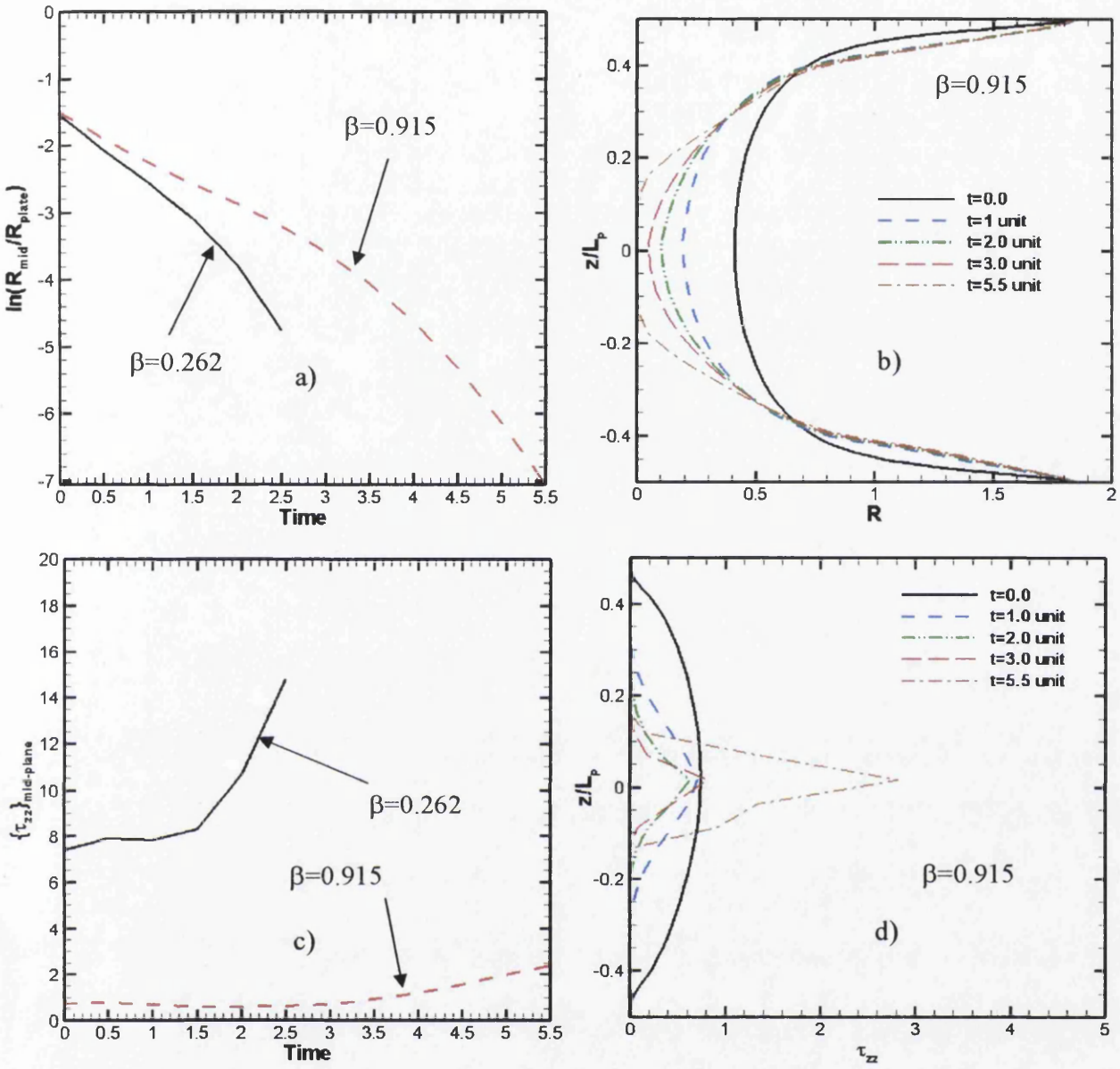

Fig. 7.26: β-ratio comparison (0.262, 0.915); Giesekus; midplane a) R(t), b) τ_{zz}; free-surface (β=0.915) c) R(t), d) τ_{zz}; L/D=2, Ca^{-1}=0.1, F_g=0.122

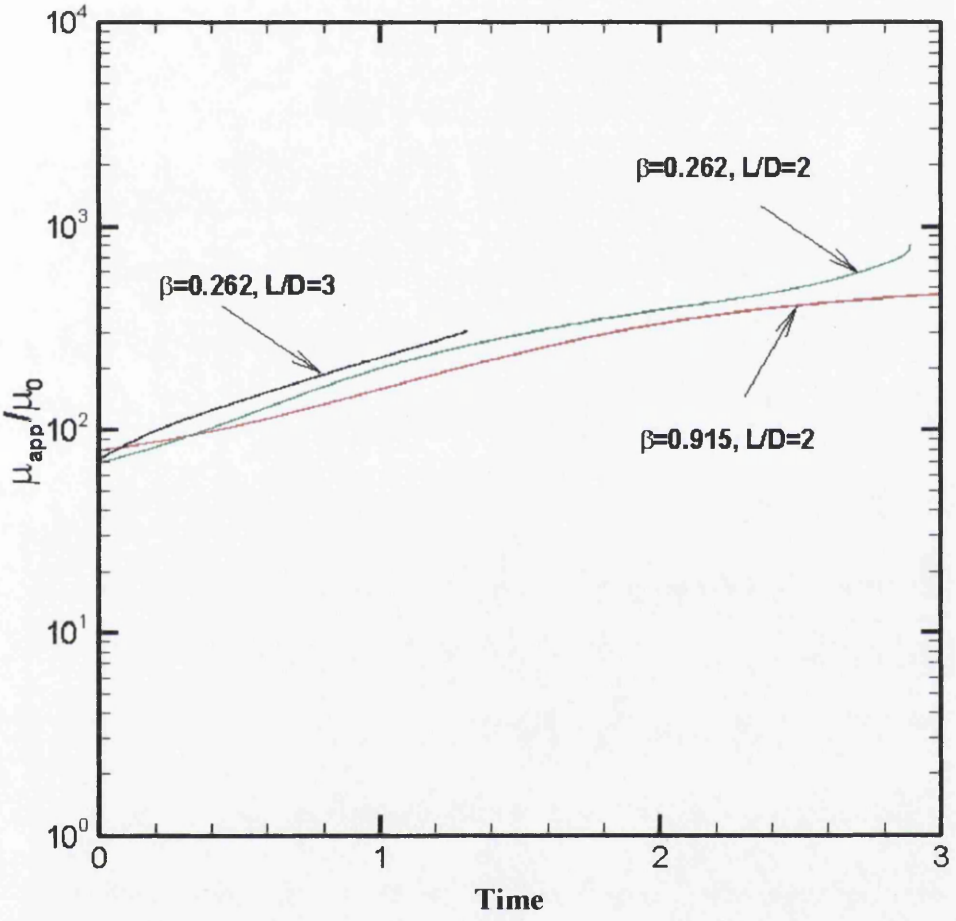

Fig. 7.27: Apparent extensional viscosity estimation; Giesekus model; F_g=0, Ca^{-1}=0.1

Chapter 8

Concluding Remarks and Suggestions

8.1 Concluding remarks

Simulation of axisymmetric filament-stretching and step-strain of viscoelastic fluid flows in two-dimensional geometry has been presented in this work. Effort has been placed upon relating fluid dynamic response to background rheometrical properties, such as extensional and shear viscosity. In particular, axial stress response in extensional flows displays a dependence on the degree of strain-hardening. That is, for fluids exhibiting less strain-hardening under prevailing stretching conditions, extra axial stress rises less sharply in magnitude. Stress and stretch fields also depend upon the associated material functions. It is possible to discern dominant deformation regimes in some instances within a specific region. As an example under stretching mode, fluid along the mid-plane centreline experiences pure elongational flow, whilst farther from the filament centre, larger magnitudes for shear stress are observed in the foot-zones near the end-plates (where strain-rates are practically zero due to no-slip boundary condition). On the feet and close to the plates, important shear effects are anticipated which may potentially lead to foot-pinching under certain circumstances. Hence, in extension-dominated zones (mid-filament region),

extensional viscosity becomes an important parameter, whilst in regions of strong shear, the fluid response is governed by shear viscosity.

Through this study, a hybrid finite element/finite volume (*fe/fv*) numerical scheme is employed, which has been developed by the computational rheology (INNFM) group at Swansea University. In chapters four to seven, solutions are validated against results and predictions appearing in the literature.

First, the Oldroyd-B constitutive equation has been considered. This model is of a relatively high strain-hardening nature, and has been selected to predict rheological behaviour of a wide range of polymeric solutions and melts. Several modifications have been proposed since the introduction of the original model. Under filament stretching, the influence of the non-dimensional quantities on the flow is gathered. These quantities control the degree of strain-hardening, the onset of shear-thinning and the viscoelastic contribution. The next step was to provide corresponding predictions for viscoelastic fluids in filament-stretching cylindrical geometries, where radial evolution, stress and velocity fields are reported for different levels of solvent fraction and aspect-ratios. Alternatively, less strain-hardening representations, with the linear version of the Phan-Thien/Tanner (PTT) model and the Giesekus model, were also implemented with variation of ξ and α parameters, respectively.

Comparison across the three viscoelastic models presents the advantage of varying the strain-hardening response with little variation in shear-thinning viscosity. Upon this basis, the influence of extensional viscosity and Trouton ratio was investigated for shear-thinning fluids in the context of filament-stretching. In addition, the influence of anisotropy and the numerical difficulties introduced by this factor have been observed. It was concluded that the instabilities provoked by the anisotropy parameter are boosted at larger α-values, where the anisotropy-free case for the Giesekus model corresponds to the Oldroyd response. A comparison has been included with the LPTT model at two different levels of ξ-parameter $\xi=\{0,0.13\}$, with variation in shear response, similar dynamic behaviour and slightly less strain-

hardening properties at $\xi=0$. At Hencky-strains larger than three, bead-like structure starts to emerge for the earlier shear-thinning/more strain-hardening LPTT ($\xi\neq0$) fluid, features which are observed neither in the equivalent Giesekus nor LPTT ($\xi=0$) instances.

The scheme of ALE-h_y-fV has proven its capability in dealing with numerical challenges and grasping sharp differences in flow structure and filament curvature throughout flow evolution. The quality of solutions generated for the single-mode approximation has been confirmed through analyses performed on full-filament and quarter-domain problems. At larger levels of Hencky-strain, multi-mode approximation has shown deeper stress penetration across the filament span.

Gravitational forces create a directional bias to the shape of the filament and counterbalance the effect of surface tension.

An effective comparison has been made between a compressed-mesh approach and a Volume-of-Fluid alternative. Solution quality and levels of ε_{crit} for the *CM*-approach with *ALE*-formulations ($\boldsymbol{u}_m\approx\boldsymbol{u}$) have been found superior to those for the *VOF*-scheme.

Regarding the discrete treatment of the dynamic free-surface , the sensitivities and deficiency of employing the kinematic condition ($\partial h/\partial t$) to determine surface level $h(z,t)$ have been illustrated empirically. In the particle-tracking technique (dx/dt), free-surface movement is carried out with further flexibility and less restriction, and hence, it allows for capturing zones of larger curvature adjustment with improved precision. In the shear boundary layer, near the plates at the feet of the filament, this effect is most prominent. Applying the *ALE/CM*-strategy with particle-tracking yields quantitative measures via Trouton ratio, extensional viscosity, minimum filament radius, deformation rates and stress, all of which provide close agreement with the results recorded in the literature.

Disregarding body forces/surface tension influences in the context of filament-stretching, the influence of variation in *shear-thinning and tension-thickening* properties has been analysed, concentrating upon comparison of results for LPTT(ξ=0 and ξ=0.13) and Giesekus models. Reduction in *strain-hardening* as with the Giesekus model and rising (α), tends to lead to less (τ_{zz}) development. Whilst, shear stress effects are dominant near the moving-plates, and by raising the mobility factor these shearing effects begin to decline. Thus, in an $\alpha \rightarrow 0$ regime, when shearing influence is augmented, the filament foot is more pinched and the filament mid-section thickens. In contrast, when $\alpha \rightarrow 1$, exaggerated thinning is detected at the filament mid-section, due to the corresponding reduction in hardening and extension experienced there.

Contrasting single- and multi-mode axial stress representation at the filament-centre, discrepancy in stress local maxima appears even at the relatively low levels of Hencky-strain of ε=0.2 units (and fully so by ε=1.0). Under multi-mode modeling, the impact of the shortest modes is conspicuous in the axial penetration of stress through the filament (lengthwise), whilst providing uniform radial penetration. For larger levels of Hencky-strain ($\varepsilon \geq 0.8$ units), the largest mode represents the major contributing factor to the extra-stress, most notably in terms of axial stress. In early stretching stages, dominance switches between the modes, with the second mode taking over by ε=0.2 units, and barely any disparity is discerned between first and second modes across the intermediate range ($0.2<\varepsilon<0.8$ units). Under single or multi-mode approximations and in the cases where body/surface tension forces are absent, both the Giesekus and LPTT(ξ=0) fluids yield similar trends. There are no signs of bead-like structures formation, retaining symmetrical filament-shapes and stress distribution patterns (axial stress), even at large Hencky-strains of ε>3 units. Inclusion of capillary forces does not alter this finding. In contrast, multi-mode LPTT (ξ=0.13) solutions, apart from capillary force inclusion or exclusion, provide a single symmetrical bead-like structure, but only at larger strain levels beyond ε>3.4 units, as opposed to ε=3.2 units for the single-mode instance.

Under an Oldroyd-B single-mode approximation, linear versus exponential-stretching configurations have also been compared, with predicted solutions validated closely against theoretical solutions. Under the linear-stretching mode, axial stress relaxation has been observed during the stretching process, hence proving less restrictive to the overall stretching period. This lies in stark contrast to the exponential-counterpart, where axial stress grows exponentially. The dynamically declining stretch-rate of the linear-stretching configuration accounts for such a relaxation in stress, unlike its exponential counterpart. Likewise, the trend in Trouton ratio is monotonically rising with Hencky-strain under exponential-stretching, whilst with linear-stretching, far lower levels of Trouton ratio are attained. Radial velocity minima (V_r^{min}) at the mid-plane prove considerably lower for linear-stretching than under exponential-stretching up to equivalent Hencky-strain levels of ε=1.8 units. Under linear-stretching mode and at higher strain levels, radial velocity minima do not display a tendency to migrate towards the plate-regions (as occurs with exponential retraction). Nonetheless, developing filament shapes at equivalent lengths (Hencky-strains) do not exhibit significant difference across the various modes of stretching.

The capillary thinning (*CaBER*) step-strain filament stretching process has been simulated using a CM/*ALE* hybrid *fe/fv* method numerical procedure. Three constitutive models (Oldroyd-B, Giesekus and LPTT) have been studied for various fluid aspect-ratios. Prediction of the mid-filament radius R_{mid} evolution, and filament shape, conducted on a low polymeric Boger-type fluid (Oldroyd-B), has indicated qualitative agreement with equivalent experiments from the literature. No beads or asymmetries have emerged in such an instance. As the aspect-ratio rises (from two, to three, to ten), the radial fluctuations decline in magnitude so that they are absent at the largest aspect-ratio of ten. The development of radial-fluctuations is hindered by the excessive strain-hardening properties of the Oldroyd model. Whilst these fluctuations are more apparent for the intermediate-level strain-hardening LPTT model and absent for the weakly strain-hardening Giesekus model.

The low polymeric Boger-type fluid, with Oldroyd models and two further aspect-ratios, provides qualitative agreement with the relevant experiments reported in the literature. Further investigation is demanded to resolve some deviation caused by start-up of step-strain. The plate motion, in the present simulations is suddenly brought to rest (impulsive step-change), yet this is difficult to approximate experimentally. In the solvent-dominated instance with the aspect-ratios investigated, no beads-like formation or radial fluctuations have been observed. Through step-strain studies, predicted estimates have been derived for apparent extensional viscosity and principal relaxation time for both low and high polymeric fluids. Close agreement has been achieved with the underlying experimental data, both on the trend (range of values) in extensional viscosity and estimated relaxation time.

8.2 Suggestions for further study

No-slip conditions have been applied on the end-plates, in all instances studied in this work. Considering slip conditions and comparison against present results may prove a fruitful topic in future studies.

Single eXtended Pom-Pom (SXPP) model is of a relatively new class of constitutive equations, developed mainly from physical arguments and several modifications have been proposed since the introduction of the original model by McLeish and Larson. There is little research performed to study the dynamic response of this model in filament-stretching and step-strain. As such, it is proposed to study this model fluid behaviour, both under the contexts of filament-stretching and step-strain, with possible inclusion of an alternative version of the pom-pom model termed λ^2XPP. This provides access to modelling system structure, through entanglement and concentration (branched/linear architecture, mono-/polydispersed systems).

In experimental research, it is practically impossible to study step-strain under instantaneous sudden halt of the moving plates. As indicated in the appendix of chapter seven, a paper has recently been submitted for publication including the

gradual cessation of filament-stretching. Further studies are proposed along this line through parameter variation to investigate the wave-like behavior of radial fluctuations and their physical interpretation, covering both instances of linear and exponential initial stretching.

A combination of filament-stretching and step-strain processes study may be an interesting prospective topic, through which a filament is subject to intermittent stretching and step-strain.

The numerical study of torsional rheometers and investigation of differences with *FISER* and *CaBER* rheometers can be another appealing area of research.

The thorough study of step-strain following linear filament-stretching is commended for its associated dynamic response in terms of radial evolution and stress growth and relaxation. Comparison against the literature for its exponential counterpart would be most informative.

Since in experimental work, emergence of bubbles is common when filaments are subjected to stretching, it would be helpful to simulate the step-strain process with either a single- or multiple-bubbles located at different positions along the filament.

Other fruitful study proposals may include modeling filament break-up as a helpful tool in the study of filament shape and dynamic response after failure; different initial filament sample shapes based on initial stresses and parameter feasibility study on final aspect ratio.

List of Figures

List of Tables

Glossary

ALE	Arbitrary Lagrangian-Eulerian
b.i.	boundary integral
Bo	Bond number
Ca	capillary number
CaBER	Capillary Breakup Rheometry
CAD	Computer Aided Design
CFD	Computational Fluid Dynamics
CM	Compressed Mesh
CONNFFESSIT	calculation of non-Newtonian flows: finite elements and stochastic simulation technique
De	Deborah number
DEVSS	discrete elastic viscous stress
DOP	dioctyl phthalate
FD	finite difference
FE	finite element
FEM	finite element method
FENE	finitely extensible nonlinear elastic
FISER	filament stretching extensional rheometer
FV	finite volume
fe/fv	hybrid finite element/finite volume
gp	Gauss quadrature point
INNFM	Institute of Non-Newtonian Fluid Mechanics
K-BKZ	Kaye, Bernstein, Kearsley and Zapas
LCM	Lower-Convected Maxwell
LPTT	Linear Phan-thien/Tanner
mdc	median dual cell
MAC	marker and cell
MRR	modified rotational rheometer
MSF	molecular stress function
nc	number of nodes
nt	number of nodes in the generic element
PEO	polyethylene oxide
Re	Reynolds number
TCP	tricresyl phosphate
TGPC	Taylor Galerkin pressure correction
Tr	Trouton ratio
UCM	Upper-Convected Maxwell

VOF	Volume-of-Fluid
WM	White-Metzner

List of Publications

1- H. Matallah, M.J. Banaai, K.S. Sujatha and M.F. Webster
Modelling filament stretching flows with strain-hardening models and sub-cell approximations *Journal of Non-Newtonian Fluid Mechanics, Vol.* **134**, *Iss.1-3, 10 March2006, pp.77-104*

2- K.S. Sujatha, H. Matallah, M.J. Banaai and M.F. Webster
Computational predictions for viscoelastic filament stretching flows: ALE methods and free-surface techniques (CM and VOF)
Journal of Non-Newtonian Fluid Mechanics, Volume **137**, *Issues 1-3, 30 August 2006, Pages 81-102*

3- H. Matallah, K.S. Sujatha, M.J. Banaai and M.F. Webster
Single and multi-mode modelling for filament stretching flows
Journal of Non-Newtonian Fluid Mechanics, Volume **146**, *Issues 1-3, 25 October 2007, Pages 92-113*

4- K.S. Sujatha, H. Matallah, M.J. Banaai and M.F. Webster
Modeling step-strain filament-stretching (CaBER-type) using ALE techniques
Journal of Non-Newtonian Fluid Mechanics, In Press, Available online 2 June 2007,

5- K.S.Sujatha, H.Matallah, M.J.Banaai and M.F.Webster, June, 2005
Computational Predictions for Viscoelastic Filament Stretching Flows: *ALE* methods and free-surface techniques (*CM* and *VOF*), Report # **CSR 7-2005**

6- K.S.Sujatha, H.Matallah, M.J.Banaai and M.F.Webster,
Modelling Filament Stretching Flows with Strain-hardening Models and Sub-cell Approximations, Report # **CSR 9-2005**

7- H. Matallah, M.J. Banaai, K.S. Sujatha and M.F. Webster,
Modelling Filament Stretching Flows with Strain-hardening Models and Sub-cell Approximations - Part II, Report # **CSR 16-2005**

8- H. Matallah, K.S. Sujatha, M.J. Banaai and M.F. Webster
Multi-mode simulation of filament stretching flows, Report # **CSR 11-2006**

9- K.S.Sujatha, H.Matallah, M.J.Banaai and M.F.Webster,
Modeling step-strain filament-stretching (*CaBER*-type) using ALE techniques
Report # **CSR 12-2006**

10- M.F. Webster, H. Matallah, K.S. Sujatha and M.J. Banaai
Numerical modelling of step-strain for stretched filaments
Submitted for publication to the journal of *Non-Newtonian Fluid mechanics*,
June 2007

References

[1] H. Giesekus, A simple constitutive equation for polymer fluids based on the concept of deformation-dependent tensorial mobility, *J. Non-Newtonian Fluid Mech.* **11** (1982) 69-109.

[2] J.-M. Li, W.R. Burghardt, B. Yang, B. Khomami, Flow birefringence and computational studies of a shear thinning polymer solution in axisymmetric stagnation flow, *J. Non-Newtonian Fluid Mech.* **74** (1998) 151-193.

[3] M. Yao, G.H. McKinley, B. Debbaut, Extensional deformation, stress relaxation and necking failure of viscoelastic filaments, *J. Non-Newtonian Fluid Mech.* **79** (1998) 469-501.

[4] R. Sizaire, V. Legat, Finite element simulation of a filament stretching extensional rheometer, *J. Non-Newtonian Fluid Mech.* **71** (1997) 89-107.

[5] A. Bach, H.K. Rasmussen, P.-Y. Longin, O. Hassager, Growth of non-axisymmetric disturbances of the free surface in the filament stretching rheometer: experiments and simulation, *J. Non-Newtonian Fluid Mech.* **108** (2002) 163-186.

[6] O. Hassager, M.I. Kolte, M. Renardy, Failure and nonfailure of fluid filaments in extension, *J. Non-Newtonian Fluid Mech.* **76** (1998) 137-151.

[7] H.K. Rasmussen, O. Hassager, Three-dimensional simulations of viscoelastic instability in polymeric filaments, *J. Non-Newtonian Fluid Mech.* **82** (1999) 189-202.

[8] H.M. Wagner, P. Ehrecke, P. Hachman, J. Meissner, A constitutive analysis of uniaxial, equibiaxial and planar extension of a commercial linear high-density polyethylene melt, *J. Rheol.* **42** (1998) 621-638.

[9] F. Langouche, B. Debbaut, Rheological characterisation of high density polyethylene with a multi-mode differential viscoelastic model and numerical simulation of transient elongational recovery experiments, *Rheol. Acta* **38** (1999) 48-64.

[10] M.F. Webster, H. Matallah, K.S. Sujatha, Sub-cell approximations for viscoelastic flows-filament stretching, *J. Non-Newtonian Fluid Mech.* **126** (2005) 187-205.

[11] W.F. Noh, A time dependent two space dimensional coupled Eulerian Lagrangian code, *Meth. Comput. Phys.* **3** (1964).

[12] C.W. Hirt, A.A. Amsden, J.L. Cook, An arbitrary Lagrangian-Eulerian computing method for all flow speeds, *J. Comput. Phys.* **14** (1974) 227-253.

[13] T.J.R. Hughes, W.K. Liu, T.K. Zimmermann, Lagrangian-Eulerian finite element formulation for incompressible viscous flows, *Comput. Methods Applied Mech. Eng.* **29** (1981) 329-349.

[14] M. Yao, S.H. Spiegelberg, G.H. McKinley, Dynamics of weakly strain-hardening fluids in filament stretching devices, *J. Non-Newtonian Fluid Mech.* **89** (2000) 1-43.

[15] H. Matallah, P. Townsend, M.F. Webster, Viscoelastic multi-mode simulations of wire-coating, *J. Non-Newtonian Fluid Mech.* **90** (2000) 217-241.

[16] H. Matallah, P. Townsend, M.F. Webster, Viscoelastic computations of polymeric wire-coating flows, *Int. J. Num. Meth. Heat Fluid Flow* **12** (2002) 404-433.

[17] S.L. Anna, G.H. McKinley, Elasto-capillary thinning and breakup of model elastic liquids, *J. Rheol.* **45** (2001) 115-138.

[18] A.V. Bazilevsky, V.M. Entov, A.N. Rozhkov, Liquid filament micro rheometer and some of its applications, *Third European Rheology Conference, D.R. Oliver(ed.)* (1990) 41-43.

[19] M. Stelter, G. Brenn, A.L. Yarin, R.P. Singh, F. Durst, Validation and application of a novel elongational device for polymer solutions, *J. Rheol.* **44** (2000) 595-616.

[20] A. Tripathi, P. Whittingstall, G.H. McKinley, Using filament stretching rheometry to predict standard formation and processability in adhesive and other non-Newtonian fluids, *Rheol. Acta* **39** (2000) 321-337.

[21] V.M. Entov, E.J. Hinch, Effect of a spectrum of relaxation times on the capillary thinning of a filament of elastic liquid, *J. Non-Newtonian Fluid Mech.* **72** (1997) 31-53.

[22] D.W. Bousfield, R. Keunings, G. Marrucci, M.M. Denn, Nonlinear analysis of the surface tension driven breakup of viscoelastic filaments, *J. Non-Newtonian Fluid Mech.* **21** (1986) 79-97.

[23] Y. Christanti, L.M. Walker, Surface tension driven jet break up of strain-hardening polymer solutions, *J. Non-Newtonian Fluid Mech.* **100** (2001) 9-26.

[24] N. Phan-Thien, R.I. Tanner, A new constitutive equation derived from network theory, *J. Non-Newtonian Fluid Mech.* **2** (1977) 353-365.

[25] N. Phan-Thien, A non-linear network viscoelastic model, *J. Rheol.* **22** (1978) 259-283.

[26] V.G. Levich, *Physicochemical Hydrodynamics*,Pentice-Hall, Englewood Cliffs,N.J., (1962).

[27] R. Keunings, An algorithm for the simulation of transient viscoelastic flows with free surfaces, *J. Comput. Phys.* **62** (1986) 199-220.

[28] H. Matallah, P. Townsend, M.F. Webster, Recovery and stress-splitting schemes for viscoelastic flows, *J. Non-Newtonian Fluid Mech.* **75** (1998) 139-166.

[29] G. Ianniruberto, G. Marrucci, A multi-mode CCR model for entangled polymers with chain stretch, *Journal of Non-Newtonian Fluid Mechanics* **102** (2002) 283-395.

[30] P.W. Grant, M.F. Webster, X. Zhang, Coarse grain parallel simulation for incompressible flows, *Int. J. Num. Meth. Eng.* **41** (1998) 1321-1337.

[31] M.F. Webster, H.R. Tamaddon-Jahromi, M. Aboubacar, Transient viscoelastic flows in planar contractions, *J. Non-Newtonian Fluid Mech.* **118** (2004) 83-101.

[32] M. Aboubacar, M.F. Webster, Development of an optimal hybrid finite volume/element method for viscoelastic flows, *Int. J. Num. Meth. Fluids* **41** (2003) 1147-1172.

[33] K.S. Sujatha, H. Matallah, M. J. Banaai, M.F. Webster, Computational predictions for viscoelastic filament stretching flows: ALE methods and free-surface techniques (CM and VOF), *J. Non-Newtonian Fluid Mech.* **137** (2006) 81-102.

[34] M.S. Chandio, H. Matallah, M.F. Webster, Numerical simulation of viscous filament stretching flows, *Int. J. Num. Meth. Heat Fluid Flow* **13** (2003) 899-930.

[35] F. Dupret, J.M. Marchal, Loss of evolution in the flow of viscoelastic fluids, *J. Non-Newtonian Fluid Mech.* **20** (1986) 143-171.

[36] O.C. Zienkiewicz, J.Z. Zhu, Superconvergence and the superconvergent patch recovery, *Finite Element in Analysis and Design* **19** (1995) 11-23.

[37] T. Sridhar, V. Tirtaatmaja, D.A. Nguyen, and R.K. Gupta, Measurement of extensional viscosity of polymer solutions, *J. Non-Newtonian Fluid Mech.*, **40** (1991) 271-280.

[38] V. Tirtaatmaja and T. Sridhar, A filament stretching device for measurement of extensional viscosity, *J. Rheol.*, **37** (1993) 1081-1102.

[39] M. Yao and G.H. McKinley, Numerical simulation of extensional deformations of viscoelastic liquid bridges in filament stretching devices, *J. Non-Newtonian Fluid Mech.*, **74** (1998) 47-88.

[40] R.W.G. Shipman, M.M. Denn and R. Keunings, Mechanics of the 'falling plate' extensional rheometer, *J. Non-Newtonian Fluid Mech.*, **40** (1991) 281-288.

[41] M.I. Kolte, H.K. Rasmussen and O. Hassager, Transient filament stretching rheometer II: Numerical simulation, *Rheol. Acta*, **36** (1997) 285-302.

[42] S. Gaudet and G.H. McKinley, Extensional deformation of non-Newtonian liquid bridges, *Comput. Mech.*, **21** (1998) 461-476.

[43] S.H. Spiegelberg, D.C. Ables and G.H. McKinley, The role of end-effects on measurements of extensional viscosity in viscoelastic polymer solutions with a filament stretching rheometer, *J. Non-Newtonian Fluid Mech.*, **64** (1996) 229-267.

[44] E. Grande, M. Laso and M. Picasso, Calculation of variable-topology free-surface flows using CONFESSIT, *J. Non-Newtonian Fluid Mech.*, **113** (2003) 127-145.

[45] D.O. Olagunju, A 1-D theory for extensional deformation of a viscoelastic filament under exponential stretching, *J. Non-Newtonian Fluid Mech.*, **87** (1999) 27-46.

[46] G.H. McKinley and T. Sridhar, Filament-stretching rheometry of complex fluids, *Annu. Rev. Fluid Mech.*, **34** (2002) 375-415.

[47] J. Eggers, Nonlinear dynamics and breakup of free-surface flows, *Rev. Mod. Phys.*, **69** (1997) 865-929.

[48] E. Thompson, Use of pseudo-concentrations to follow creeping viscous flows during transient analysis, *Int. J. Num. Meth. Fluids,* **6** (1986) 749-761.

[49] K. Ravindran and R.W. Lewis, Finite element modelling of solidification effects in mould filling, *Finite Elements in Analysis and Design,* **31** (1998) 99-116.

[50] C.W. Hirt and B.D. Nichols, Volume of fluid (VOF) method for the dynamics of free-surface boundaries, *J. Comput. Phys.*, **39** (1981) 210-225.

[51] M. Maronnier, M. Picasso and J. Rappaz, Numerical simulation of free-surface flows, *J. Comput. Phys.*, **155** (1999) 439-455.

[52] S.E. Navti, K. Ravindran, C. Taylor and R.W. Lewis, Finite element modelling of surface tension effects using a Lagrangian-Eulerian kinematic description, *Comput. Methods Appl. Mech. Engrg.*, **147** (1997) 41-60.

[53] M.F. Tomé, B.Duffy and S. McKee, A numerical technique for solving unsteady non-Newtonian free surface flows, *J. Non-Newtonian Fluid Mech.*, **62** (1996) 9-34.

[54] M.F. Tomé, L.Grossi, A. Castelo, J.A. Cuminato, N. Mangiavacchi, V.G. Ferreira, F.S. de Sousa and S. McKee, A numerical method for solving three-dimensional generalised Newtonian free surface flows, *J. Non-Newtonian Fluid Mech.*, **123** (2004) 85-103.

[55] J.E. Matta, R.P. Tytus, Liquid stretching using a falling cylinder, *J. Non-Newtonian Fluid Mech.* **67** (1990) 47-76.

[56] M. Goldin, J. Yerushalmi, R. Pfeffer, R. Shinnar, Breakup of a laminar capillary jet of a viscoelastic fluid, *J. Fluid Mech.* **38** (1969) 689-711.

[57] H. Chang, E.A. Demekhin, E. Kalaidin, Iterated stretching of viscoelastic jets, *Phys. Fluids* **11** (1999) 1717-1737.

[58] M.S.N. Oliveira, R. Yeh, G.H. McKinley, Iterated stretching, extensional rheology and formation of beads-on-a-string structures in polymer solutions, *J. Non-Newtonian Fluid Mech.* **137** (2006) 137-148.

[59] D.V. Boger, K. Walters, Rheological Phenomena in Focus, *Elsevier Science, New York* (1993).

[60] A. Baloch, P. Townsend, M.F. Webster, On two and three dimensional expansion flows, *J. Comput. Fluids* **24** (1995) 863-882.

[61] H. Matallah, M.J. Banaai, K.S. Sujatha, M.F. Webster, Modelling filament stretching flows with strain-hardening models and sub-cell approximations, *J. Non-Newtonian Fluid Mech.* **134** (2006) 77-104.

[62] K. Foteinopoulou, V.G. Mavrantzas, J. Tsamopoulos, Numerical simulation of bubble growth in Newtonian and viscoelastic filaments undergoing stretching, *J. Non-Newtonian Fluid Mech.* **122** (2004) 177-200.

[63] J. Koplik, J.R. Banavar, Extensional rupture of model non-Newtonian fluid filaments, *Phys. Rev.* **E67** (2003) 1-12.

[64] R.G. Larson, Constitutive equations for polymer melts and solutions, *Butterworths, Boston, USA* (1988).

[65] P. Szabo, Transient filament stretching rheometer I: Force balance analysis, *Rheol. Acta* **36** (1997) 277-284.

[66] D.M. Hawken, H.R. Tamaddon-Jahromi, P. Townsend, M.F. Webster, A Taylor-Galerkin based algorithm for viscous incompressible flow, *Int. J. Num. Meth. Fluids* **10** (1990) 327-351.

[67] F.P.T. Baaijens, S.H.A. Selen, H.P.W. Baaijens, G.W.M. Peters, H.E.H. Meijer, Viscoelastic flow past a confined cylinder of a LDPE melt, *J. Non-Newtonian Fluid Mech.* **68** (1997) 173-203.

[68] G.H. McKinley, O. Brauner, M. Yao, Kinematics of filament stretching in dilute and concentrated polymer solutions, *Korea-Australia Rheolgy Journal* **13** (2001) 29-35.

[69] G.H. McKinley, Visco-elasto-capillary thinning and break-up of complex fluids, *Hatsopoulos Microfluids Laboratory report* **05-P-04** (2005).

[70] J. van Nieuwkoop, M.M.O. Muller von Czernicki, Elongation and subsequent relaxation measurements on dilute polyisobutylene solutions, *J. Non-Newtonian Fluid Mech.* **67** (1996) 105-123.

[71] L.E. Rodd, T.P. Scott, J.J. Cooper-White and G.H. McKinley, Capillary break-up rheometry of low-viscosity elastic fluids, *Applied Rheology,***15** (2005) 12-27

[72] A. V. Bazilevsky, V.M. Entov, M.M. Lerner, and A.N. Rozhkov, Failure of polymer solution filaments, Polymer Science Ser. A), **39**(3), (1997), 316-324.

[73] A. V. Bazilevsky, V.M. Entov and A.N. Rozhkov, Failure of an Oldroyd liquid bridge as a method of testing the rheological properties of polymer solutions filaments, Polymer Science Ser. A, **43**(7), (2001), 1161-1172.

[74] G.H. McKinley and A.Tripathi, How to extract the Newtonian viscosity from capillary breakup measurements in a filament rheometer, J. Rheol., **44**(3), (2000), 653-671.

[75] M.I. Kolte and P. Szabo, Capillary thinning of polymeric filaments, *J. Rheology*, **43** (1999) 609-626.

[76] M. Renardy, Similarity solutions for jet breakup for various models of viscoelastic liquids, *J. Non-Newtonian Fluid Mech.*, **104** (2002)65-74.

[77] M. Renardy, A numerical study of the asymptotic evolution and breakup of Newtonian andviscoelastic jets, *J. Non-Newtonian Fluid Mech.,* **59** (1995)267-282.

[78] M. Renardy, Some comments on the surface tension driven breakup (or the lack of it) of viscoelastic liquid jets, *J. Non-Newtonian Fluid Mech.,* **51**(1994)97-107.

[79] N. Willenbacher, Elongational viscosity of aqueous thicker solutions from capillary breakup elongational rheometry (CaBER), Proc. X1V th Int. Cong. Rheol., Seoul, (S.Korea) August 2004.

[80] C.Clasen, J. Eggers, M.A. Fontelos, J. Li, G.H.McKinley, The beads-on-string structure of viscoelastic threads, J. Fluid Mech. **56** (2006) 283-308.

[81] R.J.English, private communications, (2007).

[82] S.Chang and A.S. Lodge, Comparison of rubbler-like liquid theory with stress growth data for elongation of a low density branched polymer melt, *Rheol. Acta,* **11** (1972) 127-129.

[83] Y. Ide and J.L. White, The spinnability of polymer fluid filaments, *J. Appl. Polym. Sci.,* **20** (1976) 2511-2531.

[84] R. F. Liang and M. R. Mackley, Rheological characterization of the time and strain dependence for polyisobutylene solutions, *J. Non-Newtonian Fluid Mech*, **52** (1994) 387-405.

[85] R.V. Southwell, *Relaxation methods in engineering science*, Oxford (1940).

[86] O.C. Zienkiewicz and Taylor, The finite element method, Vol.1, McGraw-Hill(1994).

[87] S.V. Patankar and D.B. Spalding, *A calculation procedure for heat, mass and momentum transfer in three-dimensional parabolic flows*, Int.J.Heat Mass Transfer, **15** (1972) 1787-1806

[88] C.Hirsh, Numerical Simulation of Internal and External Flows, vol. 2:Wiley (1990)

[89] K.Nakajima and Y. Kallinderis, *Comparison of finite element and finite volume methods for incompressible viscous flows*, AIAA J. **32** (1993)1091-1093

[90] J. Mattiussi, *An analysis of finite volume, finite element and finite difference methods using some concepts from algebraic topology*, J.Comp. Phys. **307** (1993) 133-289.

[91] R. Keunings, On the high Weisenberg number problem, *J. Non-Newtonian Fluid Mech.* **20** (1986) 209-226.

[92] K. Walters and M. F. Webster, *The Distinctive CFD challenges of computational rheology*, ECCOMAS 2001, Swansea.

[93] W.Ritz, U ber eine neue Methode zur Lo sung gewisser Variationsprobleme der mathematischen Physik, *Zeitschrift fur Angewandte Mathematic and Mechanik*, **35** (1909)1-61.

[94] R.Courant, *Variation methods for the solution of problems of equilibrium and vibrations*, Bull. Am. Math. Soc. **49** (1943) 1-239.

[95] M.Turner, R.Clough, H. Martin, and L.Topp, *Stiffness and deflection analysis of complex structure*, J.Aero.Sci. **23** (1956) 805-823.

[96] J.H. Argyris, *Recent Advances in Matrix Methods of structural Analysis*, Pergamon, NY, 1954

[97] R. W. Clough, *The Finite Element Method in Plane Stress analysis, Proceeding of the 2nd ASCE Conference*, Pittsburgh, (1960) 345-378

[98] O.C.Zienkiewicz and Y.K. Cheung, *Finite elements in the solution of field problems, The Engineer*, **220** (1965) 507-510.

[99] H.C. Martin, *Introduction to matrix methods of structural analysis*, McGraw-Hill (1966).

[100] J.T. Oden, Finite Elements of non-Linear Continua, McGraw-Hill, 1972.

[101] P.W. Chang, T.W.Pattern, and B. A. Finlayson, Collaction and Galerkin finite element methods for viscoelastic fluid flow-I, Comp. Fluids, **7** (1979) 267-283.

[102] I. Christie, D.F. Griffiths, A.R.Mitchel and O. C. Zienkiewicz, *Finite element Methods for second differential equations with significant first derivatives*,Int, J.Num. Meth. Eng. **10** (1976) 1389-1366.

[103] T. G. R. Hughes, *A simple scheme for developing 'upwind' finite elements*, Int. J. Num. Meth. Eng. **12** (1978) 1359-1365.

[104] G. D. Raithby and K.E. Torrance, *Upstream-weighted differencing schemes and their application to elliptic problems involving fluid*, Comp. Fluids, **2** (1974) 191- 206.

[105] A. N. Brooks and J.R. Hughes, *Streamline upwind / Petrov- Galerkin) formulation for convection dominated flows with particular emphasis on the incompressible Navier-Stokes equations,* Comp. Meth. Appl. Mech. Eng, **32** (1982) 199-259.

[106] T. Sato and S.M. Richardson, Explicit numerical simulation of time dependent viscoelastic flow problems by finite element/ finite volume method, J. Non-Newt. Fluid Mech. **51** (1994) 249-279.

[107] P.Wapperom and M.F. Webster, A second order hybrid finite element/ finite volume method for viscoelastic flows, J. Non-Newt. Fluid Mech. **79** (1998) 405-431.

[108] D. J. Acheson, Elementary fluid dynamics, Clarendon (1990).

[109] H.A. Barnes, J.F. Hutton, K. Walters, *An Introduction to Rheology*, Elsevier, (1989).

[110] M.S. Chandio, Numerical Study of Model, Industrial and Free-Surface Flows. In: Computer Science, Vol. Philosophiae Doctor, University of Wales, Swansea, Swansea, U.K., 2002, p. 208.

[111] R. Sizaire, *keyFE2 User Manual*, (2004).

[112] R.B. Bird, R.C. Armstrong, O. Hassager, *Dynamics of Polymeric Liquids, Volume 1: Fluid Mechanics*, John Wiles & Sons, Inc., (1987).

[113] J.C. Maxwell, On the dynamical theory of gases, *Philosophical Transactions of the Royal Society A* **157** (1867) 49-88.

[114] R.I. Tanner and K. Walters, "*Rheology: An Historical Perspective*", Elsevier, Amsterdam (1998).

[115] M.J. Crochet, A.R. Davies, and K. Walters, "*Numerical Simulation of Non-Newtonian Flow*", Elsevier, Amsterdam (1984).

[116] R. Keunings, in "*Fundamentals of Computer Modeling for Polymer Processing*", (Ed. C.L. Tucker III), Carl Hanser Verlag, Munich (1989), pp. 402-470.

[117] M.J. Crochet, Numerical simulation of viscoelastic flow: a review. *Rubber Chem. Techn., Rubber Reviews* **62** (1989) 426-455.

[118] F.P.T. Baaijens, Mixed finite element methods for viscoelastic flow analysis: A review *J. Non-Newtonian Fluid Mech.* **79** (1998) 361-385.

[119] R. Keunings, "*Advances in the Computer Modelling of the Flow of Polymeric Liquids*", *Comp. Fluid Dyn. J.* (2000).

[120] R.G. Larson, "*The Structure and Rheology of Complex Fluids*", Oxford University Press, New York (1999).

[121] H.C Öttinger, "*Stochastic Processes in Polymeric Fluids: Tools and Examples for Developing Simulation Algorithms*", Springer, Berlin (1996).

[122] R.B. Bird, C.F. Curtiss, R.C. Armstrong and O. Hassager, "*Dynamics of Polymeric Liquids Vol. 2: Kinetic Theory*", 2nd Ed., John Wiley, New York (1987).

[123] P.S. Doyle and E.S.G. Shaqfeh, Dynamic simulation of freely-draining, flexible bead-rod chains: Start-up of extensional and shear flow, *J. Non-Newtonian Fluid Mech.* **76** (1998) 43-78.

[124] P.S. Doyle, E.S.G. Shaqfeh, G.H. McKinley and S.H. Spiegelberg, Relaxation of dilute polymer solutions following extensional flow, *J. Non-Newtonian Fluid Mech.* **76** (1998) 79-110.

[125] T.C.B. Kwan and E.S.G. Shaqfeh, Brownian dynamics simulations of the stress and molecular configuration of polymers in exponential and linearly-ramped shear flow, *J. Non-Newtonian Fluid Mech.* **82** (1999)139-165.

[126] R.G. Larson, H. Hu, D.E. Smith and S. Chu, Brownian dynamics simulation of a DNA molecule in an extensional flow field, *J. Rheol.* **43** (1999) 267-304.

[127] L. Li, R.G. Larson and T. Sridhar, Brownian dynamics simulations of dilute polystyrene solutions, *J. Rheol.* **44** (2000) 291-322.

[128] L. Li and R.G. Larson, Comparison of Brownian Dynamics Simulations with Microscopic and Light-Scattering Measurements of Polymer Deformation under Flow, *Macromol.* **33** (2000) 1411- 1415.

[129] R. Sizaire, G. Lielens, I. Jaumain, R. Keunings and V. Legat, On the hysteretic behaviour of dilute polymer solutions in relaxation following extensional flow *J. Non-Newtonian Fluid Mech.* **82** (1999) 233- 253.

[130] M.R.J. Verhoef, B.H.A.A. van den Brule and M.A. Hulsen, On the modelling of a PIB/PB Boger fluid in extensional flow, *J. Non-Newtonian Fluid Mech.* **80** (1999) 155- 182.

[131] T.T. Perkins, D.E. Smith and S. Chu, Single polymer dynamics in an elongational flow, *Science* **276** (1997) 2016-2021.

[132] D.E. Smith and S Chu, Response of flexible polymers to a sudden elongational flow, *Science* **281** (1998) 1335-1340.

[133] D.E. Smith, H.P. Babcock and S. Chu, Single-Polymer Dynamics in Steady Shear Flow, *Science* **283** (1999) 1724-1727.

[134] M. Doi and S.F. Edwards, "*The Theory of Polymer Dynamics*", Clarendon Press, Oxford (1986).

[135] G. Ianniruberto and G. Marrucci, On compatibility of the Cox-Merz rule with the model of Doi and Edwards, *J. Non-Newtonian Fluid Mech.* **65** (1996) 241-246.

[136] D.W. Mead, R.G. Larson and M. Doi, A Molecular Theory for Fast Flows of Entangled Polymers, *Macromol.* **31** (1998) 7895-7914.

[137] G. Marrucci and G. Ianniruberto, Open problems in tube models for concentrated polymers, *J. Non-Newtonian Fluid Mech.* **82** (1999) 275-286.

[138] G. Marrucci, F. Greco and G. Ianniruberto, "*Possible Role of Force Balance on Entanglements*", IUPAC Prague Meeting on Rheology of Polymer Systems, *Macromolecular Symposia*, in press (2000).

[139] G. Marrucci, F. Greco and G. Ianniruberto, "*Integral and Differential Constitutive Equations for Entangled Polymers with Simple Versions of CCR and Force Balance on Entanglements*", submitted to *Rheol. Acta*, January 2000.

[140] C.C. Hua, J.D. Schieber and D.C. Venerus, Segment connectivity, chain-length breathing, segmental stretch, and constraint release in reptation models. III. Shear flows *J. Rheol.* **43** (1999) 701-717.

[141] T.C.B. McLeish and S.T. Milner, in "*Advances in Polymer Science*", Vol. **143**, Springer verlag, Berlin (1999) pp. 195-255.

[142] C.L. Tucker (Ed.), "*Fundamentals of Computer Modeling for Polymer Processing*", Hanser Publishers, Munich (1989).

[143] T.C.B. McLeish and R.G. Larson, Molecular constitutive equations for a class of branched polymers: The pom-pom polymer, *J. Rheol.* **42** (1998) 81-110.

[144] R.J. Blackwell, T.C.B. McLeish and O.G. Harlen, Molecular drag–strain coupling in branched polymer melts, *J. Rheol.* **44** (2000) 121-136.

[145] R. Keunings, On the Peterlin approximation for finitely extensible dumbbells, *J. Non-Newtonian Fluid Mech.* **68** (1997) 85-100.

[146] D.V. Boger, Viscoelatic flows through contractions, *Ann. Rev. Fluid Mech.* **19** (1987) 157-182.

[147] J.P. Rothstein and G.H. McKinley, Extensional flow of a polystyrene Boger fluid through a 4 : 1 : 4 axisymmetric contraction/expansion , *J. Non-Newtonian Fluid Mech.* **86** (1999) 61-88.

[148] A.M. Grillet, A.G. Lee and E.S.G. Shaqfeh, Observations of ribbing instabilities in elastic fluid flows with gravity stabilization, *J. Fluid Mech.* **399**

(1999) 49-83.

[149] P. Pakdel and G.H. McKinley, Cavity flows of elastic liquids: purely elastic instabilities, *Phys. Fluids* **10** (1998) 1058-1070.

[150] A.M. Grillet, B. Yang, B. Khomami and E.S.G. Shaqfeh, Modeling of viscoelastic lid driven cavity flow using finite element simulations *J. Non-Newtonian Fluid Mech.* **88** (1999) 99- 131.

[151] J.M. Piau, Capillary rheometry for polymer melts, *Macrom. Symp.* **143** (1999) 269-289.

[152] Y.R. Fan, R.I. Tanner and N. Phan-Thien, Galerkin/least-square finite-element methods for steady viscoelastic flows, *J. Non-Newtonian Fluid Mech.* **84** (1999) 233-256.

[153] J. Sun, M.D. Smith, R.C. Armstrong and R.A. Brown, Finite element method for viscoelastic flows based on the discrete adaptive viscoelastic stress splitting and the discontinuous Galerkin method: DAVSS-G/DG, *J. Non-Newtonian Fluid Mech.* **86** (1999) 281-307.

[154] E. Brasseur, M.M. Fyrillas, G.C. Georgiou and M.J. Crochet, The time-dependent extrudate-swell problem of an Oldroyd-B fluid with slip along the wall, *J. Rheol.* **42** (1998) 549-566.

[155] R. Sureshkumar, M.D. Smith, R.C. Armstrong and R.A. Brown, Linear stability and dynamics of viscoelastic flows using time-dependent numerical simulations, *J. Non-Newtonian Fluid Mech.* **82** (1999) 57-104.

[156] P. Szabo, J.M. Rallison and E.J. Hinch, Start-up of flow of a FENE-fluid through a 4:1:4 constriction in a tube, *J. Non-Newtonian Fluid Mech.* **72** (1997) 73-86.

[157] P.Y. Huang, H.H. Hu and D.D. Joseph, Direct simulation of the sedimentation of elliptic particles in Oldroyd-B fluids, *J. Fluid Mech.* **362** (1998) 297-325.

[158] G.B. Bishko, O.G. Harlen, T.C.B. McLeish and T.M. Nicholson, Numerical simulation of the transient flow of branched polymer melts through a planar contraction using the 'pom–pom' model, *J. Non-Newtonian Fluid Mech.* **82** (1999) 255-273.

[159] P. Halin, G. Lielens, R. Keunings and V. Legat, The Lagrangian particle method for macroscopic and micro–macro viscoelastic flow computations, *J. Non-Newtonian Fluid Mech.* **79** (1998) 387-403.

[160] X. Gallez, P. Halin, G. Lielens, R. Keunings and V. Legat, The Adaptive Lagrangian Particle Method for Macroscopic and Micro-Macro Computations of Time-Dependent Viscoelastic Flows, *Comp. Meth. Appl. Mech. and Engng.* **180** (1999) 345-364.

[161] P. Wapperom, R. Keunings and V. Legat, The backward-tracking Lagrangian particle method for transient viscoelastic flows, *J. Non-Newtonian Fluid Mech.* **91** (2000) 273-295.

[162] G. Mompean and M. Deville, Unsteady finite volume simulation of Oldroyd-B fluid through a three-dimensional planar contraction *J. Non-Newtonian Fluid Mech.* **72** (1997) 253-279.

[163] S.C. Xue, R.I. Tanner and N. Phan-Thien, Three-dimensional numerical simulations of viscoelastic flows – predictability and accuracy, *Comp. Meth. Appl. Mech. Engng.* **180** (1999) 305-331.

[164] S.C. Xue, N. Phan-Thien and R.I. Tanner, Fully three-dimensional, time-dependent numerical simulations of Newtonian and viscoelastic swirling flows in a confined cylinder: Part I. Method and steady flows, *J. Non- Newtonian Fluid Mech* **87** (1999) 337-367.

[165] T.N. Phillips and A.J. Williams, Viscoelastic flow through a planar contraction using a semi-Lagrangian finite volume method *J. Non-Newtonian Fluid Mech.* **87** (1999) 215-246.

[166] H.K. Rasmussen, Time-dependent finite-element method for the simulation of three-dimensional viscoelastic flow with integral models, *J. Non-Newtonian Fluid Mech.* **84** (1999) 217-232.

[167] A.P.G. van Heel, M.A. Hulsen and B.H.A.A. van den Brule, Simulation of the Doi–Edwards model in complex flow, *J. Rheol.* **43** (1999) 1239-1260.

[168] E.A.J.F. Peters, M.A. Hulsen and B.H.A.A. van den Brule, Instationary Eulerian viscoelastic flow simulations using time separable Rivlin–Sawyers constitutive equations, *J. Non-Newtonian Fluid Mech.* **89** (2000) 209- 228.

[169] A.N. Beris and C.D. Dimitropoulos, Pseudospectral simulation of turbulent viscoelastic channel flow, *Comp. Meth. Appl. Mech. Engng.* **180** (1999) 365-

392.

[170] R. Kupferman and M.M. Denn, Simulation of the evolution of concentrated shear layers in a Maxwell fluid with a fast high-resolution finite-difference scheme, *J. Non-Newtonian Fluid Mech.* **84** (1999) 275-287.

[171] S. Kumar and G.M. Homsy, Direct numerical simulation of hydrodynamic instabilities in two- and three-dimensional viscoelastic free shear layers, *J. Non-Newtonian Fluid Mech.* **83** (1999) 249-276.

[172] F.P.T. Baaijens, An iterative solver for the DEVSS/DG method with application to smooth and non-smooth flows of the upper convected Maxwell fluid, *J. Non-Newtonian Fluid Mech.* **75** (1998) 119-138.

[173] R. Aggarwal, R. Keunings and F.-X. Roux, Simulation of the flow of integral viscoelastic fluids on a distributed memory parallel computer, *J. Rheol.* **38** (1994) 405-419.

[174] P. Henriksen and R. Keunings, Parallel computation of the flow of integral viscoelastic fluids on a heterogeneous network of workstations, *Int. J. Num. Meth. In Fluids* **18** (1994) 1167-1183.

[175] R. Keunings, Parallel finite element algorithms applied to computational rheology, *Comput. in Chem. Engng.* **19** (1995) 647- 669.

[176] N. Phan-Thien and H.S. Dou, Parallelisation of an unstructured finite volume code with PVM: viscoelastic flow around a cylinder, *J. Non-Newtonian Fluid Mech.* **77** (1998) 21-51.

[177] R. Ahmed, R.F. Liang and M.R. Mackley, The experimental observation and numerical prediction of planar entry flow and die swell for molten polyethylenes, *J. Non- Newtonian Fluid Mech.* **59** (1995) 129-153.

[178] W.H. Hartt and D.G. Baird, The confined flow of polyethylene melts past a cylinder in a planar channel, *J. Non-Newtonian Fluid Mech.* **65** (1996) 247-268.

[179] C. Beraudo, A. Fortin, T. Coupez, Y. Demay, B. Vergnes and J.F. Agassant, A finite element method for computing the flow of multi-mode viscoelastic fluids: comparison with experiments, *J.Non-Newtonian Fluid Mech.* **75** (1998) 1-23.

[180] A.C.B. Bogaerds, W.M.H. Verbeeten, G.W.M. Peters and F.P.T Baaijens, 3D viscoelastic analysis of a polymer solution in a complex flow, *Comp. Meth. Appl. Mech. Engng.* **180** (1999) 413-430.

[181] A.W. Liu, D.E. Bornside, R.C. Armstrong and R.A. Brown, Viscoelastic flow of polymer solutions around a periodic, linear array of cylinders: comparisons of predictions for microstructure and flow fields, *J. Non-Newtonian Fluid Mech.* **77** (1998) 153-190.

[182] E. Mitsoulis, Numerical simulation of entry flow of fluid S1, *J. Non-Newtonian Fluid Mech.* **78** (1998) 187-201.

[183] J.F.M. Schoonen, F.H.M. Swartjes, G.W.M. Peters, F.P.T. Baaijens and H.E.H. Meijer, A 3D numerical/experimental study on a stagnation flow of a polyisobutylene solution, *J. Non-Newtonian Fluid Mech.* **79** (1998) 529-561.

[184] M.A. Zirnsak and D.V. Boger, Axisymmetric entry flow of semi-dilute xanthan gum solutions: prediction and experiment, *J. Non-Newtonian Fluid Mech.* **79** (1998) 105-136.

[185] W.R. Burghardt, J.M. Li, B. Khomami and B. Yang, Uniaxial extensional characterization of a shear thinning fluid using axisymmetric flow birefringence, *J. Rheol.* **43** (1999) 147-165.

[186] G.W.M. Peters, J.F.M. Schoonen, F.P.T. Baaijens and H.E.H. Meijer, On the performance of enhanced constitutive models for polymer melts in a cross-slot flow, *J. Non-Newtonian Fluid Mech.* **82** (1999) 387-427.

[187] B. Yang and B. Khomami, Simulations of sedimentation of a sphere in a viscoelastic fluid using molecular based constitutive models, *J. Non-Newtonian Fluid Mech.* **82** (1999) 429-452.

[188] J. Remmelgas and L.G. Leal, Computational studies of the FENE-CR model in a two-roll mill, *J. Non-Newtonian Fluid Mech.* **89** (2000) 231-249.

[189] D. Rajagopalan, "*Computational Analysis of Techniques to Determine Extensional Viscosity from Entrance Flows*", submitted to *Rheol. Acta* (Sept. 1999).

[190] J.C. Heinrich, P.S. Huyakorn, O.C. Zienkiewicz, and A.R. Mitchell, an upwind finite element scheme for two-dimensional convective transport equation, Int. J. Num. Meth. Eng. **11** (1977) 134-143.

[191] R.Prabhakar, J.Ravi Prakash, and T.Sridhar, Effect of configuration-

dependent intermolecular hydrodynamic interaction on elastocapillary thinning and breakup of filaments of dilute polymer solutions, J. Rheol. **50**(6), (2006) 925-947

[192] V.C. Barroso, J.M. Maia, Evaluation by means of stress relaxation (after a step strain) experiments of the viscoelastic behavior of polymer melts in uniaxial extension, *Rheol. Acta* **41** (2002) 257-264.

[193] M.A. Fontelos, J. Li, On the evolution and rupture of filaments in Giesekus and FENE models, *J. Non-Newtonian Fluid Mech.* **118** (2004) 1-16.

[194] K.S.Sujatha, H.Matallah, M.J.Banaai, M.F. Webster, Modelling step-strain filament-stretching (CaBER-type) using ALE techniques, *in press J. Non-Newtonian Fluid Mech. (2007)*